AD-A120 516 SHOCK-INDUCED CHEMICAL REACTIONS IN CONDENSED MATTER 1/3
(U) WASHINGTON STATE UNIV PULLMAN DEPT OF PHYSICS
G E DUVALL ET AL. AUG 82 N00014-77-C-0232

UNCLASSIFIED F/G 20/13 NL

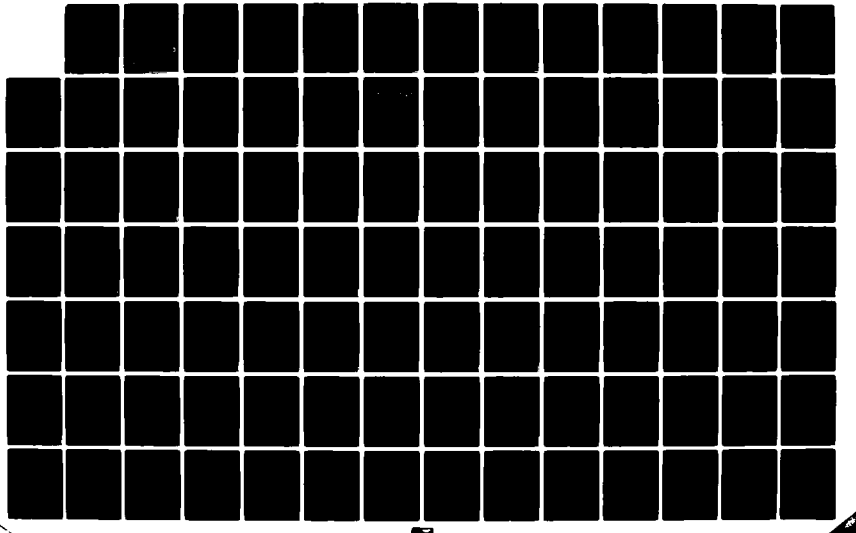

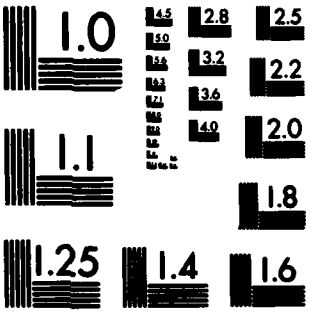

SECURITY CLASSIFICATION OF THIS PAGE (When Data Entered)

(12)

REPORT DOCUMENTATION PAGE

READ INSTRUCTIONS BEFORE COMPLETING FORM

1. REPORT NUMBER	2. GOVT ACCESSION NO. AD-A120 516 / 3. RECIPIENT'S CATALOG NUMBER
4. TITLE (and Subtitle) Shock-Induced Chemical Reactions in Condensed Matter	5. TYPE OF REPORT & PERIOD COVERED Technical, 4/1/78 - 6/30/82
	6. PERFORMING ORG. REPORT NUMBER
7. AUTHOR(s) George E. Duvall, Principal Investigator; Stephen A. Sheffield, Kendal M. Ogilvie; C. Robert Wilson, Paul M. Bellamy	8. CONTRACT OR GRANT NUMBER(s) N00014-77-C-0232
9. PERFORMING ORGANIZATION NAME AND ADDRESS Physics Department Shock Dynamics Lab. Washington State University Pullman, WA 99164-2814	10. PROGRAM ELEMENT, PROJECT, TASK AREA & WORK UNIT NUMBERS
11. CONTROLLING OFFICE NAME AND ADDRESS Office of Naval Research 800 N. Quincy Street Arlington, VA 22217	12. REPORT DATE August, 1982
	13. NUMBER OF PAGES
14. MONITORING AGENCY NAME & ADDRESS (if different from Controlling Office) Office of Naval Research, Resident Representative University District Bldg, Rm 422 1107 NE 45th Street Seattle, WA 98195	15. SECURITY CLASS. (of this report) UNCLASSIFIED
	15a. DECLASSIFICATION/DOWNGRADING SCHEDULE

16. DISTRIBUTION STATEMENT (of this Report)

Approved for public release; distribution unlimited

17. DISTRIBUTION STATEMENT (of the abstract entered in Block 20, if different from Report)

DTIC ELECTE OCT 19 1982 S D F

18. SUPPLEMENTARY NOTES

19. KEY WORDS (Continue on reverse side if necessary and identify by block number)

Shock Waves	Decomposition
Condensed Matter	Reaction Rate
Carbon Disulfide	Spectroscopy

20. ABSTRACT (Continue on reverse side if necessary and identify by block number)

Some background information is given on fast reactions, detonations, shock waves. Research at Washington State University on liquid CS_2 is summarized. Techniques for and results of measurements of characteristic reaction times are given in Section IV. A double shock method was used, a double wave observed, and times ranged from less than 10 nsec at 150 kb to several hundred nsec at 80-90 kbars. An induction time was observed in some experiments and a quasi-coherent electrical signal appears to have

DD FORM 1 JAN 73 1473

SECURITY CLASSIFICATION OF THIS PAGE (When Data Entered)

generated in the reaction process. Reflection and absorption spectroscopy are reported in Section V. Reflection measurements show that the shocked liquid behaves like a poor conductor in the spectral range 2500 - 4000 Å for shock pressures greater than about 20 kb. Transmission measurements show that extinction extends into the visible as shock pressures increase. The shift is linear with pressure about 20 kbars, but the dependence is more complicated at higher pressures. The observations do not appear to be compatible with static pressure and temperature measurements, but this observation requires further substantiation.

SHOCK-INDUCED CHEMICAL REACTIONS IN CONDENSED MATTER

SHOCK-INDUCED CHEMICAL REACTIONS IN CONDENSED MATTER

George E. Duvall, Principal Investigator
Stephen A. Sheffield*
Kendal M. Ogilvie†
C. Robert Wilson
Paul Bellamy

Shock Dynamics Laboratory
Department of Physics
Washington State University
Pullman, Washington 99164

FOREWORD

The research described here has been a group effort but S. A. Sheffield and K. M. Ogilvie have been the major contributors through their dissertation efforts which are summarized in Sections IV and V. Their dissertations, which are available from the Washington State University Library, contain much more detail than is given here, and they should be consulted by persons planning research in this field. The format is not uniform throughout. To make it so would have introduced more errors than I care to contemplate. However, it is uniform within sections, and references are listed at the end of each section.

The report contains a good deal of background information on shock-induced reactions. This may be useful to those unfamiliar with the field. Others will want to concentrate on Sections IV and V. The report was assembled in haste and flows less smoothly than I would like, but I hope it will serve a useful purpose.

I had intended to give a searching examination of the various physical mechanisms of shock-molecule interactions in Section VI, but it turned out to be too time-consuming and to speculative, so it will wait until another time.

The report was assembled by Ms Debra Maggiora, who performed a minor miracle in reordering figure numbers, references, etc. Errors remaining are, I'm afraid, mine rather than hers. Also, I am grateful to suggestions and comments made by P. S. P. Wei of the Boeing Aerospace Company.

G. E. Duvall

CONTENTS

FIGURES AND TABLES

I. INTRODUCTION

1.1 Fast Reactions

An obvious fact, often ignored, is that chemical reactions and continuum dynamics are essentially and unavoidably coupled in principle. Only in the limits of weak waves, very slow reactions or very small samples are they uncoupled.

The constitutive relations for a chemically reacting substance consist of an equation of state for the unreacted substance, an equation of state for the reaction products, and a rate equation which couples mechanical and chemical parameters. For example

$$\dot{p} = C_F^2 \dot{\rho} + J\dot{\alpha} \tag{1a}$$

$$\dot{T} = A\dot{p} + B\dot{\alpha} \tag{1b}$$

where C_F is the frozen sound speed and the coefficient J depends on the rates of change of energy and volume with α. J may be positive or negative depending on the heat of reaction and volume of the reaction products.[1,2] For one dimensional linearized plane flow Eq. (1a) yields

$$\frac{\partial^2 p}{\partial t^2} - C_F^2 \frac{\partial^2 p}{\partial x^2} = J\frac{\partial^2 \alpha}{\partial x^2}$$

The reaction acts as a source term for the pressure waves. A more complete formulation would show that these waves, in turn, heat the medium and this heat may cause the reaction to spread.

The reaction may be called "fast" if the characteristic time for completion is less than the largest dimension of the system divided by the frozen sound speed. The strengths of waves normally required to produce reactions are large enough that non-linear effects come into play, and in such cases shock waves are formed. Thus we come to the subject of this report on shock-induced chemical reactions. It is evident from this brief discussion that there is adequate theoretical reason to investigate the dynamics of chemical reactions in material media even without practical considerations. The latter, however, exist in abundance. In fact, current interest in the mechanisms of shock-induced chemical reactions in condensed matter stems from two practical problems: detonation processes in high explosives and remarkable chemical changes reported by Soviet scientists in materials recovered after having been shocked to high pressure.

1.2 Explosions--A Relation between Shocks and Chemical Reactions

Alfred Nobel, in 1863, introduced the detonator to initiate nitroglycerine and showed "the first insight into the important role of a strong shock, as distinct from heating, in the process of initiation."[3] This was the beginning of the modern era of using high explosives in rock breaking applications.

During this same period, the theory of shocks was developing, primarily applied to gases. The work by Rankine[4] in 1869 and Hugoniot[5] in 1887 concerning the statement of the conservation laws for a steady shock resulted in what is now known as the Rankine-Hugoniot jump conditions. These relations form the cornerstone for steady shock theory today.

Chapman[6] in 1899 and Jouguet[7] 1905 used the theory of shocks to develop a theory to explain the steady detonation problem and thus began

to link, in theory, shocks to the chemical reaction which takes place in a detonating high explosive.

In 1942, von Neumann[8] developed a theory that incorporated shock theory into the reacting part of a steady detonation wave. He theorized that there are a number of partially reacted Hugoniots between the unreacted and the fully reacted Hugoniots. Since the unreacted explosive cannot be expected to react before the shock wave hits it, he argued, the shock carries it to a very high pressure and then as reaction occurs, the locus of states traverses the partially reacted Hugoniots and finally ends up at the fully reacted steady state corresponding to the Chapman-Jouguet state.

The von Neumann model is shown in Fig. 1 where OC is the Rankine-Hugoniot (R-H) curve of the unreacted explosive and ABD is the R-H curve of the reaction products. The dotted line OC is the Rayleigh line connecting the initial and shock states in the explosives. The assumptions of the model are that i) the inert material is shocked to the state C so rapidly that no reaction occurs, and ii) that the flow is one-dimensional and steady in coordinates attached to the shock front. The consequences of these assumptions are that the locus of states starts at O, rises rapidly to C, and decreases more slowly to the "Chapman-Jouguet" (C-J) point B as the reaction progresses to completion. The resulting profile is shown schematically in Fig. 2. The region to the left of the C-J plane is assumed to be inert and is often called the (G. I.) Taylor wave. It expands according to the flow equations of an inert gas.

This model was described independently by Zeldovich[9] and Doering.[10] It is usually called the "ZND" model. The ZND theory is quite successful in describing the relations among mechanical variables in steady detonation of condensed explosives. Elaborate, semi-empirical computer codes exist for relating chemical formulations to detonation pressures and velocities[11] in such cases. It is now believed that both fundamental assumptions are violated to some degree in some instances: i.e., in some cases there may be reaction in the shock front, and flow may be non-steady and to some degree multi-dimensional.

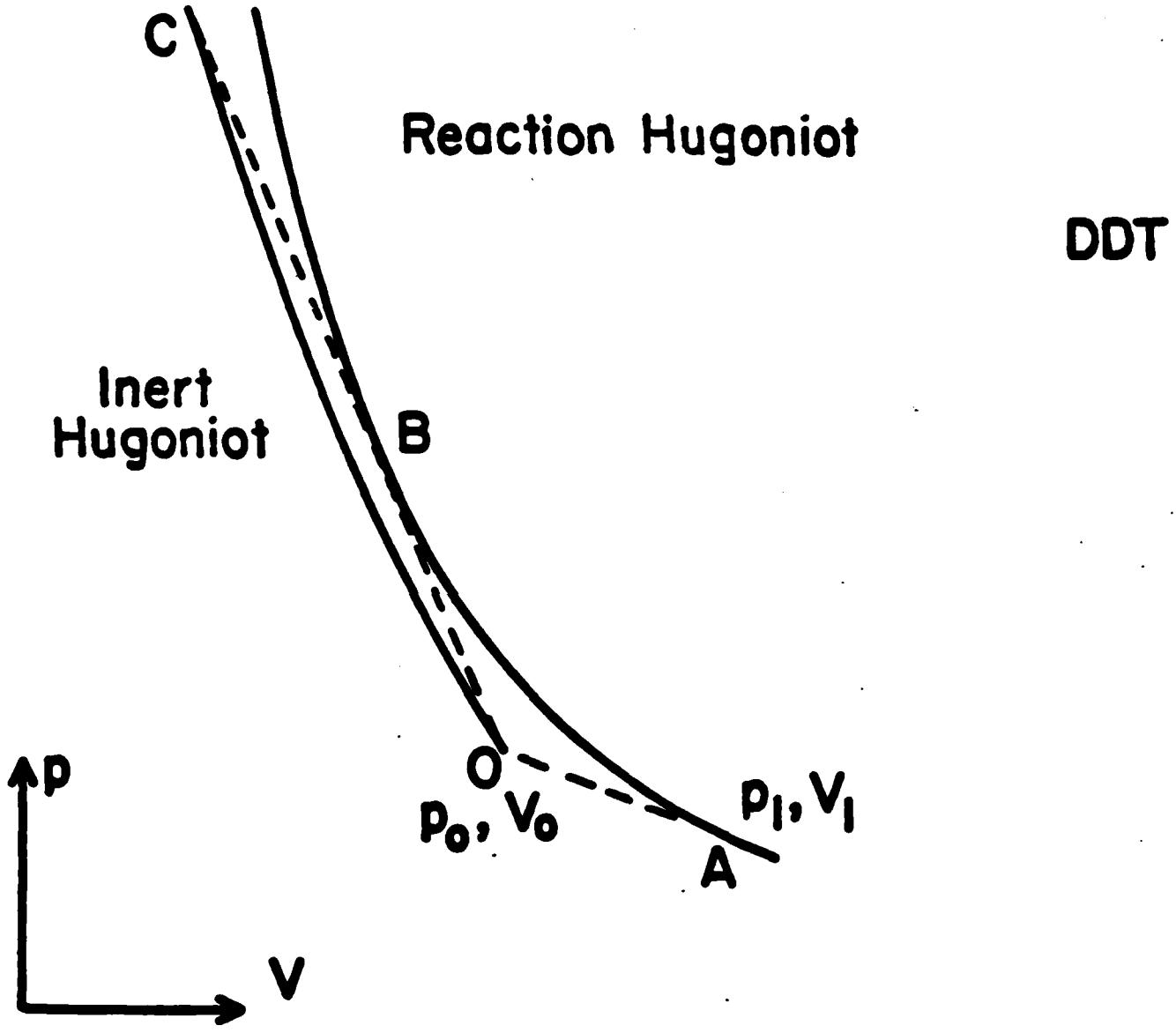

Fig. 1 The ZND Detonation Model in the P-V Plane.

C-J, ZND THEORY

NO REACTION IN SHOCK FRONT
COMPLETE REACTION IN "REACTION ZONE"
D=U+C AT END OF REACTION ZONE
C-J HYPOTHESIS

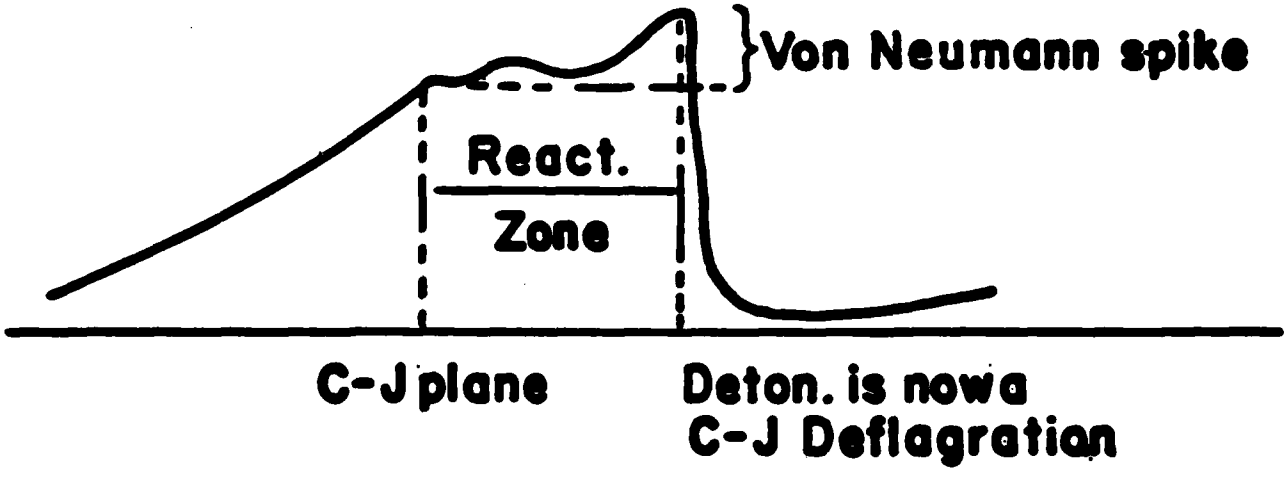

Fig. 2 Schematic Representation of Pressure Profile Produced by a steady ZND Detonation.

Of more importance than these questions are those relating to the two principal practical problems of detonation: will a given chemical substance detonate reliably in a particular configuration, and how sensitive is it to accidental initiation? These are usually formulated as the "critical" or "failure diameter" and "initiation" problems. The latter is sometimes called the "DDT" problem: Deflagration to Detonation Transition.

1.2.1 Critical Diameter for Detonation

Theories of the critical diameter have been given by H. Jones,[13] Eyring et al.,[14] Wood and Kirkwood,[15] V. Rozing and Iu. B. Khariton,[16] Dremin,[17] Chaiken and Edwards,[18] and Apin and Bobylev.[19] Less encompassing contributions have been made by many others. Khariton, Jones and Dremin address the problem of cooling of the reaction zone near the boundary of the detonating charge by the rarefaction which originates where detonation front and charge boundary intersect. Eyring et al. and Wood and Kirkwood developed the hydrodynamics of curved detonation fronts in some detail and applied their results to finite cylinders with homogeneous first order reactions. Apin and Bobylev and Chaiken and Edwards have considered the problems of grain burning in powered and heterogeneous explosives. Each of these theoretical developments has had some success in correlating data on diameter-dependence of detonation velocity in some substances. None of them has been used successfully to predict failure diameter in a substance for which steady detonation has not been demonstrated. Moreover, each of them appears to fail in some critical way when applied to a variety of detonating systems.

For example, the diameter dependence of detonation velocity in liquid TNT and nitromethane is fitted by the theory of Eyring et al., but a variety

of high-density heterogeneous explosives show unrelated behavior.[20] The Wood and Kirkwood theory relates detonation velocity to curvature of the wave front near the charge axis. Curvature is difficult to measure, but in at least two cases it appears to fit data for heterogeneous explosives passably well.[20,21] Enig and Petrone found that Dremin's quenching theory explains the temperature dependence of detonation velocity in nitromethane[22] but Titov et al., who measured critical diameters in cast TNT at temperatures of 20.4, 77.4, and 291°K, found that changes with temperature had the wrong sign, if Arrenhius kinetics apply, whatever theory is used.[23]

Chaiken and Edwards[18] have gone a bit farther than others inasmuch as they have explicitly introduced two different reaction processes in a simplistic theory which produces a pleasing correlation of critical diameter measurements among various Group I and Group II explosives; but their theory is incapable of predicting critical diameters from fundamental physical, chemical and geometric properties.

The near-success of these theories of detonation based on ad hoc assumptions about the reaction process and the role of the shock in initiating reactions has encouraged workers in the field to believe that just a slight improvement in the descriptive parameters may be all that is required to enable us to understand non-ideal detonation processes. But results experienced to date do not justify such optimism and suggest, by implication, that what is required is a more fundamental look at shock waves and the chemical reactions they produce. Condensed explosives have some characteristics which tend to disqualify them as suitable subjects for studies of this kind in the laboratory. The reacting molecules are normally complex, so the reactions will be complex. Reaction zones in explosives which detonate in laboratory sizes are small, so the

resolution required for studies in the reaction zone is inordinately large. And the destructive action of explosives complicates the experiments, both in preparation of specimens for study and in containment of explosions.

1.2.2 Initiation of Detonation

Accidents in the use of explosives were common in early years. Their causes were cloaked in mystery and attempts to clarify and categorize explosives, handling, and safety problems were manifold. One result of this concern was development of a battery of tests for rating the safety of any given explosive formulation: drop tests, thermal tests, spark tests, friction tests, etc. Operation of the tests was not well understood. Nonetheless, a manageable situation had been reached by World War II, though accidents had not been eliminated. During World War II there was strong interest in the explosive process, in new explosives, and in using old explosives in new ways. The scientific community was brought into the field to an unprecedented extent, and more detailed formulations of the problems of initiation and detonation were developed than ever before.[24-28]

It was realized a generation ago that experiments in which initiation of detonation was produced by single passage of a shock wave offered potential for understanding the initiation process that is absent in drop tests. Various versions of the shock test have been used,[29] but the flying plate test is most attractive because of its relative simplicity of interpretation, based on assumptions of one-dimensional plane flow.[30]

In the flying plate experiment a uniform shock wave of duration, t, determined by the flyer thickness is generated. Amplitude of the shock wave is determined by speed and equation of state of the flyer and by the equation

of state of the explosive sample. Observations which can be made are limited. Mean velocity of the shock wave in the sample can be determined as a function of sample thickness; recently, pressures recorded by gauges imbedded in the sample have been reported.[37,38] Photographic observations can be made, and if the sample is transparent, these may give detailed information about the speed and local character of the shock and the induced reaction. The principal results of such experiments have been to define values of mechanical parameters which are required to initiate detonation and to verify the speculation that the explosive reaction may start at flaws or inhomogeneities, or that it may (apparently) be a bulk phenomenon labelled "thermal explosion." As an example of the mechanical parameter criterion, it is found that, for some explosives, detonation is initiated when P^2t exceeds a characteristic value. For other explosives the exponent of P may differ from two.

Detailed models of the evolution of the initiating reaction into a stable detonation wave have been built for comparison with plate or other experiments, and these meet with varying degrees of success. Difficulties are probably due to the use of relatively simple models for the reaction process and for the enormous variations in chemical and physical properties of explosives.

In attempting to define the initiation problem in a way which points toward possible solutions, it is useful to divide the process into several reasonably distinct sub-processes. No such classification is unique, but the following division provides a framework for considering various aspects of the total problem:

1. Microscopic physical conditions required to start the chemical reaction.

If initiation is mechanical or thermal, stress, time and temperature must be prescribed. The initiation may be heterogeneous or homogeneous, though given the nature of condensed matter, apparently homogeneous reactions are simply heterogeneous on a small scale. Critical dimensions must also be included in this determination: The volume of material reacting must exceed some critical size in order for the reaction to grow; or there must be adjacent sites which can combine to produce an overall stable volume. If the initiation is not mechanical or thermal, as, e.g., photoinitiation, there may be other physical factors which are important, like bond resonance. For thermally induced reaction, the reaction parameters and their variations with pressure or stress must be determined. For mechanical initiation, the creation of inhomogeneous sites must be described.

2. Mechanisms by which the initiation conditions are established in any particular initiation process.

For thermal and mechanical processes which can be treated as homogeneous, where thermal explosion theories are believed to apply, this is a relatively simple problem. The available energy is simply distributed over the heated or shocked or compressed volume in a suitably uniform way. For heterogeneous initiation the problem is much more difficult. Gamow[24] treated initiation of granular explosives by assuming that mechanical energy of compression was irreversibly converted to heat

through friction and that this heat was distributed throughout the explosive grains in a manner defined by the heat conduction equations. Other mechanisms, including jetting, fracture, adiabatic compression have been invoked by various workers.

Afanas'ev and Bobolev[31] have carried out a thorough and careful analysis of drop tests and concluded that the evidence is overwhelming that the initiation process is heterogeneous. They have ventured to suggest that the mechanism responsible for the heterogeneity is shear-induced plastic flow or slip. However, they have not taken into account the possibility that the rate law at high temperatures and pressures is quite different from that at low temperatures and pressures.[32] Other observations, as well as theoretical considerations, certainly suggest very strongly that initiation is heterogeneous.[29]

3. Processes by which the initial reactions spreads from a point or set of points and becomes a progressing volume reaction with a well-defined front, i.e., a deflagration.

In the stage before the reaction becomes self-supporting, it must be supported by the initiating agency. In the case of mechanical or thermal initiation, this means that supporting temperature and pressure must be maintained until the rate of release of energy from the reaction equals or exceeds losses to the surrounding, unreacted material. The processes of growth of the reaction during this critical period depend entirely on detailed properties of the explosive. If initiation occurs

at a few points, well-separated, growth of the individual reaction volume is controlling. It may proceed along planar flaws, it may be quasispherical, or it may have a strongly random component in a mixture of binder and subcritical grains. Pressure increments resulting from incremental reaction may or may not be important in promoting the reaction, depending on both chemical and physical properties. If initiation points are closely spaced so that the reaction is quasi-homogeneous, the reacting volume may be sufficiently large that when the reaction has proceeded beyond a critical point, it may change from subcritical to supercritical nearly discontinuously. Construction of a variety of theoretical models for various geometries and properties may shed useful light on this step.

4. Processes involved in the transition from deflagration to detonation.

Bowden[28,33] and Bobolev and Dubovik[34-36] have mapped the progress of reactions in small samples initiated in impact machines. They found the reaction front accelerating smoothly to a speed of a few hundred meters per second, then changing almost discontinuously to high or low order detonation. Details depend on the explosive. Experiments in which detonation is initiated by plate impact on unconfined explosives appear to show analogous behavior as indicated, for example, by gage records like those reported by Kennedy and Nunziato[37] and by Wackerle, Johnson, and Halleck.[38] It seems likely that the development of accidental explosions, typified by the detonation of rocket motors, follows a similar course, though such cases are hardly subject to careful experimental study.

It should be evident from the preceding description that the technical problems of initiation are enormous and that no simplistic analysis is likely be to effective in describing them. Microscopic processes are central to the entire problem. These consist of chemical changes in the molecules produced by the shock, defects which are produced in the shock front, and response of the explosive molecules to stress and temperature in their local environment.

The deflagration to deformation transition is particularly important in thermal initiation. Some notes on the logical framework for this process are given in Appendix A.

One of the characteristics of explosives which makes microscopic modelling difficult is that they are usually rather large molecules, so reaction paths are many and complex. Another difficulty is in the violence and speed of reaction, which places severe restraints on the kinds of measurements which can be made. It is a fundamental precept of research that if the problem one wishes to understand is too complicated to understand, then a simpler problem embodying some aspects of the real problem is studied. This suggests that, instead of studying explosives with large molecules, one study explosives with simple molecules; or, even better, small molecules which decompose under the action of shock waves, but not violently. A practical benefit from such study, besides the insight into explosive processes, may be an understanding of chemical processes in shock which will lead to the development of methods for synthesizing new materials.

1.3 Alteration of the Chemical and Physical Constitution of Materials by Shock

For at least sixty years investigators have been shocking samples with explosives or by impacting and examining them for shock-induced changes.[40] The intensity of this kind of investigation has increased since World War II. In the Soviet Union it has become highly refined and systematized. Several hundred papers on the shock chemistry and synthesis of condensed organic and inorganic substances have appeared in the last twenty years. Shock compression has come to be regarded in the USSR as a useful and practical technique for synthesis of materials having unusual properties, and research is continuing at a strong pace.[41]

There is substantial evidence to indicate that chemical changes wrought by shocks are not explicable in terms of pressure and temperature, but that the shock front itself is involved. Graham has called this the "catastrophic shock" effect, and has adduced considerable evidence to support its reality.[42]

In the postwar period, also, there have been a substantial number of dynamic measurements in liquids which attest to shock-induced changes in their chemical or physical states. In these experiments, properties such as opacity, conductivity, shock velocity, temperature, pressure, etc., were measured. Anomalous results in some materials have led experimenters to postulate the occurence of various types of transitions and reactions. Interpretation of such experiments is frequently confused because of similar effects produced by phase transitions and chemical reactions. A summary of experiments is contained in Table I.

Walsh and Rice[43] (1957) showed that carbon tetrachloride (CCl_4) becomes increasingly opaque in a shock, beginning at 60 to 80 kbar, and becomes completely opaque at 130 to 170 kbar. Doran and Ahrens[44] (1963) state

TABLE I --Summary of Some Shock Experiments on Liquids Showing Reactions or Transitions (From S. A. Sheffield Dissertation)

Reference	Material	Pressure Range kbars	Property Measured	Results
Walsh and Rice (1957) Ref. 43	Water	30-100	Opacity	No change
	CCl_4	10-170	Opacity	Slight opacity at 60 to 80 kbars increasing to complete opacity at 130 to 170 kbars
	Benzene (C_6H_6)	80-110	Opacity	No change
	Ethanol (C_2H_5OH)	70-110	Opacity	No change
Doran and Ahrens (1963) Ref. 44	CCl_4	170	Electrical Conductivity	Good Conductor
Cook and Rogers (1963) Ref. 60	Methanol	96-107	Shock Velocity	No transitions observed
	CCl_4	12-129	Shock Velocity	No transitions observed
	C_6H_6	5-78	Shock Velocity	No transitions observed
	CS_2	4-67	Shock Velocity	No transitions observed
Dick (1964) Ref. 45	CCl_4	28-170	Shock Velocity Elec. Cond.	No discontinuities observed. Becomes conductive starting at 70 kbars and is a good conductor at 120 kbars

TABLE I --Continued

Reference	Material	Pressure Range kbars	Property Measured	Results
Dick (continued) (1964) Ref. 45	C_6H_6	27-140	Shock Velocity Elec. Cond.	No discontinuities observed, no change in conductivity observed
Mitchell and Keeler (1968) Ref. 46	CCl_4	65-160	Elec. Cond.	Conductivity increased from 10^{-7} at 65 kbars to ≈1 at 160 kbars
David and Hamann (1959) Ref. 47	Water	33-130	Elec. Cond.	Conductivity continually increased as pressure increased
David and Hamann (1960) Ref. 48	Glycerol	160	Elec. Cond.	No change
	Acetone	160	Elec. Cond.	No change
	Water	161	Elec. Cond.	Became a conductor
	Methyl alcohol	152	Elec. Cond.	Became a conductor
	Acetic acid	175	Elec. Cond.	Became a conductor
	Propionic acid	162	Elec. Cond.	Became a conductor
Hamann and Linton (1966) Ref. 49	Water	10-130	Elec. Cond.	Conductivity increases from 10^{-7} to ~1. Postulated to be self-ionization

TABLE I --Continued

Reference	Material	Pressure Range kbars	Property Measured	Results
Dick (1968)	C_6H_6	20-400	Shock Velocity	Cusp in Hugoniot at 133 kbars
(1970) Ref. 45, 57	CS_2	20-500	Shock Velocity Elec. Cond.	Cusp in Hugoniot at 62 kbars. Conductivity increased significantly near 80 kbars
	CCl_4	30-600	Shock Velocity	Break in Hugoniot at 165 kbars
	Liq. N_2	20-400	Shock Velocity	Break in Hugoniot at 135 kbars
Voskoboiniko and Bogomolov (1968) Ref. 61	CCl_4	80-200	Temperature	No transition mentioned
	CCl_4-C_6H_6 Solution	120-160	Temperature	No transition mentioned
Kormer, Yushko, and Krishkevich (1968) Ref. 52	CCl_4	200-600	Temperature	Cusp from 200 kbars to 300 kbars. Attributed to solid-liquid phase transition
Kormer (1968) Ref. 53	CCl_4	200-600	Reflectivity	Anomalous result above 300 kbars as yet unexplained
	Water	40-100 Double shock	Opacity	Went opaque in second shock attributed to freezing

TABLE I. --Continued

Reference	Material	Pressure Range kbars	Property Measured	Results
Dick and Warnes (1970) Ref. 62	Chloroform ($CHCL_3$)	?	Shock Velocity	Transition at 250 kbars
	Hexane (C_6H_{14})	?	Shock Velocity	No transition
	Cyclohexane (C_6H_{12})	?	Shock Velocity	No transition
Yakusheva, Yakushev, and Dremin (1971) Ref. 54	C_6H_6	?	Opacity	Opaque at 135 kbars
	CCl_4	?	Opacity	Opaque at 80 kbars
	Acetone	?	Opacity	Opaque at 100 kbars
	Dichloroethane	?	Opacity	Opaque at 120 kbars
	Nitromethane	?	Opacity	Opaque at 80 kbars. All these attributed to chemical reaction
Lysne (1971) Ref. 63	CCl_4	2-12	Shock Velocity Pressure	No freezing but a non-linear particle velocity-shock velocity relationship
Lysne (1972) Ref. 64	CS_2	6 & 11	Shock Vel.& Pres.	Partial velocity-shock velocity relationships are all nonlinear at low pressures. Sound speed at zero pressure used as another data point.
	C_6H_{14}	1.4 & 3.3	Shock Vel.& Pres.	
	$CHCL_3$	3.3 & 6.2	Shock Vel.& Pres.	
	CH_2I_2	6.9 & 15.4	Shock Vel.& Pres.	

TABLE I --Continued

Reference	Material	Pressure Range kbars	Property Measured	Results
Lysne (continued) (1972) Ref. 64	C_6H_6	1.2, 5.2 & 7.2	Shock Vel.& Pres.	
	C_6H_{12}	1.8 & 4.2	Shock Vel.& Pres.	
Dick (1972) Ref. 65	Liq. Deuterium	47-500	Shock Velocity	Double shock in the 130 to 500 kbars region
	Liq. Hydrogen	47-500	Shock Velocity	Did not say but probably about the same as above
Afanasenkov et al. (1974) Ref. 56	CCl_4	Used other people's data	Calculated Hugoniot of products	Attributes temp. cusp to decomposition from 200 to 270 kbars
	CS_2	Used other people's data	" + temp. meas.	Meas. temp. 500°K higher than calculation, indicates decomposition
	C_6H_6	Used other people's data	" + temp. meas.	Meas. temp. higher than calculated, indicates pyrolysis of benzene
	Isoprene	Used other people's data	" + temp. meas.	Meas. temp. higher than calculated, indicates polymerization

TABLE I. --Continued

Reference	Material	Pressure Range kbars	Property Measured	Results
Yakushev, Nabatov, and Yakusheva (1974) Ref. 56	Acrylonitrile (CH_2:CHCN)	20-120	Shock Velocity	Cusp at 43 kbars
	Acrylonitrile (CH_2:CHCN)	?	Particle Velocity	A two wave shape was observed but considerable scatter in data, first wave corresponds to 43 kbars
	Acrylonitrile (CH_2:CHCN)	Up to 70	Light Absorption (Opacity)	At 49 kbars begins to lose transparency--opaque at 70 kbars in less than 0.1 microseconds
	Acrylonitrile (CH_2:CHCN)	21-107	Specific Resistance	At 38.3 kbars no change. At 60.3 kbars resistance very low
	Acrylonitrile (CH_2:CHCN)	5.4-43	Dielectric Permeability	Became a conductor above 43 kbars
	Acrylonitrile (CH_2:CHCN)	21-107	Shock Polarization	There is an induction time to high conductivity

TABLE I --Continued

Reference	Material	Pressure Range kbars	Property Measured	Results
Yakushev, Nabatov, and Yakusheva (continued)	Acrylonitrile (CH_2:CHCN)	240	Recover and analyze products	Large amounts of ammonia evolved on opening container. A sort, velvet black powder remained. X-ray showed lines of hexagonal graphite. Weight loss when heated at 500°C was 6.7%. The material decomposed to ammonia and carbon.
Harvey and Dick (1975) Ref. 66	Liq. Ammonia (NH_3)	20-400 at 203°K	Shock Velocity	No transition or cusps observed
Dick (1975) Ref. 57	1-3 1-4 Cyclohexadiene (C_6H_8)	?	Shock Velocity	Some evidence of a high pressure transition
	Toluene ($C_6H_5CH_3$)	?	Shock Velocity	Transition at 120 kbars
	C_6H_6	?	Shock Velocity	Transition at 133 kbars
	Cyclohexene (C_6H_{10})	?	Shock Velocity	No transition observed
	C_6H_{12}	?	Shock Velocity	No transition observed

that CCl_4 is a good conductor at 170 kbar. Dick[45] (1964) indicates CCl_4 begins to conduct at 70 kbar and is a good conductor above 120 kbar. Mitchell and Keeler[46] (1968) measured the conductivity of CCl_4 from 65 to 160 kbar and found it continuously increased by seven orders of magnitude over this range. Hamann et al.[47-49] (1959, 1960, 1966) measured the conductivities of several liquids in 150 to 170 kbar shocks and found that some were good conductors. The conductivity of water was measured at many pressures up to 130 kbar and found to continually increase; the reason for the changes was postulated to be self-ionization.

Dick[50,51,59] (1968, 1970) showed that benzene (C_6H_6), carbon disulfide (CS_2), CCl_4, and liquid nitrogen all have transitions of some kind at 133, 62, 165, and 135 kbar, respectively. Kormer et al.[52,53] (1968) indicate water becomes opaque (which they interpreted as evidence of freezing) in a double shock, and that temperature measurements of CCl_4 show it has an anomalous behavior between 200 and 300 kbar, which is attributed to a solid-liquid phase transition.

Yakusheva, Yakushev, and Dremin[54] (1971) showed that C_6H_6, CCl_4, acetone (C_3H_6O), dichloroethane ($C_2H_2Cl_2$), and nitromethane (CH_3NO_2) became opaque at pressures above 135, 80, 100, 120, and 85 kbar, respectively. They attributed this opacity to decomposition and the formation of free carbon. Afanasenkov et al.[55] (1974) measured temperatures of carbon disulfide and benzene shocked above the transition and found them to be higher (by 500°K in the case of carbon disulfide) than calculated for shock heating only. They also calculated P-V Hugoniots for postulated products of reaction and showed the P-V data for carbon disulfide and benzene above the transition to be very close to calculated values. Yakushev, Nabatov, and Yakusheva[56] (1974) measured shock velocity, particle velocity, light absorption (opacity), electrical

conductivity, dielectric permeability, and shock polarization and did recovery experiments on acrylonitrile (C_3H_3N). They observed anomalous behavior beginning about 43 kbar and explained it by saying a decomposition reaction took place. The recovery experiments supported this explanation. Dick[57] (1975) states that transitions in benzene ring materials depend on the number of carbon double bonds, with lower transition pressures associated with larger numbers of double bonds.

The anomalous behavior in liquids has been explained chiefly by three possible mechanisms: phase transitions, polymerizations, and chemical reactions. It is possible that all of these have been involved in some of the experiments while only one may have been involved in others, but separating the effects has not yet been possible. Many experimenters have looked for liquid-solid phase transitions, but only Kormer et al.[52] claim to have observed it. The idea has been expressed several times (see Ref. 43 for example) that too much ordering is required for this type of transition to take place in the microsecond time scales of a shock experiment. Chemical reactions, primarily of the decomposition or pyrolysis type, explain many of the transitions,[54-56,58] but since little is known about this process, the explanations are not yet completely substantiated. However, these recent papers[54-56] indicate that chemical reactions in other than high explosives can take place in a shock environment. They also show that reactions yield large enough changes in measureable parameters that conventional shock measurement techniques will yield accurate information about properties like reaction time if the experiments are carefully done.

REFERENCES TO SECTION I

1. Y. Horie and G. E. Duvall, "Shock Waves and the Kinetics of Solid-Solid Transitions," Proc. Army Symposium on Solid Mechanics, Baltimore, Maryland. September 1968. Published by Army Mechanics and Material Research Center (AMMRC) Watertown, MA.

2. D. J. Andrews, J. Comp. Phys. 7, 310 (1971).

3. C. H. Johansson and P. A. Persson, Detonics of High Explosives (Academic Press, Inc., New York, 1970), pp. 2-3.

4. W. J. M. Rankine, Trans. Roy. Soc. London 160, 227 (1870).

5. H. Hugoniot, Journal de l'e cole Polytechnique 58, 1 (1889).

6. D. L. Chapman, Lond. Edinb. Dubl. Phil. Mag. 47, 90 (1899).

7. E. Jouguet, J. Math. Pures. Appl. 60, 347; 61, 1 (1905).

8. J. von Neumann, "Progress Report on the Theory of Detonation Waves," OSRD Report No. 549 (1942).

9. Ya. B. Zeldovich, "On the theory of the propagation of detonation in gaseous systems." Zh. Eksp. Teor. Fix. 10:542-568 (1940). (English translation: NACA TM 1261, 1960).

10. W. Doering, Ann. Phys. 43, 421 (1943).

11. The TIGER code is an example. M. Cowperthwaite at SRI International has contributed significantly to it.

12. W. Fickett and W. C. Davis, Detonation (University of California Press, California, 1979).

13. H. Jones, Proc. Roy. Soc. (London) A189, 415 (1947).

14. H. Eyring, R. E. Powell, G. H. Duffey and R. B. Parlin, Chem. Rev. 45, 69 (1949).

15. W. W. Wood and J. G. Kirkwood, J. Chem. Phys. 22, 1920 (1954).

16. V. Rozing and Iu. B. Khariton, Dokl. Akad. Nauk SSSR 26, 360 (1939).

17. A. N. Dremin, Dokl. Phys. Chem. 147, 845 (1962).

18. R. F. Chaiken and J. C. Edwards, Acta Astronautics 3, 795 (1976).

19. A. Ia. Apin and V. K. Bobylev, Dokl. Akad. Nauk SSSR 58, 241 (1947).

20. A. W. Campbell and R. Engelke, "Diameter Effects in High-Density Heterogeneous Explosive," in Sixth Symposium (International) on Detonation (Office of Naval Research, Arlington, Virginia, 1976) ACR-221, p. 642.

21. L. G. Green and E. James, Jr., "Radius of Curvative Effect on Detonation Velocity," in Fourth Symposium (International) on Detonation (Office of Naval Research, Washington, D.C., 1965), ACR-126, p. 86.

22. J. W. Enig and F. J. Petrone, "The Failure Diameter Theory of Dremin," Fifth Symposium (International) on Detonation (Office of Naval Research, Arlington, Virginia, 1970), ACR-184, p. 99.

23. V. M. Titov, V. V. Sil'Vestrov, V. V. Kratsov and I. A. Stadnitshenko, "Investigation of Some Cast TNT Properties at Low Temperture," in Sixth Symposium (International on Detonation (Office of Naval Research, Arlington, 1976), ACR-221, p. 36.

24. G. Gamow, "Tentative Theory of Mechanical Sensitivity," NAVORD-ERM-4, 12/09/43.

25. G. B. Kistiakowsky, E. Bright Wilson, Jr., and R. S. Halford, "The Hydrodynamic Theory of Detonation and Shock Waves," in Underwater Explosion Research, Vol. 1, The Shock Wave, pp. 209-261. Published by ONR, 1950.

26. G. I. Taylor and M. Jones, "Note on the Lateral Expansion Behind a Detonation Wave," written for th Advisory Council on Scientific Research and Technical Development, Ministry of Supply (1942).

27. W. Doering and G. Burkhardt, "Contributions to the Theory of Detonation," Technical Report No. F-TS-1227-IA, Wright-Patterson AFB, Dayton, Ohio, 1949 (Translation).

28. Much work on initiation is summarized by Bowden and Yoffe in
a) Initiation of Growth of Explosion, Cambridge, 1952, and
b) Fast Reactions in Solids, Butterworths, 1958.

29. Much of this work is summarized in Energetic Materials, I, H. D. Fair and R. F. Walker, eds. (Plenum Press, NY 1977).

30. See, e.g., D. B. Hayes in Proc. of 6th ONR Detonation Symposium, p. 76, for discussion and references. This series of symposia is probably the single best source of information on progress in the field.

31. G. T. Afanas'ev and V. K. Bobolev, Initiation of Solid Explosives by Impact, Israel Program for Scientific Translations, Jerusalem, 1971.

32. H. Eyring, ONR Workshop on Denotation, October 22-24, 1979.

33. F. P. Bowden and M. P. McQuie, Nature 206, 380 (1965).

34. G. T. Afanas'ev, V. K. Bobolev, A. V. Dobovik, and V. S. Zhuchenko, in Sbornik "Vzryvnoe delo", N. 63/20, Moskva, "Nedra", p. 86 (1967).

35. V. K. Bobolev and A. V. Dubovik, Prik. Mek. i Tekh. Fiz. 2, 150 (1965).

36. A. V. Dubovik and V. K. Bobolev in Sbornik "Vzryvnoe del", No. 63/20, Moskva, "Nedra", p. 72 (1967).

37. J. E. Kennedy and J. W. Nuziato, J. Mech. Phys. Solids 24, 107 (1976).

38. J. Wackerle, J. O. Johnson, P. M. Halleck, 6th Symposium on Detonation, (ONR, 1976), p. 20.

39. M. W. Evans and P. M. Ablow, Chem. Rev. 61, 129 (1911). See also various experimental papers in the 6th Symposium on Detonation.

40. C. A. Parsons, Phil. Trans. Roy. Soc. A220, 67 (1920).

41. Various papers in Chapter I of Shock Waves in Condensed Matter-1981, Proceeding of AIP Conference, Menlo Park, California. June 23-25, 1981.

42. R. A. Graham, J. Phys. Chem. 83, 3048 (1979).

43. J. M. Walsh and M. H. Rice, J. Chem. Phys. 26, 815 (1957).

44. D. G. Doran and T. J. Ahrens, Stanford Research Institute Report PGO-4100 (1963).

45. R. D. Dick, Bull. Am. Phys. Soc. 9, 547 (1964).

46. A. C. Mitchell and R. N. Keeler, Rev. Sci. Instr. 39, 513 (1968).

47. H. G. David and S. D. Hamann, Trans. Faraday Soc. 55, 72 (1959).

48. H. G. David and S. D. Hamann, Trans. Faraday Soc. 62, 1043 (1960).

49. S. D. Hamann and M. Linton, Trans. Faraday Soc. 62, 2234 (1966).

50. R. D. Dick, Bull. Am. Phys. Soc. 13, 579 (1968).

51. R. D. Dick, J. Chem. Phys. 52, 6021 (1970).

52. S. B. Kormer, K. B. Yushko, and G. V. Krishkevich, Soc. Phys. JETP 27, 879 (1968).

53. S. B. Kormer, Sov. Phys. Uspk. II, 229 (1968).

54. O. B. Yakusheva, V. V. Yakushev, and A. N. Dremin, High Temp.-High Pres. 3, 261 (1971).

55. A. N. Afanasenkov, I. M. Voskoboinikov, M. R. Gogulya, and A. I. Karkov, Fiz. Goreviya i Vzryva 10, 392 (1974).

56. V. V. Yakushev, S. S. Nabatov, and O. B. Yakusheva, Fiz. Goreviya i Vzryva 10, 583 (1974).

57. R. D. Dick, Bull. Am. Phys. Soc. 20, 1514 (1975).

58. S. D. Hamann, "Effects of Intense Shock Waves," in Advances in High Pressure Research (Academic Press, 1966) Vol. 1, edited by R. S. Bradley.

59. R. D. Dick, "Shock Wave Compression of Benzene, Carbon Disulfide, Carbon Tetrachloride, and Liquid Nitrogen," Los Alamos Scientific Lab. Report LA=3915 (1968).

60. M. A. Cook and L. A. Rogers, J. Appl. Phys. 34, 2330 (1963).

61. I. M. Voskoboinikov and V. M. Bogomolov, JETP Letters 7, 264 (1968).

62. R. D. Dick and R. H. Warnes, Bull. Am. Phys. Soc. 15, 1626 (1970).

63. P. C. Lysne, J. Chem. Phys. 55, 5242 (1971).

64. P. C. Lysne, J. Chem. Phys. 57, 492 (1972).

65. R. D. Dick, Bull. Am. Phys. Soc. 17, 1092 (1972).

66. W. B. Harvey and R. D. Dick, Bull. Am. Phys. Soc 20, 48 (1975).

II. PROBLEMS OF SHOCK EXPERIMENTATION

The results of experiments to be described in this report are probably of greater interest to those outside the "shock wave community" than to its members. A great deal of work has been done on chemistry stimulated by shock waves in gases. Very little has been done on condensed matter. The condition of shock experiments in solids and liquids are quite different from those in gases in various particulars. Pressures are very much higher and temperatures are much lower. Duration of the shocked state is limited to nanoseconds or microseconds compared to milliseconds for gases. Very important is the fact that there is no "rigid wall" for lateral confinement of condensed matter shocks. This implies that transverse probing of the state behind the shock is not usually feasible--existence of the unique state of uniaxial strain which makes the one-dimensional, plane, time-dependent shock easy to analyze is limited by the inexorable inward progress of lateral rarefactive waves generated at free surfaces by passage of the shock. This dictates the shape of the sample. It must be a disk of thickness small compared to its lateral dimensions and shock fronts must be parallel to the face of the disk. Diagnostic probes must sample changes in the direction of shock propagation and only in the region where the uniaxial strain state is retained for the duration of the experiment.

Probes are generally of two types: those which sample time-varying conditions in a plane parallel to the shock front, and those which sample a finite volume extending a significant distance in the direction of propagation. The former are exemplified by free surface measurements, quartz gages, electromagnetic velocity (EMV) gages and manganin resistance gages. The

latter are required for resistivity, piezoelectricity, and optical transmission measurements. Examples of EMV gage and optical transmission measurements are described in Sections IV and V, respectively.

Generation of shock waves is by the impact of explosion or of a projectile against a sample. The impact must be planar within a few seconds of arc, and diagnostic instruments must be activated within the few hundreds of nanoseconds when the sample is in the shocked state. Picosecond timing has become commonplace in various kinds of pulsed laser experiments, but is yet to be achieved in shock experiments. The reason is that "mechanical jitter" due to uncertainty in positions and dimensions of physical components normally ranges from about 50 to 250 nsecs, depending on the particular experiment.

The experiments are, of course, single shot affairs. A few microseconds after impact, the event and the experiment are over. A very good experimentalist with a good machinist and some additional technical help, can build and fire a difficult shot about every two weeks, provided the design does not change and there are moderately small parametric changes. This does not include analysis time, which can easily add another week and a half per shot, or experiment design time.

The consequences of this slow rate are that each experiment must be designed to give as much information as possible and that design must be careful and thorough, if anything at all is to be achieved.

Experimentation is further complicated by the generating mechanism. Whether it is explosive or projectile impact, the presence of the generator severely restricts access to the impact face of the cell. This has little effect on in-plane gage measurements. It presents serious problems for volume-dependent measurements. In some cases it is possible to get around these restrictions, as can be seen in Section V.

There is a further problem in doing new kinds of shock experiments. There is considerable lore and technical art involved in shock experimentation. When a new problem arises, like spectroscopy, it takes some time and creative skill to develop the necessary arts. To do spectroscopy, for example, suitable light sources must be developed, windows which remain transparent under shock must be found, luminescence of structural materials must be examined, etc.

Furthermore, it is necessary to develop an equation of state for each substance or mixture studied. In experiments where shocks are created by projectile impact, the principal controllable parameter which determines shock strength is projectile velocity. From this it is necessary to calculate pressure and temperature in the sample as a function of time. This is done by combining the equations of continuum mechanics with equations of state for each significant substance in the experiment: impactor, front of cell, sample, back of cell. Equations of state for condensed materials are not usually well known, and creating one from available data is a mixture of art and science. Since pressure in a shock wave can be obtained directly from the jump conditions, pressures calculated from these synthesized equations of state will be reasonably accurate. Temperatures, however, are not normally measured in shock experiments, so there is essentially no check on temperature values obtained from the synthetic equations of state. Consequently, the calculated temperature is more in the nature of an ordering parameter than a true temperature. This is an unfortunate circumstance which can be corrected in time; for the present, it can only be noted.

One of the important data sets used to synthesize an equation of state is the R-H curve for ambient initial conditions. These exist for many materials. When they do not, additional experiments are required to produce one.

III. CHOICE OF SAMPLE MATERIALS

It should be evident from the comments of the preceding section that investigation of reactions in a given substance or mixture of substances will require a major investment of time and funds. This means that careful thought must be given to sample selection.

There should be good reason to believe that (i) the system selected will react under pressure and temperature conditions which can be reached with available experimental facilities, (ii) its study will lead to enlightenment on some chemical or physical principal, (iii) the scale of reaction, i.e., time and space, lies in the accessible range of experimentation, (iv) safety hazards can be handled adequately. In our case, which was a pioneering venture, there appeared to be two candidates, based on study of the literature cited in Table I, Section 1.3: acrylonitrile and liquid CS_2.

Table I shows the comparison for CS_2 and acrylonitrile. The data for the two materials are about the same except in the molecular structure and density. CS_2 has a far simpler structure and, therefore, the simpler decomposition reaction mechanism.

TABLE I --Comparison of Carbon Disulfide and Acrylonitrile as Candidates for Further Experiments

Material	Hugoniot Anomaly (kbar)	Particle Velocity at which Anomaly Occurs (mm/μsec)	Density g/cm^3	Molecular Structure	High Explosive
Carbon Disulfide (CS_2)	62	1.35	1.26	S=C=S	no
Acrylo-nitrile (C_3H_3N)	43	1.40	0.806	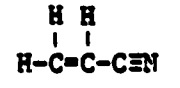	no

As indicated previously, Walsh and Rice[1] and later Cook and Rogers[2] did Hugoniot measurements on CS_2. Neither of them found any evidence of reaction although one point measured by Rice and Walsh was apparently in the reacted region.

R. Dick[3,4] did a large group of shots on CS_2 using explosive plane wave generators to provide the shocks and found the anomalous behavior to begin at 62 kbar but could not measure a two-wave structure (see Fig. 3.1). He also could not say definitely what type of reaction was occurring, although he seemed to favor the conversion to the "black, solid CS_2" first discovered by Bridgman[5] in static experiments.

Lysne[6] made two low pressure shots on CS_2 in which he measured the pressure and shock velocity, primarily to see if the data indicated that the shock velocity-particle velocity Hugoniot extrapolated to sound speed. He found no indication of anomalous behavior in the 0 to 11 kbar pressure range.

Butcher et al.[7] did a number of static high pressure tests at elevated temperatures on CS_2 to produce and study the "black solid CS_2" Bridgman had discovered earlier. From their data and Bridgman's data, they constructed a diagram that is reproduced in Fig. 3.2. They indicate the "black solid CS_2" is formed only in a relatively small region as indicated in the figure and that at temperatures and pressures above this, decomposition occurs. The regions marked decomposition is where the shock results of Dick (with the reaction occurring) are located.

Afanasenkov et al.[8] combined the work of Butcher et al.[7] and Dick[3,4] to do some interesting calculations. They assumed a decomposition reaction to carbon and sulfur was taking place and combined the carbon and sulfur Hugoniots using the stoichiometric ratio to calculate a Hugoniot for the

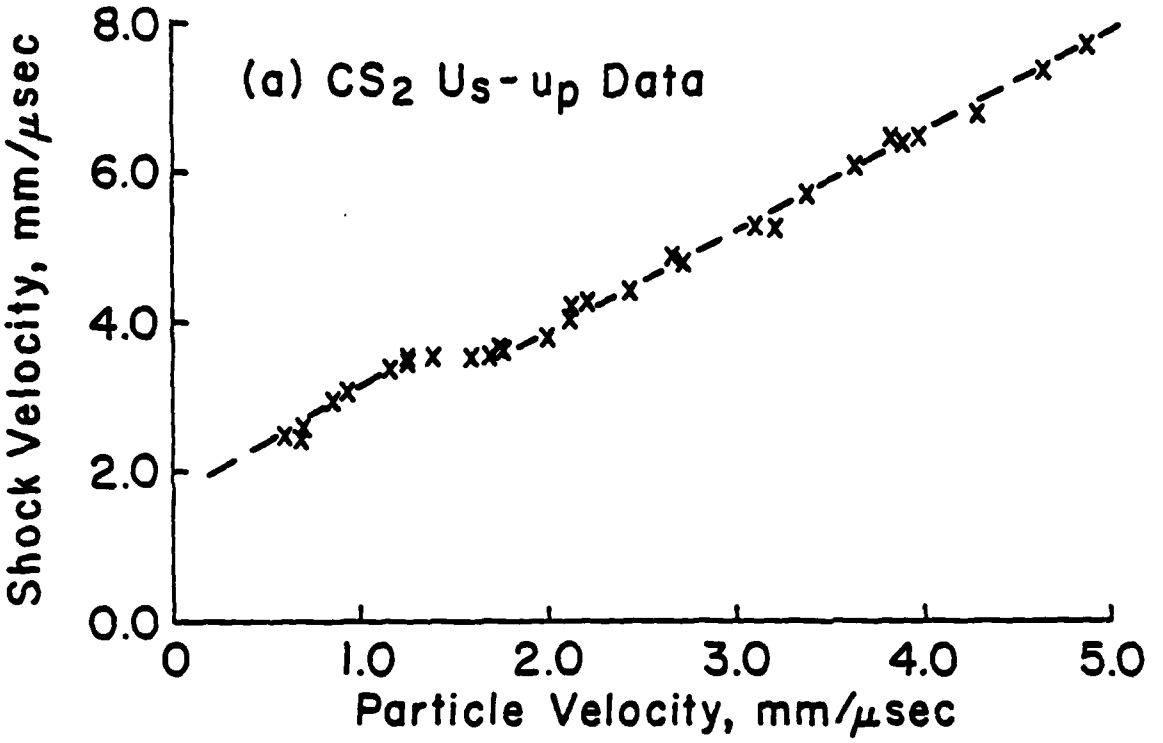

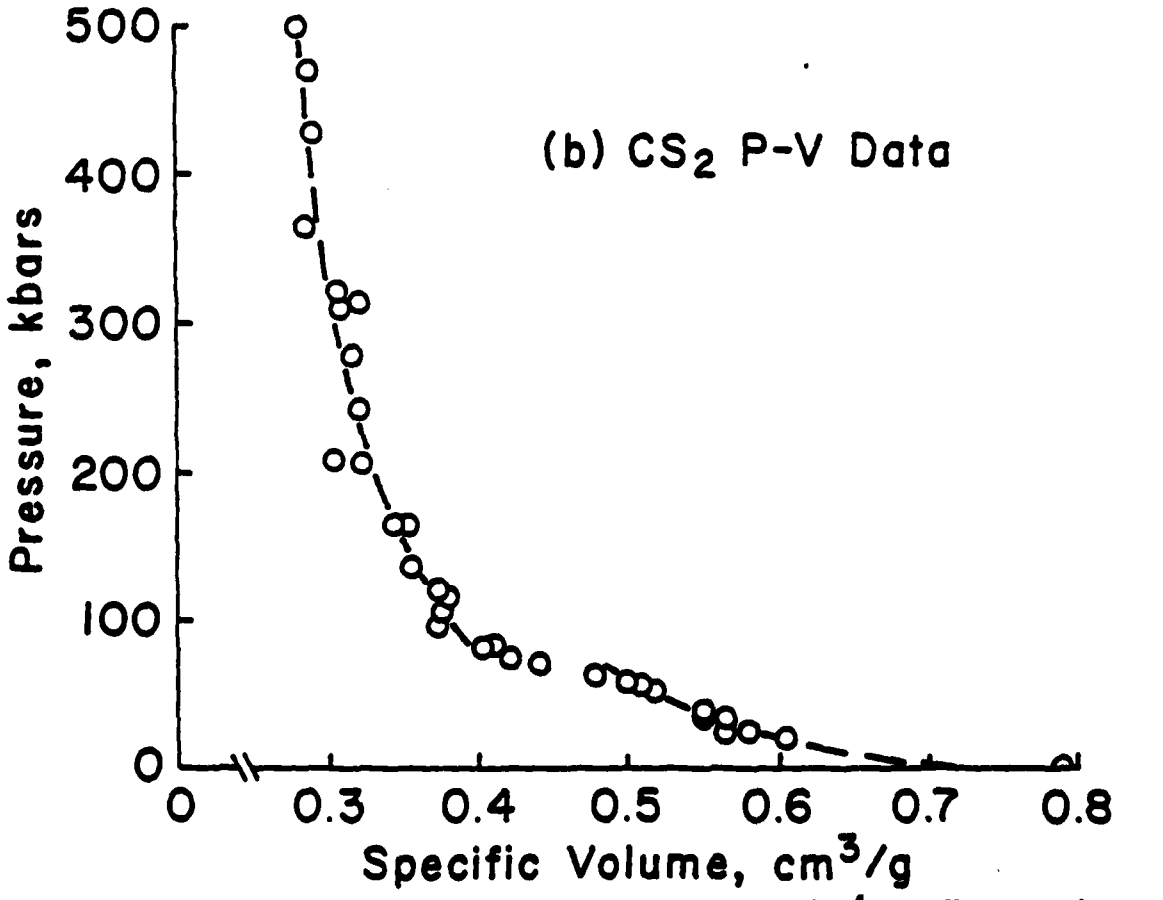

Fig. 3.1 --Plot of R. Dick's Data from Ref. [4] in U_s-u_p and P-V Space. The cusp is apparent in both plots.

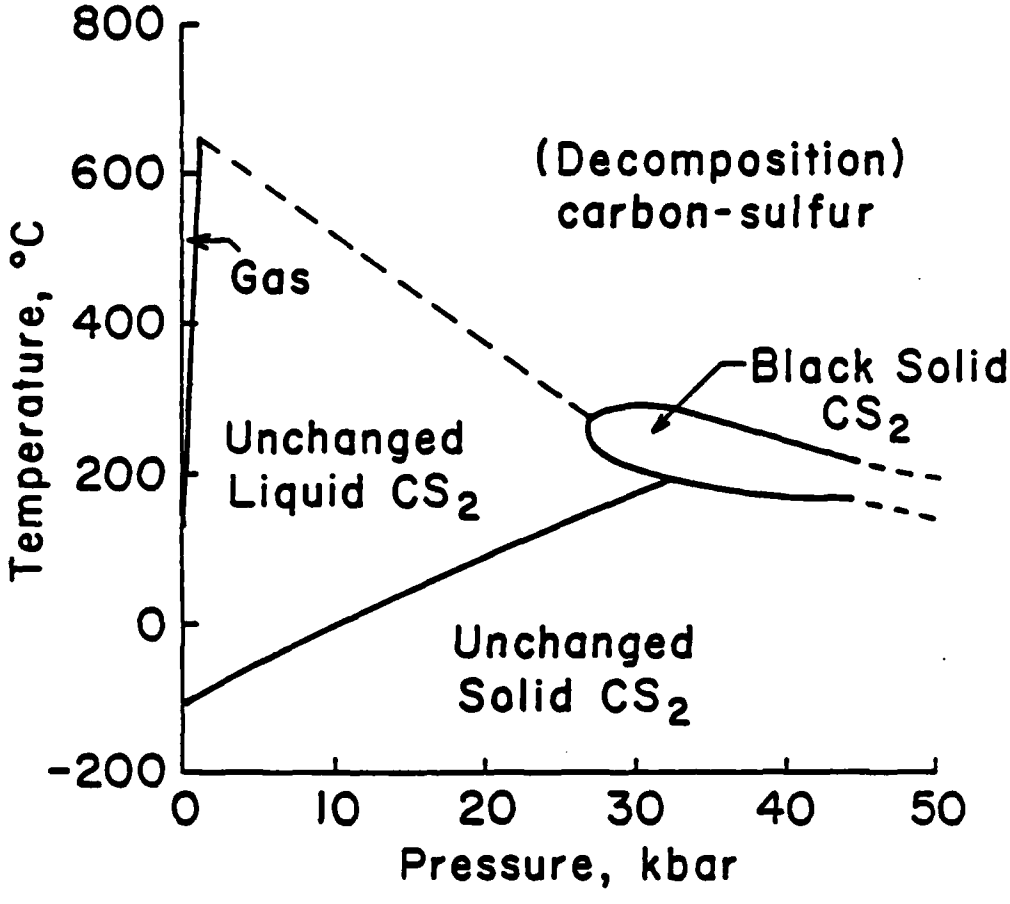

Fig. 3.2 --Temperature-Pressure Diagram Constructed by Butcher et al. in Ref. 7. The cusp observed by R. Dick occurs well up into the region marked "Decomposition."

products. This curve went right through Dick's data above the anomalous behavior. They also measured the temperature by a brightness technique and found it to be 3000°K, about 500°K higher than their calculations indicate it should be. Using both the reacted Hugoniot data and the temperature measurement they argued that a decomposition reaction was taking place.

A rather lengthy study on acrylonitrile was done by Yakushev, Nabatov, and Yakusheva[9] in which they observed a cusp in the Hugoniot at 43 kbar, based on shock velocity measurements. They also used an electromagnetic particle velocity gage and measured what appears to be a two-wave structure but they said the scatter in the data was so great that it was not possible to "establish unambiguously the nature of the second discontinuity in the mass velocity." The measurement reproduced was 12 mm into the liquid. Among several other tests, recovery experiments were done where the acrylonitrile was shocked to 240 kbar and then recovered. Upon opening they discovered the evolution of large amounts of ammonia with a black velvet powder remaining which was identified by x-ray diffraction as hexagonal graphite. Using this data they speculated the decomposition reaction is

$$CH_2{=}CH{-}CN \longrightarrow 3C + NH_3.$$

This work on acrylonitrile is the first good work done on non-explosives for the purpose of identifying a decomposition reaction taking place in a shock.

Acrylonitrile is such a complicated molecule that the reaction mechanism could involve several tens of intermediate reactions before the C and NH_3 are formed, but this work shows rather conclusively that a decomposition reaction is taking place at some point during the shocking process.

Carbon disulphide decomposition has been extensively studied because of the simplicity of its linear triatomic molecule.[10-14] The kinetics of CS_2 decomposition in the vapor phase has been studied using shock tube and optical spectroscopy techniques. The two principal works are by Gaydon and colleagues, who measured absorption spectra,[11] and Arnold and colleagues, who measured emitted light.[13] In the former work, absorption was measured for CS_2, CS and S_2. The latter two species appeared as the former disappeared, and the results were compatible with the assumption that reaction was occurring according to

$$CS_2 \longrightarrow CS + \frac{1}{2} S_2 \tag{1}$$

Arnold et al.[13] measured light emission throughout the visible spectrum. They felt their results to be incompatible with Eq. (1) and proposed

$$CS_2 + CS_2 \longrightarrow CS_3 + CS \tag{2}$$

$$CS_3 + M \longrightarrow CS_2 + S + M \tag{3}$$

They also found an induction time preceding the reaction for temperatures below 2600°K, whereas Gaydon et al.[11] found no evidence of induction. Both groups of workers agreed that the reaction was second-order in CS_2 concentration, with reaction constants

$$k_2 = 10^{14.2} e^{-43.7\text{kcal/RT}}, \quad \text{Gaydon et al.} \tag{4}$$

$$k_2 = 10^{11.53} e^{-45.2\text{kcal/RT}}, \quad \text{Arnold et al.} \tag{5}$$

In experiments where CS_2 vapor has been excited by electron impact or UV light, it appears to be common to observe spectra of CS and S but not S_2. This is peculiar because the heat of formation of S_2 relative to S under standard conditions is about -34 kcal/mol. Extrapolation of the decomposition rate for the reaction of Eq. (2) to the temperature and concentration produced by a shock wave in liquid CS_2 leads to a reaction rate of approximately $10^{-1}/\mu sec$ whereas the shock experiments of R. Dick (see Table I, Section 1.3) suggest that it may be about three orders of magnitude faster than this. With this much guidance from past work, it is evident that a search for CS in the reaction products and a measure of its rate of appearance could be useful in unravelling the basic kinetics.

With these considerations, it was decided to work on liquid CS_2. The reasons can be summarized as follows:

1. It has a linear tri-atomic molecule and an extensive literature on its chemistry exists.
2. Spectroscopic studies of the kinetics of gas phase decomposition have yielded specific but controversial reaction models.
3. Single-shock Hugoniot measurements have been made which show a cusp in the neighborhood of 50 kbars, which indicates chemical decomposition or a phase change.
4. Existing information on the static phase diagram suggests that the observed reaction is a decomposition.
5. The density of liquid CS_2 is great enough that the pressures and temperatures required for reaction can be produced in a double-shock experiment with the WSU gas gun.

6. Absorption lines in CS, which appear to be a most likely intermediate species, lie within the spectral range of the time-resolving spectrograph available to us.
7. CS_2 can be handled in our shock facility without serious hazard.

The experimental program was planned in two phases. The first was a set of mechanical measurements intended to map out the regions of shock pressure and temperature where reaction occurred and to determine reactions rates under the various conditions achieved. The second was to be a spectroscopic study which would enable us to identify reaction products and follow their growth and decay as reaction proceeded. The first phase was successfully completed and is described in Section IV. The second phase has turned up some unusual and unexpected phenomena and is still in progress. It is described in Section V.

REFERENCES TO SECTION III

1. J. M. Walsh and M. H. Rice, J. Chem. Phys. 26, 815 (1957).

2. M. A. Cook and L. A. Rogers, J. Appl. Phys. 34, 2330 (1963).

3. R. D. Dick, J. Chem. Phys. 52, 6021 (1970).

4. R. D. Dick, "Shock Wave Compression of Benzene, Carbon Disulfide, Carbon Tetrachloride, and Liquid Nitrogen," Los Alamos Scientific Lab. Report LA-3915 (1968).

5. P. W. Bridgman, Proc. Am. Acad. Arts Sci. 74, 399 (1942).

6. P. C. Lysne, J. Chem. Phys. 57, 492 (1972).

7. E. G. Butcher, M. Alsop, J. A. Weston, and H. A. Gebbie, Nature 199, 756 (1963).

8. A. N. Afanasenkov, I. M. Voskoboinikov, M. F. Gogulya, and A. I. Karkov, Fiz. Goreviya i Vzryva 10, 392 (1974).

9. V. V. Yakushev, S. S. Nabatov, and O. B. Yakusheva, Fiz. Goreviya i Vzryva 10, 583 (1974).

10. L. P. Blanchard and P. LeGoff, Canad. J. Chem. 35, 89 (1957).

11. A. G. Gaydon, G. H. Kimbell, and H. B. Palmer, Proc. Roy. Soc. A279, 313 (1964).

12. H. A. Olschewski, J. Troe, and H. Gg. Wagner, Ber. d. Bunsenger. Physik. Chem. 70, 1060 (1966).

13. S. J. Arnold, W. G. Brownlee, and G. H. Kimbell, J. Phys. Chem. 74, 8 (1970).

14. T. C. Peng and H. V. Lilenfeld, J. Phys. Chem. 79, 2203 (1975).

IV. REACTION RATES IN CS_2*

The goals of this study were

1. To determine as much as possible about reaction mechanisms and kinetics from conventional shock experiments.
2. To observe the evolution of a two wave shock structure in a chemically reacting system.
3. To create an equation of state suitable for pressure and temperature calculations in strong shocks for off-Hugoniot states.
4. To determine how reaction rate is affected by changes in the pressure-temperature state.

4.1 Plan of Experiments

Although it is believed that the anomaly in the Hugoniot recorded by R. Dick and the associate behavior reported here result from a decomposition reaction, the terms "transition" and "reaction" will be used interchangeably.

Shock parameters were measured by imbedding several electromagnetic particle velocity gages in the liquid sample so that both particle velocity and shock arrival times could be continuously recorded during the times of interest. From these records shock velocity can also be determined.

The particle velocities at which the CS_2 undergoes transition are typically 1.35 mm/μsec for a single shock and greater for a double shock. The light gas gun available at WSU cannot produce 1.35 mm/μsec in the CS_2 in a single shock, so a double shock experiment was designed. The experimental design is illustrated in Fig. 1.4. The target was placed in a magnetic field

* Note that in all of Section IV, Tables, Figures, and Equations are labelled in a consistent fashion, but the system does not conform to that used in the other sections.

during the shot so it was necessary to use sapphire, an insulator, when a high impedance material was required.

As can be seen from Figs. 1.4a and 1.4c, the sapphire faced projectile drives a shock into the PMMA which then traverses the CS_2 as a relatively low pressure wave. When the shock reaches the sapphire back plate, a high pressure wave (state 3') is driven back into the already shocked CS_2. The experiment can be designed so the high pressure wave is above the transition pressure and a reaction is produced.

States 1, 2, 3, and 3', which are reached at various times during the experiment, are labeled in Figs. 1.4b and 1.4c. These designations for the particular state they represent will be used in the remainder of this thesis to maintain consistency.

Gages were placed at the PMMA-CS_2 interface, in the middle of the CS_2, and at the CS_2-sapphire interface. The character of outputs from these gages can be inferred from Fig. 1.4c. Figure 1.5a illustrates what the particle velocity-time profiles might be expected to look like. Corresponding pressure-time profiles are shown in Fig. 1.5b, although these profiles cannot easily be constructed from the particle velocity-time data, and no attempt has been made to do so. Pressures attained after each jump were calculated from the jump conditions, however.

Notice the first reflected wave and the second reflected wave have been labeled the R_1 wave and R_2 wave, respectively, in Fig. 1.5. These designations will be used throughout the remainder of this section for the sake of brevity.

Analysis of the gage records yields unreacted Hugoniot data (state 1) as well as information which can be used to calculate states 2, 3, and 3'.

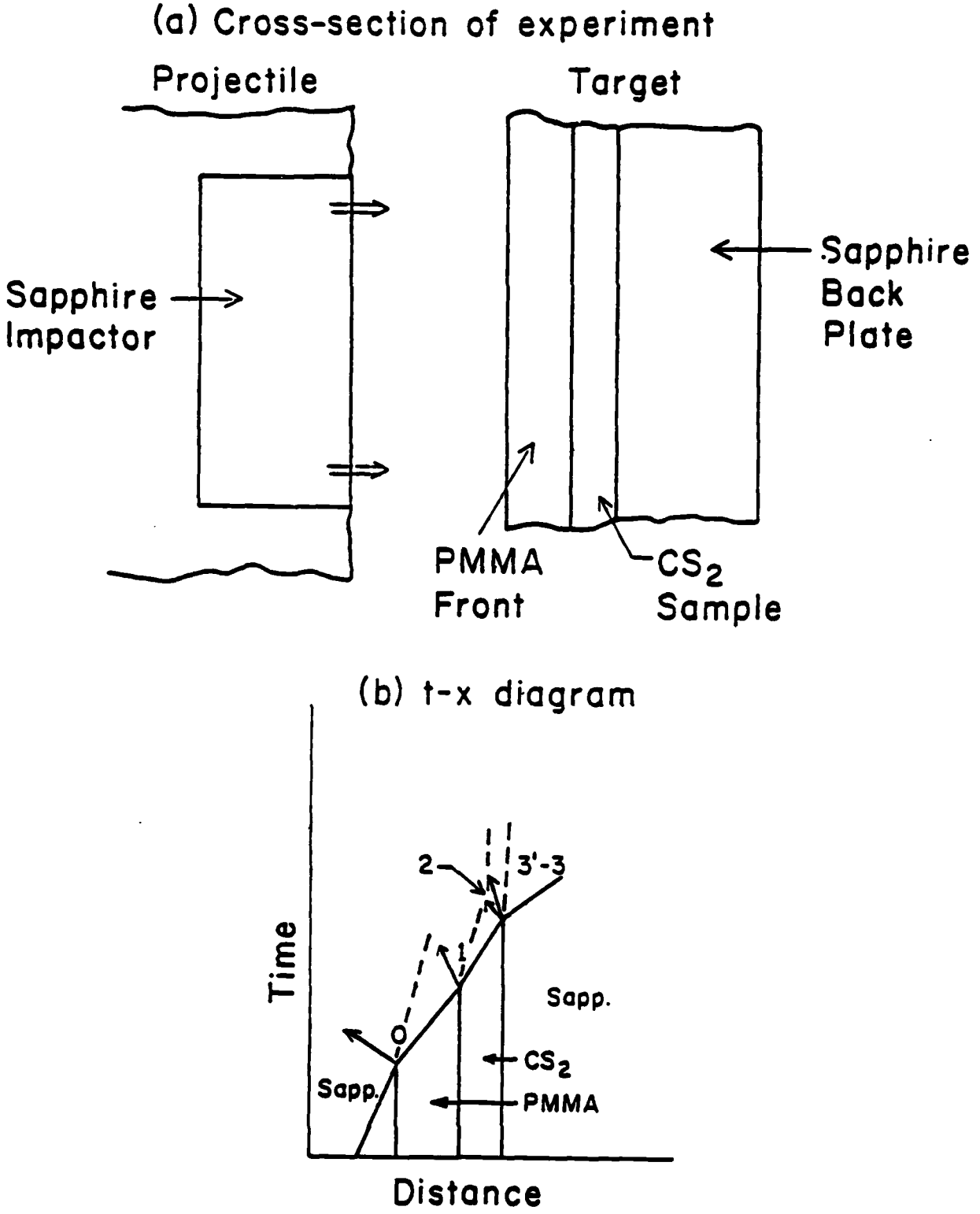

Fig. 1.4.--Experimental Sketch and Shock Diagrams for the CS_2 Experiments. (a) shows the experimental layout, i.e. a sapphire impactor hitting a CS_2 cell with a PMMA front and a sapphire back. (b) shows the direction of the shocks produced and the various states achieved.

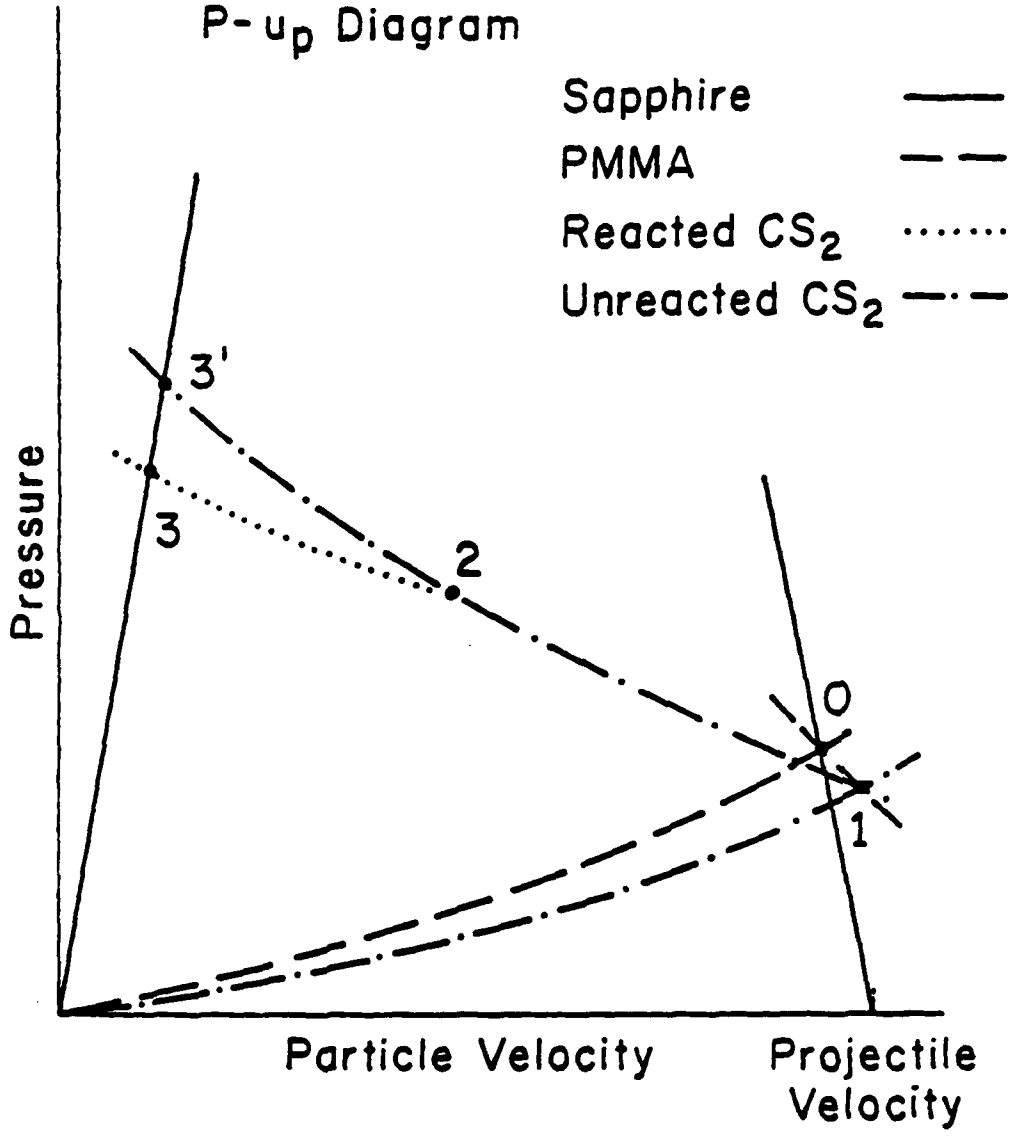

Fig. 1.4 (continued). (c) shows the states achieved in pressure-particle velocity space. Notice the relaxation that takes place from state 3' to state 3 as the reaction proceeds.

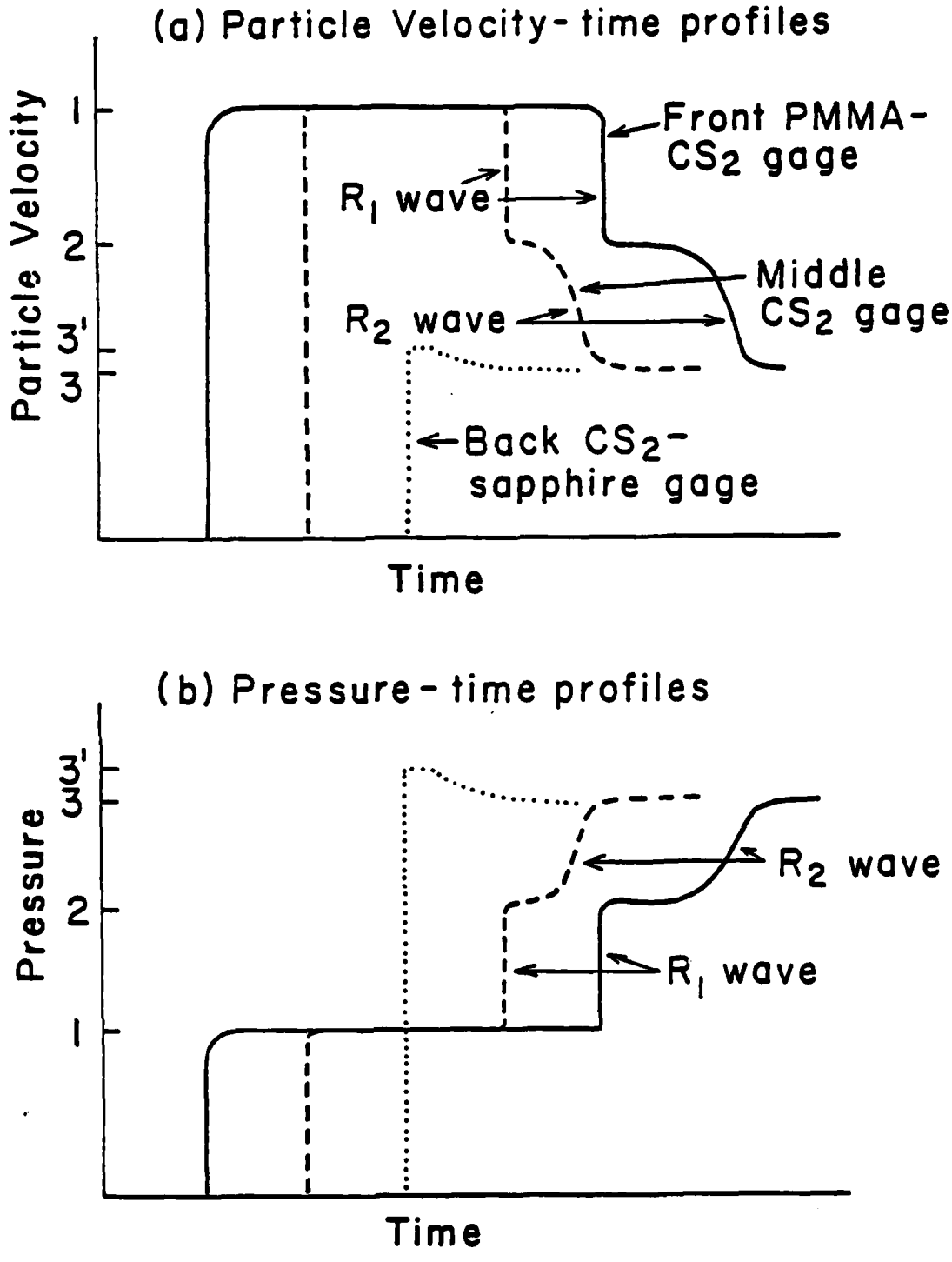

Fig. 1.5.--Wave Profiles Expected from a Three Gage Experiment. (a) shows particle velocity waveforms to be measured in the experiment. (b) shows corresponding pressure profiles although these are not measured or calculated in this study. The first and second reflected waves have labeled the R_1 wave and R_2 wave, respectively.

An unexpected noise associated with the reaction was measured as part of the CS_2-sapphire gage data.

Reaction rates can be estimated from five separate pieces of data: particle velocity decay, noise decay, induction time to the start of reaction, initial reflected shock decay (R_1 wave decay) and wave structure of the evolving R_2 wave (R_2 wave structure). All the data yield only estimates because the exact nature of their relation to the reaction rate is not yet established or because estimates had to be made for certain pieces of needed information.

Equations of state for the unreacted CS_2 and also the reaction products were developed so temperature calculations and one-dimensional wave propagation calculations could be made to simulate the experiments. These added some insight as to what was happening during the reaction.

4.2 THEORETICAL AND EXPERIMENTAL CONCEPTS

Application of the Rankine-Hugoniot Jump Conditions

Statements of the conservation of mass, momentum and energy across a steady shock wave (called the Rankine-Hugoniot jump conditions) can be written as:[36]

$$P - P_o = \rho_o(U_s - u_{po})(u_p - u_{po}) \quad \text{(momentum)} \tag{2.1}$$

$$\frac{\rho_o}{\rho} = 1 - \frac{u_p - u_{po}}{U_s - u_{po}} \quad \text{(mass)} \tag{2.2}$$

$$E - E_o = \frac{1}{2}(P + P_o)(V_o - V) \quad \text{(energy)} \tag{2.3}$$

where u_p is particle velocity, U_s is shock velocity, ρ is density, V is specific volume ($1/\rho$), E is specific internal energy and P is pressure. The subscript "o" refers to the condition ahead of the shock, and unsubscripted variables denote conditions behind the shock. The material is assumed to be in an equilibrium condition at each of these states.

The experiments outlined in Section 1.4 involve several waves (see Fig. 1.5). The first shock propagates into a material at rest, bringing the material to state 1 (see Fig. 1.4). The first reshock wave (R_1 wave) propagates in the opposite direction and takes the material from state 1 to state 2. The second reshock wave (R_2 wave) propagates behind the R_1 wave and takes the material from state 2 to state 3. Appropriate jump conditions for each of these waves are tabulated in Table 2.1. It should be pointed out that the algebraic signs of the shock velocities and particle velocities must be correct. For example, from Fig. 1.4b, shock velocity U_{s1} is positive since the

4.2 THEORETICAL AND EXPERIMENTAL CONCEPTS

Application of the Rankine-Hugoniot Jump Conditions

Statements of the conservation of mass, momentum and energy across a steady shock wave (called the Rankine-Hugoniot jump conditions) can be written as:[36]

$$P - P_o = \rho_o(U_s - u_{po})(u_p - u_{po}) \quad \text{(momentum)} \tag{2.1}$$

$$\frac{\rho_o}{\rho} = 1 - \frac{u_p - u_{po}}{U_s - u_{po}} \quad \text{(mass)} \tag{2.2}$$

$$E - E_o = \frac{1}{2}(P + P_o)(V_o - V) \quad \text{(energy)} \tag{2.3}$$

where u_p is particle velocity, U_s is shock velocity, ρ is density, V is specific volume $(1/\rho)$, E is specific internal energy and P is pressure. The subscript "o" refers to the condition ahead of the shock, and unsubscripted variables denote conditions behind the shock. The material is assumed to be in an equilibrium condition at each of these states.

The experiments outlined in Section 1.4 involve several waves (see Fig. 1.5). The first shock propagates into a material at rest, bringing the material to state 1 (see Fig. 1.4). The first reshock wave (R_1 wave) propagates in the opposite direction and takes the material from state 1 to state 2. The second reshock wave (R_2 wave) propagates behind the R_1 wave and takes the material from state 2 to state 3. Appropriate jump conditions for each of these waves are tabulated in Table 2.1. It should be pointed out that the algebraic signs of the shock velocities and particle velocities must be correct. For example, from Fig. 1.4b, shock velocity U_{s1} is positive since the

TABLE 2.1.--Jump Conditions Applied to Experiments in This Study

Shock Being Considered	State Ahead of Shock	State Behind Shock	Momentum Jump Condition	Mass Jump Condition	Energy Jump Condition
Initial Shock	$P=0,\ u_{po}=0$ $V=V_o,\ \rho=\rho_o$ $E=E_o$	$P_1,\ \rho_1$ $V_1,\ U_{s1}$ $u_{p1},\ E_1$	$P_1 = \rho_o U_{s1} u_{p1}$ (Eq. 2.4)	$\frac{\rho_o}{\rho_1} = 1 - \frac{u_{p1}}{U_{s1}}$ (Eq. 2.5)	$E_1 - E_o =$ $\frac{1}{2} P_1 (V_o - V_1)$ (Eq. 2.6)
First Reshock (R_1 wave)	$P_1,\ V_1,\ \rho_1$ $E_1,\ u_{p1}$	$P_2,\ \rho_2$ $V_2,\ U_{s2}$ $u_{p2},\ E_2$	$P_2 - P_1 =$ $\rho_1 (U_{s2}-u_{p1})(u_{p2}-u_{p1})$ (Eq. 2.7)	$\frac{\rho_1}{\rho_2} = 1 - \frac{(u_{p2}-u_{p1})}{(U_{s2}-u_{p1})}$ (Eq. 2.8)	$E_2 - E_1 =$ $\frac{1}{2}(P_2+P_1)(V_1-V_2)$ (Eq. 2.9)
Second Reshock (R_2 wave)	$P_2,\ V_2,\ \rho_2$ $E_1,\ u_{p2}$	$P_3,\ \rho_3$ $V_3,\ U_{s3}$ $u_{p3},\ E_3$	$P_3 - P_2 =$ $\rho_2 (U_{s3}-u_{p2})(u_{p3}-u_{p2})$ (Eq. 2.10)	$\frac{\rho_2}{\rho_3} = 1 - \frac{(u_{p3}-u_{p2})}{(U_{s3}-u_{p2})}$ (Eq. 2.11)	$E_3 - E_2 =$ $\frac{1}{2}(P_3+P_2)(V_2-V_3)$ (Eq. 2.12)

initial shock moves from left to right but the R_1 wave moves from right to left and so U_{s2} would be negative. The particle velocities are all positive as shown in Fig. 1.4c.

Difficulties can arise in applying the jump conditions to the R_1 and R_2 waves since they have their origin in a single unsteady wave that evolves into a two wave structure. If the structure is not fully developed and steady, the jump conditions in Table 2.1 do not apply exactly. In that case the relations among physical parameters can be approximated in a progressing wave by a multiple gage analysis developed by Fowles and Williams [1] and refined by others.[2,3] Such an analysis has not been used in the present work because it is not evidently warranted and because interest lies primarily in the reflected wave region where techniques for multiple gage analysis have not been developed. Instead, the jump conditions have been applied in every case to propagating regions of rapid change in particle velocity and it is believed the errors are not large and do not significantly influence the interpretation of records.

The time dependent conservation relations can be written as [4]

$$\rho\left(\frac{\partial u_p}{\partial t}\right) + \rho u_p\left(\frac{\partial u_p}{\partial x'}\right) + \frac{\partial P}{\partial x'} = 0 \qquad \text{(momentum)} \qquad (2.13)$$

$$\frac{\partial \rho}{\partial t} + u_p\left(\frac{\partial \rho}{\partial x'}\right) + \rho\left(\frac{\partial u_p}{\partial x'}\right) = 0 \qquad \text{(mass)} \qquad (2.14)$$

$$\frac{dE}{dt} = -P\left(\frac{dV}{dt}\right) + \frac{dQ}{dt} \qquad \text{(energy)} \qquad (2.15)$$

where dQ is the heat added per unit mass and $d/dt = \partial/\partial t + u_p(\partial/\partial x')$ is the convective derivative. These are most tractable when solved numerically in the form of difference equations in a one-dimensional wave propagation code. This is the approach which has been taken to simulate the experiments.

Equations of State for Unreacted CS_2 and Reacted Products

The jump conditions provide three equations among the five unknown variables, P, u_p, U_s, V, and E behind the shock front. If two variables are measured (as is the case in this study) the mechanical state and the P-V-E thermodynamic state are determined.

A relation between P and V for all possible shocks running into a state P_o,V_o is called a Rankine-Hugoniot or Hugoniot P-V curve. In what follows it, along with other relationships among shock parameters ($P-u_p$, U_s-u_p, T-P, etc.), will be called simply the Hugoniot. If it is known, it provides a fourth equation, so that the other four parameters can be determined if one of the five is measured.

The Hugoniot curve is a single locus of points on the three dimensional equation of state surface. In order to produce a numerical simulation based on Eqs. (2.13) - (2.15), a complete equation of state is required. Moreover, since time-dependent reactions will be investigated, a model for transitions from initial to final state is required. Since temperature is expected to play an important role in the reaction process, it must be calculated. There is not enough information about the thermodynamic behavior of CS_2 and its decomposition products to determine exact equations of state, so thermodynamic calculations will be based on an equation of state synthesized from the limited data which are available, following examples set by Andrews,[5] Hayes,[6] and others.[7-9] The remainder of this section is devoted to a description of the equations of state used here. Reference 10 is a useful compendium of CS_2 properties and references.

Unreacted CS_2 Equation of State

The unreacted CS_2 equation of state for this study was based on Bridgman's[11] isotherm to 12 kbar and shock Hugoniot data. Specific heat at constant volume (C_V) and the Gruneisen parameter (Γ) were taken from the thermodynamic data at $P = P_o = 1$ atmosphere and $T = T_o = 293°K$. Functional relations for C_V and Γ were developed so that unreacted Hugoniot data could be matched.

The particular form chosen for the unreacted CS_2 equation of state includes a Murnaghan equation[12] to describe the isothermal P(V) relation,

$$P = \frac{K_{To}}{N}\{(\frac{V_o}{V})^N - 1\} \tag{2.16}$$

where K_{To} is the isothermal bulk modulus at P_o and T_o, V_o is the initial specific volume, and N is an adjustable parameter. The isothermal bulk modulus is obtained by differentiating Eq. (2.16):

$$K_T = K_{To}(\frac{V_o}{V})^N . \tag{2.17}$$

C_V was assumed to have the form

$$C_V = C_{Vo}(a + b(\frac{V}{V_o})) . \tag{2.18}$$

Since $C_V = C_{Vo}$ when $V = V_o$, $b = 1-a$ and Eq. (2.18) can be written as

$$C_V = C_{Vo}(a + (1-a)\frac{V}{V_o}) . \tag{2.19}$$

There are certain compatibility relations between C_V and Γ that must be satisfied to maintain thermodynamic consistency. Fowles[13] developed the relation,

$$\left(\frac{\partial C_V}{\partial V}\right)_T = \frac{T}{V}\left\{\Gamma\left(\frac{\partial C_V}{\partial T}\right)_V + C_V\left(\frac{\partial \Gamma}{\partial T}\right)_V\right\} . \qquad (2.20)$$

When Eq. (2.19) is substituted in Eq. (2.20) and the result integrated, the resultant relation for Γ is,

$$\Gamma = \Gamma_o + \frac{(1-a)\ \ln(T/T_o)}{1 + a\left(\frac{V_o}{V} - 1\right)} + f(V) \qquad (2.21)$$

where Γ_o is zero pressure Γ, T_o is the starting temperature, and $f(V)$ is an arbitrary function of V. The final form for Γ/V which was used is,

$$\frac{\Gamma}{V} = \frac{\Gamma_o}{V_o}\left(\frac{V_o}{V}\right)\left[1 + \frac{(1-a)\ \ln(T/T_o)}{\left(\frac{\Gamma_o}{V_o}\right)V_o\left(1 + a\left(\frac{V_o}{V} - 1\right)\right)} + \frac{c\left(1 - \frac{V}{V_o}\right)^d}{\left(\frac{\Gamma_o}{V_o}\right)V_o}\right] \qquad (2.22)$$

where a, c, and d are adjustable constants.

Equations (2.16), (2.19), and (2.22), with initial values and a set of constants a, c, and d, are enough to calculate pressure, volume relations on the Hugoniot curve. This was done for various values of a, c, and d, and the set which gave the best fit was chosen. These, with initial values of thermodynamic variables, are given in Table 2.2.

These relationships provide a description of a complete equation of state surface for unreacted CS_2. Values for each of the thermodynamic variables may be calculated by integrating on the surface to the desired point.

TABLE 2.2.--Unreacted CS_2 Equation of State Parameters (Reference State, P_o = 1bar, T_o = 293°K)

Parameter	Value
C_{Vo}	0.624×10^{-5} Mbar $cm^3/g°K$
E_o	0.01176 Mbar cm^3/g
S_o	1.98×10^{-5} Mbar $cm^3/g°K$
V_o	0.7918 cm^3/g
Γ_o/V_o	2.108 g/cm^3
K_{To}	0.012 Mbar
T_o	293°K
N	7.1
a	2.4
c	1.5
d	0.45

Reacted Products Equation of State

Obtaining an equation of state for the reacted products was more difficult than for the unreacted CS_2, primarily because the exact nature of the products is not known. It has been assumed that the products are a stoichiometric mixture of carbon and sulfur, 0.1578 gram of carbon and 0.8422 gram of sulfur per gram of products. This assumption allows one to estimate what some of the equation of state parameters might be in order to have a starting point.

The form of the equation of state is much the same as that for the unreacted CS_2, namely, the Murnaghan form for the isotherm (Eq. 2.16), a constant C_V, and a constant Γ/V.

Dick's data[14] above the transition region provided the information to which the reacted product equation of state was matched. The basic intent of the matching procedure was to match P-V-E states obtained from Dick's data and the energy jump condition with P-V-E states calculated by the reacted product equation of state.

The final parameters determined for use in the reacted product equation of state are listed in Table 2.3.

TABLE 2.3.--Reacted Product Equation of State Parameters (Reference State, P_o = 1bar, T_o = 293°K)

Parameter	Value
C_{Vo}	1.0×10^{-5} Mbar $cm^3/g°K$
E_o	0.0
S_o	0.911×10^{-5} Mbar $cm^3/g°K$
V_o	0.480 cm^3/g
Γ_o/V_o	1.87 g/cm^3
K_{To}	0.100 Mbar
T_o	293°K
N	5.0

Chemical Thermodynamics

According to Callen,[15] one can postulate a fundamental equilibrium relation in which internal energy is a function of entropy, volume and mole number of the constituents. For a system of CS_2 reacting to form sulfur and carbon, the fundamental relation is

$$\bar{E} = \bar{E}(\bar{S},\bar{V},N_1,N_2,N_3) \tag{2.26}$$

where $N_1 = N_{CS_2}$, $N_2 = N_S$, and $N_3 = N_C$. One can differentiate this and use the usual definitions of temperature, pressure and chemical potential to obtain

$$d\bar{E} = Td\bar{S} - Pd\bar{V} + \sum_{i=1}^{3} \mu_i dN_i \tag{2.27}$$

where μ_i is the chemical potential of the i^{th} species. The mole numbers are related through the stoichiometry of the reaction so that a reaction coordinate can be defined as

$$\frac{dN_1}{\nu 1} = \frac{dN_2}{\nu 2} = \frac{dN_3}{\nu 3} = d\bar{x} \tag{2.28}$$

where $\bar{x}$ is the reaction coordinate and ν_i is the stoichiometric coefficient (negative for reactants and positive for products). This can be used in Eq. (2.27) to obtain

$$dE = TdS - PdV + dx \sum_{i=1}^{3} \mu_i \nu_i \tag{2.29}$$

where the entire relation has been divided by a factor of proportionality[15] which is a constant so E, S, and V are now specific quantities and x is dimensionless.

The same kind of development can be carried out for the Gibbs free energy representation to yield

$$dG = -SdT + VdP + dx \sum_{i=1}^{3} \mu_i \nu_i \qquad (2.30)$$

where G is specific Gibbs free energy. Sometimes the summation term is called by another name

$$\Delta G_{T,P} = \sum_{i=1}^{3} \mu_i \nu_i \, , \qquad (2.31)$$

so Eq. (2.30) becomes

$$dG = -SdT + VdP + \Delta G_{T,P} dx \, . \qquad (2.32)$$

Gibbs free energy is often used as a criterion for determining whether or not a reaction at a constant temperature and pressure proceeds; since, as one can see from Eq. (2.30), dG is directly related to dx. Callen has shown that for a material at constant temperature and pressure the Gibbs free energy is minimized at equilibrium. This means that if, at constant temperature and pressure, the Gibbs free energy of the products is less than that of the reactants, the reaction tends to proceed.

The definition of Gibbs free energy is

$$G = E + PV - TS \, . \qquad (2.33)$$

In normal chemical reactions the PV part of G is very small (E is on the order of 0.02 Mbar cm^3/g and PV is on the order of 0.000001 Mbar cm^3/g). As

pressure increases, say to 10 kilobars, the PV term becomes on the order of 0.01 Mbar cm^3/g. It is easy to see that in shock experiments very different things can happen to G since both temperature and pressure increase, whereas in normal chemistry only temperature changes.

The Gibbs free energy of formation can be calculated from the enthalpy of formation and the entropy at standard conditions. The values for CS_2 and the products (carbon and sulfur) are

$$\Delta G_{f_{298}}(CS_2) = 0.00857 \text{ Mbar } cm^3/g$$

and

$$\Delta G_{f_{298}}(\text{Carbon + Sulfur}) = 0.0 \text{ Mbar } cm^3/g$$

which indicates that CS_2 is in metastable equilibrium with respect to its decomposition products, i.e., it tends to decompose at room temperature. The rate is so slow that it would take years to produce measurable amounts, however. It is interesting to note, that many of the liquids that react in a shock are metastable at standard conditions.

Since the CS_2 is being shocked to high pressure and temperature states in the experiments, it is of interest to calculate the Gibbs free energy for both CS_2 and the reacted products to see if the products have a lower Gibbs free energy. This has been done using the equations of state previously discussed. In both the principal Hugoniot and the reshock Hugoniot regimes of interest, the Gibbs free energy of the products is always less than that of CS_2. Although this analysis was made at temperatures and pressures along the Hugoniot (which change as reaction proceeds), it does demonstrate that from an equilibrium thermodynamic standpoint, CS_2 tends to decompose into its products in the state regions of interest.

The only reaction rate law which will be considered here is that for a simple decomposition:

$$dx/dt = A \exp(-E/RT)$$

where x is the function reacted, E is activation energy, and A is frequency constant. In measurements to be reported here, the simplest rate-related variable is a relaxation time,

$$\tau = 1/\dot{x} = \exp(E/RT)/A$$

Graphs of $\ln \dot{x}$ verses $1/T_{calc}$ will be used to estimate E and A.

Reaction Rate Data from Evolution of Two Wave Structure

The general theory of kinetics of shock induced phase transitions has been addressed in detail by several researchers.[4,5,6,16] Much of the formalism applies directly to the kinetics of chemical reactions. Evolution of the two wave structure that results from a reacting material is illustrated in Fig. 2.6. This figure represents "snapshots" of the particle velocity-distance profile at several times during the evolutionary period. According to Hayes,[17] wave profiles measured during the evolutionary period provide at least four different pieces of information, each related to the reaction rate. The four are: decay of the first wave (called R_1 wave decay), delay in forming the second wave (called R_2 wave delay), particle velocity transients at the loading interface, and the structure between the two waves (called R_2 wave structure). It is obvious that the reaction rate in a chemically reacting wave is changing from a relatively slow rate at the beginning to a very high rate toward the end so that these different

observables would be expected to yield different rates associated with different times during the reaction. The R_2 wave delay is difficult to measure and will be ignored in the following discussion.

R_1 Wave Decay

A relation has been developed to relate the particle velocity decay in the R_1 wave to the reaction rate at the Lagrangian position where the reactive wave starts. The relation is

$$\left(\frac{\partial x}{\partial t}\right)_h = \frac{\left[\rho_o U - \frac{\rho_o a_s^2}{U}\right]\left(\frac{\partial u}{\partial t}\right)_h + \left[\rho_o U + \frac{\rho_o a_s^2}{U}\right]\left(\frac{\partial u}{\partial t}\right)_\xi}{\Delta V\left[\frac{K_{S,x}}{V_x} - P\left(\frac{\Gamma}{V}\right)_x\right] - \Delta E\left(\frac{\Gamma}{V}\right)_x} \qquad (2.40)$$

where ρ_o is ambient density of the material. a_s is frozen sound speed. K_s is frozen bulk modulus, ΔV and ΔE are changes in specific volume and internal energy experienced by a mass element in going from the initial to the reacted state. Subscripts refer to a position immediately behind the shock front and h to an arbitrary Lagrangian position. U is shock velocity and Γ is the Gruneisen parameter.[18]

Suffice it to say that this evaluation can be made only at h = 0, where $\left(\frac{\partial u}{\partial t}\right)_{h=0}$ is negligible and $\left(\frac{\partial u}{\partial t}\right)_\xi$ is the initial particle velocity decay in the R_1 wave. Since this can be estimated from the measured data and all other parameters can be calculated from the equation of state of unreacted CS_2 (since x = 0 in the wave front), an estimate for $\left(\frac{\partial x}{\partial t}\right)_{h=0}$ can be made.

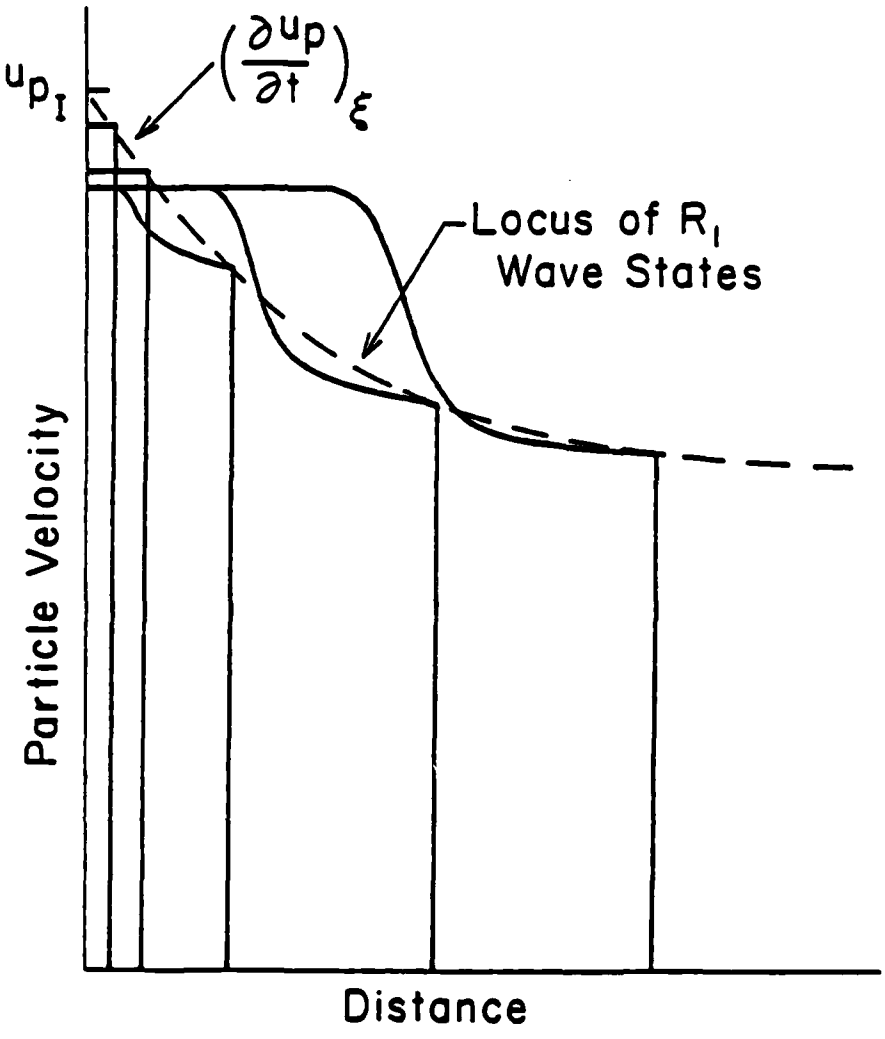

Fig. 2.6.--Snapshots of the Particle Velocity Profile for an Evolving Two Wave Structure in a Reacting Material. This illustration applies to the single shock case. U_{pI} is the initial particle velocity as the wave begins to propagate.

Loading Interface Particle Velocity Transients

The particle velocity measured at the downstream CS_2-sapphire interface (see Fig. 1.4c) will decrease from 3' to 3 as the reaction progresses. A relaxation time (τ) for the reaction to be completed can be obtained from the particle velocity-time history. The reciprocal of this time provides an estimate of the average value of the reaction rate at this interface,

$$\bar{\dot{x}} \approx \frac{1}{\tau} . \tag{2.41}$$

R_2 Wave Structure

Quite obviously, the reaction rate varies a great deal from the top of the R_1 wave to the top of the R_2 wave, starting out slowly and then increasing rapidly as the temperature increases. The slope of the R_2 wave front is most likely where the major part of the reaction occurs; it therefore provides another estimate of the reaction rate. If one multiplies this slope by the reciprocal of the change in velocity,

$$\bar{\dot{x}} = \left(\frac{\Delta u_p}{\Delta t}\right)_{R_1-R_2} \left(\frac{1}{\Delta u_{p_{R_1-R_2}}}\right) \tag{2.42}$$

an estimate of reaction rate results. Obviously this assumes all the reaction occurs in the R_2 wave front and it would therefore be expected to yield a low upper limit on the reaction rate.

Particle Velocity Measurements with Electromagnetic Gages

The electromagnetic gage consists of a conductor placed perpendicular to a magnetic field. As the conductor moves, it cuts the field lines and acts essentially as a voltage source that obeys the relation[19]

$$\varepsilon = B\ell v \times 10^{-4} \tag{2.43}$$

where ε is induced voltage in volts, B is the magnetic field strength in gaus, ℓ is the length of the conductor in millimeters, and v is the conductor velocity in mm/μsec.

There are several things one must keep in mind when using these gages in a shock environment:

1. Effects of gage material and thickness on the material being measured.
2. Movement of leads at the edges of the experiment.
3. Mutual inductance between gages in multiple gage experiments.

Each of these will be briefly discussed in the following subsections.

Gage Material and Thickness

Since the electromagnetic gage is an in-material gage, the shocking up process between the gage and the material is of interest. Figure 2.7 is a representation of this shocking up process between a high impedance gage and a low impedance medium. Notice the rounding in the front that continues past the gage and the perturbation traveling into the already shocked region on the left. If the gage is thin enough the rounded wave will rapidly shock

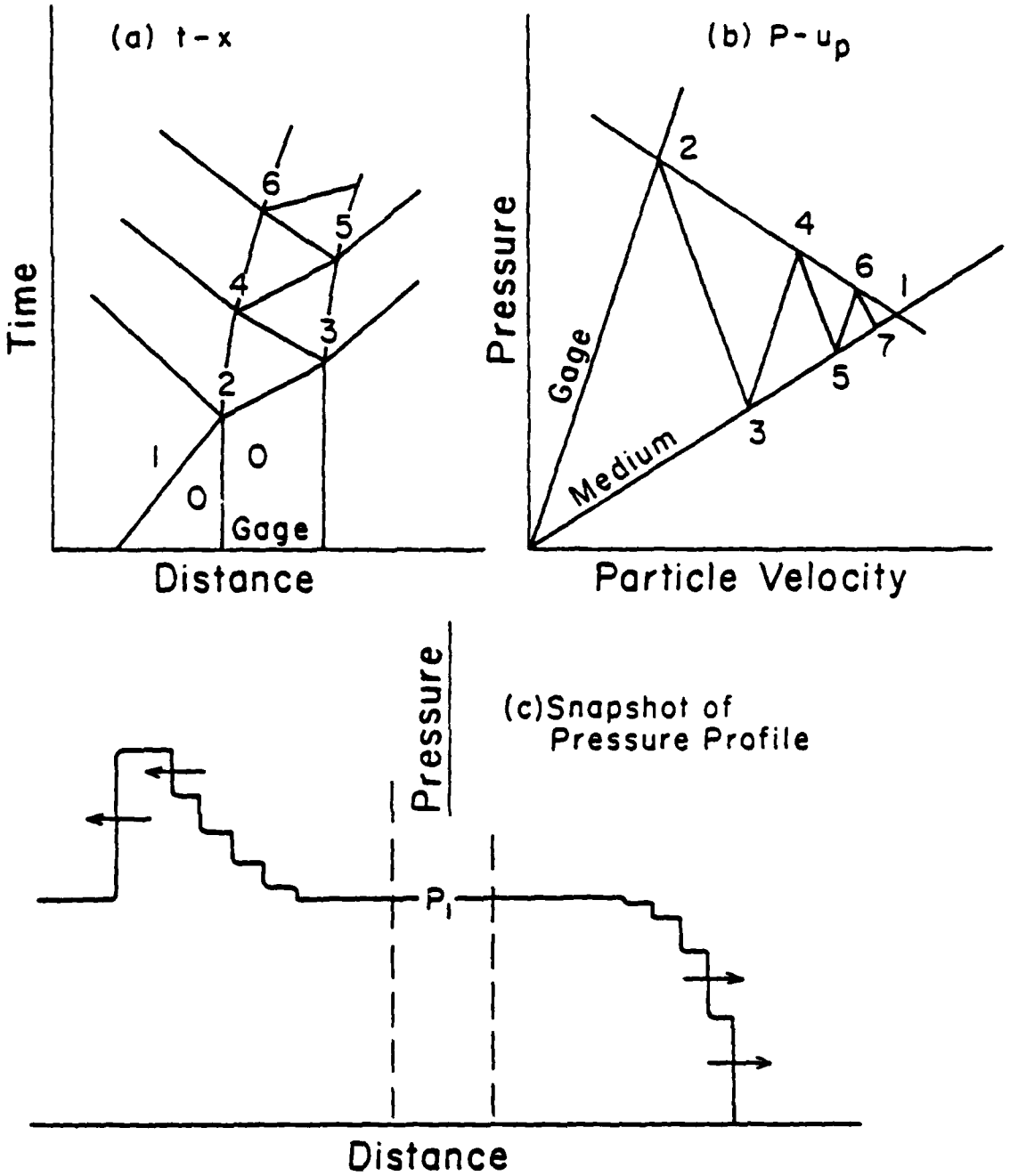

Fig. 2.7.--Electromagnetic Gage Shock-Up Process. (a) shows the waves generated. (b) shows the pressure-particle velocity states attained. (c) is a snapshot of the pressure profile showing the rounded wavefront proceeding past the gage and the perturbation moving to the left in the already shocked material. These diagrams apply to a high impedance gage in a low impedance medium.

up as the small waves overtake the front and the perturbation traveling to the left will be depleted by the rarefactions from behind, thus leaving the medium in the desired state.

When dealing with temperature sensitive reactions, one must be cognizant of the possibility that reaction may occur in the high pressure perturbation moving to the left, thereby causing a much larger perturbation that affects the whole experiment.

The ideal gage would be one that matches the medium in impedance. The alternative is to make it very thin, i.e., a few microns thick.

Lead Movement

The leads connecting the conductor to the recording circuit must come out parallel to the magnetic field (or else in a position so that it does not cut the field as it moves) to maintain a constant effective conductor length. As the experiment progresses, the outside edges of the experiment lose one-dimensionality and it is conceivable the leads begin to spread. This spreading would manifest itself on the records as a gradual increase in the particle velocity, which should remain constant. These type of results have been observed but as yet no one has attempted to quantify the effect. The records from the experiments in this study indicate this was not large enough to worry about.

Multiple Gage Mutual Inductance

Using very simple relationships for the mutual inductance between two gages in a multiple gage experiment, the worst case was found to be two gages, one on top of the other, separated by a layer of the material being shocked. For gages 2 mm apart, the mutual inductance was calculated to be 0.025×10^{-6} henries. Voltage is generated between these two circuits only

when the current in one or the other is changing since

$$\varepsilon = M \frac{di}{dt} \tag{2.44}$$

where ε is the induced voltage, M is the mutual inductance and i is the current. Assuming a current change of 20 milliamps in 10 nanoseconds leads to an induced voltage of 50 millivolts. This would last only while the current was changing and should therefore be manifest as spikes on the records. Some of these have been observed, but they do not alter the data appreciably.

4.3 EXPERIMENTAL PROCEDURE

General Comments on Experimental Facility

All experiments were performed on the 44 foot long, 4 inch bore light gas gun operated by the Shock Dynamics Laboratory at Washington State University. The characteristics and performance of the gun are documented in Ref. 20. It is capable of delivering a projectile at velocities ranging from 0.2 to 1.35 mm/μsec, although the higher velocities are somewhat more difficult to attain because the projectile must withstand the harsh environment of high pressure (6000 PSI) while having a mass of only half a kilogram.

The target area in the gun is evacuated to less than 10^{-3} Torr prior to firing to eliminate the air cushion which would otherwise form. This area is large enough to accommodate an electromagnet for experiments requiring particle velocity measurements. Adjustments can be made on the target assembly so the projectile-target tilt is controlled to less than a milliradian.

Projectile velocity is measured as a result of the projectile shorting 4 sets of velocity pins just prior to impact. Signals from these shorting pin pairs are routed through a pulse shaping network to both a time interval counter and an oscilloscope. Velocity measurements on the order of ±0.5% are possible with this system.

The instrumentation facility consists of nine Tektronix oscilloscopes (one 7844, two 7904's, two 454's, and four 585's) which can all be used at one time if necessary. The 7000 series scopes have interchangeable amplifiers (7A13 and 7A19) and interchangeable time bases (7B70 and 7B71).

Signals from the experiment are carried from the target chamber to the instrumentation rack via four RG213U coaxial cables isolated from ground.

CS_2 Cell Design and Fabrication

The design and fabrication of the cell to contain the CS_2 evolved as experimentation progressed, primarily due to problems encountered and a desire to obtain as much information as possible from each experiment. Design, fabrication, and problem areas will be addressed in the next two subsections.

Design and Construction of the Cell

During the course of experimentation, five different cell designs were used. The differences are outlined in Table 3.1. All cells were constructed from layers of polymethylmethacrylate (PMMA)[21] which were lapped, polished, and epoxied together. PMMA was chosen because it is transparent, easy to work with, and a reasonably good shock impedance match to CS_2, particularly at higher pressures. It, like all plastics, is a viscoelastic material which gives rise to steady rounded shocks propagating through it.

A pictorial breakdown of the parts which make up a cell of the C type is shown in Fig. 3.1. The gages were mounted on kapton sheets prior to assembly. Layers were epoxied together using Epon 815 epoxy allowing approximately 24 hours for each epoxy joint to cure. Over 12 separate epoxy operations were required in the construction of the more complicated cells such as the C type.

Sapphire back plates were single crystal sapphire, unoriented, but most likely in the 60° orientation. They were purchased[22] this way to keep the costs down since oriented z-cut sapphire costs approximately two times more.

TABLE 3.1.--CS_2 Cell Configurations

Designation	Front Face Material	Back Face Material	Number of Gages	Placement of Gages*					
				F	MF	M	MB	B	BS
A	PMMA	PMMA	2	x				x	
B	PMMA	Sapphire	2	x				x	
C	PMMA	Sapphire	3	x		x		x	
D	PMMA	Sapphire	4	x		x		x	x
E	PMMA	Sapphire	4	x	x		x	x	

* F = Front gage at CS_2-PMMA interface.

MF = Gage in CS_2 approximately 0.7 mm from front face.

M = Gage in CS_2 approximately 1.0 mm from front face.

MB = Gage in CS_2 approximately 1.3 mm from front face.

B = Back gage at CS_2-Sapphire interface approximately 2mm from front face.

BS = Gage between two layers of sapphire in the back plate.

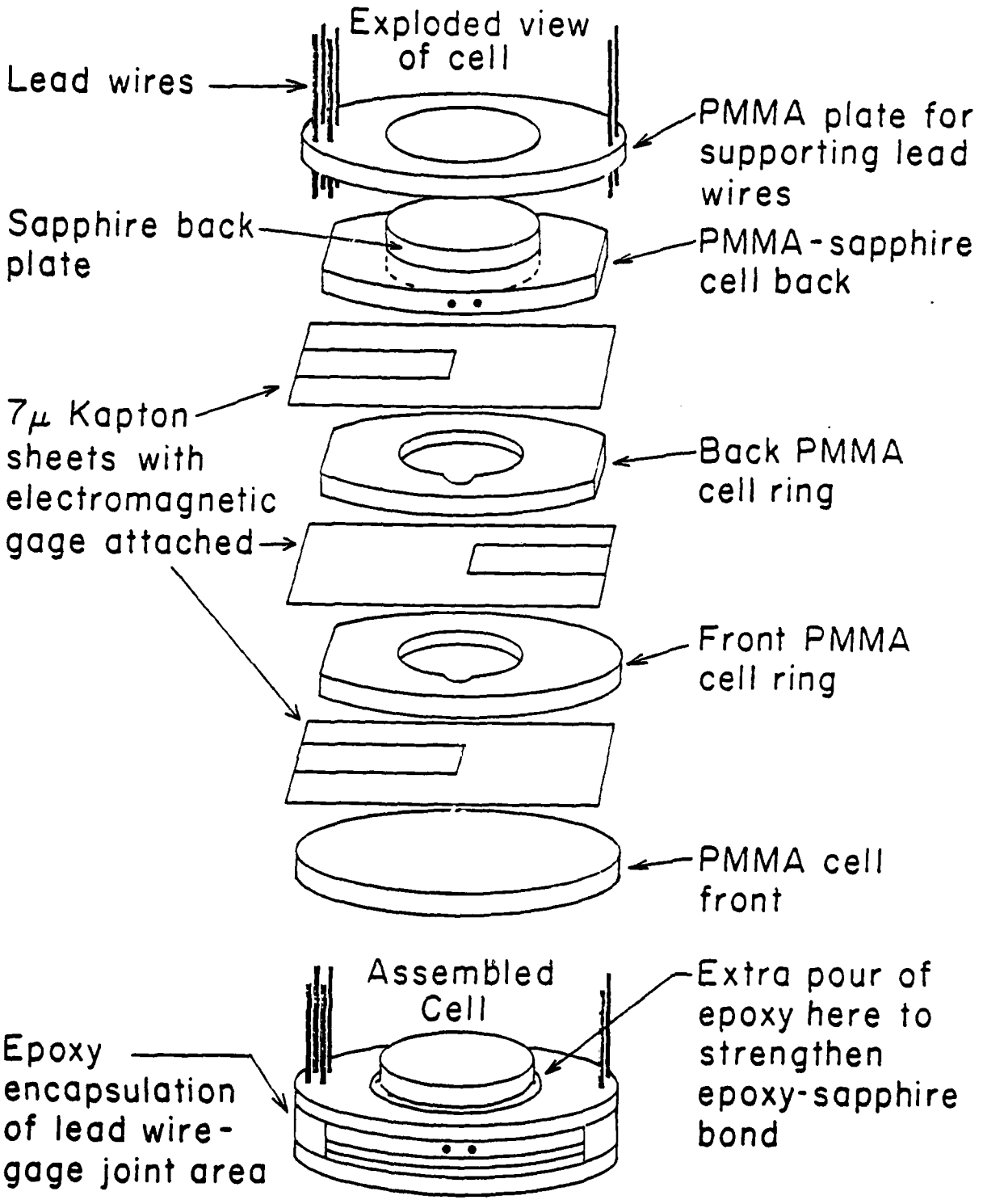

Fig. 3.1.--Exploded View of a Three Gage CS_2 Cell. The cell is assembled by epoxying the various layers together.

Compatibility of the CS_2 with cured Epon 815 epoxy, kapton and PMMA was checked by placing these materials in CS_2 for several days and then looking carefully for visual signs of degradation. They were all found to be compatible, although no attempt to quantify the results was made. One epoxy, Dow DER332 resin with Hysol 3561 hardener, was found to be incompatible with CS_2.

The electromagnetic gages were designed by Fowles and Koller[23,24] of this laboratory and are purchased[25] mounted on a 50 micron thick kapton backing which is later removed. The gages are 5 microns thick copper with the leads and end 0.5 mm wide. Effective length (approximately 6.5 mm) is determined by taking an average of the inside and outside length of the end. The leads are 25.4 mm long. There is a center tap to be used with differential amplifier measurements, if desired. Prior to assembly in the cell, the gages were epoxied onto 7 micron thick kapton to make it easier to handle them and also to provide support for the gages suspended in the CS_2.

Access to the cell for filling was provided by two holes drilled in the side and into the sample area in the PMMA back plate ring. Soft copper tubes[26] 1.58 mm outside diameter by 0.56 mm inside diameter were inserted in the holes but not into the sample cavity. These were epoxied in at the time the cell was potted into the target plate. Soft copper was used because it is non-magnetic and easy to seal by crimping after the liquid has been inserted.

Figure 3.2 is a sketch of the finished target assembly ready to be filled with CS_2. A number of construction details have been covered only briefly and several others (such as attaching leads and cables to the gages, building up the leads with solder, potting the cell in the target ring, testing the finished cell, etc.) have been skipped entirely.

There were a number of characteristics, other than those specified in Table 3.1, which changed from cell to cell. These differences are detailed in Table 3.2 for each of the 14 cells used in the CS_2 shots.

Difficulties Encountered

A number of problems were encountered during the course of experimentation and changes were made to correct the deficiencies on later cells. Table 3.3 is a listing of the problems, reasons for the problems, and the solution developed to overcome it.

Projectile Design and Preparation

In these experiments, the primary function of the projectile body was to hold the sapphire impactor in such a fashion that it would impact the cell with a minimum amount of tilt as illustrated in Fig. 3.3. Because of the nature of the experiments, stringent constraints were put on the projectile design. Since the experiment was carried out in a magnetic field, the projectile must be nonconductive or at least have a nonconductive nose on it. The high velocities necessary to achieve the desired state in the CS_2 required the projectiles be light but at the same time able to withstand the extremely harsh environment of being accelerated by 6000 psi helium.

Projectile Design

Three different projectile designs were tried which are illustrated in cross-sectional views in Fig. 3.4. The all nylon projectile (Fig. 3.4a) was abandoned because it did considerable damage to the magnet interior when it shattered. The aluminum-PMMA projectile (Fig. 3.4b) was only good for low velocity shots because it was too heavy. Nylon-syntatic foam projec-

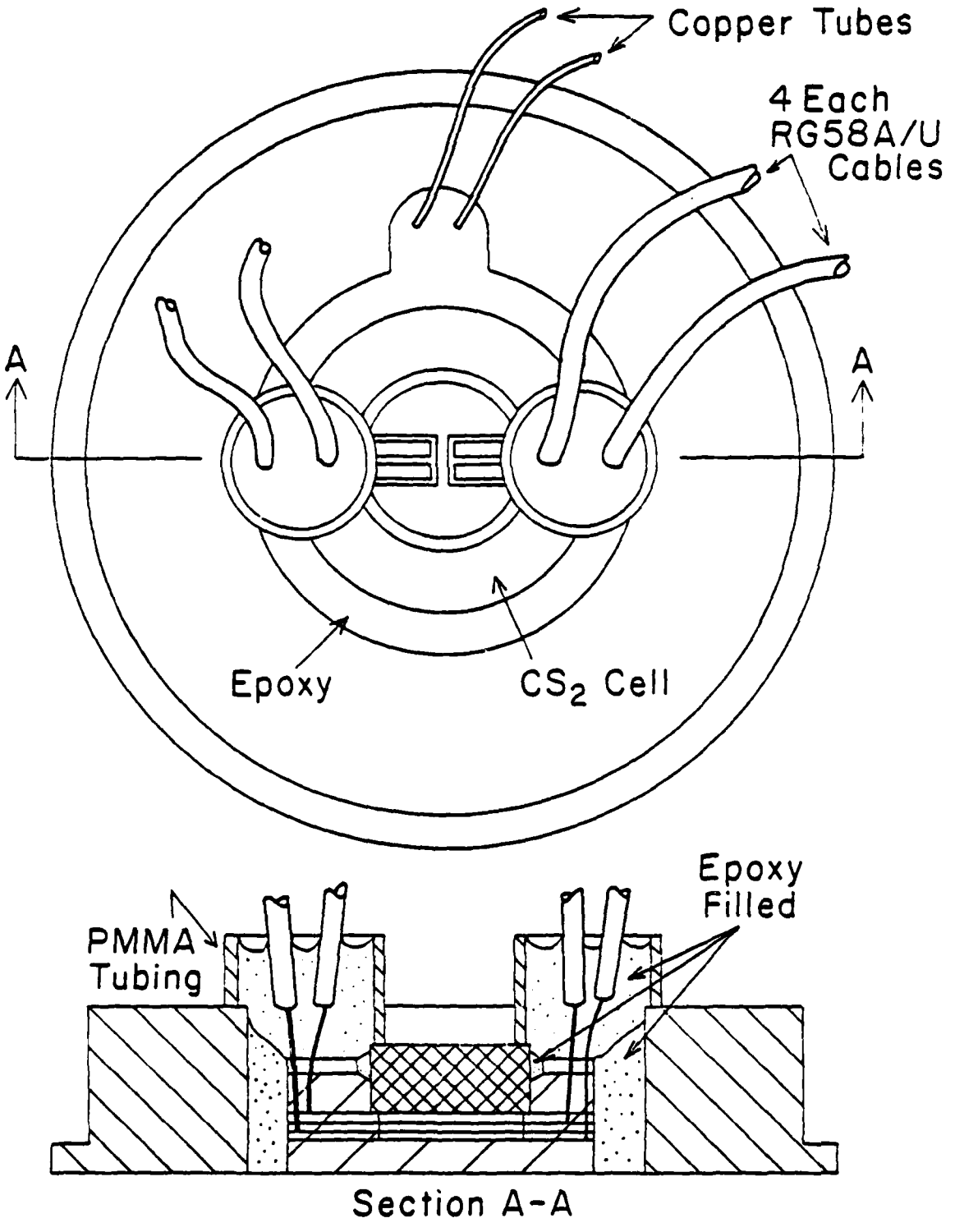

Fig. 3.2.--Finished Four Gage Target Assembly. The gages are visible from the back of the target so the gage leads can be visually aligned to make them parallel to the magnetic field.

TABLE 3.2.--Characteristics of Experimental CS_2 Cells

Shot No.	Cell Type	PMMA Front Thickness (mm)	CS_2 Cavity Size Diameter (mm)	CS_2 Cavity Size Thickness (mm)	Sapphire Back Plate Diameter (mm)	Sapphire Back Plate Thickness (mm)	Kapton on Front Face	Kapton on Back Face	Gage Leads Built Up
77-003	A	1.43	20	2.06	PMMA Back Plate		No	No	No
77-020	A	2.01	20	2.00	PMMA Back Plate		No	No	No
77-044	A	1.91	20	1.94	PMMA Back Plate		No	No	No
77-045	B	2.01	20	1.84	25.4	6.35	No	No	No
77-050	B	1.95	20	1.84	25.4	12.76	No	No	No
77-055	C	2.03	20	2.00	25.4	12.76	No	No	No
77-062	C	2.29	20	1.99	25.4	12.75	Yes	No	Yes
77-070	C	3.74	20	1.98	25.4	12.76	Yes	No	Yes
77-071	C	3.57	20	1.98	25.4	6.40	Yes	No	Yes
77-094	D	3.37	23	2.02	25.4	8.43*	Yes	Yes	Yes
77-095	D	3.30	23	1.95	25.4	8.45*	Yes	Yes	Yes
77-103	D	4.47	28	2.18	31.8	6.39	Yes	Yes	Yes
77-106	E	4.46	28	2.22	31.8	6.40	Yes	Yes	Yes
77-107	E	4.53	28	2.19	31.8	6 39	Yes	Yes	Yes

*Two pieces glued together with gage between.

TABLE 3.3.--Cell Construction Problem Areas and Solutions

Problem Area	Reason for Problem	Solution
The PMMA front face plate cracked when in contact with CS_2 and under stress.	A common problem called stress cracking in plastics. Mechanical, not a chemical problem.	Epoxied a layer of 7 μ kapton over the PMMA to isolate it from the CS_2.
Epoxy bonds around the sapphire back plate cracked and CS_2 leakage occurred.	Bonds were very thin and subject to stresses during cell construction.	After the cell was completed another thick pour of epoxy was made around the sapphire.
Gage recording times were too short to allow observation of the two wave structure.	Particle velocity gradients caused the gage leads to break.	The leads inside the PMMA were built up with indium solder.
Epoxying gages to substrate was difficult.	Epoxy bond under gage was too thin so gage stuck more to the 50 micron apton back than to the substrate.	Developed a procedure to epoxy the gages with a controlled amount of weight applied.
Kapton gage planes moved in CS_2 upon filling.	Not sure why yet.	Got around the problem by using the initial shock velocity to position the intermediate gages.

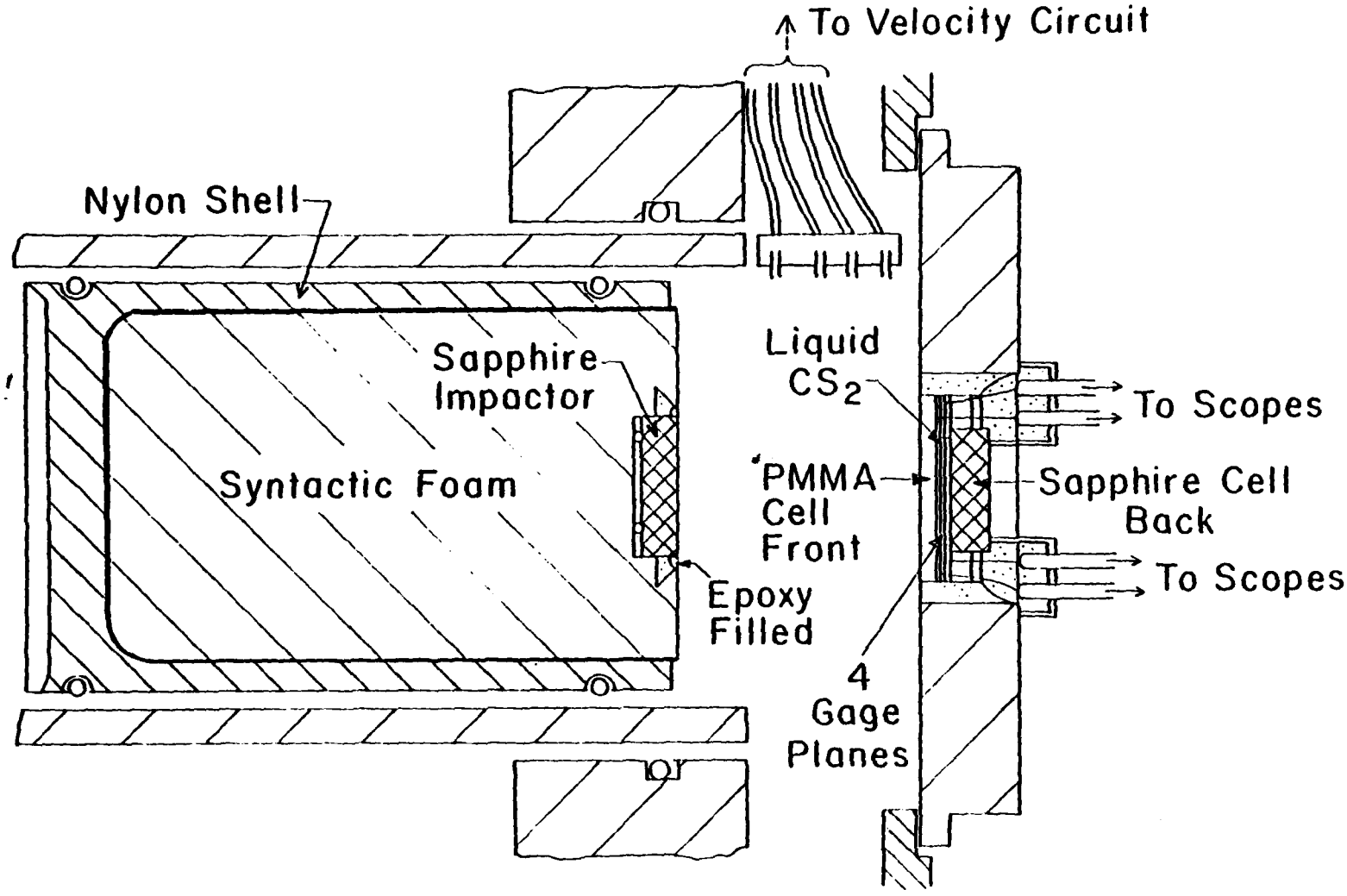

Fig. 3.3.--Cross-Section of Projectile and Target Assembly Just Before Impact.

tiles (Fig. 3.4c), patterned after an SRI design,[27] were used for nearly all the shots.

Each projectile had a brass trigger pin shorting strip (1.5 mm thick by 10 mm wide, covering 120° of arc) positioned on the outside edge as shown in Fig. 3.4. Apparently the projectile did not rotate appreciably during its travel down the barrel since the strip, with only one exception, shorted the velocity pins.

Projectile Preparation

In order to minimize tilt at impact, the projectile front was lapped and checked for perpendicularity with the sides. The maximum acceptable tolerance was 0.01 milliradians out of perpendicularity. This process was completed prior to the installation of the sapphire impactor because of the difficulty in lapping sapphire.

Sapphire used for the impactor was of the same type used for the cell back plate--unoriented, single crystal.[22] Dimensions for the impactors, along with other projectile properties, for each shot are listed in Table 3.4. Figure 3.5 shows the impactor before installation (grooves were cut to give the epoxy something to key on) and after. It was epoxied into the projectile with Epon 815 epoxy. Notice the rubber O-ring which was placed in the bottom of the cutout to hold the sapphire firmly against a lapped flat steel plate which was weighted (about 10 Kg) to make it sit on the lapped projectile face while the epoxy cured. Measurements indicated the impactor was parallel with the projectile face to within 0.06 milliradian.

Projectile mass was a big consideration and the nylon-syntactic foam projectiles were found to be the lightest ones yet designed for this gun.

Velocities of 1.2 mm/μsec were easy to attain with 1.30 mm/μsec possible (and achieved in another set of experiments). The mass of each of the projectiles used in this study is given in Table 3.4.

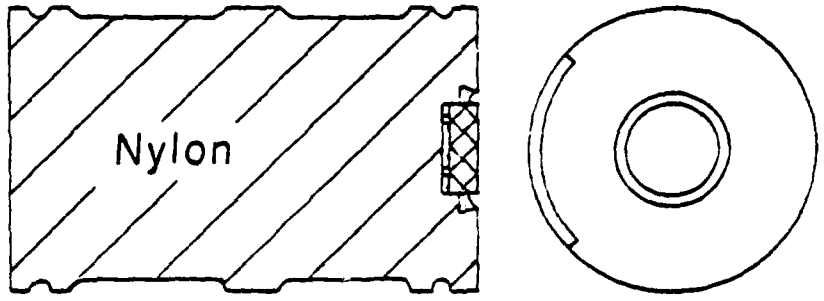

(a) Nylon projectile configuration

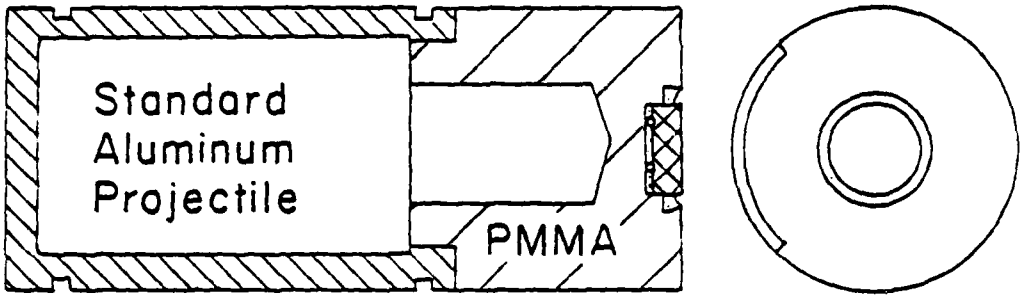

(b) Aluminum-PMMA projectile

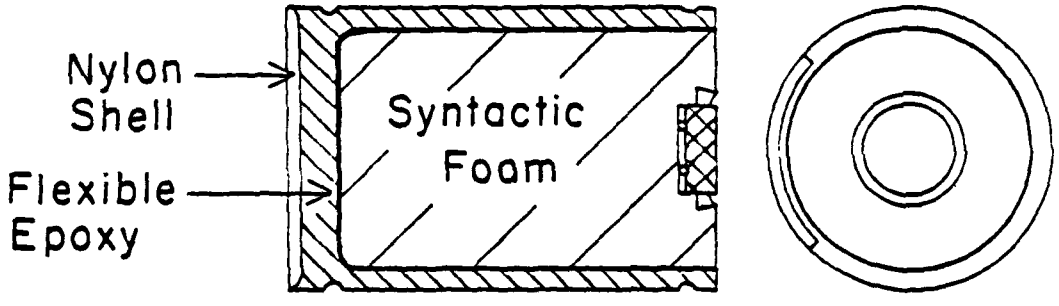

(c) Nylon-syntactic foam projectile

Fig. 3.4.--Cross-Sections of the Three Types of Projectiles Used. The nylon-syntactic foam projectile was used for nearly all the shots.

TABLE 3.4.-- Projectile Properties

Shot No.	Projectile Type	Mass (Kg)	Length (cm)	Sapphire Impactor Diameter (mm)	Sapphire Impactor Thickness (mm)	Breech Used: Double Diaphragm	Breech Used: Wrap Around
77-003	All Nylon	1.496	17.8	25.4	3.05	x	
77-020	Aluminum-PMMA	1.921	29.2	25.4	6.35		x
77-044	Nylon-Syn. Foam	0.923	15.2	25.4	6.41	x	
77-045	Nylon-Syn. Foam	0.677	10.9	25.4	6.35	x	
77-050	Nylon-Syn. Foam	0.989	15.4	25.4	6.41		x
77-055	Aluminum-PMMA	1.919	29.2	25.4	6.40		x
77-062	Nylon-Syn. Foam	1.138	16.7	25.4	6.40		x
77-070	Nylon-Syn. Foam	1.124	16.6	25.4	12.76	x	
77-071	Nylon-Syn. Foam	1.349	18.9	25.4	12.75	x	
77-094	Nylon-Syn. Foam	1.392	33.9	25.1	12.75	x	
77-095	Nylon-Syn. Foam	1.246	18.1	25.4	12.75	x	
77-103	Nylon-Syn. Foam	0.878	13.1	31.8	12.60	x	
77-104	Nylon-Syn. Foam	0.863	13.1	31.8	12.70		x
77-105	Nylon-Syn. Foam	0.878	13.1	? .8	12.68		x
77-106	Nylon-Syn. Foam	1.025	15.4	31.8	12.68	x	
77-107	Nylon-Syn. Foam	1.118	16.4	31.8	12.70	X	

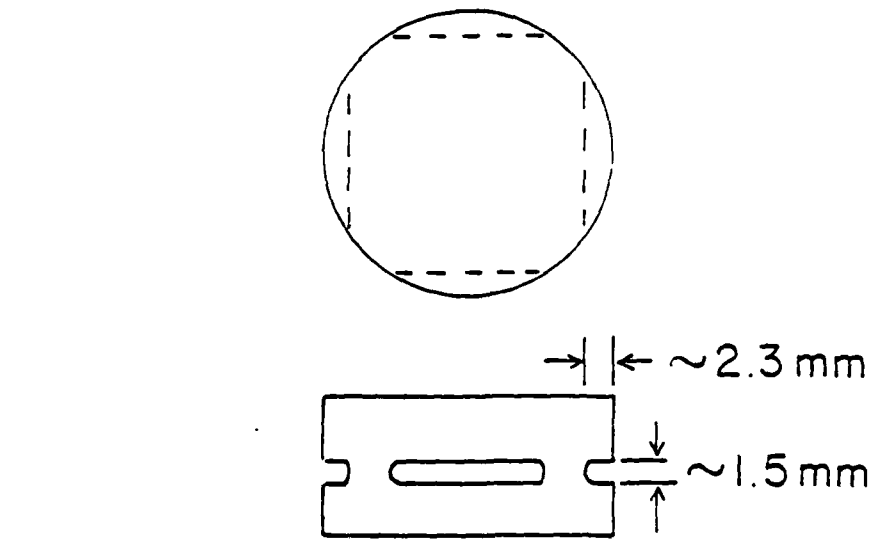

(a) Sapphire before installation

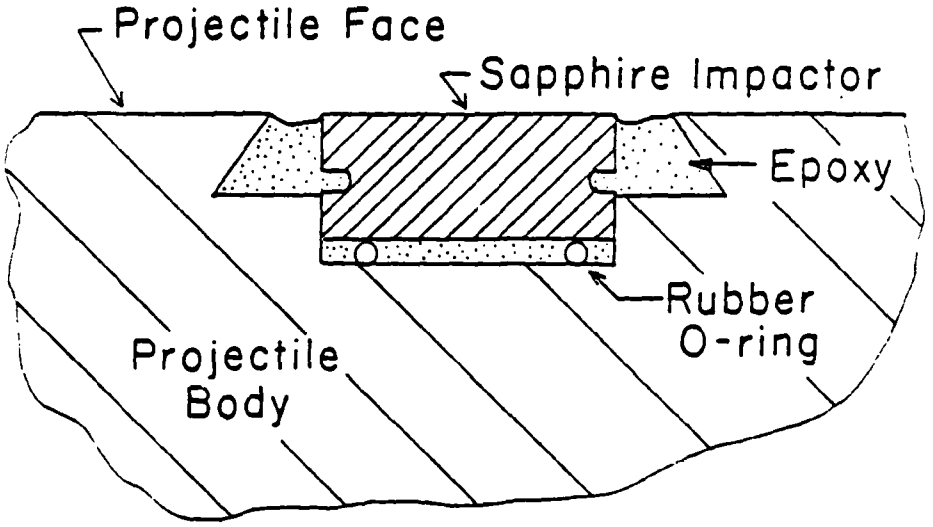

(b) Sapphire impactor glued in place

Fig. 3.5.--Sapphire Impactor Installation in Projectile. The rubber O-ring was used to keep the impactor flush with the projectile face during the epoxy operation. Slots were made in the impactor for the epoxy key on.

4.4 RESULTS

Results of the experiments on CS_2, along with calculations based on the equations of state introduced in Section 4.2, will be present in this chapter. Also included are the results of calculations using a one-dimensional wave propagation code to simulate some of the experiments. A complete discussion of both the calculated and experimental results will be presented in the next chapter.

General Shot Data

Sixteen usable experiments were performed in the course of this study: 14 with CS_2, one with H_2O and one with a cell made entirely of PMMA. The general information for each of these shots is listed in Table 4.1. Particle velocity waveforms were time-correlated and then plotted so the various information could be obtained for the initial shock and the two reflected shocks. Time-correlated data for shots 77-106, 77-070, and 77-020 are shown in Figs. 4.1, 4.2, and 4.3, respectively. Notice in Fig. 4.1 the particle velocity decreases as each of the two reflected shocks passes the gage plane. Also notice the fiducial marks that were used to time-correlate the data.

Two data reduction problems will be discussed at this point. [illegible] the cells were filled, the intermediate kapton gage planes wrinkled, so final gage positions were considerably different from those when the cell was constructed. Because of this solidly mounted gages were used to determine the initial shock [illegible] intermediate gage positions were back [illegible]

AD-A120 516 SHOCK-INDUCED CHEMICAL REACTIONS IN CONDENSED MATTER (U) WASHINGTON STATE UNIV PULLMAN DEPT OF PHYSICS G E DUVALL ET AL. AUG 82 N00014-77-C-0232 2/3

UNCLASSIFIED F/G 20/13 NL

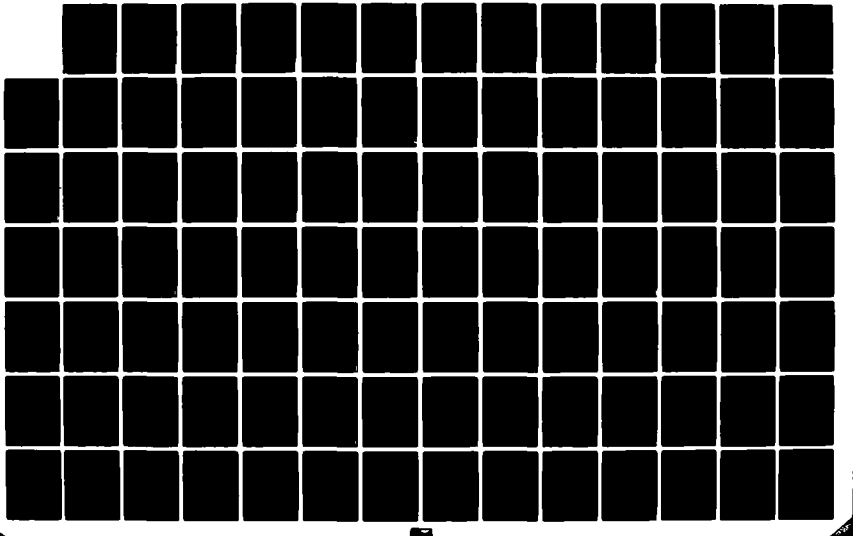

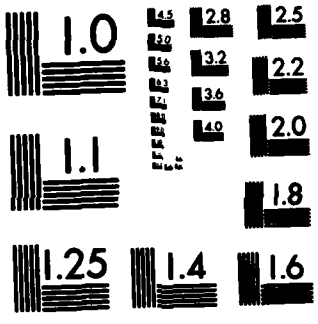

TABLE 4.1.--General Shot Information

Shot No.	Temperature °C	Projectile Velocity (mm/μsec)	Magnetic Field (Gauss)	Material	Cell Type	Gage Distances from Front Gage in mm: Middle Front Gage	Middle Gage	Middle Back Gage	Back Gage
77-003	23	0.885	2140	CS_2	A	---	---	---	2.060
77-020	23	0.589	2150	CS_2	A	---	---	---	2.001
77-044	23	1.10	2142	CS_2	A	---	---	---	1.942
77-045	23	1.21	2149	CS_2	B	---	---	---	1.844
77-050	23	0.829	2130	CS_2	B	---	---	---	1.835
77-055	23	0.865	2130	CS_2	C	---	1.100*	---	2.012
77-062	23	0.821	2145	CS_2	C	---	1.071*	---	1.986
77-070	23	1.02	2145	CS_2	C	---	1.007*	---	1.976
77-071	23	0.923	2145	CS_2	C	---	1.044*	---	1.978
77-094	23	0.96**	2140	CS_2	D	---	1.075*	---	2.017
77-095	23	0.990	2140	CS_2	D	---	1.015*	---	1.951
77-103	23	0.869	2140	CS_2	E	---	---	1.341*	2.182
77-104	23	0.948	2140	PMMA	E	1.067	---	2.096	3.142
77-105	23	0.805	2140	H_2O	E	0.595*	---	1.392*	2.169
77-106	23	1.09	2140	CS_2	E	0.577*	---	1.213*	2.217
77-107	23	0.982	2135	CS_2	E	0.611*	---	1.281*	2.192

*Positioned by using shock velocity computation.

**Estimated, velocity data lost.

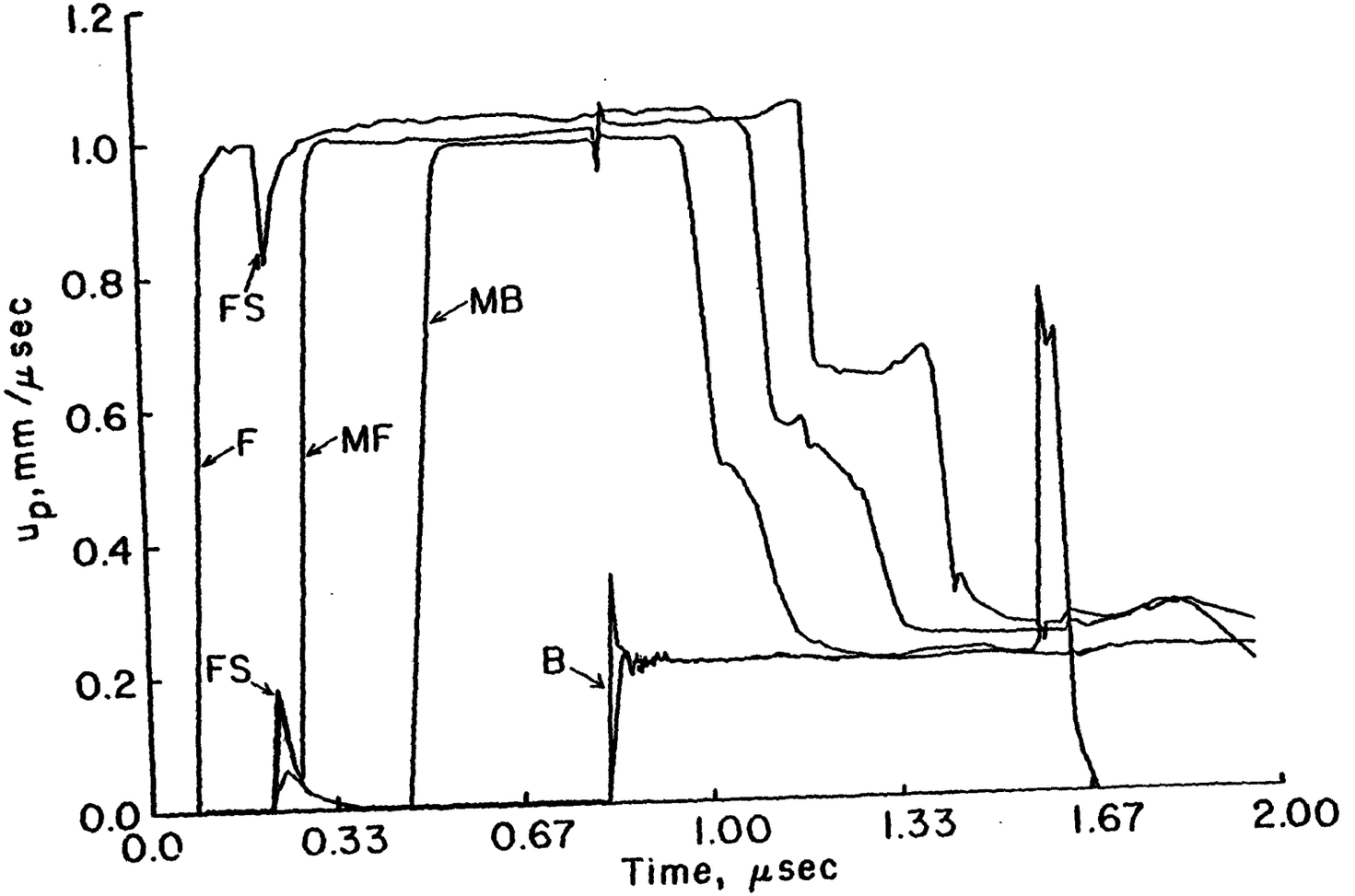

Fig. 4.1.--Time-Correlated Particle Velocity Waveforms for Shot 77-106. F, MF, MB, and B are the front (PMMA-CS_2) gage, middle-front gage in CS_2, middle-back gage in CS_2, and back (CS_2-sapphire) gage signals, respectively. Fiducial signals are labeled FS.

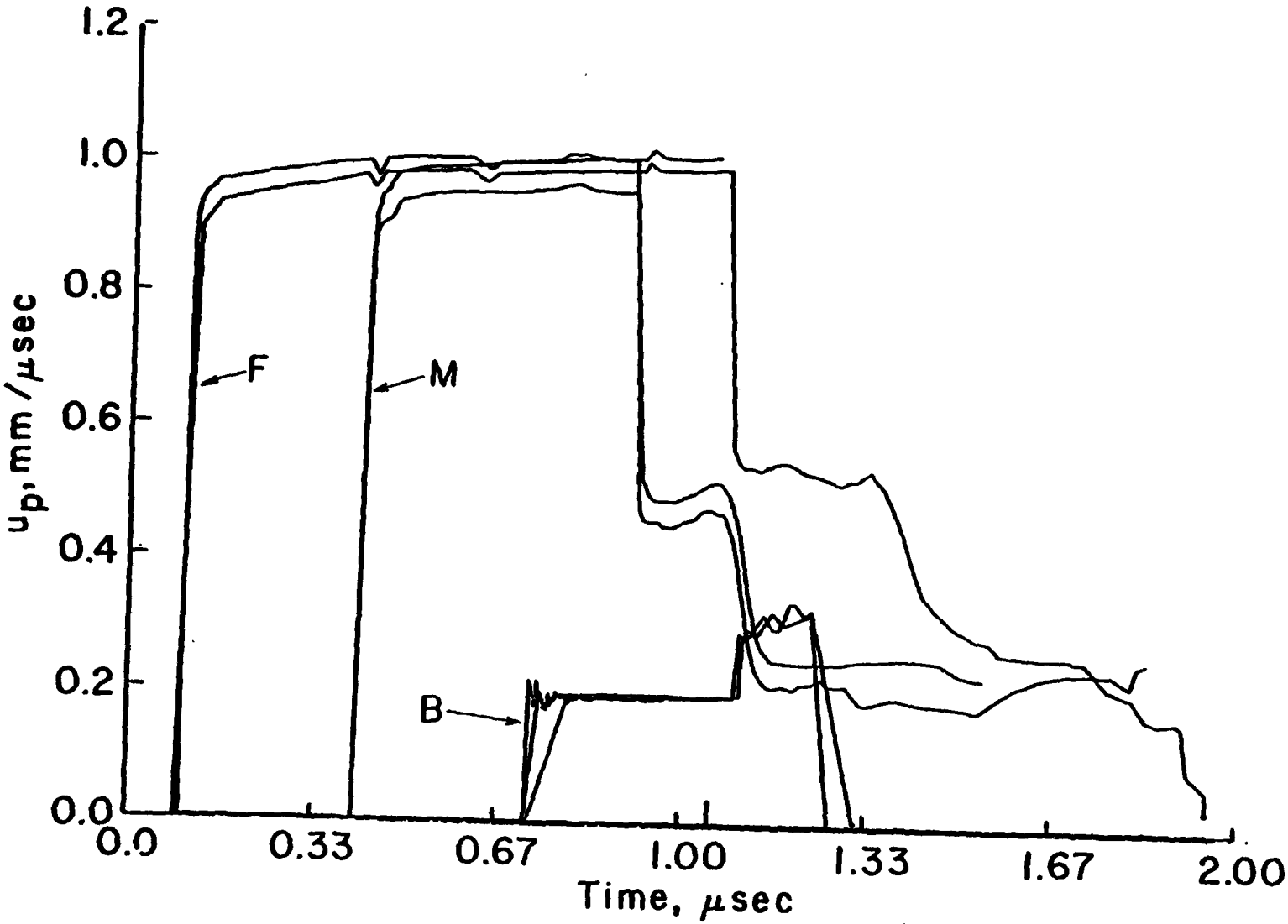

Fig. 4.2.--Time-Correlated Particle Velocity Waveforms for Shot 77-070. F, M, and B are the front (PMMA-CS_2) gage, middle CS_2 gage and back (CS_2-sapphire) gage signals, respectively.

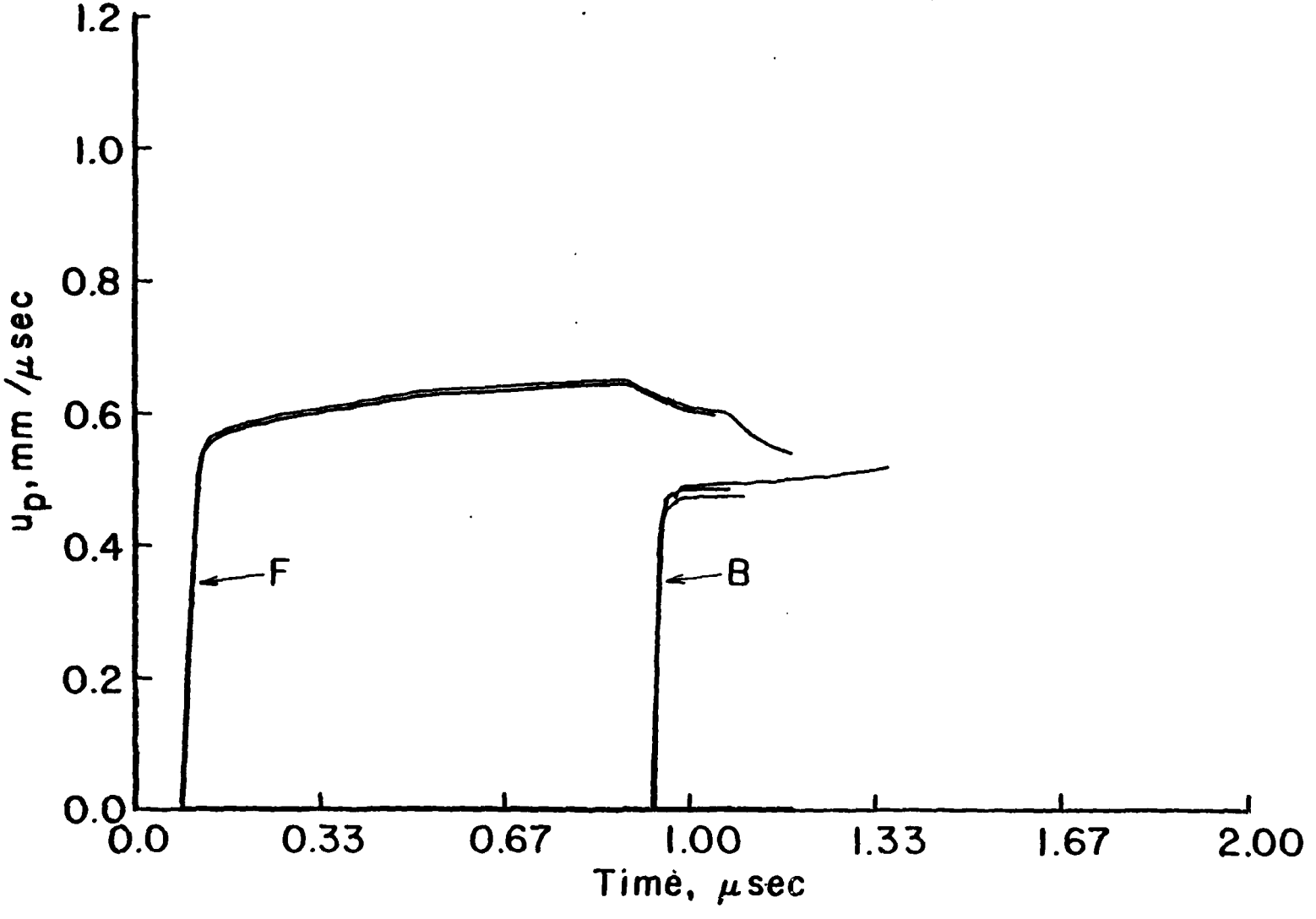

Fig. 4.3.--Time-Correlated Particle Velocity Waveforms for Shot 77-020. F and B are the front (PMMA-CS_2) gage and the back (CS_2-PMMA) gage signals, respectively.

The second problem is readily observable from Fig. 4.1 and 4.2, that of different scopes yielding a different particle velocity waveform even though they were hooked to the same gage. Obviously a number of things might cause this result: bad calibrations from scope to scope, different kinds of scopes recording the same pulse differently, D-C calibration techniques being used to calibrate even though pulses are being recorded, base line shifts, etc. It is likely that all of these are involved to a greater or lesser extent to make the particle velocity amplitudes vary by up to 10%. Two mock shots were carried out using a pulse generator to simulate the waveforms in regular experiments. The results were essentially identical to the shot data, i.e., voltages of the pulses varying by up to 10%. The decision was then made to average the particle velocity amplitude data and use the mean as the measured value. Data obtained by doing this on the CS_2, H_2O, and PMMA shots are consistent with results of other experiments, as will be discussed later.

Unreacted Hugoniot Data

In each experiment the initial shock is nonreactive and therefore yields an unreacted Hugoniot point. Fourteen new Hugoniot points between 17 and 50 kbar were generated in this study and are tabulated in Table 4.2. Maximum and minimum values of particle velocity for state 1 are tabulated along with the mean value which was used in the calculations to determine P_1, V_1, and E_1. One particle velocity for each waveform was used in the averaging procedure. The appropriate value for the intermediate gage waveforms was apparent because the waveforms were essentially flat on top. CS_2-PMMA gage

TABLE 4.2.--CS_2 Unreacted Hugoniot Data, State 1

Shot No.	Initial Density (g/cm^3)	Measured Shock Velocity (mm/μsec)	Measured Particle Velocity			Calculated Hugoniot Data		
			Maximum (mm/μsec)	Minimum (mm/μsec)	Mean (mm/μsec)	Pressure (kbars)	Specific Volume (cm^3/g)	Internal Energy (Mbar cm^3/g)
77-003	1.26	2.81	0.879	0.862	0.871	30.8	0.548	0.00379
77-020	1.26	2.38	0.580	0.575	0.577	17.3	0.602	0.00166
77-044	1.26	3.22	1.09	1.05	1.07	43.4	0.530	0.00573
77-045*	1.26	3.28	1.21	1.14	1.17	48.3	0.511	0.00683
77-050	1.26	2.73	0.826	0.775	0.800	27.5	0.561	0.00320
77-055	1.26	2.45	0.685	0.643	0.664	20.5	0.579	0.00220
77-062	1.26	2.70	0.781	0.763	0.770	26.2	0.568	0.00296
77-070	1.26	3.17	0.986	0.945	0.965	38.5	0.552	0.00466
77-071	1.26	2.90	0.892	0.825	0.869	31.7	0.556	0.00377
77-094	1.26	2.88	0.985	0.882	0.928	33.7	0.538	0.00431
77-095	1.26	2.92	1.000	0.897	0.933	34.3	0.540	0.00436
77-103	1.26	2.79	0.980	0.808	0.829	29.1	0.558	0.00343
77-106	1.26	3.07	1.033	0.969	0.995	38.5	0.537	0.00495
77-107	1.26	2.98	0.921	0.869	0.901	33.8	0.554	0.00406

*May have been reacting in first shock; reshock pressure above elastic limit of sapphire.

values were harder to pick because of the viscoelastic nature of the PMMA. A value just above the major part of the wave front rounding was used. Figure 4.4 illustrates the waveform position of the particle velocities used, A being the value for the PMMA-CS_2 gage and B being the value for the intermediate gages.

Shock velocity was calculated from the front and back gage data as previously mentioned. Since both shock velocity and particle velocity were measured quantities, no other information was required to completely determine the P-V-E values of state 1. It was unnecessary to know the PMMA Hugoniot exactly or to use the projectile velocity in obtaining this state.

Unreacted CS_2 Reshock States

Reshock states in the CS_2 were obtained from the measured data in two ways. For the shots that did not immediately react, the initial particle velocity measured by the CS_2-sapphire gage, along with the known sapphire Hugoniot, yield the reshock state 3' pressure and particle velocity (Fig. 1.4c). These data for six of the shots are tabulated in Table 4.3 along with state 1 data. Note that shots 77-003, 77-020, and 77-044 do not appear in reshock tables because they had PMMA back plates. Also included in the table are calculated reshock states based on the unreacted CS_2 EOS. The calculations were made using the initial state P_1 as the reference point for the reshock calculation. The final state (3') was obtained graphically from the point where the left going reshock Hugoniot crossed the right going sapphire Hugoniot as shown in Fig. 1.4c. The sapphire Hugoniot used in the calculations was that measured by Barker and Hollenback,[28]

$$U_s = 1.119 + 1.0\, u_p \ (\text{cm}/\mu\text{sec}) \ . \qquad (4.1)$$

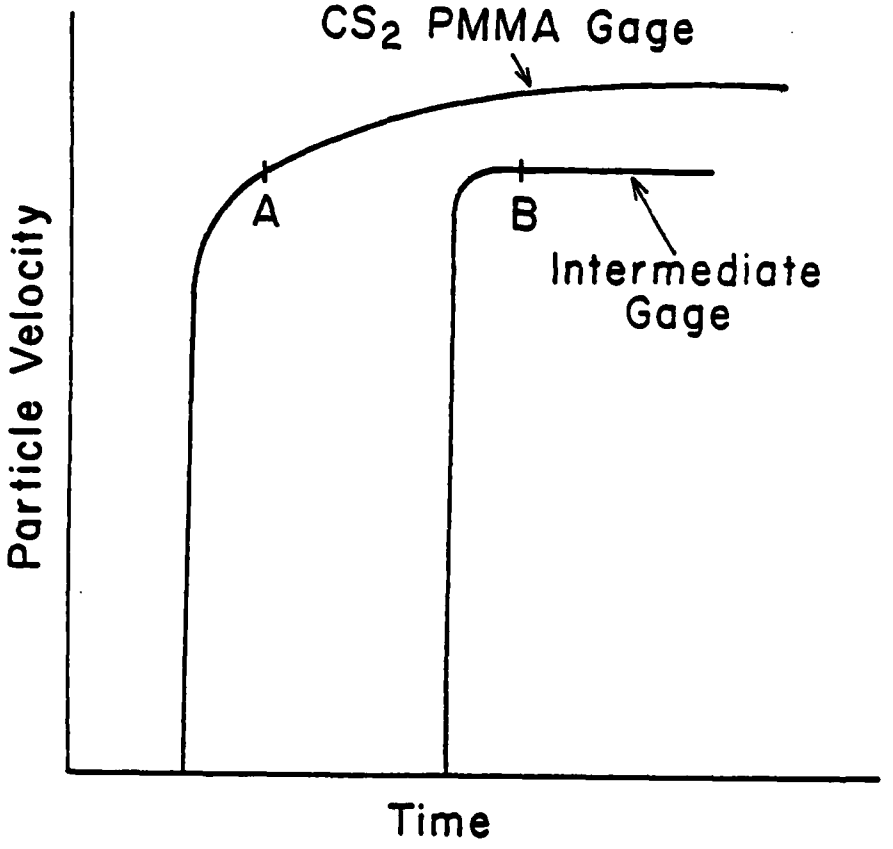

Fig. 4.4.--Positions of State 1 Particle Velocities on Waveforms. A was the position chosen for the front (PMMA-CS_2) gage signal and B was the position chosen for the intermediate gage signals. Note that the intermediate gage signals are essentially flat-topped while the front gage signals show structure due to the viscoelastic nature of PMMA.

TABLE 4.3.--Calculated and Measured Unreacted CS_2 State 3' Reshock States

	Initial State				Measured Reshock State from CS_2-Sapphire Gage		Calculated Reshock State from Unreacted CS_2 EOS			
Shot No.	u_{p1} (mm/μsec)	P_1 (kbars)	V_1 (cm^3/g)	$T_1^{\dagger}$ (°K)	$u_{p3'}$ (mm/μsec)	$P_{3'}$ (kbars)	$u_{p3'}$ (mm/μsec)	$P_{3'}$ (kbars)	$V_{3'}$ (cm^3/g)	$T_{3'}$ (°K)
77-045	1.17	48.3	0.511	1058	*	*	0.295	133.5	0.447	1521
77-050	0.800	27.5	0.561	741	0.158	71.5	0.166	75.0	0.484	1042
77-055	0.664	20.5	0.579	636	0.121	54.5	0.121	55.1	0.505	879
77-062	0.770	26.2	0.568	722	0.158	71.5	0.156	71.4	0.487	1013
77-070	0.965	38.5	0.552	908	*	---	0.236	106.0	0.461	1295
77-071	0.869	31.7	0.556	804	0.190	86.2	0.193	86.8	0.474	1139
77-094	0.928	33.7	0.538	835	0.185	83.9	0.204	92.7	0.470	1186
77-095	0.933	34.3	0.540	844	*	---	0.210	94.1	0.469	1198
77-103	0.829	29.1	0.558	765	0.167	75.6	0.177	79.4	0.480	1079
77-106	0.995	38.5	0.537	908	*	---	0.236	106.0	0.461	1295
77-107	0.901	33.8	0.554	836	*	---	0.206	92.8	0.470	1187

†Calculated temperature using unreacted CS_2 EOS.

*Initial state not determinable.

The second method used to obtain reshock states was to use the measured state 2 data for the R_1 wave. Shock velocity was determined graphically from a t-x diagram. Particle velocity was taken as the mean of those measured at the top of the R_1 wave; one value for each scope record was used in the mean calculation. Pressure and specific volume were calculated using Eqs. (2.7) and (2.8) with state 1 that given in Table 4.3. Table 4.4 contains the resulting R_1 wave data. It is believed that these data are not as reliable as those obtained by the first method because of wave evolution and also because of inaccuracies in the particle velocity measurements which are compounded each time the next calculation is made. Also included in Table 4.4 are calculated reshock states made by using the unreacted CS_2 EOS with P_1 as the reference pressure and P_2 as the final pressure. Temperatures are only approximate, but no errors can be assigned because of EOS uncertainties.

Reacted Product Data

There are two methods to obtain reacted product information from the experimental measurements. One is to use the relaxed particle velocity (state 3 in Fig. 1.4c) from the CS_2-sapphire gage data and the other is to calculate, from measured shock and particle velocities, state 3 which lies behind the R_2 wave. As previously indicated, the first method gives the most reliable information because it is a direct measurement.

State 3 particle velocities from the CS_2-sapphire gage are tabulated in Table 4.5 along with the pressure calculated using the sapphire data (Eq. 4.1) in the momentum jump condition. Also included in this table are state 3 values calculated from the measured R_2 wave data. The shock velocity was determined graphically. Pressure and specific

TABLE 4.4.--Calculated and Measured Unreacted CS_2 R_1 Wave, State 2, Reshock States

Shot No.	Initial State u_{p1}	P_1	V_1	Reshock State from R_1 Wave Data U_{s2} (mm/μsec)	u_{p2} (mm/μsec)	P_2 (kbars)	V_2 (cm^3/g)	Calculated Reshock State from Unreacted CS_2 EOS u_{p2} (mm/μsec)	P_2 (kbars)	V_2 (cm^3/g)	T_2 (°K)
77-045	same as in Table 4.3			-2.74	0.83	74.3	0.467	0.814	74.3	0.490	1215
77-050*				---	---	---	---	---	---	---	---
77-055				-2.45	0.12	49.8	0.478	0.121	55.1	0.505	879
77-062				-2.86	0.157	65.4	0.472	0.157	71.4	0.487	1013
77-070				-2.85	0.47	72.7	0.480	0.548	72.7	0.489	1116
77-071				-2.65	0.33	65.8	0.471	0.407	65.8	0.495	1020
77-094				-3.09	0.35	76.9	0.461	0.355	76.9	0.483	1099
77-095				-3.42	0.40	77.3	0.474	0.370	77.3	0.483	1106
77-103				-3.19	0.22	73.0	0.473	0.242	73.0	0.486	1042
77-106				-3.09	0.53	73.9	0.476	0.536	7.39	0.488	1122
77-107				-3.14	0.41	69.5	0.487	0.435	69.5	0.491	1058

*Gage broken prematurely, no R_1 wave data measured.

†No R_2 wave, calculated data from Table 4.3.

TABLE 4.5.--Measured State 3 for Reacted Products

	Relaxed CS_2-Sapphire Gage Data		R_2 Wave Data			
Shot No.	u_{p3} (mm/μsec)	P_3 (kbars)	U_{s3} (mm/μsec)	u_{p3} (mm/μsec)	P_3 (kbars)	V_3 (cm^3/g)
77-045	0.24	109.3	-1.68	0.24	106	0.357
77-070	0.190	86.2	-1.27	0.23	81.4	0.414
77-071	0.171	77.4	-0.48	0.17*	68.6	0.378
77-094	0.167	75.6	-0.69	0.16	81.2	0.377
77-095	0.181	82.0	-1.07	0.17	84.4	0.400
77-103	0.145	65.5	-0.45	0.15*	74.0	0.424
77-106	0.205	93.1	-1.60	0.22	87.8	0.407
77-107	0.176	79.7	-1.21	0.17	77.5	0.415

*Estimated particle velocity.

volume were calculated using Eqs. (2.10) and (2.11) along with state 2 values determined by the R_1 wave analysis.

Relaxation Data from CS_2-Sapphire Gage

Measurements at the CS_2-sapphire gage yielded some interesting data concerning the reaction. Figure 4.5 is an idealized drawing of a gage record showing the various features and data available. At the time of reaction onset a high frequency noise was measured that had a decay time longer than the particle velocity decay time. Because of the noise it was impossible to determine the exact nature of the particle velocity decay. Data for this decay were estimated by drawing a curve through the noise at what appeared to be the mean position. Noise decay time was also estimated but it was difficult to tell the end of the noise from normal noise on the approximately 100 millivolt signals. For many of the shots the induction time was so small that it was not resolvable in the 10 to 20 nsec risetime of the gage.

Waveforms for some of the CS_2-sapphire gage measurements are contained in the data records of Sec. 4.1, but the details cannot be determined from them. The measurements and estimations were made on expanded waveforms. Information from this exercise is tabulated in Table 4.6 along with calculated temperatures ($T_{3'}$) and pressures ($P_{3'}$) from Table 4.3 as a reference.

Particle Velocity Relaxation in the R_1 Wave Front

As indicated in Sec. 4.2, the initial particle velocity decay rate in the R_1 wave, $(\partial u_p/\partial t)_\xi$, is needed to make the calculation to estimate the reaction rate. This can be obtained by plotting changes in particle velocity as the wave propagates. It starts out with a small value (state 3') which increases as it travels because the wave is left-traveling in a medium moving to the right. Figure 4.6 is a plot of R_1 wave front particle velocity versus

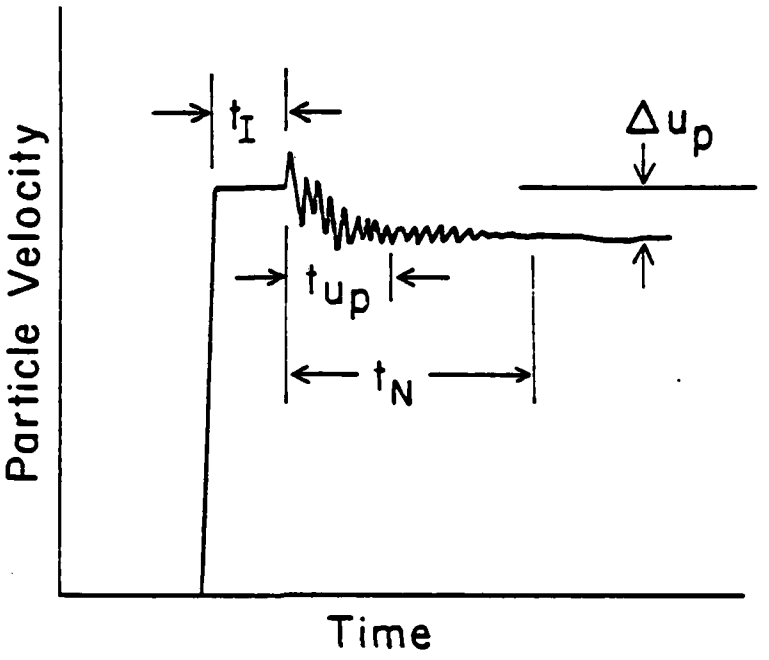

Fig. 4.5.--Idealized CS_2-Sapphire Gage Record. t_I is the induction time, t_N is the noise decay time, t_{up} is the particle velocity decay time, and Δu_p is the particle velocity decrease.

TABLE 4.6.--Reaction Data from CS_2-Sapphire Gage

Shot No.	Calculated Reshock Data: Pressure $P_{3'}$ (kbars)	Calculated Reshock Data: Temperature $T_{3'}$ (°K)	Induction Time t_I (μsec)	u_p Decay Time t_{u_p} (μsec)	Noise Decay Time t_N (μsec)	Δu_p (mm/μsec)	Approx. Noise Period (μsec)	Initial u_p Decay Rate du_p/dt_2 (mm/μsec^2)
77-045†	133.5	1521	<0.010	---	0.12	---	0.007	---
77-050*	75.0	1042	---	---	---	---	---	---
77-055*	55.1	879	---	---	---	---	---	---
77-062*	71.4	1013	---	---	---	---	---	---
77-070	106.0	1295	<0.006	0.05	0.13	0.046††	0.007	---
77-071	86.6	1138	0.049	0.08	0.17	0.019	0.008	0.44
77-094	92.7	1185	0.056	0.06	0.33	0.018	0.025	0.38
77-095	94.0	1198	<0.018	0.06	0.34	0.030††	0.010	---
77-103	79.3	1078	0.31	0.40	none	0.022	none	0.099
77-106	106.0	1295	<0.012	0.04	0.11	0.031††	0.007	1.27
77-107	92.8	1187	<0.018	0.08	0.24	0.035	0.008	---

*No evidence of reaction.

†Had an odd waveform possibly due to reaction in the initial wave.

††Estimate based on calculated state 3' particle velocity (see Table 4.3) as the initial state.

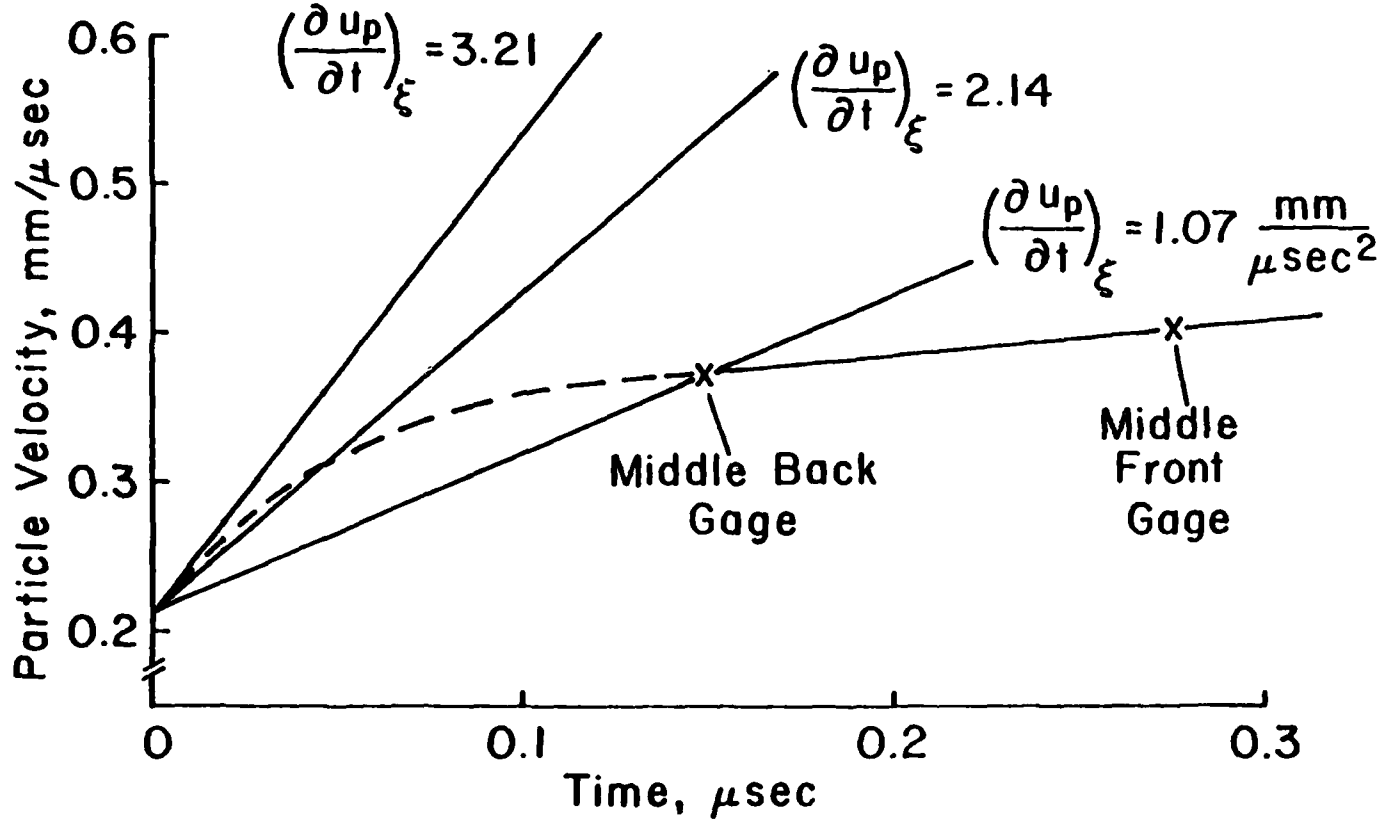

Fig. 4.6.--R_1 Wave Decay for Shot 77-107. The initial part of the decay curve is estimated as represented by the dashed line. The value chosen for $(\partial u_p/\partial t)_\xi$ on this shot is 2.5 mm/μsec^2.

time for shot 77-107. The method used to estimate the desired decay rate is illustrated in the figure. A decay rate obtained by using the initial particle velocity and the particle velocity of the closest gage to the back is obviously too small. If one estimates the shape of the curve, it is apparent that two to three times this rate is more reasonable. Table 4.7 is a tabulation of the various particle velocities and the associated times after reflection from the sapphire, along with what is considered a reasonable estimate of $(\partial u_p/\partial t)_\xi$ at the CS_2-sapphire interface. Only the shots with intermediate gages were examined.

Rise Time of the R_2 Wave

The rise time of the R_2 wave yields an estimate of reaction rate. A review of the waveforms indicates the R_2 wave front is usually rounded at both the top and bottom of the wave, so only the middle slope, near the inflection point, was considered in the analysis. It is also apparent the wave fronts were not always smooth so some judgment was required in deciding what to use.

Results of this analysis are listed in Table 4.8 along with the reaction rates calculated from the average value of $\Delta u_p/\Delta t$ divided by the particle velocity difference from the top to the bottom of the wave. Note that some of the waves steepen as they travel while others spread out. Any change implies that the wave is not steady and that the jump conditions used in calculating states 2 and 3 do not strictly apply. There are not enough data to say anything about a trend in this area. Some waveforms exhibited more than one slope, which may indicate more than one reaction in the wave.

Miscellaneous Experiments

Several experiments were run to determine the nature of certain problems and anomalous effects. One shot (77-104) consisted of a PMMA cell

TABLE 4.7.-- R_1 Wave Front Particle Velocity Decay

	Back Gage	Middle Gages			Front Gage		
Shot No.	Calculated $u_{p3'}$ (mm/μsec)	u_{p2} (mm/μsec)	Time From Back Gage (μsec)	u_{p2} (mm/μsec)	Time From Back Gage (μsec)	u_{p2} (mm/μsec)	Time From Back Gage (μsec)	Estimate for $(\partial u_p/\partial t)^2$* (mm/μsec^2)
77-070	0.236	0.47	0.188	---	---	0.53	0.358	3.0
77-071	0.195	0.29	0.182	---	---	0.37	0.348	1.0
77-094	0.200	0.32	0.150	---	---	0.37	0.343	1.5
77-095	0.211	0.37	0.131	---	---	0.41	0.320	2.5
77-103	0.178	0.21	0.139	---	---	0.24	0.382	0.5
77-106	0.236	0.49	0.182	0.55	0.273	0.63	0.368	2.6
77-107	0.211	0.37	0.149	0.40	0.275	0.47	0.367	2.5

*Initial value at the CS_2-sapphire interface.

TABLE 4.8.--R_2 Wave Front Reaction Rate Data

Shot No.	Δu_p From Top to Bottom of R_2 Wave (mm/μsec)	Slope of R_2 Wave Front, mm/μsec^2				Average $\Delta u_p/\Delta t$ (mm/μsec^2)	Reaction Rate (1/μsec)
		Middle Back Gage	Middle Gage	Middle Front Gage	Front Gage		
77-045	-0.59	---	---	---	-16.0	-16.0	27
77-070	-0.28	---	-4.9	---	- 2.6	- 3.7	13.2
77-071	-0.159	---	-0.93†	---	*	- 0.93	5.9
77-094	-0.183	---	-1.3†	---	- 2.2	- 1.8	9.8
77-095	-0.219	---	-3.0	---	- 1.9†	- 2.5	11.4
77-103	-0.150	-6.38	---	---	*	- 0.38	2.5
77-106	-0.325	-3.6	---	-3.5	-10.0	- 5.7	17.5
77-107	-0.234	-1.7	---	---	- 1.7†	- 1.7	7.3

*More than one slope apparent.

†R_2 wave did not reach gage during good recording time.

201

with PMMA between the gages; another shot (77-105) consisted of a regular cell filled with distilled water; and finally two shots (77-094 and 77-095) had gages between two pieces of sapphire to look at the noise generated by the reaction. These shots are discussed in the following subsections.

PMMA Shot

Shot 77-104 consisted of a regular cell with a sapphire backplate but without the cutouts for the liquid, i.e., PMMA layers were between the gages. The objectives of this shot were, first, to determine if any extraneous electrical signals were generated in the PMMA that might influence the gage outputs, and second, to examine the form of the wave transmitted through the PMMA. In the CS_2 shots, the CS_2-PMMA gages exhibited initial shock waveforms which are rounded, a characteristic of viscoelastic materials. By the time the shock reaches the middle CS_2 gage, all the rounding is essentially gone. This change was attributed to shocking up in the liquid but a check was desired.

No extraneous electrical signals were generated and rounded waveforms were recorded by each gage, even when the wave reflected from the sapphire back plate at a relatively high pressure. This substantiates the shocking up idea. Hugoniot data generated by this experiment agree well with other data.

H_2O Shot

In order to make sure the reaction data obtained in the CS_2 shots were not caused by the experimental setup, one cell was filled with distilled water, which was felt to be a nonreacting material (although there was some possibility a phase change might occur).

No anomalous gage response or two-wave structure was observed. A Hugoniot point was generated that is consistent with other measured data. This, along with the PMMA shot results, substantiate the utility of using this method for obtaining good Hugoniot data that does not depend on other parameters such as projectile velocity or interface material Hugoniot.

Sapphire Gage Shots

Two shots (77-094 and 77-095) were made in which an electromagnetic gage was sandwiched between two pieces of sapphire, which were then used for the back plate of a CS_2 cell. The purpose for doing this was twofold: to measure the particle velocity decay wave transmitted into the sapphire without the noise superimposed on it, and to see if the noise was an electrical signal propagating through the whole region rather than just noise at the CS_2-sapphire gage.

Waveforms from the shots indicate the noise is an electrical signal propagating through the whole experiment, starting, apparently, at the time reaction starts. In fact, on these and most later shots, the noise was detected on all the signals at the same time although the perturbations are quite small on the higher level signals.

Obtaining a noise-free record of the particle velocity decay was not possible because the noise was still being recorded at the time the shock arrived at the gage approximately 0.15 μsec later.

Rarefaction Speed Measurements

An unexpected piece of data was measured as a result of the sapphire impactor and PMMA cell front being relatively thin in the early experiments. A rarefaction from the interfaces traveled through the cell during the time the CS_2 was at the initial pressure, P_1. By constructing a time-distance

diagram it was possible to determine the speed of the beginning of the rarefaction (which is simply the sound speed at state 1) on three separate experiments. The data for these shots are shown in Table 4.9.

TABLE 4.9.--CS_2 Sound Speed Measurements

	State 1 Data				
Shot No.	P_1 (kbars)	U_{s1} (mm/μsec)	V_1 (cm^3/g)	Sound Speed c_1 (mm/μsec)	c_1/U_{s1}
77-003	30.8	2.81	0.548	3.03	1.08
77-044	43.4	3.22	0.530	3.62	1.12
77-055	20.5	2.45	0.579	2.73	1.11

Sound speeds obtained in this manner can be used to calculate the isentropic bulk modulus and also the Gruneisen parameter at state 1 conditions. The isentropic bulk modulus can be calculated from

$$K_S = -V\left(\frac{\partial P}{\partial V}\right)_S = \frac{c^2}{V} . \tag{4.2}$$

The Gruneisen parameter can be obtained by solving the P-V differential equation of the Hugoniot for Γ to obtain

$$\Gamma = \frac{2\left[V^2\left(\frac{dP}{dV}\right)_H + c^2\right]}{V\left[\left(\frac{dP}{dV}\right)_H (V_o - V) + (P - P_o)\right]} . \tag{4.3}$$

Values for the slope of the P-V Hugoniot were calculated using the unreacted CS_2 EOS. Results of this analysis are listed in Table 4.10.

Computer Simulation of Experiments

One-dimensional wave propagation code calculations using the POD code [29] available at WSU were made to determine if the waveforms recorded by

the particle velocity gages could be reproduced, thereby leading to a better understanding of the process. POD is a general purpose code using a second order finite difference numerical integration of the flow equations. It utilizes the von Neumann-Richtmeyer[30] artificial viscosity to prevent numerical instabilities at the shock front.

TABLE 4.10.--Calculation of K_S and Γ from Sound Speed

Shot No.	$(dP/dV)_H$ (cm/μsec)^2	K_S (mbars)	Γ	Γ/V (g/cm^3)
77-003	-0.460	0.168	2.08	3.79
77-044	-0.675	0.247	1.66	3.13
77-055	-0.296	0.129	2.01	3.47

†Calculated using unreacted CS_2 EOS.

Andrews[5] wrote an equation of state subroutine which allows a material to react according to a time dependent reaction rate relation. This subroutine requires two other subroutines be written to calculate the equation of state properties of the reactant and products. The equations of state described in Section 4.2 were used for this purpose.

Input Data

To simulate the experiments, it was necessary to provide mechanical P-V equations of state for PMMA and sapphire. The form of the P-V relation is

$$P = A + B\mu + C\mu^2 + D\mu^3 \qquad (4.4)$$

where $\mu = \frac{V_o}{V} - 1$. Parameters used for PMMA and sapphire are listed in Table 4.11. PMMA has an unnatural relation because there was no desire to

model its viscoelastic behavior but rather to provide a form that gives the proper state in CS_2 for a given projectile velocity.

TABLE 4.11.--PMMA and Sapphire EOS Constants for POD

Material	A (mbars)	B (mbars)	C (mbars)	D (mbars)	ρ_o (g/cm^3)
PMMA	0.0	0.047	-0.1388	0.5525	1.185
Sapphire	0.0	4.99	4.637	17.57	3.985

The equation of state parameters used for unreacted CS_2 and the reacted products are those of Tables 2.2 and 2.3, respectively.

Shots Modeled

Calculations were made to simulate a number of shots ranging from no reaction in the reflected wave to reaction in the initial wave. The following shots were modeled: 77-055, 77-103, 77-107, 77-071, 77-106, and 77-045.

Reaction Rate Law Used

A two-step rate law based on the complex Arrhenius rate law of Table 2.5 was used in the calculations. The rate law below 1125°K was

$$\frac{dx}{dt} = 1.3 \times 10^{15} e^{-72,500/RT} \mu sec^{-1} \quad (4.4)$$

and above was

$$\frac{dx}{dt} = 1300 e^{-10,400/RT} \mu sec^{-1} . \quad (4.5)$$

A maximum rate was established by limiting the change in x to 0.05 for each time step in order to maintain stability. This was not a serious constraint because rates up to 50 μsec^{-1} were still possible.

Results of Calculations

Calculated waveforms did not simulate the measured waveforms very well because a great deal of relaxation was calculated behind the first wave that was not observed in the experiments. Time limitations made it impossible to determine if this relaxation was an artifact of the calculations owing to interface instabilities or if other undiscovered problems were involved. For this reason, none of the wave structure results will be presented here. It is presently felt that the wave structure between the R_1 and R_2 waves may hold some very important information regarding intermediate reactions, etc. that cannot yet be interpreted because of lack of understanding.

There are several important pieces of information that result from the calculations which are rather insensitive to the wave structure. Temperature and volume changes resulting from the reaction are available from the output of the code calculations. Temperature change information is summarized in Table 4.12 and volume change information in Table 4.13.

TABLE 4.12.--Temperature Change Information from POD Calculations

Simulated Shot No.	T_1 (°K)	T_3' (°K)	T_3 (°K)	Temperature Change (T_3-T_3') (°K)
77-055	635	879	873	no reaction
77-103	766	1079	1650	571
77-107	857	1187	1720	533
77-071	808	1139	1680	541
77-106	960	1295	1770	475
77-045	1000	1521	1820	299*

*Reaction in the initial shock was apparent.

TABLE 4.13.--Volume Change Information from POD Calculations

Simulated Shot No.	V_3' (cm^3/g)	V_3 (cm^3/g)	Volume Change ($V_3'-V_3$) (cm^3/g)	Percent Change
77-055	0.505	0.503	no reaction	---
77-103	0.480	0.392	0.088	18.3
77-107	0.470	0.381	0.089	18.9
77-071	0.474	0.387	0.087	18.4
77-106	0.461	0.372	0.089	19.3
77-045	0.447	0.364	0.083	18.6

4.5 DISCUSSION OF RESULTS

This chapter comprises a discussion of the results of the previous chapter in comparison with other published data and with various ideas developed in Sect. 4.2. Discussion will include applicability of the equations of state developed for the unreacted CS_2 and reacted products, reaction rate analysis, enlightenment from code calculations, and speculation regarding the noise and reaction mechanism.

Unreacted CS_2 Hugoniot Data

Fourteen Hugoniot points for the unreacted CS_2 principal Hugoniot have been generated in this study and are plotted along with data of Cook and Rogers,[31] Lysne,[32] Dick,[14] and Walsh and Rice[33] in U_s-u_p and P-V space in Fig. 5.1. Also plotted is the calculated Hugoniot based on the unreacted CS_2 EOS. It is apparent that the data generated in this study are in agreement with the results of other experiments.

Dick's data reported in Ref. 34 were based on a 1968 revision of the Hugoniot used to determine the states in the aluminum buffer plate in front of the CS_2. The effect of changing the aluminum Hugoniot from its earlier form is indicated by six points in Fig. 5.1 with arrows from three original points to the later data.

Dick estimated the cusp in the Hugoniot to occur at approximately 62 kbars. The data plotted in Fig. 5.1 suggest that large deviations from

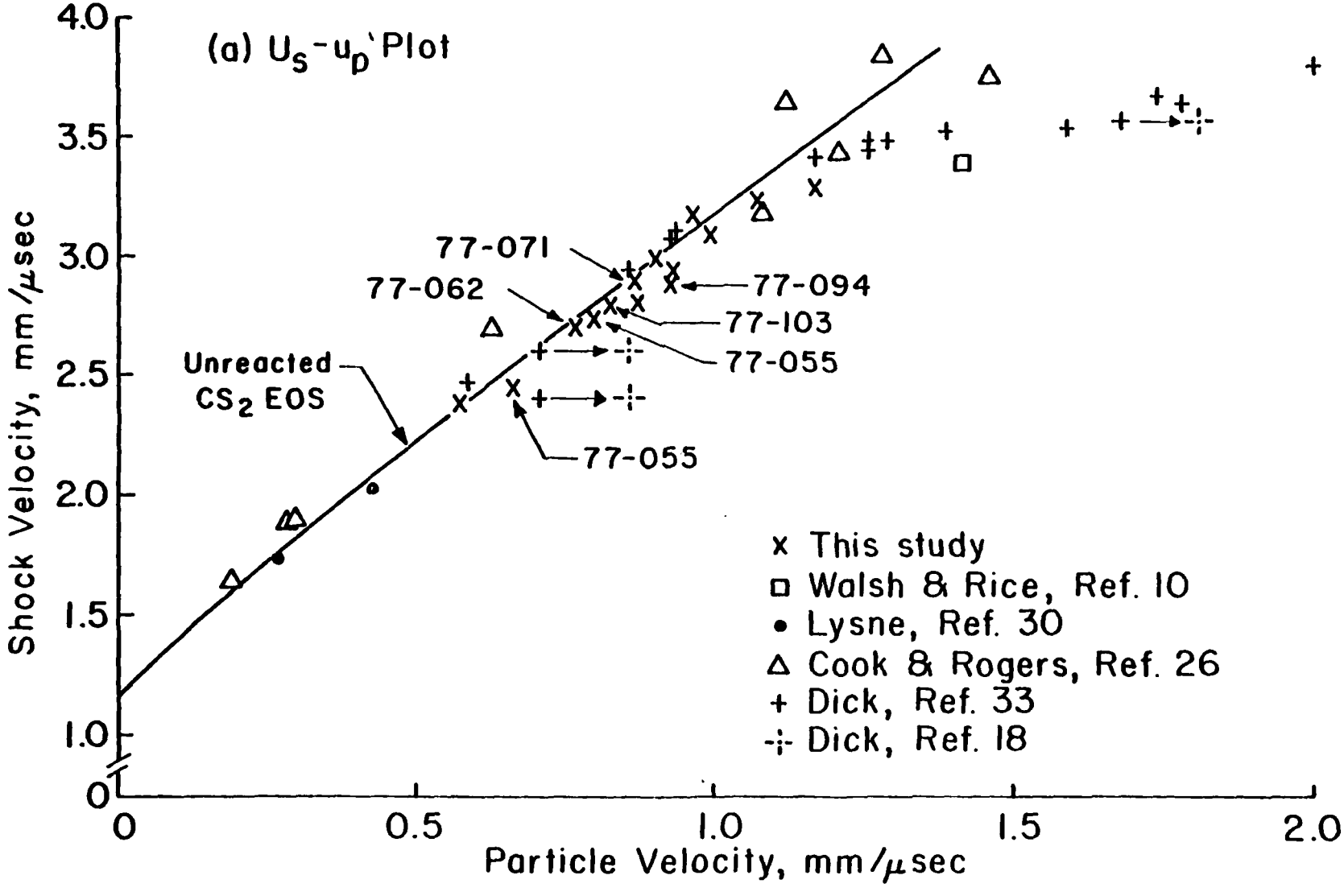

Fig. 5.1.--Comparison of Unreacted CS_2 Hugoniot Data. Lines are unreacted CS_2 EOS calculations. (a) is the U_s-u_p Hugoniot data.

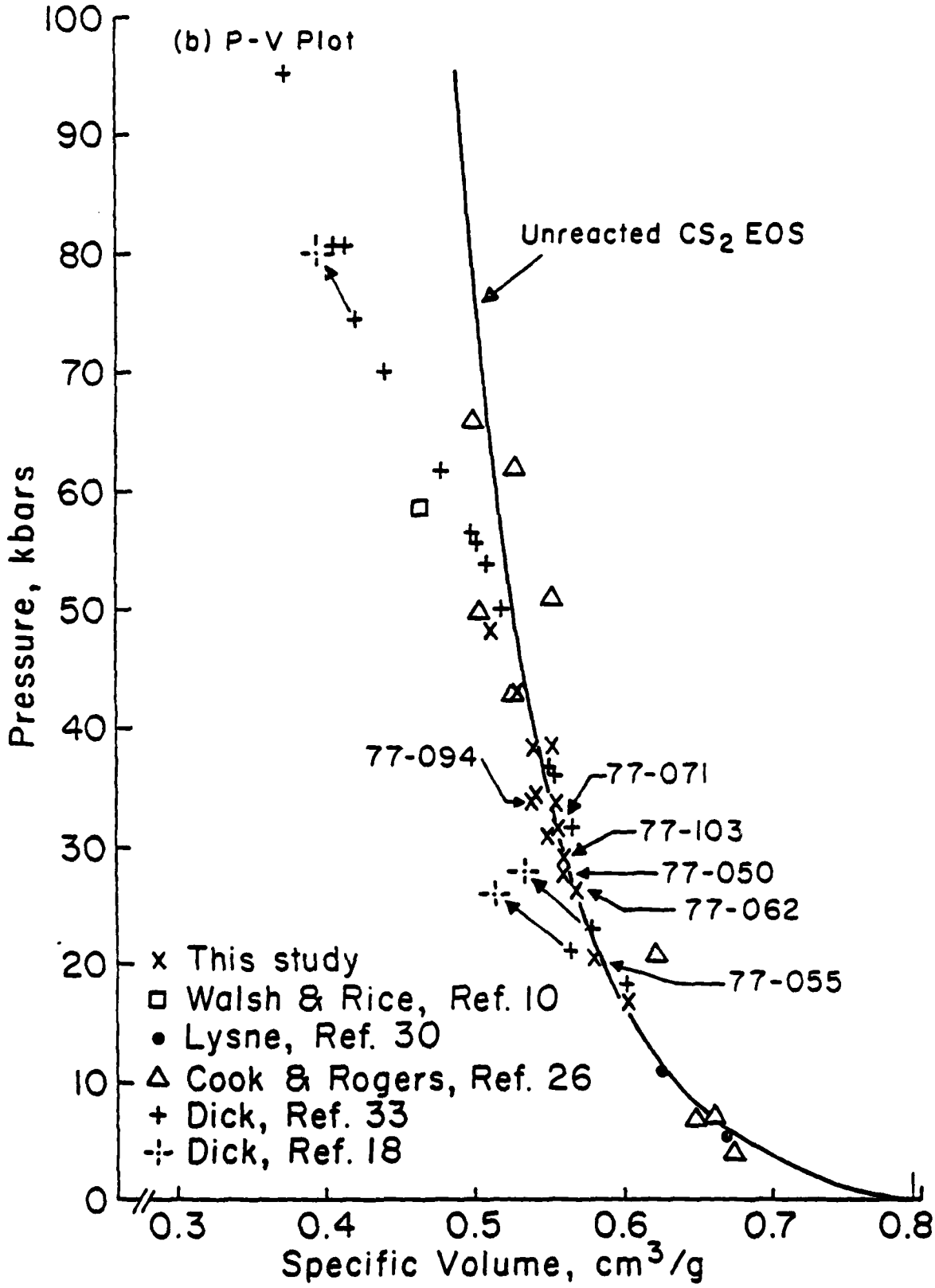

Fig. 5.1.--(Continued). (b) is the P-V Hugoniot Data.

the calculated curve begin around 50 kbars. Shot 77-045 had an anomalous CS_2-sapphire gage response that appears to have been caused by a two-wave structure indicating that reaction occurred in the initial shock. This shot had state 1 pressure of 48.3 kbars (which would be in error if the wave were reacting). Shot 77-044, with a state 1 pressure of 43.8 kbars, shows no evidence of reaction. Based on this information it is estimated that the cusp occurs in the 46 to 54 kbar range. This would also seem to indicate that a single shock study of the cusp is possible on the WSU gas gun.

Unreacted CS_2 EOS

The calculated equation of state fits the data very well up to about 45 kbars at which point the data seems to fall off in the direction corresponding to a transition.

Sound speed data lead to calculations of isentropic bulk modulus and Gruneisen parameter. These data have been plotted along with the curve that represents the unreacted CS_2 EOS model in Fig. 5.2. The bulk modulus data lie very close to the model curve. Γ/V is in the same region as the model curve but appears to have a good deal of scatter or else to be a very complicated function.

These data, along with the good fit to the Hugoniot data, suggest that the equation of state is quite good in the principal Hugoniot region. One can infer from this that the temperature calculations are reasonable although K_S and Γ/V are not the best indicators. Accurate temperature measurements are still needed.

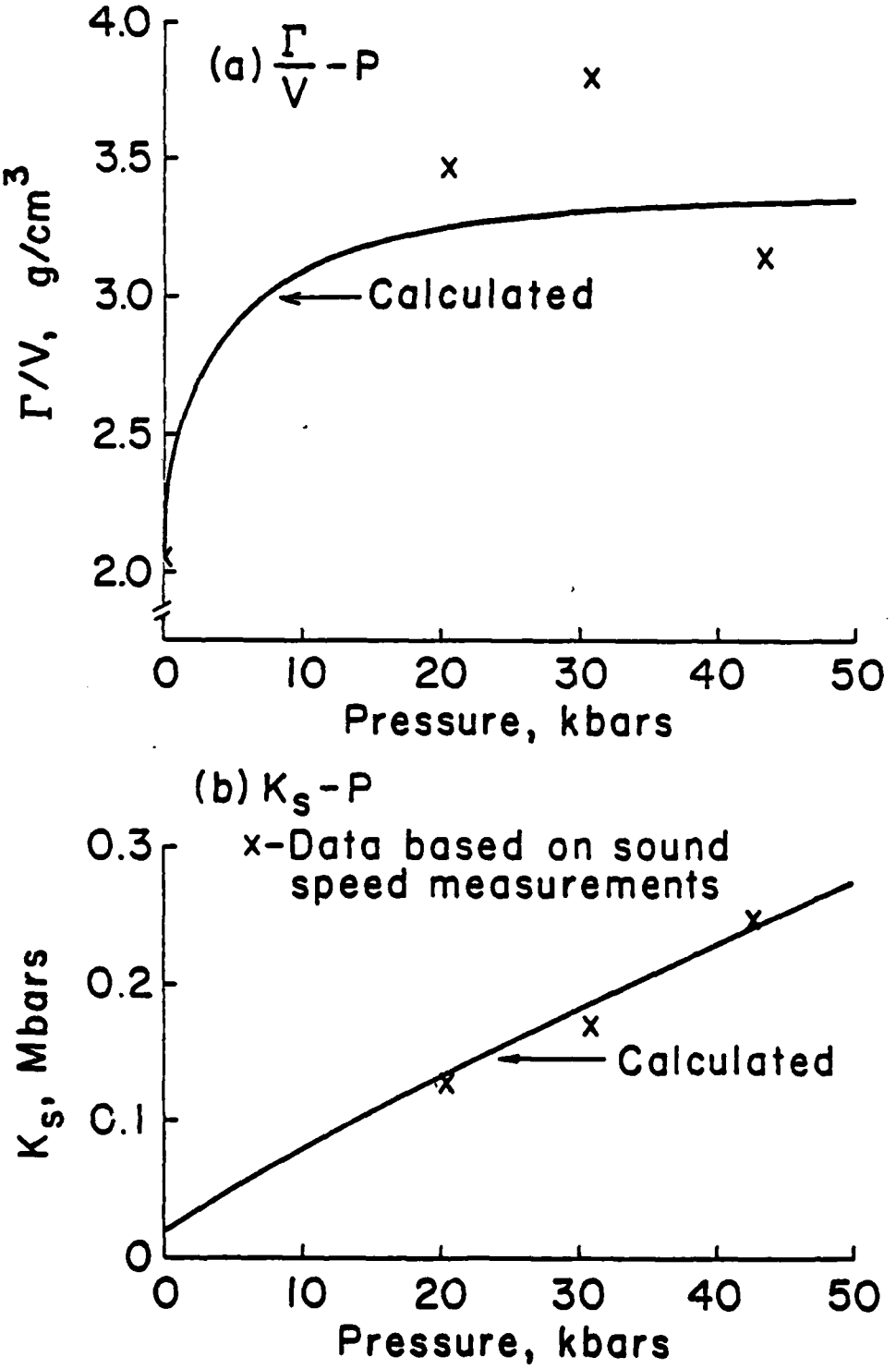

Fig. 5.2.--Comparison of Γ/V and K_s Values. Solid lines represent the calculated values based on the models used in the unreacted CS_2 EOS. Individual x's are values calculated from sound speed measurements. Plots are made versus state 1 pressures.

Unreacted CS_2 Reshock Data

A comparison has been made between the reshock data calculated from the unreacted CS_2 EOS and measured values. Two comparisons can be made, one at state 3' (the initial reshock state) and the other at state 2 after passage of the R_1 wave.

Figure 5.3 is a comparison of state 3' as measured by the CS_2-sapphire gage with calculated values for the six shots where data were available Note that three sets of points are essentially on top of each other and the calculated values are below the measured values in the other three sets.

Since the calculated points are based on an initial shock pressure, P_1, several possibilities for these differences exist. Either the EOS is wrong or the state 1 pressure is wrong or the state 3' particle velocity at the CS_2-sapphire interface is wrong. These six points have been flagged in Fig. 5.1. Notice that the shots showing good agreement (77-055, 77-062, and 77-071) all lie close to the calculated Hugoniot line, indicating the EOS gives accurate reshock states. Shots 77-103 and 77-050 are also close to the calculated Hugoniot so the difference is attributed to a high u_{p3}, measurement. Shot 77-094 does not lie very close to the calculated Hugoniot so its difference is probably caused by a relatively inaccurate state 1 measurement.

The state 3' measurements provide an independent check on both state 1 measurements and the calculated reshock Hugoniot. The agreement above indicates that both measurements and calculations are reasonably accurate.

The other comparison to be made of measurements to reshock calculations is at state 2, which occurs at the top of the R_1 wave. Figure 5.4 provides a comparison of calculated and measured P-V values for state 2 from

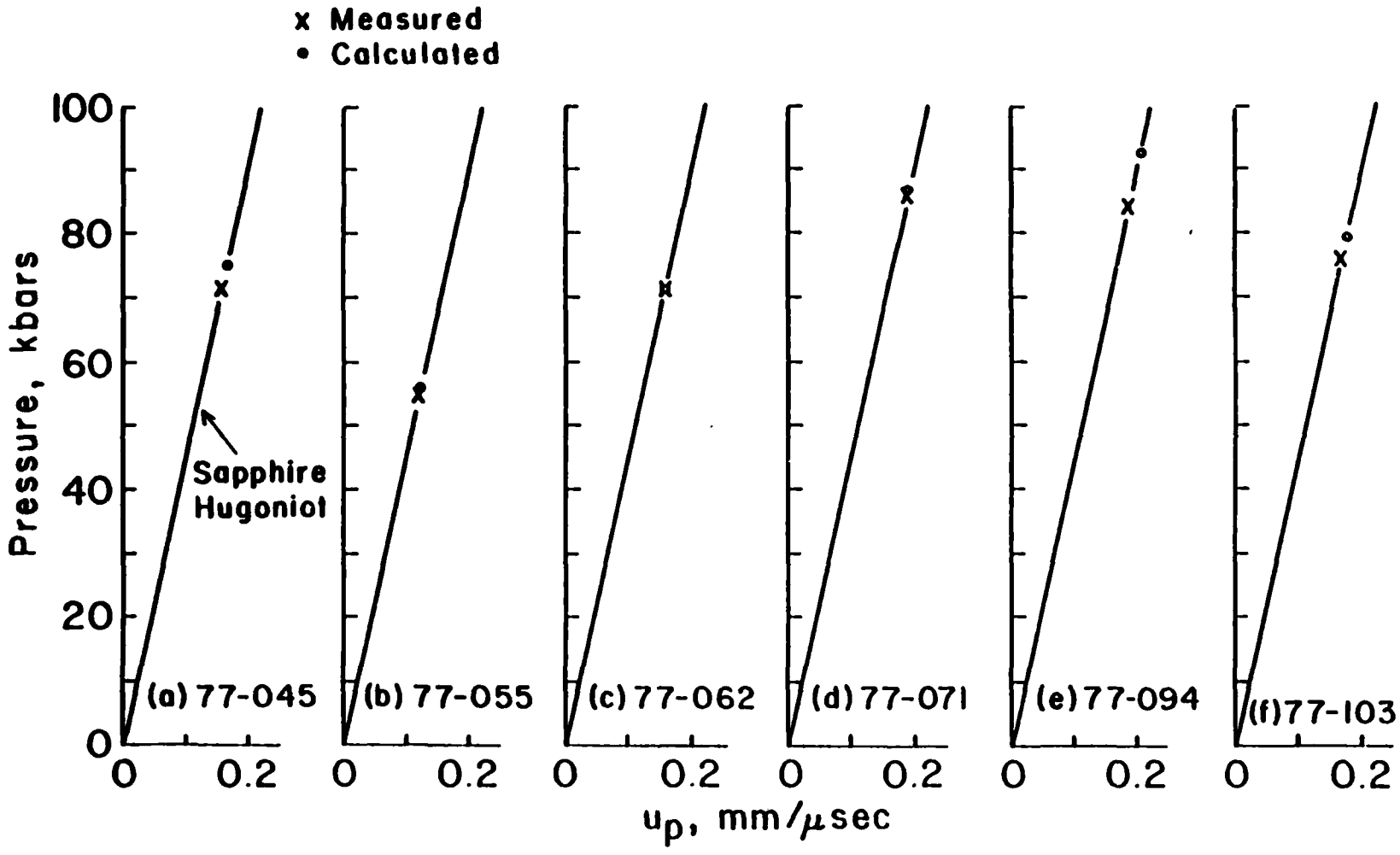

Fig. 5.3.--Comparison of Calculated and Measured State 3' Information. Measured values were obtained from the CS_2-sapphire gage before reaction was observed. Calculated values were based on the pressure at state 1 and obtained graphically by determining the point where the left going reshock Hugoniot contacted the right going sapphire Hugoniot centered at zero pressure.

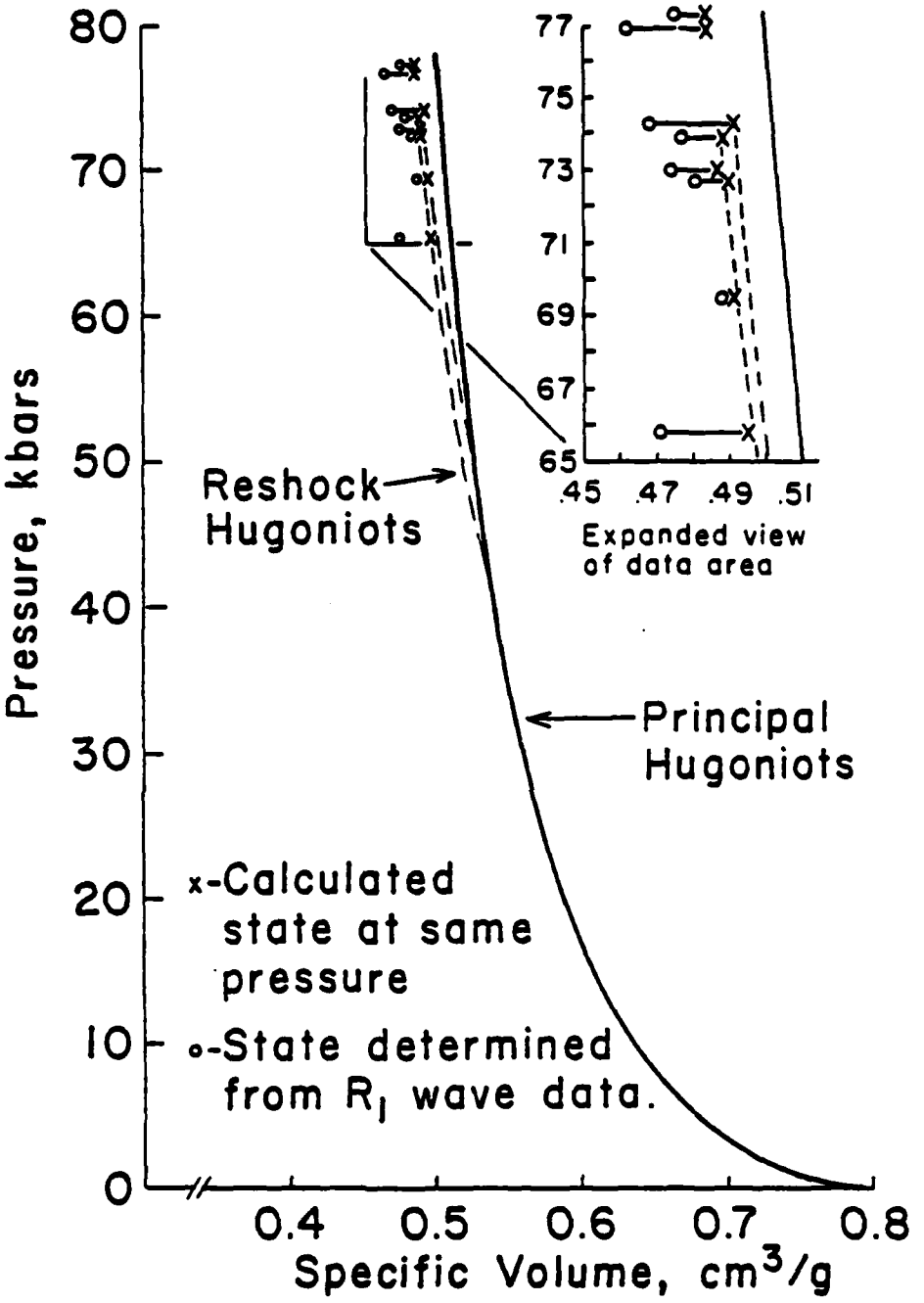

Fig. 5.4.--Comparison of Calculated and Measured State 2 Information. Measured points were determined from measured R_1 wave data. Calculated points were obtained by making reshock calculations centered at P_1 based on the unreacted CS_2 EOS with P_2 (the same as for the measured values) as the final pressure.

Table 4.4. As can be seen, all the data are to the left of the principal Hugoniot, which is as it should be but the measured states are to the left of the calculated states with difference varying widely. This seems to indicate the measured data are less accurate, possibly being influenced by the use of the particle velocities several times in the jump conditions to obtain the states.

It should also be remembered that the R_1 wave is evolving as can be seen from Table 4.7. Values of P and V in state 2 have been determined from the jump conditions, which do not strictly apply to a changing wave. This undoubtedly has also led to some inaccuracies.

Temperature Calculations Using Unreacted CS_2 EOS

Calculated temperatures have been plotted in temperature-pressure space in Fig. 5.5 with the T-P diagram developed by Butcher et al.[35] shown for comparison. Figure 5.5a shows the principal Hugoniot, the reshock Hugoniots for four shots and a line representing the locus of possible state 3' reshock states. Notice that the principal Hugoniot above 20 kbars and all the reshock end states are well up into the region labeled "decomposition to carbon and sulfur" by Butcher et al.[35] This would seem to be strong evidence that the reaction is a decomposition reaction rather than a polymerization to the black CS_2 solid as indicated by Dick[14,34] and Kusubov.[36]

Figure 5.5b is part of the same plot with the measured R_1 wave states plotted. The region of the cusp has also been indicated as being between 46 and 54 kbars as discussed previously. Two regions have been shaded in the figure. If the transition were strictly pressure determined, the R_1 wave states would be expected to lie in the vertical region. If it were temperature dependent, the states would be expected to be in the horizontal region, as most of them are. Only the data for the low pressure nonreactive

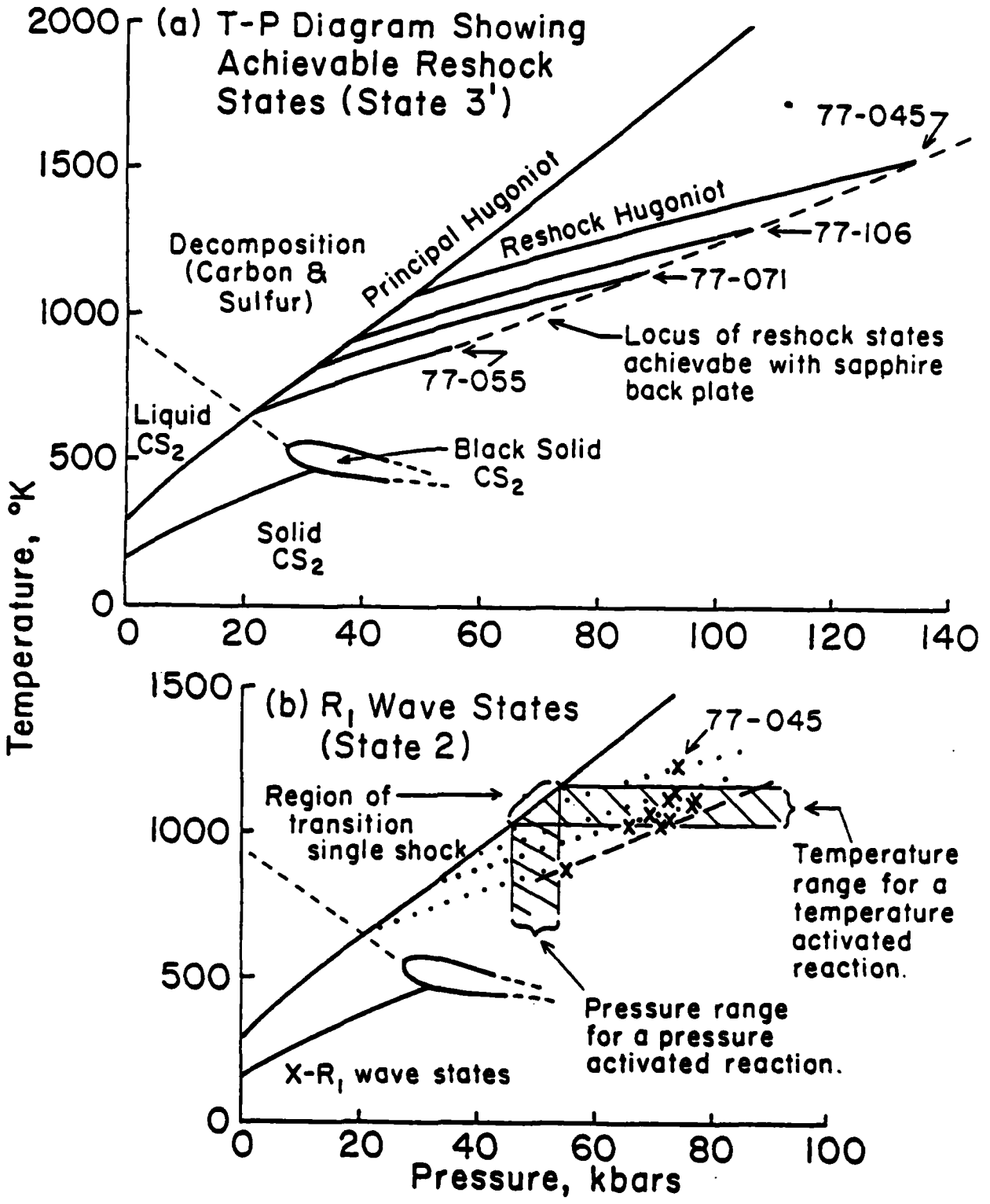

Fig. 5.5.--Temperature-Pressure Diagrams Based on Unreacted CS_2 EOS. The T-P diagram of Ref. 35 has been shown for reference purposes. Note that all states achieved in this study are in the "decomposition" region.

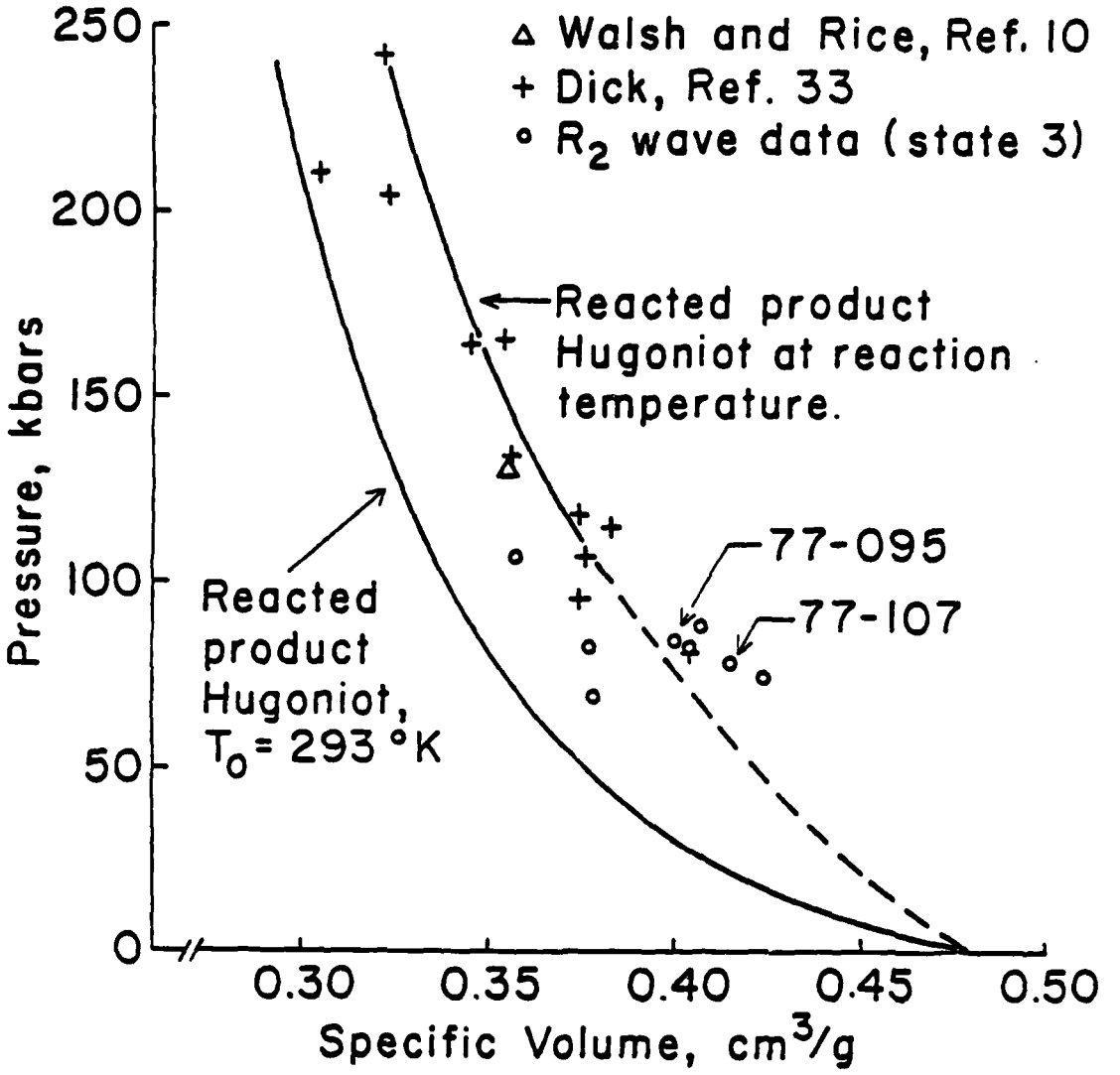

Fig. 5.6.--Reacted Product Hugoniot Information. The lines are calculated Hugoniots based on the reacted product EOS, one centered at 293°K and the other representing states achieved after reaction. Data points obtained in this study were obtained from measured R_2 wave data (state 3) in a reshock situation. Data of other experimenters were obtained in single shock experiments.

shots and that for shot 77-045 (which has previously been mentioned as probably reacting in the initial wave) are outside this region. This indicates the reaction is more closely associated with temperature than pressure and supports the hypothesis that a chemical reaction occurs in the shock. This analysis is based on steady waves and the waves in the experiments are evolving so it is impossible to say that the R_1 wave states never would evolve into the vertical region. However, a review of Table 4.7, along with the various waveforms, indicates that the greater portion of the evolution has occurred in the high pressure shots by the time the R_1 wave passes the intermediate gages.

The scatter of data is somewhat bothersome since it had been hoped that the R_1 wave temperatures would lie on a single line, but this may be due to the fact that the steady wave structure has not had time to establish itself in the approximately 1 mm of travel available in the CS_2 cell. It would be very helpful if experiments with thicker CS_2 cavities could be done to better determine the steady wave profiles. The inaccuracies discussed earlier in the R_1 wave states should also be kept in mind.

Reacted Product Data

Comparison of the measured state 3 data to that published and also to the reacted product EOS will be made in this section. In addition, comparison of the R_2 wave data to the relaxed CS_2-sapphire gage data will be made and then a discussion concerning the nature of recovered reacted products will be presented.

Reacted Product EOS Comparison

Figure 5.6 is a plot of all the reacted product Hugoniot data available in the literature[14] along with the data generated in this study. The curve to the left of the data is the Hugoniot for the reacted products

centered at an initial temperature of 293°K and one atmosphere pressure. The relative position of the two curves is as one might expect because of the high temperature along the Hugoniot at reaction temperature.

The amount of scatter in all the data is considerable but, nevertheless, the points cluster about the calculated curve. The considerable scatter in the R_2 wave data of this study may be the results of particle velocity error multiplication and unsteady waves as has been previously discussed.

Measured State 3 Data Comparison

State 3 data were also obtained from the relaxed particle velocity recorded by the CS_2-sapphire gage. Since this is a direct measurement, one would expect it to be more accurate than the R_2 wave data obtained from measured shock and particle velocity in conjunction with the R_1 wave data. Comparisons between these two data sets are made in Fig. 5.7 for the eight shots where this comparison was possible. As can be seen the R_2 wave data are sometimes higher and sometimes lower than the other data. The two points are quite close together on shots 77-107 and 77-095 and one might infer that the P-V states from R_2 wave data are accurate. These points have been singled out on Fig. 5.6 and are closer than most to the calculated Hugoniot, indicating that the calculation is reasonable.

Nature of Recovered Reacted Products

Calculations were made to estimate the temperatures one might expect by shocking 293°K reacted products. Shocking reacted products to 100 and 160 kbars would be expected to cause temperatures to increase to 600 and 1000°K, respectively. For reshocked unreacted CS_2 with a 100 kbar pressure at state 3', the temperature is about 1250°K. Add to this another 500 degrees for the reaction input and the reacted product temperature would be about 1700°K. Upon releasing the pressure, the residual temperature of the reacted

products would be on the order of 1000°K. All the known polymers (black CS_2, polymerized CS and C_3S_2 polymer) decompose well below this temperature (450°K,[35] 470°K,[82] and 360°K[82]). It seems reasonable that one should recover only carbon and sulfur in recovery experiments.

The temperatures are not to be considered extremely accurate but they do serve to point out that residual temperatures are high and would be expected to greatly influence the nature of the recovered material.

Reaction Rate Data

Five different kinds of data have been analyzed for the purpose of obtaining information about the rate law which governs the reaction process. Induction time, particle velocity decay and noise decay data were all obtained from the gage record at the CS_2-sapphire interface. R_1 wave decay and R_2 wave structure data were obtained from an analysis of the time-correlated wave forms. These will be discussed in the following subsections.

R_1 Wave Decay Calculations

R_1 wave decay data were reported in terms of particle velocity decay in Chapter 4 but were not reduced to initial reaction rate data. The first term in the numerator of Eq. (2.40) is negligible in these experiments so the equation

$$\left(\frac{\partial x}{\partial t}\right)_h = \frac{\rho_o U\left(1 + \frac{K_{S,x} V_x}{U^2}\right)\left(\frac{\partial u}{\partial t}\right)_\xi}{\Delta V \frac{K_{S,x}}{V_x} - P\left(\frac{\Gamma}{V}\right)_x - \Delta E\left(\frac{\Gamma}{V}\right)_x} \tag{5.1}$$

was used to calculate $\dot{x}$. Calculations were made using Eq. (5.1) and the calculated conditions of state 3', along with the particle velocity derivative

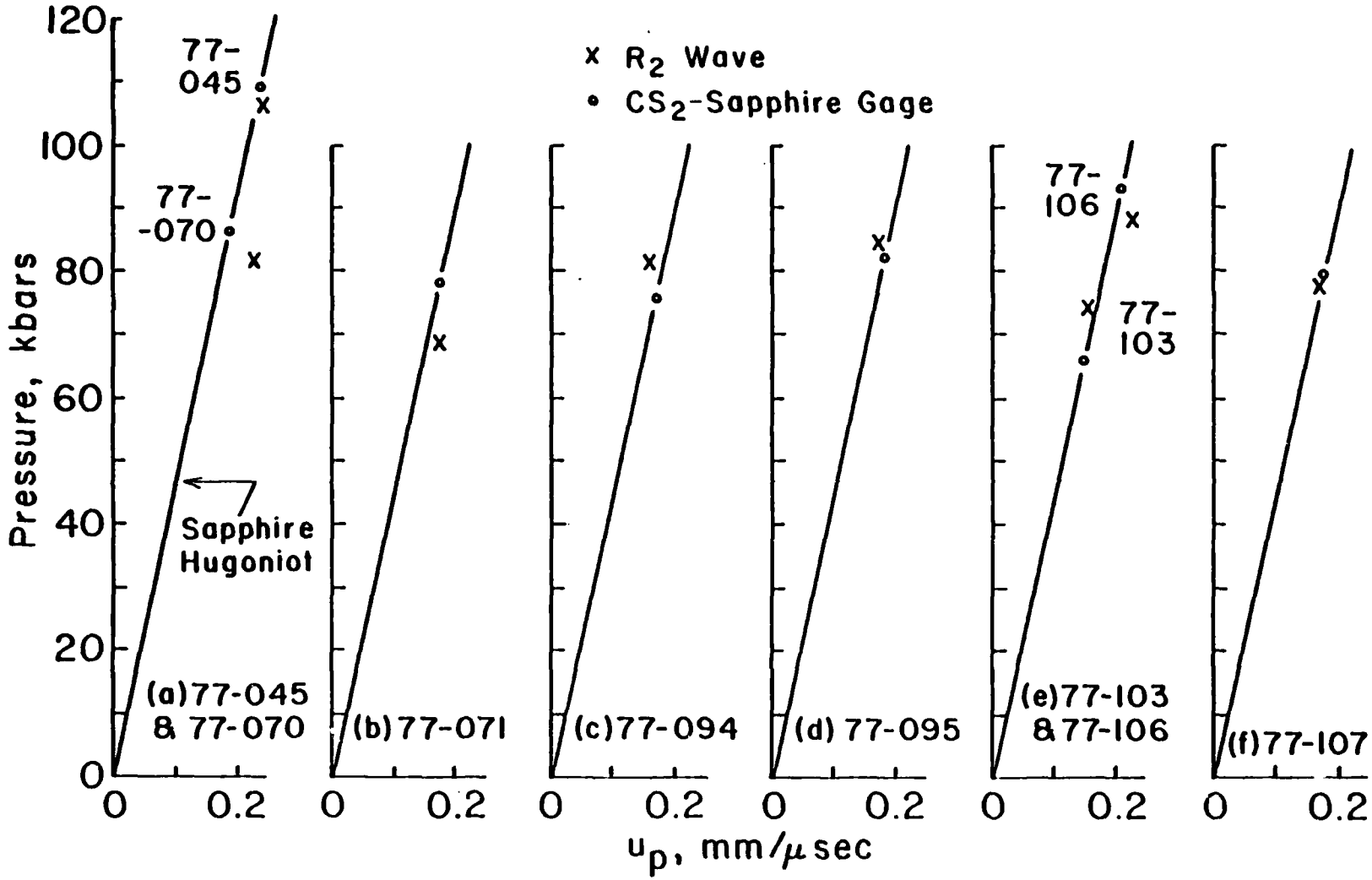

Fig. 5.7.--Comparison of Measured State 3 Data. Data represented by x's were obtained from R_2 wave measurements utilizing the jump conditions. Data represented by circles were obtained from relaxed CS_2-sapphire gage data in conjunction with the sapphire Hugoniot.

values from Table 4.7. Table 5.1 contains the results of this calculation along with estimates of ΔE, ΔV, and $K_S V/U^2$ which were used.

Reaction Rate Information Analysis

The various reaction rate values are summarized in Table 5.2 for each shot. The temperatures are those obtained from reshock calculations at state 3'. This is probably not an accurate temperature during the reaction because energy is released and the temperature increases several hundred degrees with the reaction rate likewise increasing. In the absence of more meaningful data it was used so that reaction rate versus temperature plots could be made.

All the points were plotted on Fig. 5.9 for comparison purposes. The particle velocity decay shows the highest reaction rate while the noise decay the lowest. The R_1 wave decay and R_2 wave structure points generally lie between the two. Notice that the particle velocity decay and the R_2 wave structure data appear to indicate two different rates, one below 1125°K and one above.

Induction and Relaxation Time Analysis

Table 5.2 also contains information for the induction time and particle velocity and noise relaxation times. These have been plotted as the logarithm of the time versus reciprocal temperature in Fig. 5.10. Note that the induction time points, along with the particle velocity points, indicate a highly temperature dependent low temperature rate much the same as the reaction rate data.

TABLE 5.1.--Calculation* of Reaction Rate from R_1 Wave Information

Shot No.	V_o (State 1) (cm^3/g)	State 3' Data (Calculated) V (cm^3/g)	K_S (Mbar)	P (Mbar)	Γ/V (g/cm^3)	$(\partial u/\partial t)_{\xi_2}$ ($cm/\mu sec^2$)	$\dot{x}$ (Eq. 5.1) (μsec^{-1})
77-070	0.552	0.461	0.655	0.106	4.15	0.30	16.4
77-071	0.556	0.474	0.542	0.0868	4.08	0.10	8.3
77-094	0.538	0.470	0.577	0.0927	4.10	0.15	11.0
77-095	0.540	0.469	0.585	0.0941	4.11	0.25	17.7
77-103	0.558	0.480	0.499	0.0794	4.04	0.05	5.2
77-106	0.537	0.461	0.655	0.106	4.15	0.26	14.6
77-107	0.554	0.470	0.578	0.0928	4.10	0.25	17.7

*For all calculations it was assumed that: $\Delta E = 0.01$ Mbar cm^3/g, $\Delta V = 0.08$ cm^3/g, and $K_S V/U^2 = 1.4$.

TABLE 5.2.--Comparison of Relaxation Time and Reaction Rate Information

	Induction and Relaxation Times				$\bar{\dot{x}}_{up}=1/\tau_{up}$	$\bar{\dot{x}}=1/\tau_N$	R_1 Decay	R_2 Wave Structure
Shot No.	T_3, (°K)	t_I (μsec)	t_{up} (μsec)	t_N (μsec)	(μsec^{-1})	(μsec^{-1})	$\dot{x}$ (μsec^{-1})	$\dot{x}$ (μsec^{-1})
77-045	1521	<0.010	---	0.12	---	8.3	---	27
77-070	1295	<0.006	0.05	0.13	20	7.7	16	13
77-071	1138	0.049	0.08	0.17	13	5.9	8	5.9
77-094	1185	0.056	0.06	0.33	17	3.0	11	9.8
77-095	1198	<0.018	0.06	0.34	17	2.9	18	11.4
77-103	1078	0.31	0.40	none	2.5	---	5	2.5
77-106	1295	<0.012	0.04	0.11	25	9.1	15	17.5
77-107	1187	<0.018	0.08	0.24	13	4.2	18	7.3

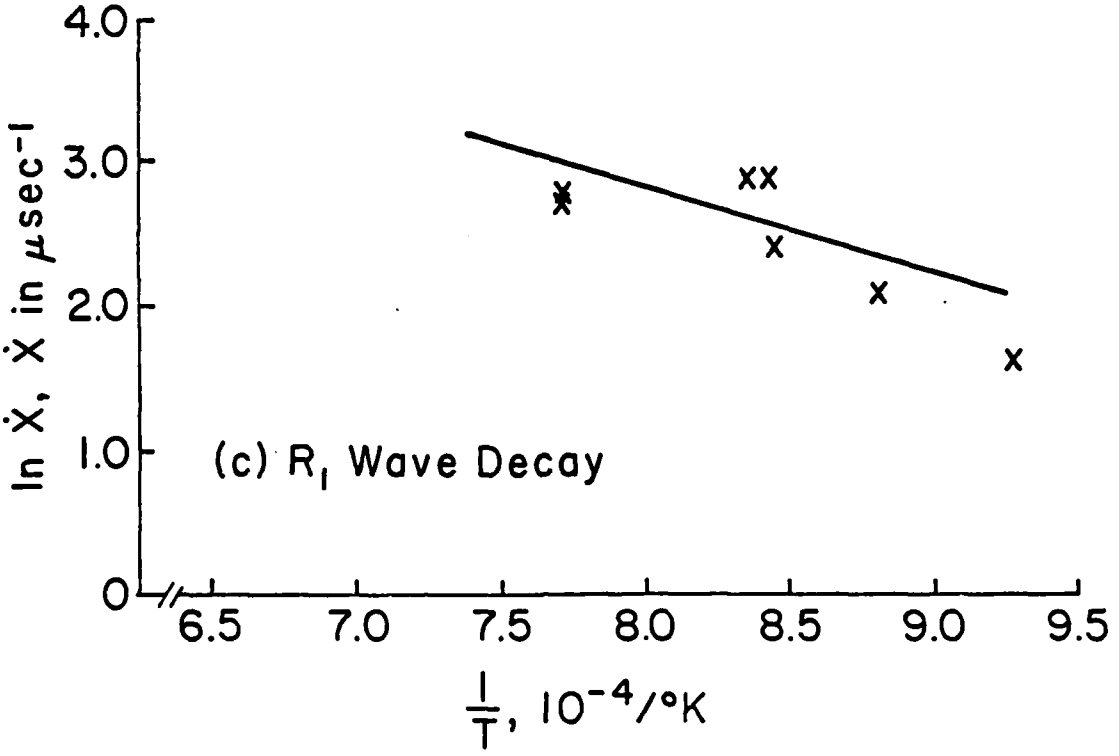

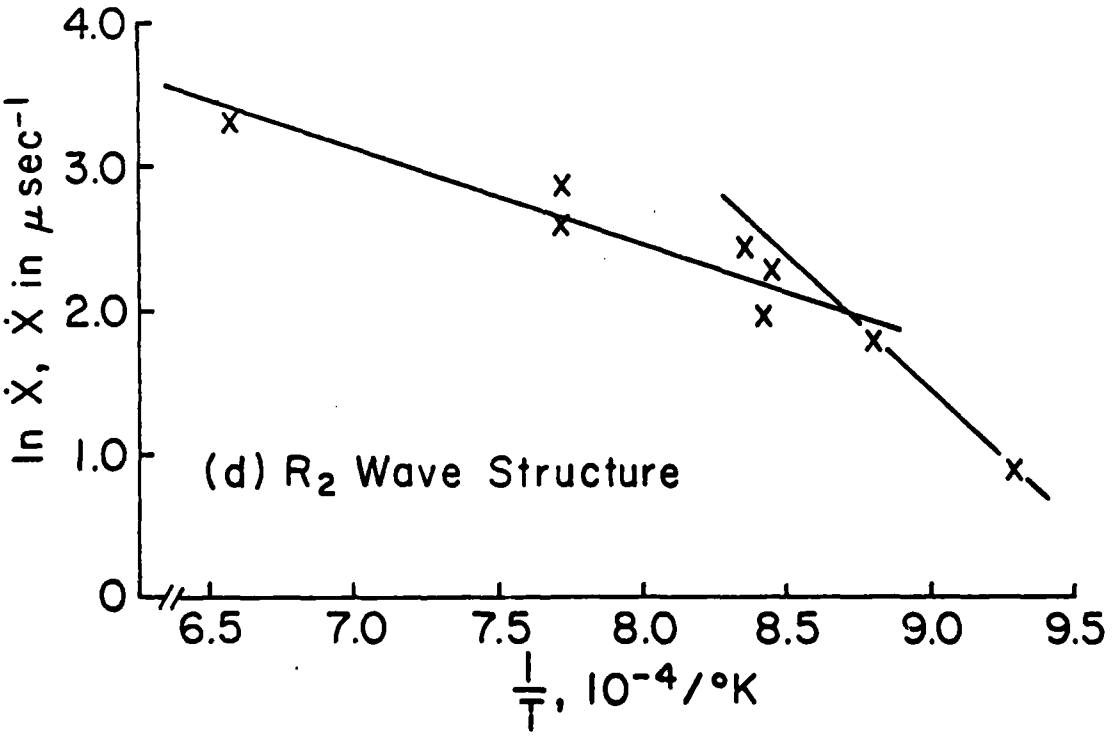

Fig. 5.8.--(Continued). (c) is from R_1 wave decay and (d) is from the R_2 wave structure.

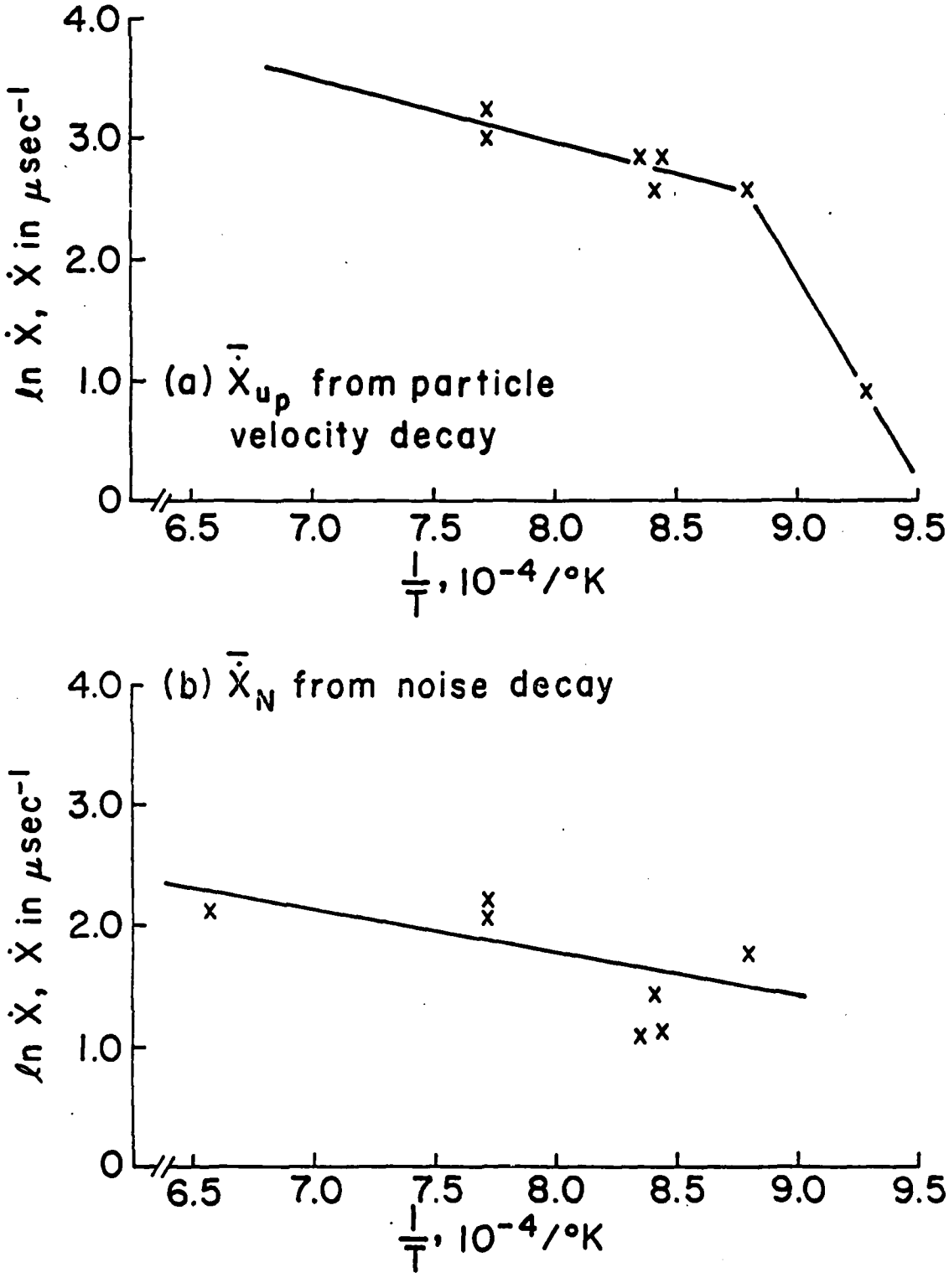

Fig. 5.8.--Arrehenius Plots of the Reaction Rate Data. (a) is from particle velocity decay. (b) is from noise decay. Temperature is T_3,.

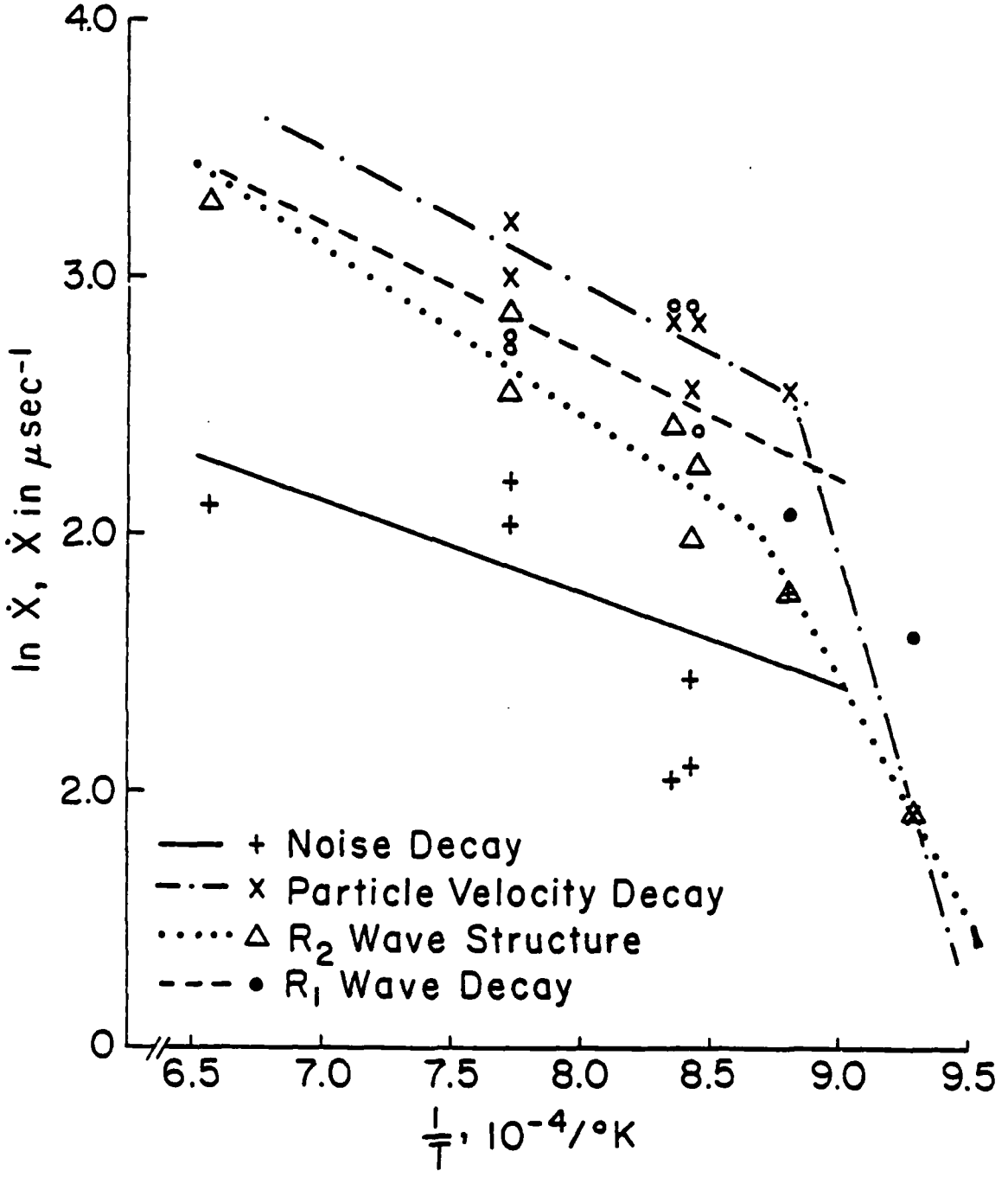

Fig. 5.9.--Comparison of Arrhenius Plots. All four estimates of the reaction rate are shown. Note that a low temperature, as well as a high temperature, rate law is indicated.

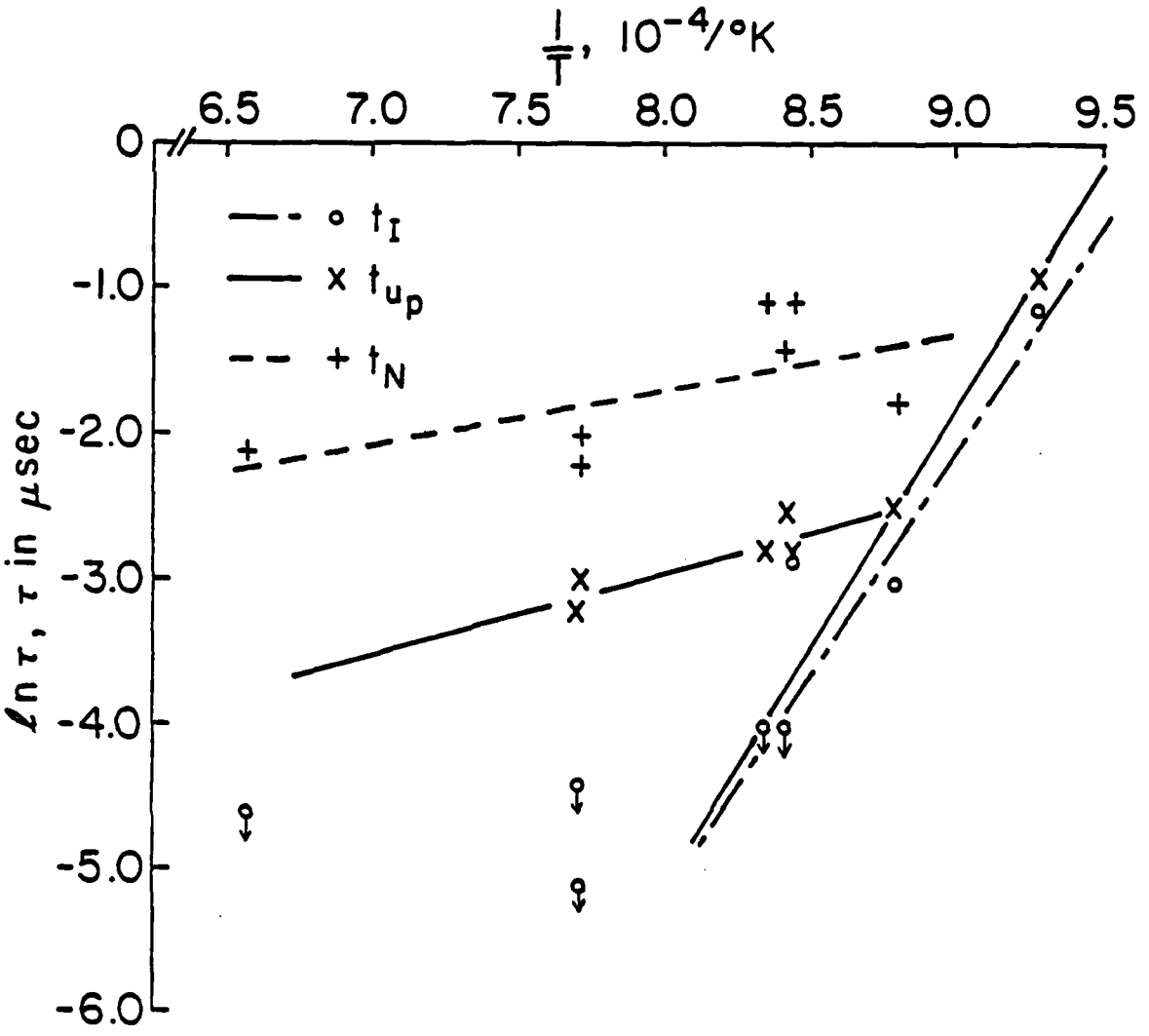

Fig. 5.10.--Induction Time and Relaxation Time Plots. t_I is the induction time, t_{up} is the particle velocity relaxation time and t_N is the noise relaxation time. Temperatures are at state 3' ($T_{3'}$).

Rate Law Parameters

Activation energy (E) and frequency factor (A) can be obtained from the various plots by assuming a zeroth order, complex Arrhenius rate law of the form

$$\dot{x} = Ae^{-E/RT} . \qquad (5.2)$$

Relaxation time data can also yield estimates of these parameters as discussed in Sec. 4.2.

Values for these parameters obtained from the various plots are tabulated in Table 5.3. Obviously, there are considerable differences in the values as one might expect from the way the rates were estimated. They do indicate, however, the difference between the two rate laws and also the magnitude of the parameters one might expect.

If one uses the particle velocity decay time constants to compare the behavior of the initial wave in shots 77-045 and 77-106 as to reaction rate, an interesting correspondence to the measured data results. Table 5.4 is a listing of the values used and the calculated reaction rate in the initial wave. It indicates that evidence of reaction should have been observable in 77-045 and not in 77-106. As indicated earlier, 77-045 had a CS_2-sapphire gage record that only seems explicable by the initial wave having a two-wave structure as a result of reaction. Shot 77-106 showed none of this anomalous behavior. This would seem to independently corroborate the low temperature rate law.

TABLE 5.3.--Reaction Rate Law Fits from Data Plots
(for Rate Law $\dot{x} = Ae^{-E/RT}$)

Rate Law Parameter	Data from Reaction Rate Plots				Data from Relaxation and Induction Time Plots		
	Particle Velocity Decay	Noise Decay	R_1 Wave Decay	R_2 Wave Structure	Noise Decay Time	Particle Velocity Decay Time	Induction Time
Low Temperature Rate							
E (cal/mole)	67,600	---	---	37,200	---	72,500	61,600
A (μsec^{-1})	1.3×10^{14}			8.7×10^{7}		1.3×10^{15}	1.1×10^{13}
High Temperature Rate							
E (cal/mole)	10,400	7,070	12,000	13,200	7,500	10,200	---
A (μsec^{-1})	1,300	102	1,980	2,370	1,150	111	---

TABLE 5.4.--Reaction Rate Calculations for the Initial Shock in Shots 77-045 and 77-106

Shot No.	P_1 kbars	T_1 (°K)	E (cal/mole)	A (μsec^{-1})	$\dot{x}$ (μsec^{-1})
77-045	48.3	1058	72,500	1.3×10^{15}	1.37
77-106	38.5	908	72,500	1.3×10^{15}	0.005

All the sets of rate law parameters are unphysical and therefore this whole analysis must be considered highly speculative. It does serve to point out that a simple overall rate law which describes the reaction accurately is not possible. It also indicates that many experiments (as is normally the case in reaction kinetic experiments) must be carried out before useful and believable reaction rate laws can be established.

Comments Regarding Induction Time

Induction times have been observed in shock tube decompositions of gaseous CS_2[37] and SO_2.[38] These observations have been explained as the time required to reach a critical concentration of a particular species. In view of this, it seems probable that the observation of an induction time in the experiments in this study is a strong indicator of a multistep reaction mechanism.

Electrical Noise

As has been briefly touched on in Chapter 4, electrical noise was recorded during the experiment. The following discussion relates what is presently known, along with some conjecture concerning the nature of it. It is possible that, once understood, this noise phenomenon might become a valuable experimental tool in diagnosis of certain chemical events.

Gage Signals with Noise

The noise was best measured by the CS_2-sapphire gage because of the low voltage output of this gage and greater sensitivity to electrical noise. Two typical records are shown in Fig. 5.11: shot 77-070 which showed no induction time and shot 77-071 which did show one. The noise is large at first, decays with time and has a frequency of about 150 MHz.

Noise Appearance

Noise appearance corresponds with the reaction as evidenced by the following observations.

1. Particle velocity decay appears at the same time as noise decay.
2. A two-wave structure is observed in the same experiments that noise is observed.
3. The reaction rate law based on noise decay time is consistent with other rate laws.
4. Noise was not observed in the PMMA experiment even though the PMMA reshock pressure was in the same range as in four CS_2 experiments where noise had been observed.

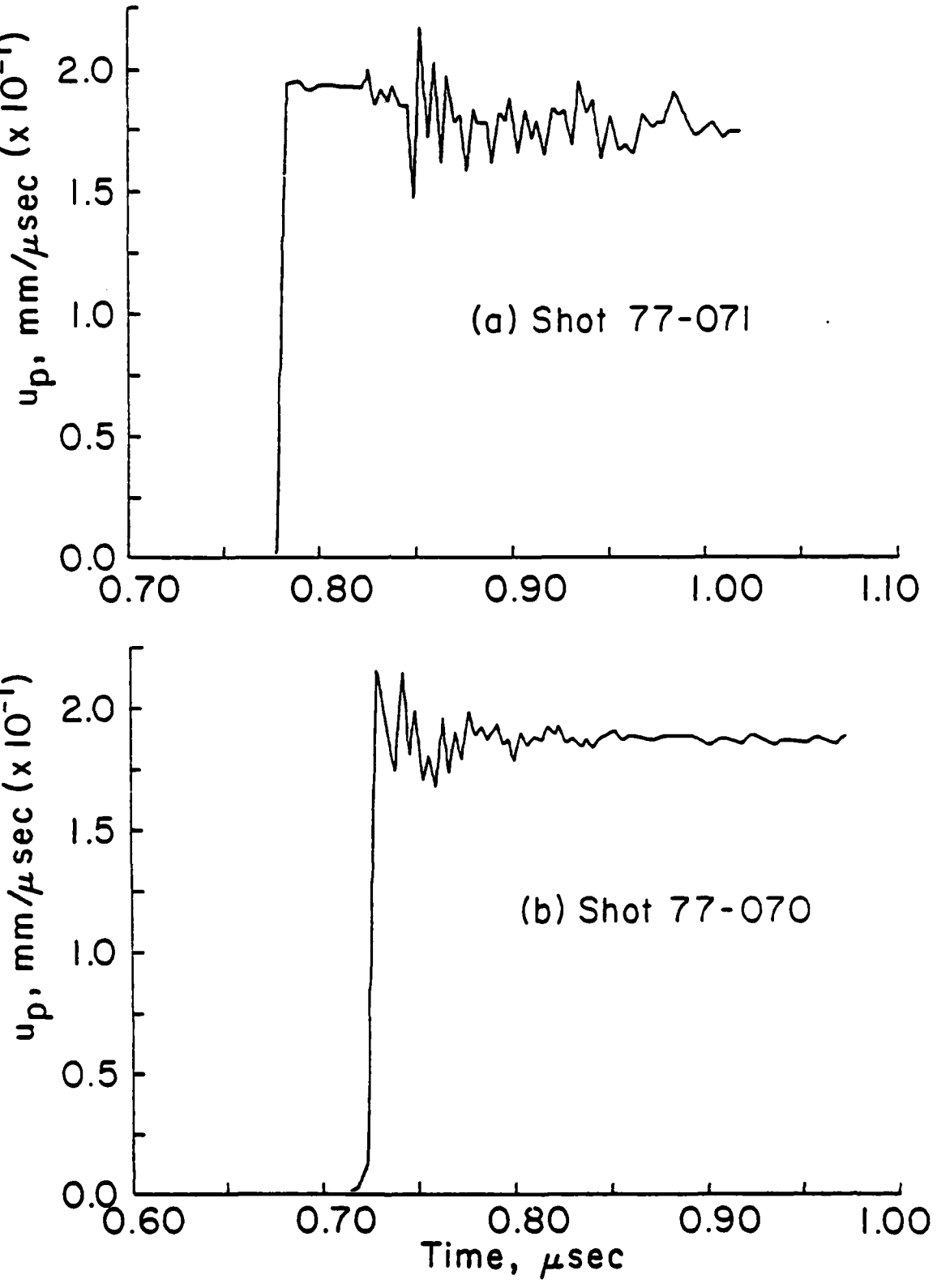

Fig. 5.11.--Selected CS_2-Sapphire Gage Data Showing Noise. Waveform in (a) shows an induction time. Both were recorded at sweep rate of 50 nanosec/div.

Nature of the Noise

The nature and cause of the electrical signal remains a mystery although a little information has been generated. As mentioned earlier, a gage sandwiched between two pieces of sapphire recorded the noise at the same time as the CS_2-sapphire gage, long before the shock arrived. The noise was also observed as a small perturbation on the other gage outputs at a corresponding time. This indicates the noise is an electrical signal that pervades the whole region.

It has been suggested that the noise may be an interaction between ions formed by the decomposition and the magnetic field. A very puzzling characteristic is that the signal appears to hit a maximum and then decay which suggests a one-time occurrence. If the noise were a result of the continuing reaction, it should have been observed during the whole experiment.

Another explanation appears to be that of a runaway first reaction (thermal explosion) that results in a large number of intermediate species forming very rapidly at the sapphire-CS_2 interface. Then as the reaction settles down to a more or less steady process, the concentration of these intermediate species drops rapidly to a much lower steady state value in the reacting wave. The one-time occurrence of the noise appears to be another indicator of a multiple step reaction mechanism.

Discussion of POD Calculations

Although it was not possible to accurately simulate the measured waveforms, it was possible to obtain information regarding the temperature and volume change resulting from the reaction. As indicated in Table 4.11, a temperature change of about 570°K was calculated for shot 77-103 which had a temperature of 1080°K at state 3'. The temperature change for shot 77-106 with a state 3' temperature of 1300°K was about 470°K. Shots 77-107 and

77-071 were between these two values. This indicates a temperature increase of about 500°K should be expected as a result of the reaction. It is interesting to note that C_3S_2 static high pressure experiments showed a temperature change of about 330°K when decomposition was observed.[39]

Table 4.12 indicates a volume change on the order of 18.5% results from the reaction. R. Dick [34] estimated 17% based on his experiments.

Calculations to simulate shots 77-045 and 77-106 showed reaction in the initial wave of the former but not the latter, as was discussed in Sec. 5.3.4. Calculated particle velocities at the CS_2-sapphire interface for shot 77-045 were much like those measured but stability problems obscured the exact nature of the calculated waveform, making it impossible to make a definitive statement.

Further details of this work are contained in Ref. 40.

4.6 SUMMARY

Unreacted CS_2

Fourteen unreacted CS_2 Hugoniot points were generated in this study using an electromagnetic gage technique, most of them from initial wave data in reshock experiments. Since both shock velocity and particle velocity were measured, these points are independent of other assumptions. They correlate well with other measured data.

Verification of the reasonableness of the unreacted CS_2 EOS, which was based on a Murnaghan isotherm and developed forms for C_v and Γ/V, came as a result of the good fit to the Hugoniot data and also from a surprisingly good comparison with K_S and Γ/V calculated from sound speed measurements on three shots. This equation of state was fit to a universal liquid Hugoniot in order to get the correct parameters, so the agreement with the Hugoniot measurements also demonstrates the applicability of the universal liquid Hugoniot to liquid CS_2.

Comparing the calculated unreacted CS_2 EOS Hugoniot with the measured data in this study and from other studies, indicates the two begin to deviate in the range of 46 to 54 kbars. One shot with an initial wave amplitude of about 48 kbars showed definite indications of reaction occurring in the initial shock. Two shots at 38.5 kbar and one at 43.4 kbar do not show any indications of initial shock reaction, which further supports the existence of a cusp in the 46 to 54 kbar region.

Measured reshock states compared quite well with calculated states but the former had quite a lot of scatter, ascribed mainly to particle velocity

error multiplication in the jump condition calculations. Reshock temperature calculations showed the dramatic effect of reshocking on the state of the material, with reshock temperatures being several hundred degrees below single shock temperatures at the same pressure. This made it much easier to control the state 3' temperatures.

A temperature-pressure diagram was plotted and all the principal Hugoniot states above 20 kbars are in the region which has been designated by Butcher et al.[35] as a decomposition region. All the reshock states in this study were also in that region.

It was observed in the measurements that a two-wave structure developed in the high pressure wave reflecting off the sapphire back plate. This two-wave structure development corresponded to observations at the CS_2-sapphire gage of particle velocity decay and also to an unexplained electrical noise signal, both of which were delayed by an induction time at the lower reshock pressures.

When the R_1 wave states were plotted on the temperature-pressure diagram, it was observed that they fell into the region one would expect for a temperature controlled rather than a pressure controlled reaction. Some uncertainty exists in this statement due to the fact that the R_1 wave was evolving during the experiments and the statement is strictly true only for a steady wave. Wave forms for the higher pressure shots indicate, however, that evolution was nearly complete by the time the R_1 wave reached the middle gage.

Thermodynamic calculations, using the equations of state developed for unreacted CS_2 and the reacted products, indicate that CS_2 is metastable with respect to a mixture of carbon and sulfur at standard conditions as well

as at principal Hugoniot and reshock Hugoniot states attained in the experiments. It seems reasonable that the shock-induced temperature rise would cause the reaction rate to increase to such an extent that CS_2 decomposition to carbon and sulfur could very well occur in the experiments.

The CS_2 metastability, temperature dependent R_1 wave, induction times and noise all add credibility to the hypothesis that the CS_2 is undergoing a chemical reaction in the shock.

Reacted Product Data and EOS

Dick's data above 100 kbars were essentially on a reacted product Hugoniot, so they were used to fit a reacted product EOS based on a Murnaghan isotherm and a constant C_V and Γ/V. It is interesting that the specific volume was treated as a fitting parameter and an initial value of 0.48 cm^3/g resulted. This correlates quite well with the density of a compacted mixture of carbon and sulfur at 0.46 to 0.48 cm^3/g.[41]

R_2 wave states were calculated by substituting the measured data in the appropriate jump conditions. In P-V space these data clustered around the calculated EOS. Relaxed particle velocity data from the CS_2-sapphire gage compares quite well with the R_2 wave data but demonstrates the inaccuracies in the R_2 wave data calculations.

Wave propagation code calculations indicate the volume change brought about by the reaction in reshock experiments is about 18.5%. The reaction-precipitated temperature change depends on the conditions at state 3'. For a T_3, of 1080°K, the change is 570°K while at 1300°K it is about 470°K.

All the known polymers of CS_2, CS, and C_3S_2 decompose below 500°K, which is much below the residual temperatures expected for the reacted products. The high residual temperature results not only from the differences

in compressibility between the CS_2 and the reacted products but also from the approximately 500°K temperature increase due to the reaction. This indicates that it would be very difficult to recover anything but carbon and sulfur from recovery experiments even if polymers were formed in the shock.

Reaction Rate Data

Five different types of measurements and estimations were used in an effort to obtain information about the reaction rate. They were induction time, particle velocity, noise decay, R_1 wave decay and R_2 wave structure data. The reaction rate data ranged from 2.5 per μsec to 27 per μsec depending on the particular type of data and shot being examined.

Plots were made of the logarithm of either reaction rate or relaxation time versus reciprocal temperature, where the temperature was that of state 3'. The particle velocity decay gave the highest reaction rates and the noise decay the lowest reaction rates, with the other two in between. Two different rate laws were suggested by the induction times, the particle velocity decay rates and the R_2 wave structure rates. The low temperature rate law (below 1125°K) was highly temperature dependent while the high temperature rate law (above 1125°K) varied considerably less with temperature but nevertheless gave quite high reaction rates.

Actual rate law parameters were determined for the zeroth order, complex Arrhenius rate law. The low temperature rate had activation energies from 37,200 to 72,500 cal/mole and frequency factors of 8.7×10^7 to 1.3×10^{15} μsec^{-1} depending on the particular data used. The high temperature rate law had activation energies from 7000 to 13,200 cal/mole with frequency factors of 102 to 2370 μsec^{-1}. Obviously these Arrhenius parameters are non-physical and the reason for this is unknown. It should be remembered, however, that all the rate law estimates were made without knowing the true

relationship between the observables and the reaction rate. When spectrographic measurements of intermediate species are made, it may be possible to determine which of the shock observables yields the best estimate of reaction rate.

The low temperature rate law was corroborated very nicely by shot 77-045 that apparently reacted in the initial wave. According to the particle velocity decay low temperature rate law it would have had a reaction rate of about 1.4 μsec^{-1} in the initial wave, so in the approximately 0.5 sec that it traveled from the front of the cell to the back, a substantial amount of reaction would have taken place. Two shots at slightly lower projectile velocities showed no evidence of reaction and the calculated rate was 0.005 μsec^{-1}, so they would not be expected to show evidence of reaction.

Induction times were observed on some of the lower pressure shots. Experimenters studying the decomposition of gaseous CS_2[37] and SO_2[38] in shock tubes have also observed induction times which they attributed to the time required for a particular molecular species to attain a critical concentration.

Both the induction time and the two reaction rates would appear to substantiate the hypothesis of a chemical reaction occurring and, moreover, suggest that a multiple step reaction mechanism is involved.

Reaction Associated Noise

Electrical noise was observed on the CS_2-sapphire gage and was found to correlate with the particle velocity decay, evolution of a two-wave structure, and reaction rate data. It was therefore assumed to be a direct result of the reaction taking place, coupled perhaps with the magnetic field.

This noise was found to pervade the whole region, have a frequency of approximately 150 MHz and be a one-time phenomenon that decays. Although very little else is known, this appears to support the idea of a chemical reaction producing some kind of charged species in the shock.

Reaction Mechanism

The information from this study does not provide any information about the reaction mechanism except to indicate by the two step rate law, the induction time, and the noise that a multiple step reaction mechanism may be involved.

REFERENCES SECTION IV

1. R. Fowles and R. F. Williams, J. Appl. Phys. 41, 360 (1970).

2. M. Cowperthwaite and R. F. Williams, J. Appl. Phys. 42, 456 (1971).

3. D. E. Grady, J. Geophys. Res. 78, 1299 (1973).

4. G. E. Duvall and R. A. Graham, Rev. Mod. Phys. 49 (1977).

5. D. J. Andrews, "Equation of State of the Alpha and Epsilon Phases of Iron," Ph.D. Thesis, Washington State University, Pullman, WA (1970).

6. D. B. Hayes, "Experimental Determination of Phase Transformation Rates in Shocked Potassium Chloride," Ph.D. Thesis, Washington State University, Pullman, WA (1973).

7. J. W. Swegle, "A Method for Performing and Interpreting Gas Gun Experiments in Two-Dimensional Strain, " Ph.D. Thesis, Washington State University, Pullman, WA (1976).

8. S. A. Sheffield, D. E. Mitchell, and D. B. Hayes, "The Equations of State and Chemical Kinetics for Hexanitrostilbene (NHS) Explosive," in Sixth Symposium (International) on Detonation, Office of Naval Research Report ACR-221 (1976), p. 748.

9. J. N. Johnson, D. B. Hayes, and J. R. Asay, J. Phys. Chem. Solids 35, 501 (1974).

10. G. Gattow and W. Behrendt, "Carbon Sulfides and Their Inorganic and Complex Chemistry" in Topics in Sulfur Chemistry, edited by A. Senning, (Georg Thieme Publishers, Stuttgart 1977), Vol. 2.

11. P. W. Bridgman, International Critical Tables (McGraw-Hill Book Co., New York 1928), Vol. 3.

12. F. D. Murnaghan, Finite Deformation of an Elastic Solid (Wiley, New York, 1951) p. 73.

13. R. Fowles, J. Appl. Phys. 39, 2973 (1968).

14. R. D. Dick, "Shock Wave Compression of Benzene, Carbon Disulfide, Carbon Tetrachloride, and Liquid Nitrogen," Los Alamos Scientific Lab. Report LA-3915 (1968).

15. H. B. Callen, Thermodynamics (Wiley, New York, 1960).

16. Y. Horie and G. E. Duvall, "Shock Waves and the Kinetics of Solid-Solid Transitions," Washington State University Shock Dynamics Lab. Report WSU SDL 69-06 (1968).

17. D. B. Hayes, "Kinetics of Shock-Induced Polymorphic Phase Transitions," Sandia Laboratories Report SAND77-0267C (1977).

18. S. A. Sheffield, "Shock-Induced Reaction in Carbon Disulfide," Ph.D. Thesis, Washington State University, Pullman, WA (1978).

19. F. W. Sears and M. W. Zemansky, University Physics (Addison-Wesley Pub. Co. Inc., Reading, Mass. 1955).

20. G. R. Fowles, G. E. Duvall, J. Asay, P. Bellamy, F. Feistmann, D. Grady, R. Michaels, and R. Mitchell, Rev. Sci. Instr. 41, 984 (1970).

21. The PMMA used in these experiments was PLEX II UVA purchased from Rohm and Hass, Philadelphia, PA 19105.

22. Sapphire was purchased from Adolf Mellor Company, P.O. Box 6001, Providence RI 02904.

23. L. Koller and G. R. Fowles, Sixth AIRPT International High Pressure Conference, Boulder, Colorado, 1977. Proceedings to be published.

24. L. Koller, "Generation and Measurement of Simultaneous Compression-Shear Waves in Arkansas Novaculite," Ph.D. Thesis, Washington State University, Pullman, WA (1978).

25. Gages are purchased as gage no. VF-FC-S1179-NRA from Micro-Measurements, Romulus, Michigan.

26. Soft copper tubing was purchased from Alaska Copper and Brass Company, Seattle, WA

27. C. F. Peterson and J. T. Rosenberg, "Dynamic Properties of Rocks Required for Prediction Calculations," Stanford Research Institute Report for Defense Nuclear Agency DNA-3579F (1974).

28. L. M. Barker and R. E. Hollenback, J. Appl. Phys. 41, 4208 (1970).

29. The POD Flow Code, Physics International, San Leandro, CA

30. J. Von Neumann and R. D. Richtmeyer, J. Appl. Phys. 21, 232 (1950).

31. M. A. Cook and L. A. Rogers, J. Appl. Phys. 34, 2330 (1963).

32. P. C. Lysne, J. Chem. Phys. 57, 492 (1972).

33. J. M. Walsh and M. H. Rice, J. Chem. Phys. 26, 815 (1957).

34. R. D. Dick, J. Chem. Phys. 52, 6021 (1970).

35. E. G. Butcher, M. Alsop, J. A. Weston, and H. A. Gebbie, Nature 199, 756 (1963).

36. A. S. Kusubov, Lawrence Livermore Laboratory (private communication).

37. S. [illegible] Arnold, W. G. Brownlee, and G. H. Kimbell, J. Phys. Chem. 74, 8 (1970)

38. B. P. Levitt and D. B. Sheen, Trans. Faraday Soc. 63, 2955 (1957).

39. A. P. Ginsbery, J. L. Lundberg, and W. E. Silverthorn, Inorg. Chem. 10, 2079 (1971).

40. S. A. Sheffield, "Shock-Induced Reaction in Carbon Disulfide," Ph.D. Thesis, Washington State University, Pullman, WA (1978).

41. E. G. Butcher, J. A. Weston, and H. A. Gebbie, J. Chem. Phys. 41, 2554 (1964).

V. TIME-RESOLVED SPECTRA OF SHOCKED LIQUID CS_2

5.1 Introduction

If one had free choice of spectral range to be studied in attempting to arrive at an understanding of shock-induced chemical reactions, he would probably choose to study vibrational and rotational levels in the infrared. Severe experimental constraints imposed by the shock environment make this a poor second choice at present. Problems of visible and near-ultraviolet spectroscopy appeared to be sufficiently challenging to engage our full attention at the outset of this program. The techniques used to obtain spectra in this region and results to date are described here.

Carbon disulphide is transparent in the visible but strongly absorbing in portions of the UV spectrum (Fig. 1). Kleman[1] describes absorption bands in gaseous carbon disulfide between 3300 and 4300 Å. Those bands to the red side of about 3660 Å are too weak to be observed in the time resolved spectra for the current experiments when the samples are at ordinary temperature and pressure. However, they may be significant as temperature and pressure are increased. This possibility will be discussed later.

Kleman's analysis of the spectrum divides it into several systems which correspond to different electronic excitations. He labels these the R, S, and V systems, and he calls some unassigned bands the U bands. Jungen, Malm, and Merer[2] continue to use Kleman's R, S, and V system notation and they identify another electronic upper state and label transitions to this state as the T system. This system includes Kleman's U bands. The lower state for each of these systems is the linear molecule $^1\Sigma_g^+$ ground state with

various levels of the vibrational bending mode, ν_2, excited. Transitions from excited levels of the vibrational stretching modes, ν_1 and ν_3, were not observed by Kleman.

The R system extends from 4300 to 3275 Å. The upper state for these transitions is a bent molecule with bending, ν_2, and symmetric stretching, ν_1, vibrations excited. The S system extends from 3700 to 3350 Å. The bending mode is the only excited vibrational upper state observed in the S system. The spectral extent of each system is shown in Fig. 1.

The T and V-systems are overlapping in the region between 3400 and 2900 Å with the T-system predominating in the red end of this region. Jungen et al. identify the T and V-systems as two Renner-Teller components[3] of a transition to a configuration which is the bent molecule analog of a $^1\Delta_u$ configuration in a linear molecule. The symmetries of these two states are $^1A_2$ for the T-system and $^1B_2$ for the V-system The absorption in the T and V-systems is much stronger than in the R and S-systems.

Douglas and Zanon[4] describe and partially analyze a system of bands which they observe between 2300 Å and 1850 Å. They call them the 2100 Å bands. As with the R, S, T, and V-systems, the 2100 Å bands are attributed to transitions to a bent excited state. This system is much stronger than any of the R, S, T, or V-systems.

Hot bands are features in the absorption spectrum of a substance which increase in strength when the temperature is increased. They have considerable effect on the carbon disulfide spectrum.[1,2,4] Kleman recorded various regions of the spectrum at 295°K and 580°K.

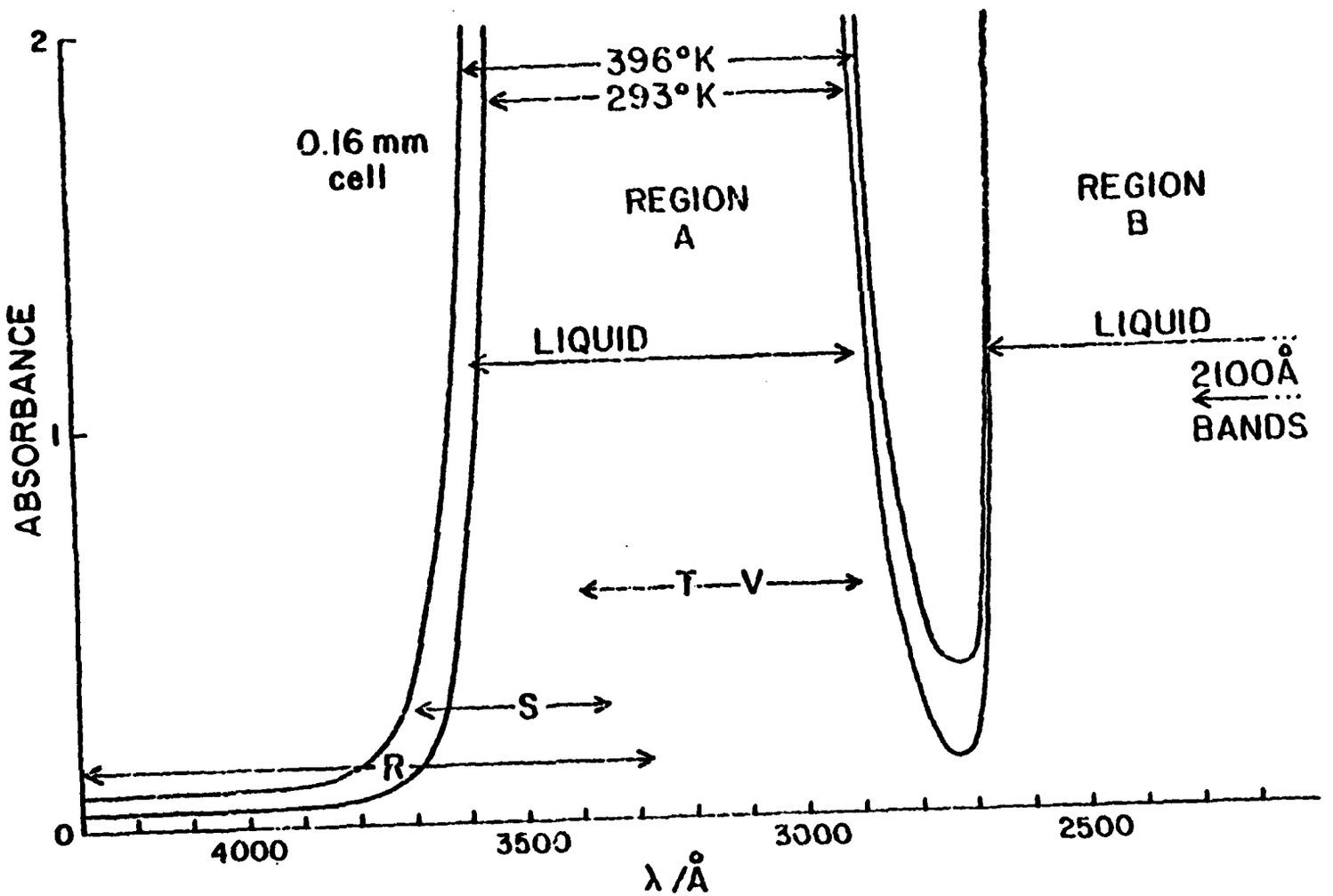

Figure 1. --Spectral Regions of Absorption in Carbon Disulfide. The R, S, T, V and 2100 Å bands are different electronic transitions in the gas phase. The lines labeled liquid show the extent of the unshocked absorption regions as seen by the streak camera in shot 81-010. The curves show the absorbance of a sample at different temperatures.

At 295°K the long wavelength end of the spectrum was extremely weakly absorbing compared to the short wavelength end. At the long end, the spectrum was recorded to 4100 Å using a sample density of 9.1 g of sample per square centimeter of the light beam. But at the short wavelength end, 3100 Å, only 1.2×10^{-3} g/cm^2 were required. The ratio of these sample densities, 7×10^3, gives a rough idea of the large difference in absorption between the R-system and the T and V-systems.

When the temperature was increased to 580°K, a cross sectional sample density of only 2.5×10^{-3} g/cm^2 was required to obtain spectra from around 4100 Å out to 4300 Å. This would indicate that at 580°K the hot bands of the R-system are becoming comparable in strength to the T and V-systems at 295°K.

The entire T-system is composed of hot bands in Jungen's analysis of the T and V-systems.[2] This is because dipole transitions from the linear $^1\Sigma_g^+$ ground state to a state with the A_2 symmetry of the T state is symmetry forbidden. So it is necessary to excite a bending mode in the ground state to see any dipole transitions to the T state. The T-system comprises nearly the entire red end of the T-V absorption region; so enhancing the strength of the T-system by increasing the temperature would make the apparent edge of the T-V system move to the red.

Douglas and Zanon have observed that many of the bands to the red side of 2150 Å in their 2100 Å system are hot bands since they see a decrease in the strength of the absorptions when the sample is cooled. These bands appear in progressions showing the energy differences between the vibrational bending modes of the ground state.

In each of the above systems of transitions, thermally excited bending vibrations of the linear ground state significantly enhance

transitions to the bent upper states. These hot bands contribute significantly to the absorption spectrum of carbon disulfide, particularly on the red ends of the various absorption regions.

Liquid carbon disulfide has two major absorption features within the spectral range, 2500 to 7000 Å, accessible in these experiments. The shorter wavelength feature is a very strong absorption with its red edge between about 2590 and 2660 Å depending on the thickness of the sample cell. This region will be referred to as absorption region B. The blue edge of this region is outside the spectral range available. The longer wavelength feature, region A, is a moderately strong absorption region between about 2900 Å and 3580 Å when seen through a 0.15 mm thick cell. In the thinnest cells, <1 μm, this region passed enough light to cause some exposure of the film even at the wavelength of maximum absorption, which was about 3200 Å.

The regions of absorption in liquid carbon disulfide correspond roughly with the regions of maximum absorption in the gas phase spectra as shown in Figure 1. However, significant differences are noted. The most striking of these is that both absorption regions extend farther to the red than their gas phase counter parts if one ignores the very weak R and S-systems. Region B extends to between 2590 Å and 2660 Å while region A extends to about 3580 Å, about 180 Å to the red side of the strong T-V systems in the gas phase spectra.

Gas phase studies of CS_2 decomposition indicate that the CS molecule is one of the earliest appearing decomposition products. The CS molecule has an absorption band in the gap between absorbing regions A and B shown in Fig. 1. It was our optimistic believe at the start of this program that passage of a shock would cause transmission in this gap to fade away, thereby enabling us to determine the rate of formation of CS. These expectations were misdirected because of the appearance of other effects which are perhaps even more interesting, as will be related.

Sheffield's experiment, described in Section IV, was designed so that the sample would be thrust into the reacting state by the first reflected shock. Cell thickness was great enough to allow it to remain in this state for the better part of a microsecond and also great enough that EMV gages could be suspended in the cell. It had two major disadvantages for spectroscopy. First was that the front of the cell, being PMMA, was opaque in the UV. Second was that cell thickness was very great compared to absorption lengths in liquid CS_2. The latter condition would make it difficult to unravel any time-dependent spectral changes occurring in the region behind the shock front. These considerations made it necessary to redesign the cell in the manner shown in Figs. 2-4. In Fig. 2, A is the impacting sapphire which strikes the front-face sapphire, B, at t = 0. D is the CS_2 sample. The rear face of the cell, E, is also sapphire. Pressure in D rings up to its final value through states 2, 3, 4, 5, etc., shown in Figs. 3 and 4. In Fig. 4, successive pressure states at the C-D boundary are shown by the solid line; mean pressure, as seen by a light ray normal to the cell, is indicated by the dotted line. Duration of states 3, 5, etc. can be adjusted by varying the thickness of D. This permits considerable flexibility in varying pressure and temperature.

B.148 Blank

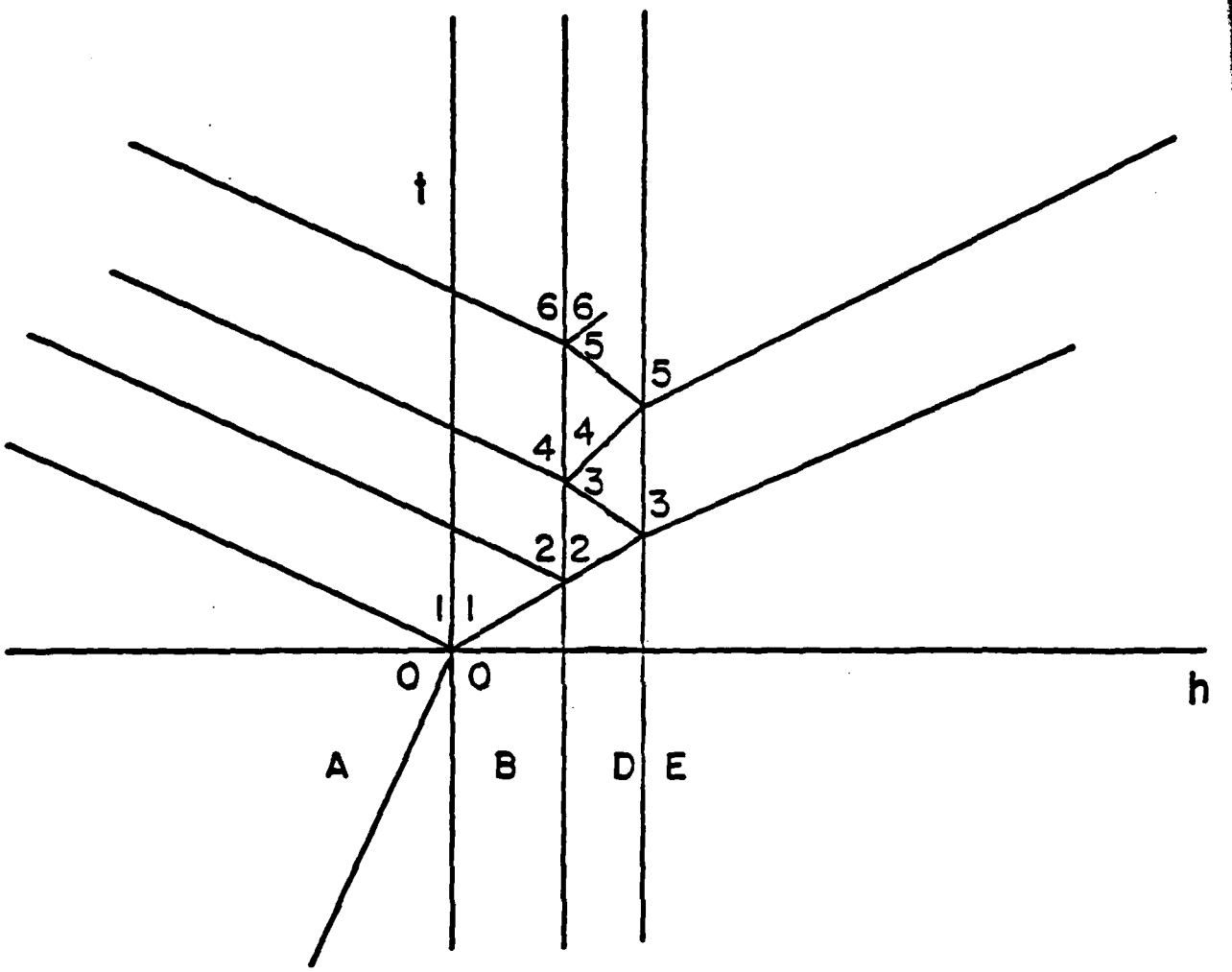

Fig. 2 Modified Cell for Spectroscopy.

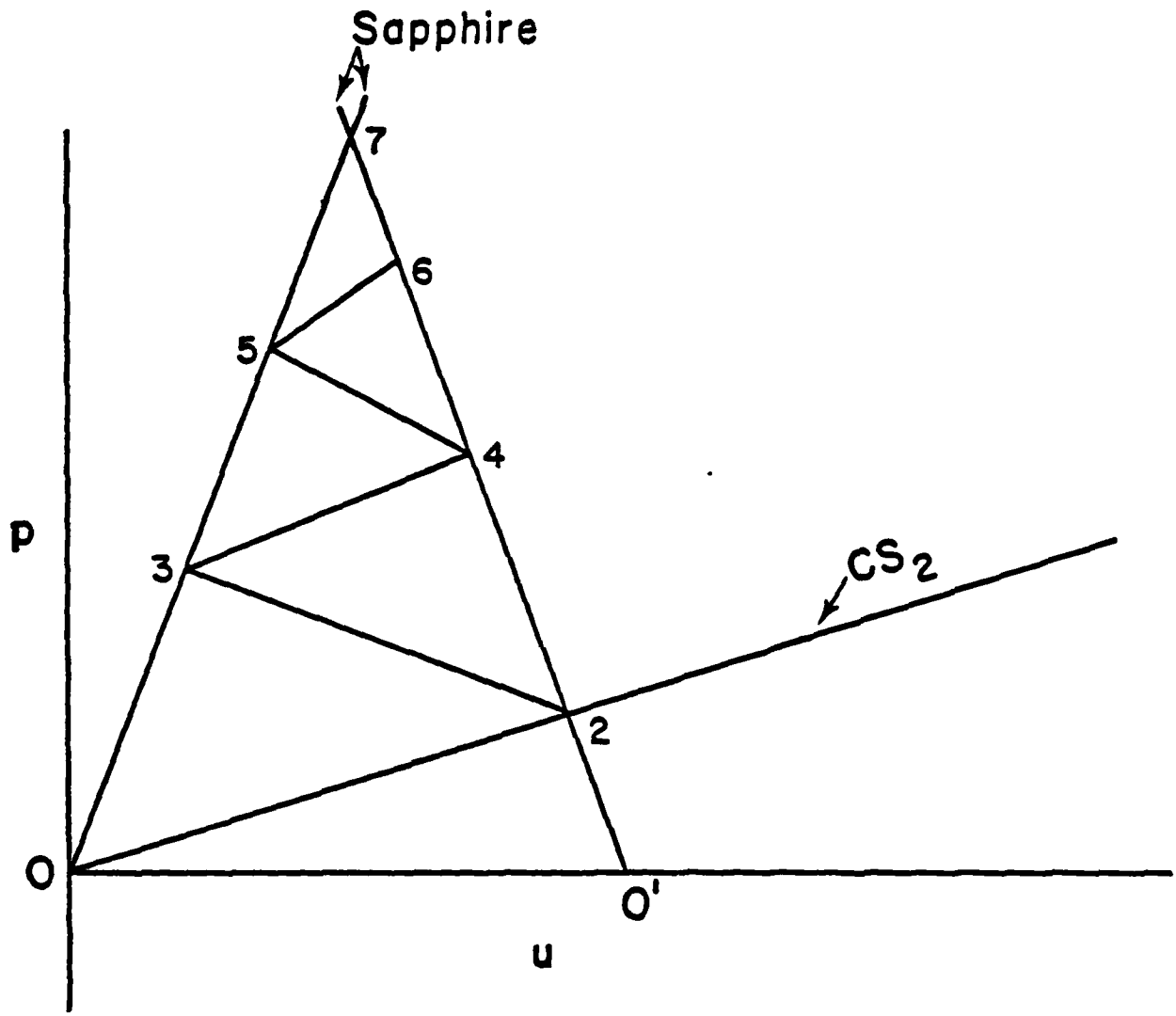

Fig. 3 Pressure States in CS_2 resulting from the impact shown in Fig. 1.2.

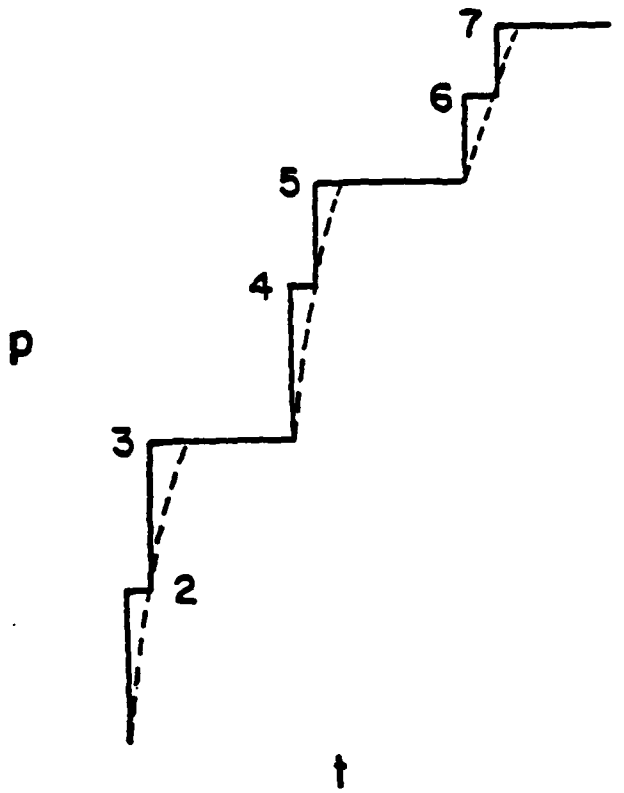

Fig. 4 $\bar{p}(t)$ in sample is represented by dotted curve. Steps show pressures of the successive shock states of Figs. 1.2 and 1.3.

The cell of Fig. 2 represents a compromise which is not altogether satisfactory. The final state is reached through a succession of shocks, which may not produce the same effects as a single strong shock. The temperature reached when the system rings up to its final pressure is closer to that of adiabatic compression then to a single shock. If transit time through the CS_2 is large compared to time resolution of the recording instrument, the effects of successive shocks can be followed, thereby increasing the amount of information obtained in a single experiment. These have come to be called "thick cell experiments." In thin cells the transit time is small compared to time resolution and the consequences of "sudden" applications of pressure and temperature can be recorded. So the experiments described have some shortcomings, but they open a new regime for study and are useful. They should not represent the last work in experimental design.

In the experiments described in the following sections the basic experimental procedure consisted of impacting a cell containing the liquid with a high speed projectile to drive a shock wave into the liquid. Simultaneously, a high intensity pulsed light source would illuminate the cell and the light transmitted through the sample would then be analyzed by a dispersion unit and a streak camera to provide a time resolved spectrum of the transmitted light.

Experiments were conducted using two variations of this idea. Both variations utilized a sapphire sample cell with a thin front or impact side and a thicker back. A sapphire impactor would strike the front of the cell sending a shock wave into the liquid in the cell cavity. In the first variation, referred to as reflection experiments, light from a xenon flashlamp was focused into the back of the cell. The light was to pass through

the cell and sapphire impactor and be reflected by an aluminum mirror vapor plated on the back of the impactor. The light would then pass through the impactor and cell a second time as shown in Figure 5. This arrangement had the advantage of keeping the mirror free of damage by the shock wave until after the experiment. It was found that the reflection from the first sapphire-liquid interface in the light path was a problem because it reached the streak camera along with the desired light signal that had passed through the cell. To get around this problem a second variation was developed in which the xenon light source was mounted behind the impactor inside the projectile as shown in Figure 6. These will be referred to as transmission or flashlamp-in-projectile experiments.

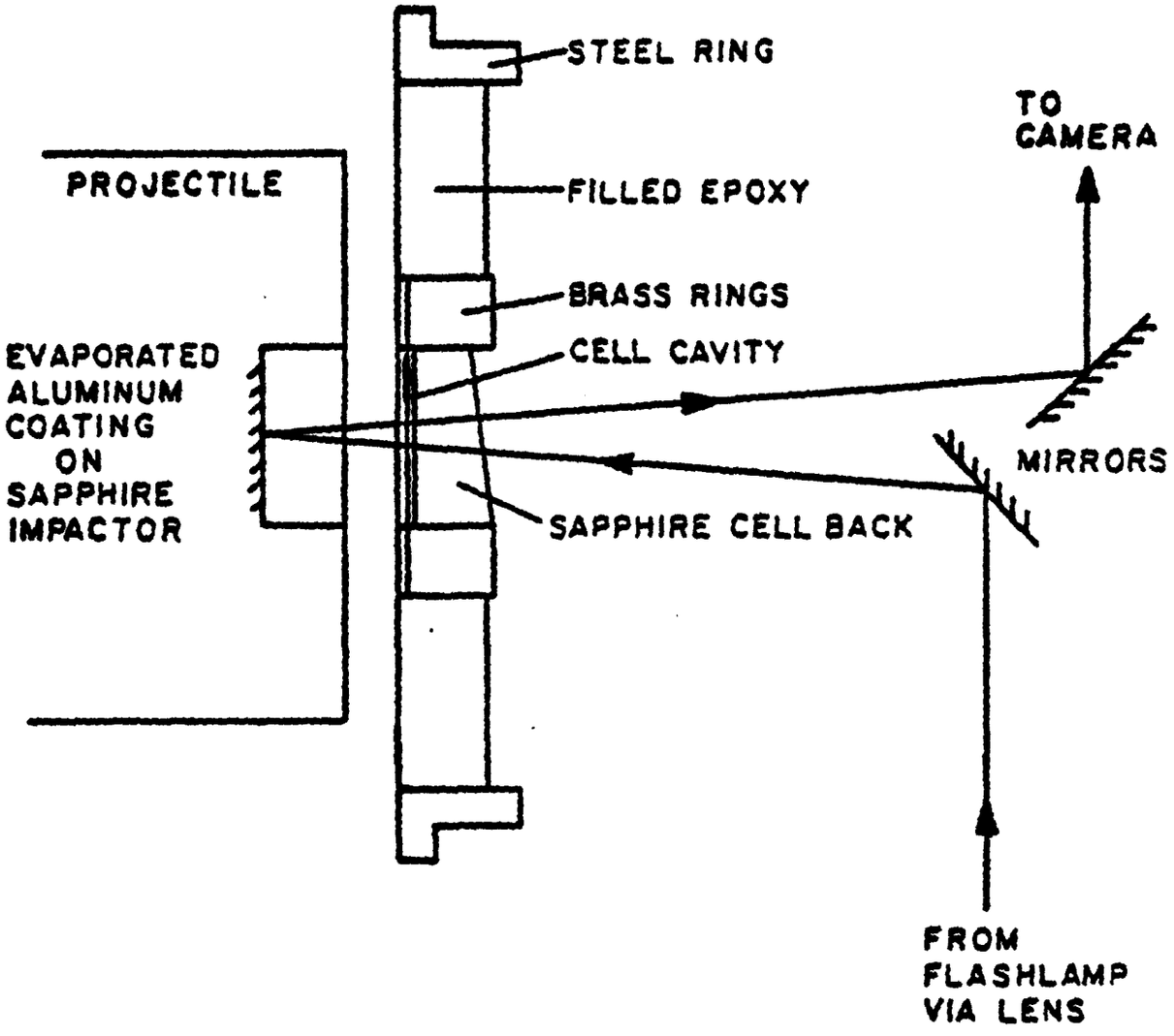

Figure 5 .—Optical Path for Reflection Experiments. This cross sectional sketch of the projectile and target shows the intended path of the light beam during a reflection type experiment. A lens, not shown, focuses an image of the flashlamp onto the impactor's mirror.

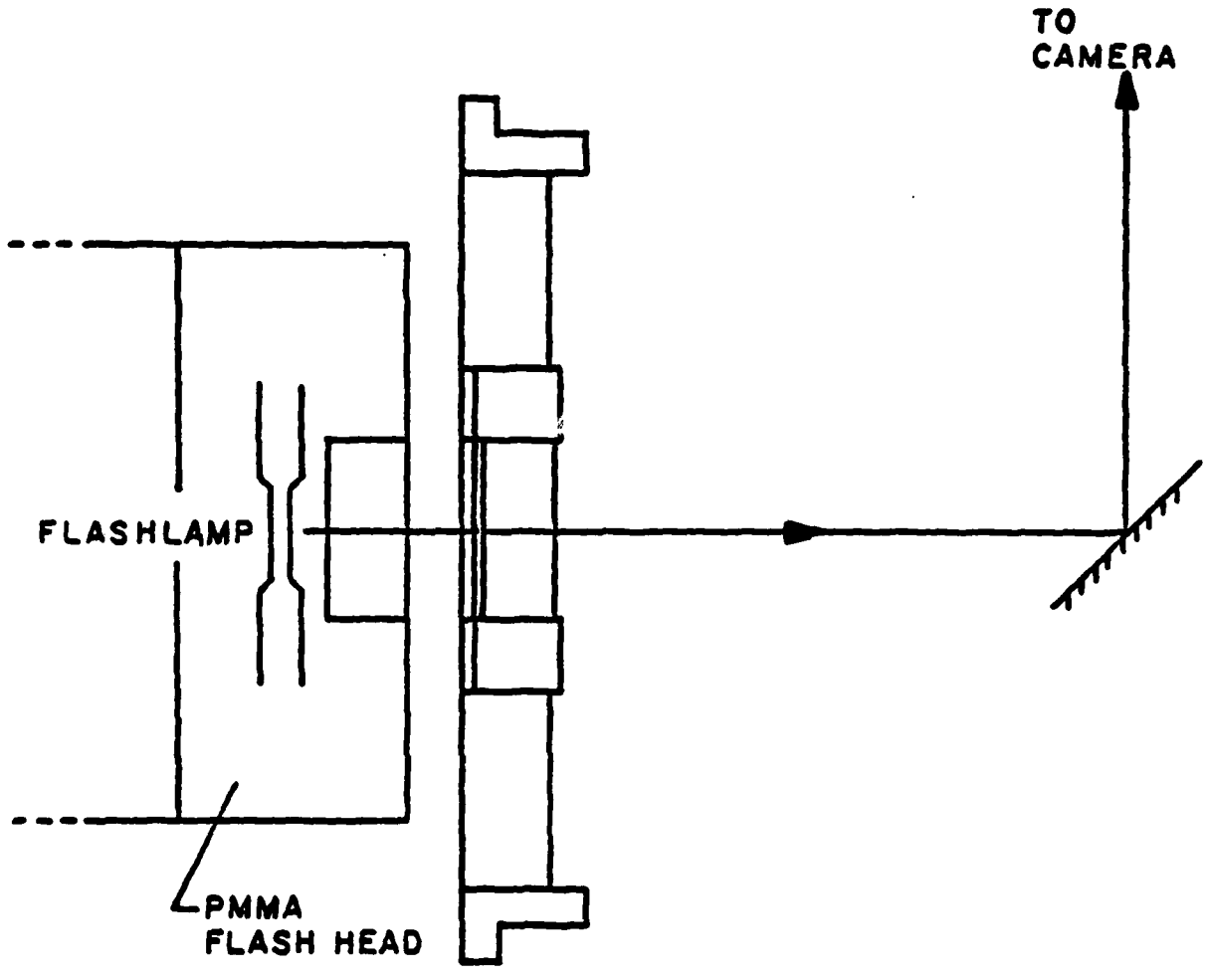

Figure 6 --Optical Path for Transmission Experiments. In transmission experiments, the flashlamp is mounted in the projectile so that light passes only one direction through the sample.

5.2 APPARATUS AND PROCEDURES

These experiments were also carried out in the Shock Dynamics Laboratory at Washington State University using the 4 inch gas gun facility augmented by a Beckman and Whitley model 1500 spectrograph, a Beckman and Whitley model 339B rotating mirror streak camera, suitable light sources, and other optical components. These are described below.

A. THE CAMERA ASSEMBLY

The Beckman and Whitley model 339B streak camera and model 1500 dispersion unit bolt together into a single camera assembly. This camera assembly is mounted above the target tank and looks vertically down into the target tank. An expendable mirror placed about 20 cm behind the target directs light from the target up into the camera assembly during both reflection and transmission experiments. The camera assembly, optics, and other components of the spectrographic system are described in the following sections, which refer to Fig. 1.

Dispersion Unit Optics

The dispersion unit optical path starts with an 11.4 cm diameter, 46 cm focal length, objective mirror which, by way of a relay mirror and quartz vacuum window, focuses an image of the target onto a slit which is adjustable in two dimensions. The slit dimensions provide control of both spectral and temporal resolution. Light passing through the slit is reflected by a relay mirror to a 10.2 cm diameter, 41 cm focal length collimating mirror. The collimated beam illuminates the plane 102 x 127 mm diffraction grating which disperses the spectral components. The dispersed

beam is focused by a 10.2 cm diameter, 81 cm focal length, collecting mirror to form a dispersed image of the slit at the output plane of the dispersion unit, which is 12 cm outside the dispersion unit housing. This output serves as the input to the streak camera.

Streak Camera Optics

The first optical element in the streak camera is a 5.1 cm diameter, 33 cm focal length, quartz field lens. This lens causes the cones of light for different wavelengths to converge in such a manner as to minimize the size of the convex mirror needed to avoid vignetting. This is accomplished by constructing the field lens to focus an image of the collecting mirror onto the convex mirror.

The next element in the streak camera, the convex mirror, spreads the dispersed beam to illuminate a 30.5 cm diameter concave primary mirror. This mirror focuses the light to a spectrally dispersed image of the slit 112 cm from the primary mirror. The rotating mirror is located 28 cm ahead of the focused image. It causes the image to sweep along a 240 degree arc of film as the mirror is rotated. The rotating mirror does not intercept all of the light in the beam. Some passes above the rotating mirror to an aperture in the back of the camera casing. An RCA type 4831 photomultiplier tube is installed in this aperture to monitor the total intensity of the light within the spectral range actually reaching the film. The rotating mirror has three reflecting faces forming an equilateral triangle so that one face is always in position to reflect light to the film. The mirror is long enough to intercept nearly the entire light cone in the horizontal direction. Each face is 7.6 cm long and 3.3 cm high.

Camera Assembly Slit and Resolution Limits

The slit which controls both the height and width of the image on the film is located at the input to the dispersion unit. The streak camera does not have a separate slit of its own. The width of the slit has a micrometer adjustment indicating slit width in units of 10 μm. This width is parallel to the direction of wavelength dispersion and so, together with the line density on the grating, can be used to adjust the spectral resolution of the apparatus. The maximum slit width possible is 3 mm, but the design of the optical system outside the camera assembly assumed that neither the height nor the width of the slit would exceed 1 mm.

The height of the slit aperture is adjustable by a stepped mask with heights of 0.274 mm, 0.482 mm, 1.978 mm and larger up to about 12 mm. Only the smallest, 0.274 mm, opening has been used. The temporal dispersion is obtained by sweeping the image of the slit in a direction parallel to the height of the slit image; so the time resolution of the instrument can be adjusted by the slit height and the rotating mirror speed. The magnification between the slit and the film is 0.99 and the spectral dispersion spreads the image out across the 25 mm usable width of the film.

The time resolution which can actually be achieved is affected by several factors which include the maximum operating speed of the rotating mirror, the spatial resolution of the film, and brightness of the light source. The Kodak 2475 recording film used is rather coarse grained, having a spatial resolution of about 10 line pairs per millimeter. This together with the 2500 revolutions per second maximum mirror speed and a 28 cm sweep arm implies a best time resolution of 11 nanoseconds. At a typical mirror speed of 2480 revolutions per second, the 0.274 mm slit yields a time resolution of about 31 nanoseconds.

With a limited light intensity available there is a trade off to be made between spectral and temporal resolution. To obtain enough light on the film when using the 600 lines/mm grating blazed for 3000 Å, it was necessary to open the spectral slit to 0.75 mm. Since this grating gives a dispersion of 41 Å/mm on the film, and the magnification between the slit and the film is nearly unity, the spectral resolution is about 30 Å. Similarly, for the 300 lines/mm and 150 lines/mm gratings the slit widths were 0.50 and 0.35 mm, respectively, giving the spectral resolutions of 40 and 55 Å. If more light were available or less time resolution were acceptable, greater spectral resolution could be achieved by closing the slit width down as narrow as 0.1 mm. For any smaller slit width the spatial resolution of the film would limit the spectral resolution.

B. PHOTOGRAPHIC FILM AND DEVELOPMENT

The photographic film selected for use in the streak camera was Kodak recording film 2475 (ESTAR-AH Base).[5,6] This film was selected for its very high speed and its spectral response. This is a coarse grained film to obtain the high film speed. Its spatial resolution is only about 10 line pairs per millimeter but this is adequate considering the slit sizes which are used.

Several other films were tried. One of these, Kodak pan film 2484, was nearly equivalent to the 2475 film. The film developing process was adjusted to obtain the maximum contrast and sensitivity without excessive increase in the film's fog level. The process that was used for all film records is:

1. Develop Kodak 2475 film in Kodak DK-50 developer at $20^{\circ}C$ for 7 min. Agitate for 15 sec after adding the developer and every 2 min thereafter.
2. Stop development using Kodak indicator stop bath at $20^{\circ}C$. Pour in the stop bath, agitate for 30 sec, and drain.
3. Fix using Kodak fixer at $20^{\circ}C$ for 10 min. Agitate for 15 sec every 2 min.
4. Wash in $20^{\circ}C$ running tap water for 25 min.
5. Rinse with distilled water and hang to dry.

C. THE OPTICAL SETUP AND ITS DESIGN

The most important consideration in the design of the optical system between the light source and the dispersion unit is to maximize the total amount of light which can be transmitted through the target and into the usable light cone of the camera, subject to the constraints imposed by the physical setup of the experiment. One of these constraints is that only a 6 mm diameter area in the center of the target cell remains free from side rarefactions for the duration of the experiment, about 1 μs. Another is that the closest the dispersion unit can be mounted to the target places the objective mirror at an optical path length of 2.9 m from the target. This 2.9 m optical path, together with the 46 cm focal length of the objective mirror implies a magnification between the target and slit of 1/5.3 so that a 5.3 mm dimension on the target is imaged into 1 mm on the slit. Since 1 mm is as large a slit opening as is needed and 5.3 mm is still smaller than the rarefaction-free center of the target cell, no additional optics are needed between the target and the object mirror.

For reflection experiments a lens must be selected to focus the light source onto the target. The lamp in this case is mounted outside the target, so a convenient location for the lens is in a target tank access port 10 cm behind and 69 cm to the side of the target. The diameter of this lens must be great enough to provide a cone of light that will completely illuminate the objective mirror. At 79 cm from the image on the target this requires a diameter of 2.10 cm plus an additional 0.66 cm for off-axis rays focused at the edge of a 1 mm wide slit. Some additional lens diameter is desirable to make alignment less critical and to allow for some tilt in the target mirror. A 6.35 cm diameter lens was selected with 0.63 cm around the perimeter covered by the lens mount, which must be rather strong

because the lens serves as a vacuum and pressure boundary for the target tank. The final effective diameter is 5.08 cm.

The lens to flashlamp distance is selected so that the image of the flashlamp will completely cover the rarefaction-free center of the target, and thus completely cover the slit. Using a 15.2 cm focal length lens, the lens to flashlamp distance is 18.8 cm. Illuminating the 6 mm diameter rarefaction-free region thus requires a flashlamp with 1.4 mm bore diameter. With a 2 or 3 mm bore flashlamp this setup allowed reasonable leeway in alignment so a commercially available 15.2 cm focal length plano-convex ultraviolet lens and a commercially available 3 mm bore flashlamp were selected.

When it was decided to mount the flashlamp in the projectile, a 3 mm bore lamp was selected. Although this is not as large as the 6 mm rarefaction-free region, it is large enough for its 0.57 mm image to completely cover the 0.274 mm height of the slit. The 0.57 mm image will not cover the maximum slit width used; the flashlamps in the projectile are oriented so that the long axis of the image of the lamp falls along the longest dimension of the slit. With this arrangement no optical elements, other than a flat relay mirror, are needed between the projectile light source and the objective mirror of the dispersion unit.

D. THE SAMPLE CELL

Design Considerations for Reflection Experiments

The first considerations were that the cell be transparent to ultraviolet light at pressures above 100 kbars and that its shock properties be known in this pressure range. These criteria led to the selection of Z-cut sapphire as the principal cell material. Barker and Hollenbach[5] describe Z-cut sapphire properties and note that it is useful as a window material up to pressures as high as 130 to 150 kbars.

Another consideration was the amount of light that would be transmitted by the sample material in the cell. The brightness available from the flashlamp was only marginally adequate for the time resolution needed so it was necessary to use a very short optical path within the cell. This limitation was compounded by the fact that the light would make two passes through the cell and by the high absorption of carbon disulfide within some wavelength regions of interest. Consideration of these limitations led to the selection of a nominal cell thickness of 0.1 mm.

It was necessary to prevent light reflected from the back surface of the cell from reaching the camera assembly. About 0.08 of the incident light is reflected from the first vacuum-sapphire interface at the back of the cell. This reflected light has not reached the carbon disulfide layer so carries no useful information.. If the back surface were parallel to the mirror behind the impactor, the back surface reflection would be parallel to and essentially coincident with the reflection from the cell mirror. Both reflected beams would enter the camera assembly. To prevent this, the back piece of sapphire was made wedge shaped with its back side tilted six degrees from parallel to its front. The Z crystal axis is perpendicular to the front face.

The question of where to place the mirror in the cell assembly received considerable attention. The mirror could have been vapor plated onto the sapphire at the front of the cell cavity. However, it was feared that the specular reflective quality of the mirror would be lost when the shock reached the mirror. In fact even a small effect on the mirror could not be tolerated because it would be impossible to tell whether a change observed in the light beam was due to the response of the sample to the shock wave or due to the response of the mirror. To avoid these problems it was decided to place the mirror behind the sapphire impactor in the projectile where it would remain unshocked for the significant part of the experiment. There was still some question as to the transmission quality of the sapphire-sapphire impact interface. Subsequent results showed a slight loss of light at impact but not enough to cause concern.

The elastic shock velocity in sapphire is about 11 mm/μsec. To obtain at least a 6 mm rarefaction free volume in the center of the cell for the duration of a 1 μsec experiment, a cell diameter of 31.8 mm was selected. Also, with this elastic shock velocity in mind a 12.7 mm thick cell back was selected to prevent the shock from reaching the back of the cell within 1 μsec.

Cell Construction

Having decided on the desired features of the sample cell it was necessary to develop the final design and the construction techniques. Fig. 7 shows the cell design used.

The front of the cell served only to confine the contents, so it was made as thin, 2.07 mm, as possible without making it impossible to mount in a supporting structure. Mounting the cell front was complicated by the need to allow the projectile to impact it without impediment on one side and the need to mount it only 0.1 mm from the back sapphire. This left only the edge of the cell front to use for holding it in place. The first cells used epoxy to hold the front sapphire in a brass ring. The brass was made slightly thinner than the front sapphire and one side was lapped flat. The brass ring and sapphire were clamped against a lapped flat steel plate as the epoxy cured. This ensured that the sapphire and brass surfaces were in the same plane.

The sapphire cell back was also mounted with epoxy in a brass ring. After the epoxy cured, the assembly was chucked in a lathe and the brass was faced off to form a surface parallel to the sapphire surface but displaced outward by an amount equal to the desired cell thickness, usually about 0.1 mm. Then, the flat side of the cell front assembly was placed against this surface. A cavity about 0.1 mm thick remained between the front and the back sapphires. To allow for filling the completed cell, two 0.25 mm holes were drilled in the brass at opposite edges of the back sapphire. The outer ends of the holes were enlarged to accept 1.6 mm copper tubing; and the inner ends were connected to the cell cavity by milled slots in the brass. To seal the assembled cell, an "O" ring groove was turned into the face of the back

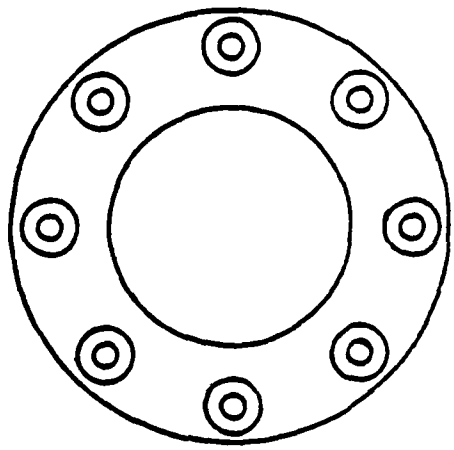

CELL FRONT

Scale 1:1

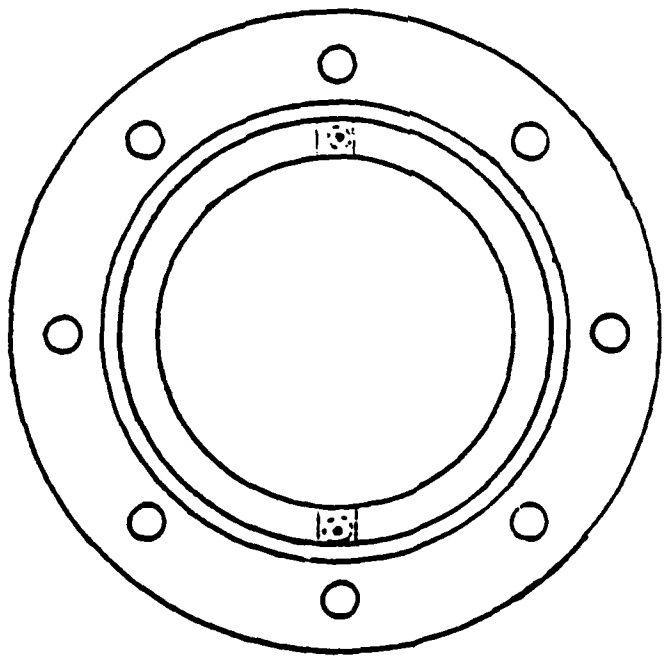

CELL BACK

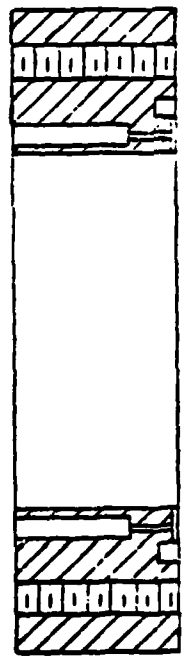

Scale 1.5:1

Figure 7 --Cell Design. The sapphire cell windows were mounted in these brass rings.

brass. Eight machine screws just outside the "O" ring held the cell together. The 6-32 flathead screws were threaded into the back brass with their heads countersunk into the front of the cell.

The narrowness and brittleness of the epoxy joint between the front sapphire and its brass ring caused some problems. As the front sapphire was tightened over the "O" ring, the brass would flex slightly and the epoxy would crack, causing leaks. Also, it was feared that sample materials such as CS_2 would leach contaminants out of the epoxy. So, on all-metal thermal-shrink method of mounting the sapphire in the brass rings was developed.

The hole in the brass ring was made 0.05 mm smaller than the sapphire and the inner brass surface was coated with a thick layer of tin-lead solder. Flux residue was removed; then this ring was heated on a flat lapped steel plate until the hole had expanded enough to allow the sapphire to be dropped in. The sapphire and brass were then firmly held against the flat plate as the plate was cooled by setting it on a thick cold metal surface. This technique developed a strong bond between the sapphire and brass. At first, two or three tries were needed to produce a leak free assembly that was acceptable in all aspects. Production efficiency was improved by placing a tight specification of 13 μm total indicated runout on the roundness of the sapphire, and by improved skill. Both front and back sapphires were mounted with this heat-shrink technique. The copper fill tubes were soldered into these cells.

The "O" ring material must be compatible with the liquid in the cell. Teflon[7] was used in early cells with carbon disulfide. Viton[7] was used in later cells because, being a more rubbery material, it seals better with less force, thereby making accurate control of cell thickness easier. Teflon and Viton are resistant to carbon disulfide. Some other "O" ring materials are not.

Thin Cell Modifications

Several cells in the range of 0.6 to 1.2 μm thickness have been constructed. These extremely thin cells were achieved by modifying the manner in which the cell front was attached to the back. Instead of facing off the back brass flat with the sapphire, the brass was faced off at a $1/2^{o}$ angle tilted up away from the sapphire. Also, the inner edge of the brass, next to the sapphire, was recessed 25 μm below the sapphire surface as shown in Fig. 8.

When the cell front assembly was screwed onto the tilted brass, it took a dish shape. The heat-shrink assembly of the front piece is strong enough to force some curvature in the front sapphire. The eight screws were carefully adjusted so that the front sapphire was symmetrically curved toward the back sapphire and touched the back sapphire in the center. It was easy to tell when the cell had been adjusted to this condition by doing the work under a monochromatic, long-coherence length light. A beautiful set of Newton's rings became apparent. When the cell was prepared for the experiment in the target tank, it had a vacuum around it and a known pressure inside. The known pressure was achieved by having the cell connected to a reservoir of the sample liquid outside the target tank at atmospheric pressure. To complete adjustment of the cell thickness, at the bench, this operating pressure in the cell was simulated by using compressed nitrogen. The screws were adjusted until the fringes in the cell showed it to be the desired thickness when there was one atmosphere of differential pressure between the inside and the outside of the cell. Thickness was checked by pressing on the front of the cell until the front and back sapphire made contact, then counting the fringes as the force was removed.

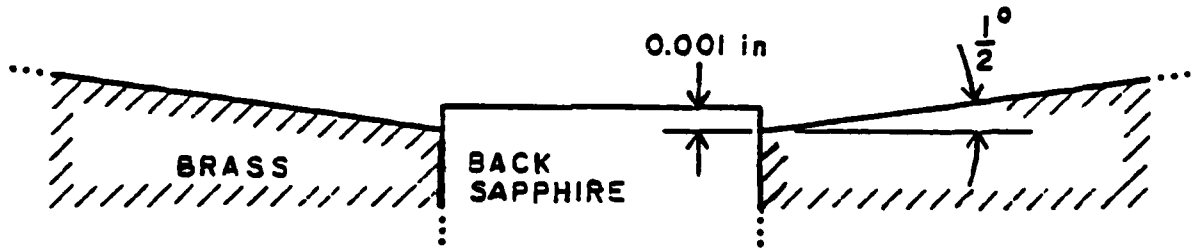

Figure 8.--Machining of Thin Cell Brass. Dimensions have been exaggerated here to show how the back brass of 1 μm thick cells was machined. The front sapphire and brass took a very slight dish shape when screwed onto the tilted brass back. Adjusting the torque on the screws allowed submicron control over the spacing between the sapphire windows.

When the cell could not be adjusted with reasonable torque on the screws, thin pieces of wire were used as shims between the front and back brass, under the outside of some or all of the screws. Considerable effort was needed to achieve final adjustment of these thin cells, but the results were stable, reproducing themselves well when the internal pressure in the cells was removed and reapplied. Cells thinner than 1 μm in the center region probed by the light beam were produced using this technique.

E. TARGET ASSEMBLY

When the sample cell was completed it was epoxied into a steel and epoxy target assembly as shown in Fig. 9. This was used to mount the cell at the muzzle of the gun. The steel ring part of the assembly was 12.7 cm i.d., 15.2 cm o.d., and about 2.5 cm from front to back. The outer 6 mm of the ring was a lip about 6 mm thick. Brass strips were clamped against this lip to hold the assembly firmly against the target holder at the muzzle. After impact the brass strips would bend back allowing the entire assembly to break away without damage to the target holder. The interior of the ring was filled to a depth of 1.6 to 1.9 cm with an epoxy potting compound containing powdered calcium carbonate filler. The front or impact face of this assembly was lapped flat before installing the cell.

In addition to the sample cell, several other components were mounted in the target assembly. These included the trigger pin, the high voltage contacts, and the rubber insulating ring. The high voltage contacts, the insulating ring, and the groove in which the insulating ring was mounted were omitted from targets used in the reflection experiments. Brackets for mounting the mirrors behind the target were also attached to the target assembly after it was mounted on the target holder.

After the face of the target assembly was lapped, a hole 5.79 cm in diameter was bored through it for mounting the cell. In transmission experiment targets, a groove 6.8 mm deep, 6.03 cm i.d., and 10.48 cm o.d. was turned into the front face surrounding the hole for the cell. Next, three holes were drilled in the epoxy for the high voltage pins and the trigger pin. The two high voltage pin holes were tapped with 8-32 threads. The trigger pin hole was 1.67 cm in diameter and the brass insert for mounting the trigger pin was epoxied into it. The three holes were 120° apart and centered on a circle of 8.10 cm diameter.

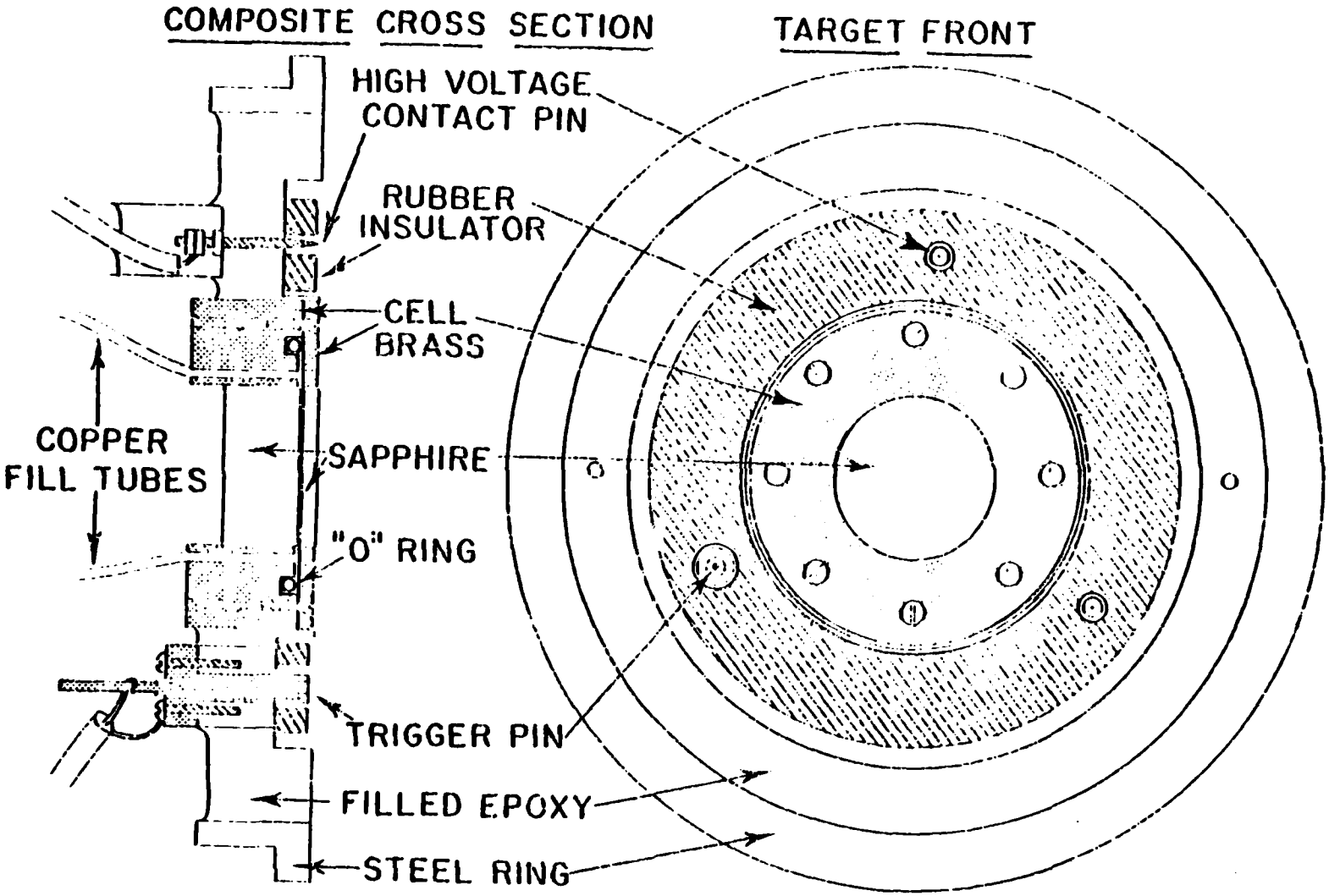

Figure 9 --Target Assembly. Not all features shown in the cross section are in the same plane. The high voltage contacts and rubber insulator were not used in reflection experiments.

The black rubber ring, 6.35 cm i.d., 9.86 cm o.d., and 5.3 mm thick, was glued into the groove in the face of the target assembly using silicone rubber sealant and Eastman adhesive. A small amount of silicone sealant was used under the ring around the high voltage pin holes to ensure good insulation. The Eastman 910 was used around the rest of the ring. Six millimeter diameter holes were cut in the rubber ring for the high voltage pins and a one centimeter hole for the trigger pin.

To mount the cell in the target assembly, the assembly was first clamped face down on a lapped flat steel plate. The edges of the cell and the hole in which it was mounted were coated with a thin layer of Epon 815 epoxy. Then the cell was inserted into the hole until the front sapphire was resting flat against the steel plate. The cell was clamped in this position until the epoxy cured.

The high voltage pins were 8-32 threaded steel rods about 3.8 cm long. A narrow tapered point, 30° total included angle, was machined onto each pin. These pins were threaded through their holes until the pointed end projected 0.25 mm beyond the rubber ring. This still left them about 1.17 mm below the surface of the target. Quick setting epoxy and a nut were applied to the pins on the back side of the target to hold them in position.

The high voltage wires were connected to the pins with two nuts. A plastic tube was attached around the wire connection and filled with epoxy so that no uninsulated conductors were exposed on the back of the target. The high voltage wires, which were 18 gauge high voltage test probe wire, were led out of the target tank by epoxying them into holes in a PMMA feed-through in a flange on an access port.

F. THE LIGHT SOURCE

Reflection Experiment Flashlamps

The light sources chosen for the reflection experiments were xenon flashlamps of one inch arc length, 3 mm bore, 450 torr xenon fill, and 1 mm thick Suprasil envelope obtained from ILC Technology, Inc. under model number L-3958. The lamps were driven by a 3.3 μf capacitor bank charged to 6000 V. The total stored energy was 60 joules. A triggered spark gap controlled the timing of the discharge. The timing of the spark gap trigger signal was obtained from a charged shorting pin in the target assembly. To help ensure rapid and consistent triggering of the flashlamps, the high voltage trigger signal to the spark gap was also connected to a trigger wire on the flashlamp.

Flashlamps for the Projectiles

Commercial flashlamps were found to be highly unreliable when mounted in the projectile. The reasons why the commercial flashlamps did not work are somewhat speculative but two possibilities seem likely. First, the flashlamp is fairly long so the envelope may fail when subjected to stresses from shrinking of the epoxy it was potted in, and from stresses induced by the acceleration in the gun. One lamp failed from epoxy shrinking stresses alone. This failed lamp was potted in a single thick pour of epoxy. Subsequent lamps were potted using three smaller pours. The second possibility comes from the fact that the electrodes extend 17 to 20 mm without support into the cavity of the flashlamp, perpendicular to the direction of acceleration in the gun. It is possible that these electrodes broke during acceleration, possibly breaking the envelope too.

AD-A120 516 SHOCK-INDUCED CHEMICAL REACTIONS IN CONDENSED MATTER (U) WASHINGTON STATE UNIV PULLMAN DEPT OF PHYSICS G E DUVALL ET AL. AUG 82 N00014-77-C-0232 3/3

UNCLASSIFIED F/G 20/13 NL

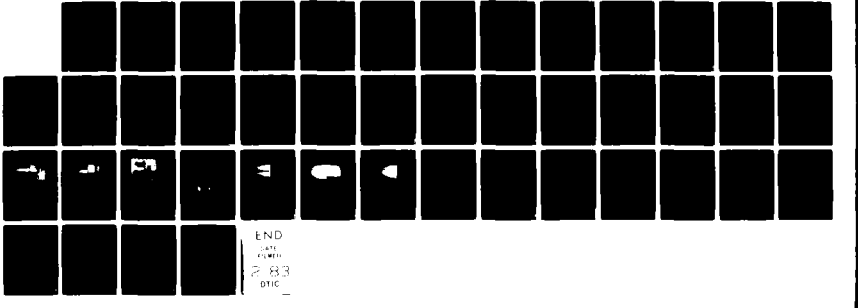

END

DATE FILMED

2 83

DTIC

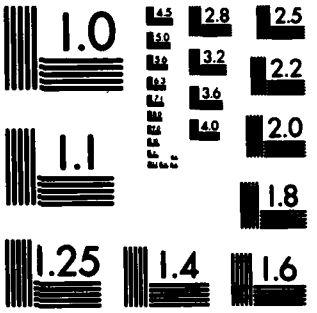

A special flashlamp design was developed for use in the projectiles. Keeping the possible failure modes in mind, the new lamps were designed as short as possible and with sturdy electrodes projecting only about 2 mm into the lamp cavity as shown in Figure 10. Since the lamps were for one shot service, the quartz envelope to electrode seals were made with Torr Seal[8] high vacuum epoxy rather than quartz to metal seals. Two 3.2 mm, 2% thoriated tungsten welding rods were used for electrodes and a 1.6 mm copper tube was epoxied in next to one of the electrodes for evacuating and back filling with xenon to 450 torr. This design proved perfectly reliable.

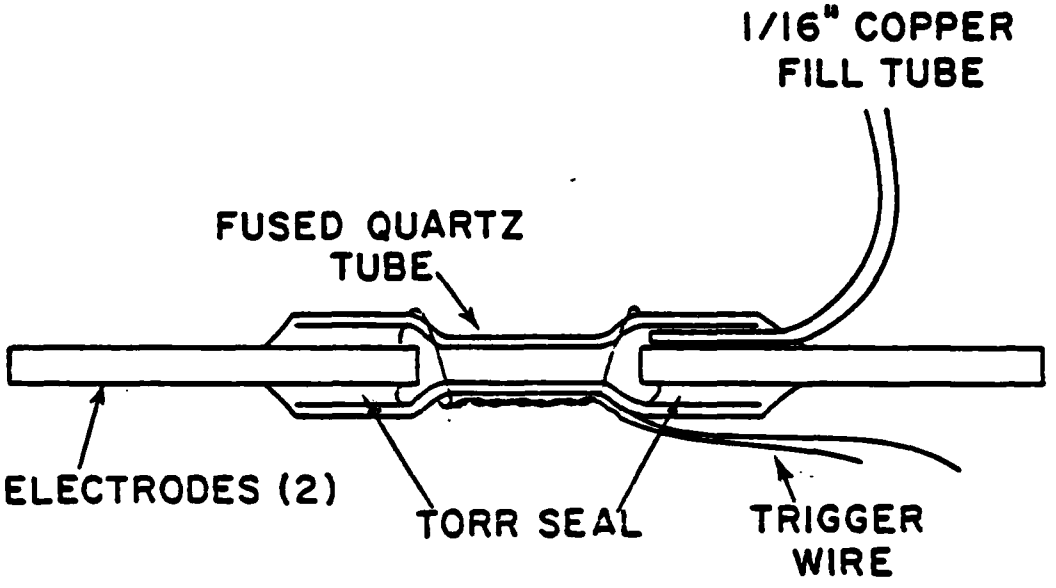

Scale 1.5:1

Figure 10.--Flashlamp for Mounting in Projectile. Torr Seal is a high vacuum epoxy with high viscosity which made it convenient for sealing the electrodes. The electrodes were 1.4 inch sections of 1/8 inch thoriated tungsten welding electrodes.

G. THE PROJECTILE

Projectiles for Reflection Experiments

Projectiles for these experiments were made by modifying the standard aluminum projectile,[1] which is a one piece hollow aluminum cylinder closed at one end. It is 10.16 cm in diameter and 20.32 cm long. A 1.9 cm thick aluminum plate was mounted on the open end and the impactor was mounted in the plate. Prior to mounting the impactor, the face of the projectile was lapped flat and perpendicular to the sides of the projectile to better than 0.01 milliradians. To ensure that the impactor face would be parallel to the face of the projectile, an "O" ring was placed in the bottom of the hole in which the impactor was to be mounted. This held the surface of the impactor slightly above the surrounding projectile face until a lapped flat steel plate was placed across the face of the projectile and weighted to compress the "O" ring. This held the impactor flat against the steel plate until the surrounding epoxy cured. In this way the impactor was mounted with its surface flush with, and parallel within 0.1 milliradian to the face of the projectile.

Projectiles with Flashlamps

To provide insulation, the flashlamp and all other projectile flash head parts were potted into a 4.1 cm thick section of polymethylmethacrylate (PMMA), which was bolted and epoxied onto the front end of a standard aluminum projectile.[9] Figures 11 and 12 show the flash head construction. Contact with the high voltage pins in the target was made by two brass contact strips mounted in a PMMA contactor ring, so that when the contactor ring hit the rubber ring, the brass strips and the high voltage were electrically insulated from the surrounding vacuum, thereby preventing any unwanted discharges.

In addition to the two high voltage contact strips in the contactor ring, there was a third contact strip which extended to the edge of the projectile diameter. This strip served to make contact with the velocity pins and the trigger pin in the target. Each of the three contact strips covered a projectile rotational angle of 90° so that projectile rotation up to 45° could be tolerated. Projectile rotation was usually less than 10° and always less than 20°. Six flathead 6-32 brass screws passing through the contact strips and the contactor ring were used, along with quick setting epoxy, to mount the contactor ring to the projectile.

To make electrical contact with the lamp, one of the bolts, passing through each high voltage contact strip, was threaded into a brass plug potted into the PMMA projectile flash head. A 12 gauge copper wire was connected to the other end of each brass plug by a screw. The other end of each wire was soldered to a brass fitting clamped to a flashlamp electrode. The final part of the lamp assembly was a thin nickel trigger wire which was wrapped around the flashlamp envelope just outside the tip of the anode, run close along the envelope on the side away from the impactor, wrapped around the envelope close over the cathode, then connected to the cathode.

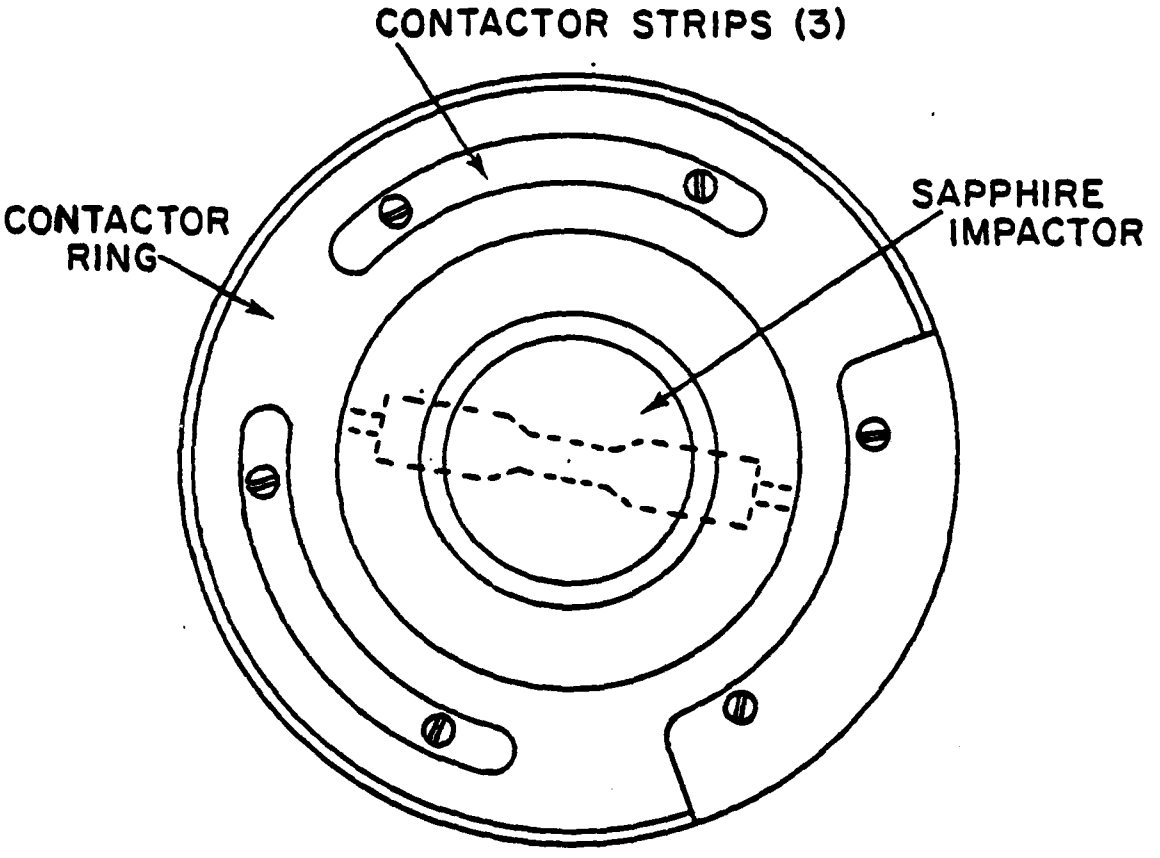

Figure 11 .--Projectile Head Face. After the flashlamp was potted into the projectile head, the projectile head was completed by installing the impactor and the PMMA contactor ring with its brass contactor strips.

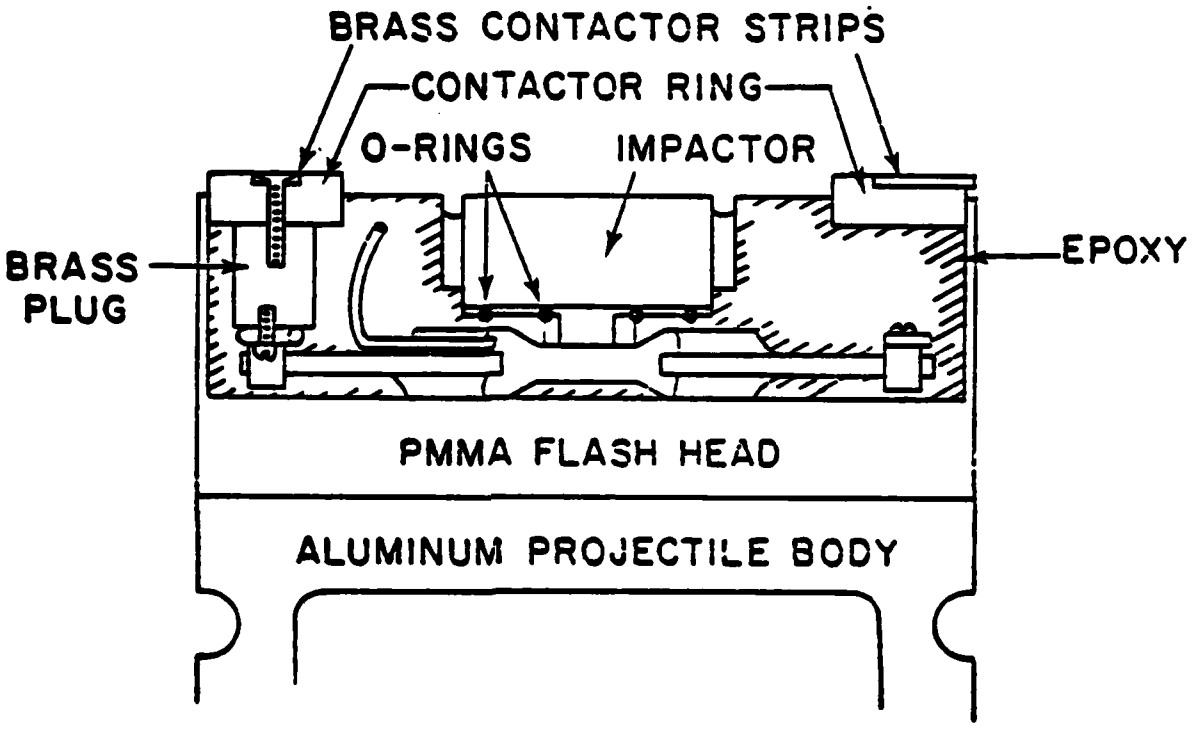

Figure 12 .--Projectile Head Cross Section. This figure shows how the flashlamp sits under the impactor and how electrical connection is made between the flashlamp and the brass contactor strips.

H. ELECTRONIC FUNCTIONS AND EQUIPMENT

Electronics were used to perform a number of tasks in conducting these experiments. These tasks included the following:

1. Provide high voltage power and a trigger signal to the flashlamp.
2. Provide timing signals to synchronize the flashlamp and oscilloscope traces with the experiments.
3. Record the signal from the photomultiplier in the streak camera.
4. Measure projectile velocity and streak camera mirror speed.

Figures 13 and 14 show the discharge circuits used to drive the flashlamps for the reflection experiments and the transmission experiments, respectively.

Figure 15 shows the circuit used to charge the trigger pin which detected arrival of the projectile at the target. Shorting the center conductor of the trigger pin to ground produced a negative voltage transient which was used to trigger the oscilloscopes and the flashlamp.

The photomultiplier which was added to the streak camera was an RCA type 4831. Since the photomultiplier is inherently much more sensitive than the photographic film, it was necessary to limit its sensitivity. This was accomplished by operating at a low cathode potential of - 650 V, and by placing a neutral filter of density 1 in the light path to the photomultiplier.

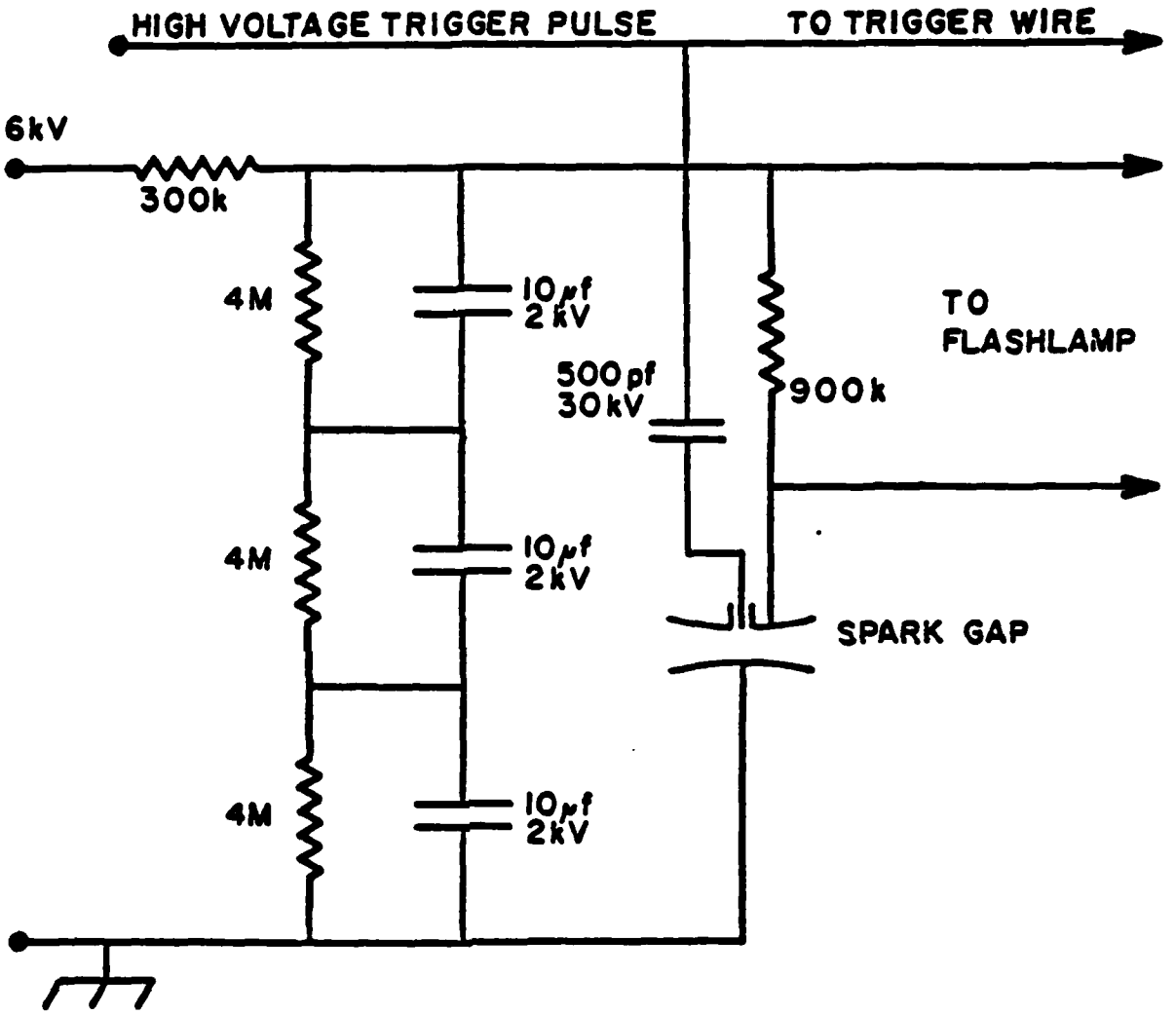

Figure 13 —Flashlamp Discharge Circuit. This circuit was used to drive the flashlamp in reflection experiments. The 300 kΩ resistance was located in the Cordin control unit. The other components were in a box near the flashlamp.

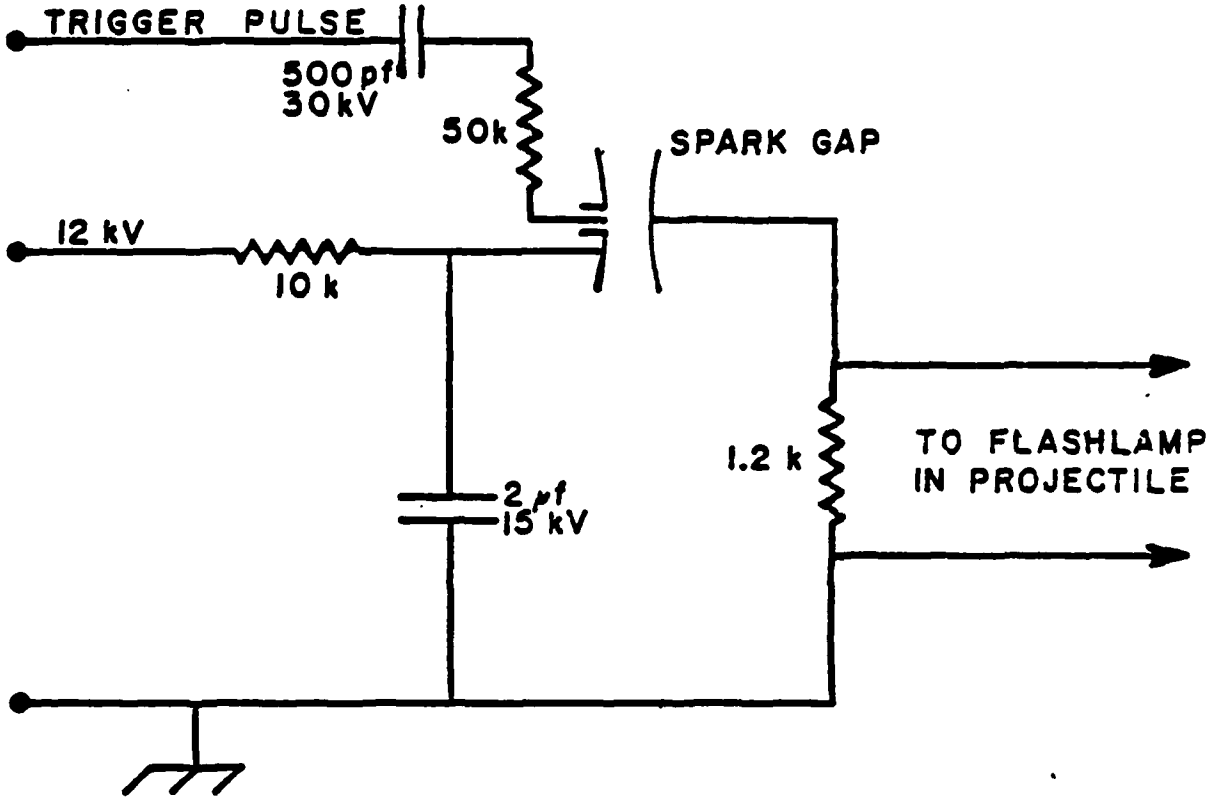

Figure 14 --Flashlamp-in-projectile Discharge Circuit.

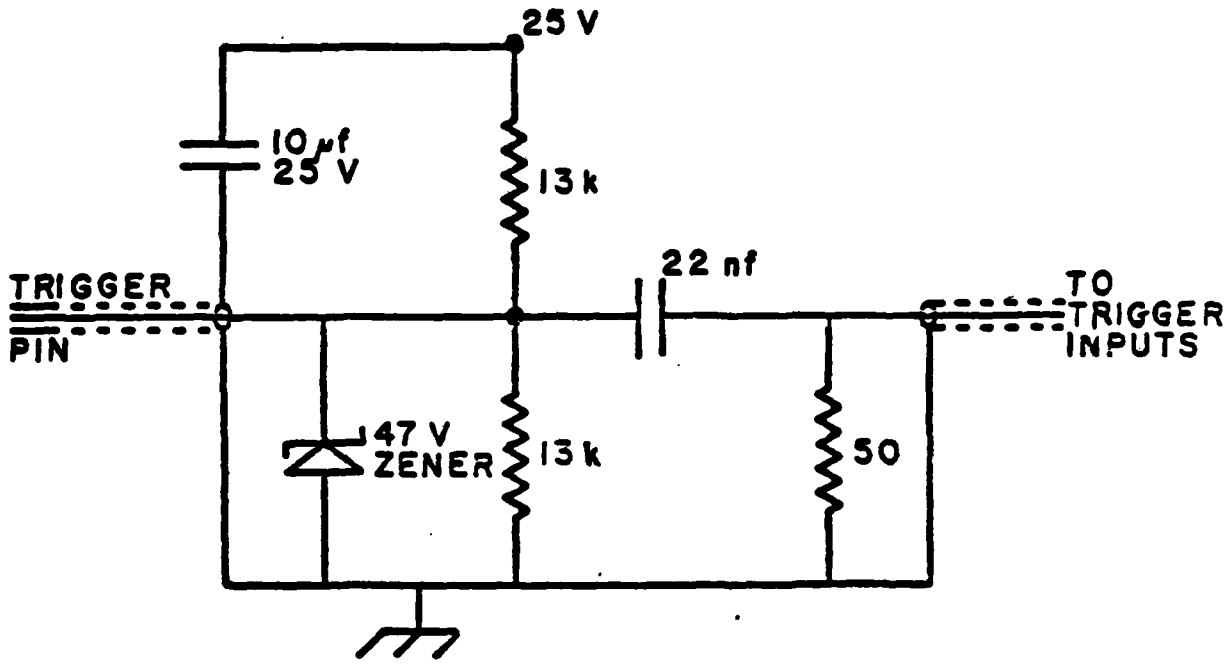

Figure 15 --Trigger Pulse Circuit.

Projectile velocity was determined by measuring the time required for the projectile to traverse the accurately measured interval between two small brass pins. There were four such pins forming three measured intervals. Associated with each measured pin was a similar grounded pin which made contact with the projectile just before the measured pin to insure that the projectile was a good electrical ground when it hit the measure pin. Tektronix DC 505-A universal counter timers were used to measure the time intervals.

The speed of the rotating mirror in the streak camera was determined by measuring the frequency of a signal from a pickup coil mounted near the magnetized rotor shaft of the streak camera mirror.

5.3 RESULTS AND DISCUSSION

Reflection Experiments

Pertinent data for each of the experiments are summarized in Table I. The 600 lines/mm grating was used in all the reflection experiments. It was set to record data only in the UV, as shown in Figs. 16-18. No reflectio measurements were made in the visible.

There were four reflection experiments with peak pressures of 99, 123, 83 and 127 kbars. Fig. 16 shows the streak camera and photomultiplier (PM) records for the 123 kbar experiment. Before the first shock enters the CS_2 the records show light transmitted through a bandpass from 2670 to 2 between two absorption regions in the CS_2 spectrum. At the time of impact th a slight decrease in light intensity. For the first 180 ns after impact, a 123 kbar shock was traveling through the front face of the cell. When it reached the CS_2-filled cavity, all light through the cell abruptly cut off for a period of about 30 or 40 ns. Light then reappeared and increased in intensity as the pressure in the cell rang up. The light which reappeared had a broad band spectrum. After reaching its peak intensity at C in the fig the light intensity recorded by the photomultiplier decayed in the interval C according to the relation

$$I(t) = I_{max}\left[0.73 + 0.27 \exp\left(\frac{-t}{280\,ns}\right)\right]$$

while the sample was held at peak pressure.

Fig. 17 shows the streak camera and PM records of the 83 kbar experiment The same features are evident, except for the decay, as were seen in the 123 kbar experiment. These included pre-impact transmission between 2850 and 2670 Å, a slight decrease in light at impact, extinction of nearly all light as the first shock tranversed the CS_2, and increasing reflection as the pressure in the sample rang up.

TABLE I

Data Summary for Reflection Experiments[a]

Shot No.	Impact Pressure, P_i (kbars)	Projectile Velocity (mm/μsec)	Cell Thickness (mm)	Pressure, Temperature & Transit Times for Reverberating Shocks			Number of Shocks Required to Reach 95% of Peak Pressure, Associated Temperature, and Time Required
				1st shock	2nd shock	3rd shock	
79-057	99	0.437	0.097	11 kbars 488°K 47 nsec	27 kbars 640°K 26 nsec	45 kbars 750°K 18 nsec	9 shocks 943°K 162 nsec
80-009	123	0.538	0.099	14 kbars 543°K 44 nsec	37 kbars 728°K 24 nsec	62 kbars 857°K 15 nsec	8 shocks 1048°K 136 nsec
80-010	83	0.365	0.069	8 kbars 453°K 36 nsec	21 kbars 580°K 21 nsec	35 kbars 676°K 15 nsec	9 shocks 866°K 128 nsec
80-013[b]	127	0.556	0.091	15 kbars 553°K 40 nsec	39 kbars 746°K 21 nsec	65 kbars 877°K 14 nsec	8 shocks 1068°K 123 nsec

600 l/mm grating, 41 Å/mm dispersion, 30 Å resolution on film.

No mirror in projectile.

There was ambiguity in the reflection setup in that light reflected from either the mirror or the CS_2 sample could reach the camera assembly and be recorded. The 127 kbar experiment shown in Fig. 18 was an attempt to determine where the reflection was occurring. The mirror was omitted in this experiment. This experiment produced a record that, after arrival of the shock at the CS_2 sample, was very similar to the 123 kbar experiment indicating that the broad band light was reflected from the shocked CS_2 layer, not the mirror. The record before impact shows some light in the 2700 Å bandpass. This was reflected from various sapphire-vacuum surfaces in the cell and impactor. The record from shot number 79-057 was very weak and is not shown, but it displayed the same general features as the other reflection experiments.

Reflection Experiment Summary

The observations made in these reflection experiments can be summarized as follows. The sample absorbed nearly all light for a period which correlates well with the time the first shock was traversing the sample cell. Following this, the sample became progressively more reflective while the pressure in the cell was ringing up. In the higher pressure experiments, 123 and 127 kbars, the reflectivity reached a peak then decayed while the sample was held at high pressure. This decay in the reflectivity did not occur in the 83 kbar experiment. The values of reflectivity were estimated to be in the range of 0.2 to 1.0, Table II

Table II --Shocked Carbon Disulfide Reflectivity Data

Shot	Maximum Pressure	$\frac{I_e}{I_p}$	Carbon Disulfide Reflectivity Max., Eq. (5.9)	Min., Eq. (5.10)
80-009	123 kbars	1.2	1	0.5
80-010	83 kbars	0.4	0.3	0.2

Transmission Experiments

Transmission experiments are summarized in Table II. All were done with a flashlamp in the projectile. The range of wavelengths was varied to cover both the near UV and the visible.

The first three transmission experiments had peak pressures of 55, 60 and 57 kbars, respectively, and used progressively thinner cells, 145, 10, and 0.8 μm, in attempts to obtain more light transmission. The first cell was thick enough that the transit times for the first few shocks could be resolved by the streak camera. Fig.19 shows the resulting streak camera record in which both absorption regions are seen to have expanded toward the red as the first shock traversed the cell. The blue edge of the central absorption band did not change. As the second shock started through the cell, the absorption regions expanded again, and the short wavelength absorption region merged with the longer wavelength region. At the time of the third shock, all light was cutoff to the edge of the film at 4070 Å.

In the next two experiments the cells were too thin for the streak camera to resolve the shock transit times, so the light was cut off abruptly, except for a slight amount at the long wavelength edge of the film in the experiment with the 0.8 μm thick cell. Records for this shot are shown in Fig. 20. The increase in light intensity at impact results from the elimination of two reflecting surfaces as the impactor and target sapphire make contact. Light cutoff occurs first in the absorption band at 3200 Å. Ring-up time, given in Table II, is 2 nsecs, and cutoff in the lower pass band (∿3050 Å) occurs approximately one nsec after shock arrival. The slit image on the film is 30 nsecs wide, so there may be considerable error in the apparent 9 nsec delay between cutoff at 3200 Å and 3050 Å.

TABLE III

Data Summary for Transmission Experiments

Shot No.	Impact Pressure, P_i (kbars)	Projectile Velocity (mm/μsec)	Cell Thickness (mm)	Pressure, Temperature & Transit Times for Reverberating Shocks			Number of Shocks Required to Reach 95% of Peak Pressure, Associated Temperature, and Time Required
				1st shock	2nd shock	3rd shock	
81-010[a]	55	0.243	0.145	5 kbars 396°K 85 nsec	12 kbars 482°K 56 nsec	19 kbars 552°K 42 nsec	11 shocks 739°K 389 nsec
81-012[a]	60	0.266	0.010	6 kbars 406°K 5.6 nsec	13 kbars 501°K 3.5 nsec	22 kbars 576°K 2.7 nsec	11 shocks 766°K 25 nsec
81-014[a]	57	0.253	0.0008	5 kbars 400°K 0.44 nsec	12 kbars 490°K 0.29 nsec	20 kbars 562°K 0.21 nsec	11 shocks 751°K 2.0 nsec
81-017[b]	58	0.257	0.0006	5 kbars 402°K 0.35 nsec	12 kbars 493°K 0.22 nsec	21 kbars 566°K 0.17 nsec	11 shocks 756°K 1.6 nsec
81-021[b]	121	0.531	0.0008	14 kbars 539°K 0.36 nsec	36 kbars 723°K 0.19 nsec	61 kbars 850°K 0.13 nsec	8 shocks 1040°K 1.1 nsec

a. 300 l/mm grating; 81 Å/mm dispersion, 40 Å resolution on film.

b. 150 l/mm grating; 163 Å/mm dispersion, 55 Å resolution on film.

The records from shot number 81-017 are shown in Fig. 21 Here the 150 line/mm grating has been used to include the visible. Cell thickness is again very small, approximately 0.6 μm, and the same delay as in the previous shot exists between shock arrival at the CS_2, as measured by extinction to 3300 Å and cutoff at 3600 Å in the pre-shock transmission region. The combined absorption regions expand abruptly to about 4100 Å then recede slightly to 3940 Å, during the next 200 nsec. The peak pressure in this experiment was 58 kbars.

The final experiment in this series was also with a thin cell, but with impact pressure P_i = 121 kbars; spectral range is again near UV and visible. Records are shown in Fig. 22. The photomultiplier record shows that integrated light intensity dropped to 0.08 of its preshock value within 20 nsec as the shock reached the carbon disulfide. The integrated intensity then increased slightly for about 30 nsec to about 0.09 of its preshock value. This small remaining intensity decayed to an undetectable level over the next 500 nsec. On the streak camera record, the 0.08 intensity level caused only a very slight darkening in the center of the film. Most of the light signal was abruptly cutoff. Some densitometer scans in the time direction are shown in Fig. 23. Rise times range from about 30 nsec to about 90 nsec. Taking the shortest values to result from streak camera resolution and densitometer response, there remains a fast relaxation time of the order of 50 nsecs to opacity in the central region in addition to the 500 nsec time for the integrated intensity recorded by the photomultiplier.

DISCUSSION

The broad features of the effect of shock waves on transmission in the liquid at an impact pressure of 58 kbars are shown in Fig. 21. Ring-up time to near impact pressure in this experiment was about 2 nsec, much less than the resolution of the recording system. Cutoff of transmitted light to 4100 Å was completed, i.e. intensity was reduced by at least a factor of ten, within the time resolution of the system. A density scan at 4750 Å shows no discontinuity when the shock enters the CS_2. The abrupt drop in intensity at wavelengths greater than 6000 Å is partially, if not entirely, due to the cutoff of UV contributions appearing in the second order.

Thickness of the cell in shot number 81-010, Fig. 19 was 145 μm, which was large enough that the effects of successive reverberations could be recorded. Three reverberations and the corresponding edge shifts of Region A are required to extinguish the upper transmission region; the lower one requires only two. The steps are blurred because of the 30 nsec window and limited spectral resolution system. With wavelengths of the successive steps chosen as shown in the figure, the dependence of shift frequency on calculated pressure and temperature is given in Fig. 22. The upper edge of the film in Fig. 19 is at the upper wavelength cutoff limit shown in Fig. 21. The linear dependence on pressure is remarkable and unexpected. Shown for comparison are a static pressure measurement at room temperature of CS_2 dissolved in ethanol made by J. Schnur and colleagues,[10] (Fig. 25), and a measurement at 123°C and near ambient pressure made in this laboratory (Fig. 24). The last mentioned point involves a subjective judgement, as can be seen by examining the displacement between the solid curves of Fig. 24. The eye, in scanning a film, picks out a point at a particular wavelength and reports it as the band edge. If this point corresponds to very small absorbance or very large absorbance, the edge displacement due to the increase in temperature will appear to be quite large. If it corresponds to intermediate absorbance, displacement is small. In the

present case two independent observers determined band edge positions by eye directly from film records at 293°K and 396°K and compared them with densitometer traces. Results were quite similar for the two observers and, when corrected for lag in the densitometer recorder, lay in the region of intermediate absorbance.

Neither static pressure nor temperature alone is adequate to explain the shifts produced by the shock waves, nor is their sum. It is possible that a combination of pressure and temperature would produce a much larger shift than either by itself, or that isolation of CS_2 molecules in solution removes some cooperative effect that is significant. It is important to note, in this regard, that Raman measurements of the symmetric stretch vibration in CS_2 are not significantly affected by the application of pressure, even above 12.6 kbars, where it transforms to a solid.[11] This supports the view that there is little molecular interaction in condensed CS_2 and that the static pressure measurements in solution can legitimately be compared with pure CS_2 measurements. It is obviously important to explore the effects of static pressure more thoroughly.

The third step in the motion of the upper band edge in Fig. 19 extends the edge to 4070 Å or beyond. Comparing this with Fig. 21 we see that this is near the ultimate limit of the edge for pressures in the neighborhood of 55-60 kbars. The third reverberation in Region A of Fig. 19 which produces this last edge motion, is seen from Table II to generate a temperature of 552°K (shot number 81-010). This is remarkably close to the temperature of 580°K at which Kleman found the absorption of R and S systems in the gas phase to be comparable to that in the T and V systems (Fig. 5.1-1). The 4300 Å upper limit of the R system lies beyond, but is comparable to the 4100 Å limit shown in Fig. 24. These near coincidences suggest that temperature may indeed play a significant, if not exclusive, role in shifting the band edges.

If temperature is significant, then it should be expected that cooling of the CS_2 in shot number 81-017 (Fig. 21) might play a role in regression of the band edge after the initial cutoff to 4100 Å. Cell thickness is only 0.6 μm. The thermal diffusion coefficient for sapphire is a hundred times greater than that of CS_2, so the sapphire acts approximately like a constant temperature sink insofar as the CS_2 layer is concerned. Using handbook values for thermal conductivity and specific heat of CS_2, and correcting for density, the 1/e-thing time for the CS_2-sapphire temperature difference is 315 nsec. The band edge in Fig. 21 after initial cutoff is quite fuzzy, but it looks as if the 1/e-thing time might be closer to 100 nsec. This is not unreasonable agreement, since diffusion may be considerably enhanced by pressure and temperature. However, regression of the band edge seems to stop at about 3940 Å. But, cooling continues and even with the 1/e-thing time of 315 nsec, temperature in the CS_2 should drop to about 325°K after 1000 nsec. The record of Fig. 21 shows nothing like this.

Cutoff of the lower passband in Fig. 19 gives less information than the upper. The apparent initial band edge at 2660 Å is influenced by rapidly diminishing sensitivity of the film with decreasing λ, by diminishing reflectivity of the grating, and by decreasing sensitivity of the camera as film edges are approached. The "true" band edge may be considerably below 2660 Å. The most we can say then is that the first, 5 kbar, shock shifts the band edge toward the red by at least 150 Å and the second shock closes the pass band entirely. If edge shift is proportional to pressure for this lower band, as for the upper, the amount of pressure required to close the 2660-2900 Å band gap does not exceed 8 kbars. Referring to Table I, we see that this is just the pressure of the first shock in shot number 80-010, so the occurrence of the cutoff region before reflection is in accord with the observations on

transmission shot number 81-010. Since first shock pressure in the other reflection shots is greater than 8 kbars, the cutoff preceding reflection is consistent with the transmission experiment in all cases.

Of the four reflection shots in Table I, three are shown in Figs. 16-18 the fourth, shot number 79-057, produced only a very faint record because of a filter in the light path and is not shown. All were in the UV.

Reflection coefficients for the experiments shown in Figs. 16 and 17 were defined in terms of the ratio PM(E)/PM(0) = R, where PM(E) is photomultiplier output in the experiment, e.g., the lower parts of Figs. 16 and 17 and PM(0) is photomultiplier output measured in a preshot test with empty cell. There is some variation in flashlamp output from shot to shot; this produced a corresponding uncertainty in R. There are six reflecting interfaces in the experiment, and these must be considered in calculating R.

Transmission and reflection coefficients for normal incidence at the interface between two refracting media are[12]

$$T = \frac{4nn'}{(n + n')^2} \qquad r = \left(\frac{n' - n}{n + n'}\right)^2 \tag{1}$$

Light signals in each section of the assembly can be divided into left-travelling signals, I_L, and right-travelling signals, I_R, as in Fig. 25. The equations for internal sections are

$$I_{R,J+1} = TI_{R,J} + (1 - T)I_{L,J+1} \tag{2}$$

$$I_{L,J} = (1 - T)I_{R,J} + TI_{L,J+1} \tag{3}$$

At the right-hand boundary the reflected light is lost because of the bevel on the back sapphire. Then

$$I_{Out} = TI_{R,5} \qquad I_{L,5} = TI_{In} \tag{4}$$

Define $R_J = I_{R,J}/I_{L,J}$; then, Eqs. (2) and (3) can be written

$$R_{J+1} = \frac{(1 - T) + (2T - 1)R_J}{1 - (1 - T)R_J} \tag{5}$$

Since $R_1 = 0.85$ is the reflectivity of the mirror at the far left, Eqs. (1) and (5) can be combined to yield a value of R for each region.

For the empty cell, denoted by superscript "e", there are only sapphire-air boundaries, so $T = 0.924$. Then $R_5^e = 0.857$. In the reflection experiment the cell is filled with CS_2. Let r_c be the reflectivity of the CS_2 sample, and let $I_{R,4} = 0$. $I_e \equiv I_{R,5}$ for the experiment, and $I_p = I_{R,5}$ for the empty cell. Then $R_5^c = r_e$ and $I_{R,5}^c$ is the light reflected from the CS_2-sapphire interface or from the shock front. Thus

$$I_{R,5}^c/R_5^c = I_{L,5} = I_{R,5}^e/R_5^e$$

or

$$R_5^c = R_5^e I_{R,5}^c/I_{R,5}^e \tag{6}$$

There is some uncertainty in the determination of R_5^c because the angle of incidence was not exactly normal and some of the reflected light did not fall on the entrance slit of the spectrograph. If no reflections are lost, Eq. (6) applies; if all are lost,

$$R_5^{c'} = I_{R,5}^c T^8 R_1/I_{R,5}^e \tag{7}$$

Eqs. (6) and (7) bound the CS_2 reflectivity. Values obtained for shots 80-009 and 80-010 are given in Table II. These values of reflectivity are extraordinarily large and are more nearly characteristic of a poor conductor than of a dielectric.

The phenomena of light extinction in the transmission experiments and of broad band reflection in the reflection experiments cannot be independent. Reflection measurements did not extend into the visible, but it is reasonable to suppose that, at pressures up to 60 kbars, reflection would cease at 4100 Å just as extinction does. Since reflection results from scattering, and extinction results from scattering plus absorption, it is evident that absorption is small compared to scattering. The magnitude of the reflection is such that it could not be generated by incoherent scattering; the solid angle subtended by the detector is too small. In order to be an effective reflector at a given frequency, the scattering must be temporally coherent, i.e., the phase lag between absorption and emission must be constant, and spatially coherent over an area of diameter d such that $\lambda/d \ll 1$. The thickness of the scattering layer must also be a small fraction of a wavelength in order that signals from front and back of the layer be additive. If we take scattering cross-section per unit area to be unity and thickness of the scattering layer to be $a \lesssim 0.1$ μm, then scattering cross section per molecule is

$$\sigma_s = 1/na$$

where n = number of molecules/cc = 0.17×10^{23}. Then

$$\sigma_s \gtrsim 10^{-17} cm^2$$

This is at least an order of magnitude greater than the absorption cross-section of CS_2 at the center of region A estimated from the film before shock arrival in Fig. 21.

The existence of a thin scattering layer of large cross section is in accord with the observation that light transmitted through a cell 0.6 μm thick is cut off as completely by the shock as in a thicker layer. This suggests that the scattering layer is associated with--perhaps takes place in--the shock front, but this is speculation. Two possible mechanisms which could account for coherent scattering of the observed magnitude are formation of conducting complexes and resonance fluorescence, possibly from excited states. Further investigations will be necessary before we can develop a more detailed understanding.

The spectrograms shown in Figs. 16 and 22 contain some evidence for the supposed decomposition reaction which initiated this work. The reflection experiment at 127 kbars impact pressure given in Fig.16 shows a decay of reflected intensity with a time constant of the same magnitude as those reported by Sheffield at the same temperature.[13] The extended cutoff shown in Fig. 23 for the 4800 Å region has a shorter relaxation time and a somewhat smaller pressure, 121 kbars. Both these phenomena may be manifestations of decomposition. The transmission record of Fig.21 is in accord with the observation by Yakushev, et al.,[14,15] of yellowing of visible light as decomposition approached.

Much of the foregoing discussion involves pressures and temperatures recorded in Tables II and III. The nature of these experiments requires that these temperatures be calculated from an equation of state. The one used here was developed by Sheffield.[12] It has some limitations, as do all such creations, but pressures should be quite accurate. Temperature errors have not been evaluated.

REFERENCES SECTION V

1. B. Kleman, Can. J. Phys. 41, 2034 (1963).

2. C. Jungen, D. N. Malm, and A. J. Merer, Can. J. Phys. 51, 1471 (1973).

3. G. Herzberg, Electronic Spectra of Polyatomic Molecules, (D. Van Nostrand Company, Inc., Princeton NJ, 1977).

4. A. E. Douglas and I. Zanon, Can. J. Phys. 42, 627 (1964).

5. G. E. Duvall, K. M. Ogilvie, R. Wilson, P. M. Bellamny, and P. S. P. Wei, Nature 296, 846 (1982) See also: K. M. Ogilvie and G. E. Duvall, J. Chem. Phys. submitted for publication (July 1982).

6. L. M. Barker and R. E. Hollenbach, J. App. Phys. 41, 4208 (1970).

7. Teflon and Viton are trademarks of DuPont Inc.

8. Torr Seal is a trademark of Varian Industrial Products.

9. G. R. Fowles, G. E. Duvall, J. Asay, P. Bellamy, F. Feistman, D. Grady, T. Michaels, and R. Mitchell, Rev. Sci. Inst. 44, 984 (1970).

10. J. Schnur, M. Abebe and P. Schoen, Naval Research Laboratory, Washington D.C. private communications.

11. A. J. Melveger, J. W. Brasch, and E. R. Lippincott, Appl. Optics 9, 11 (1970).

12. J. D. Jackson, Classical Electrodynamics, 2nd Edition (John Wiley and Sons, NY, 1975).

13. S. A. Sheffield, thesis. Washington State University (1978).

14. O. B. Yakusheva, V. V. Yakushev, and A. N. Dremin, High Temp. High Pressures, 3, 361 (1971).

15. O. B. Yakusheva, V. V. Yakushev, and A. N. Dremin, Russ. J. Phys. Chem. 51, 973 (1977).

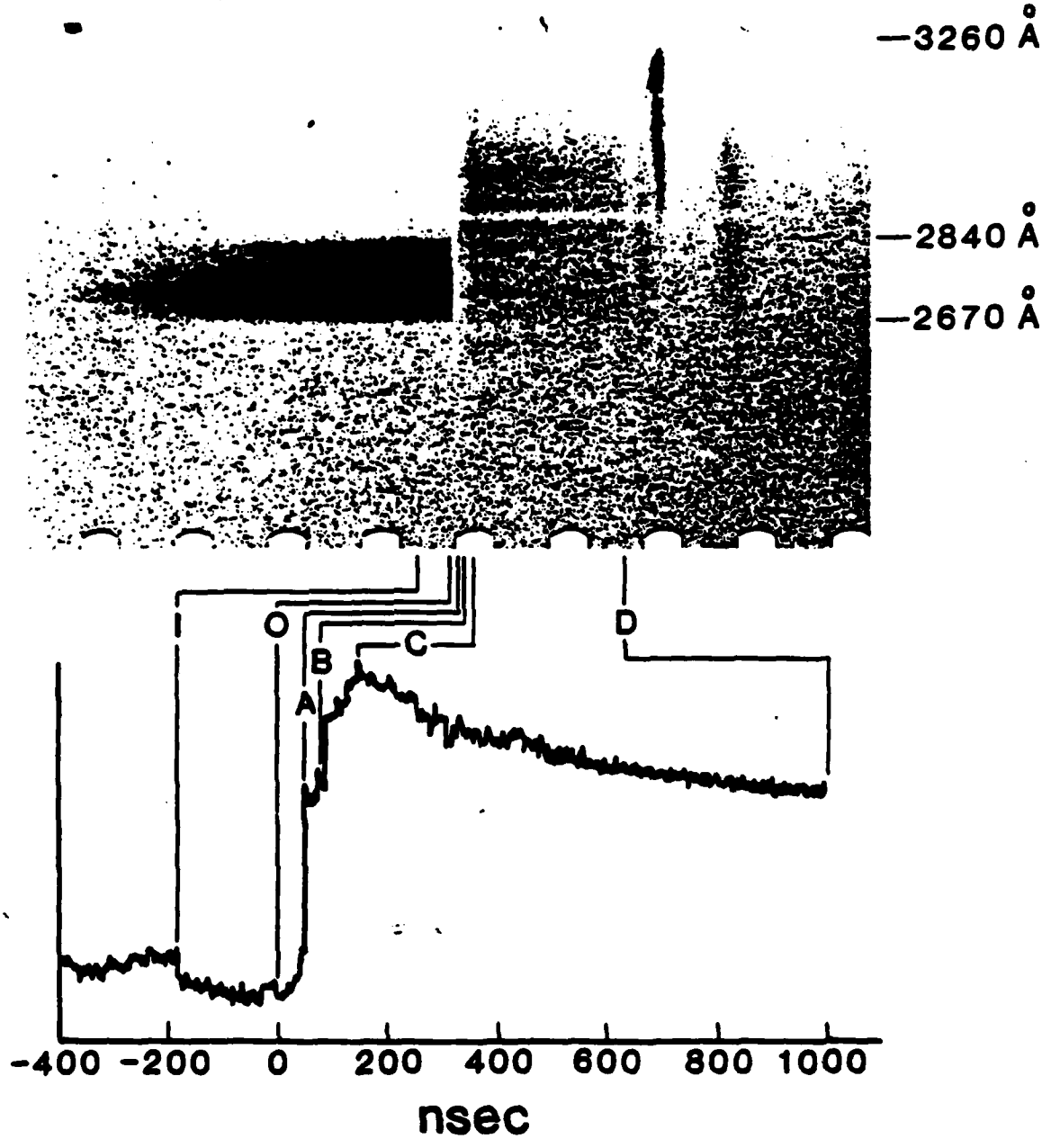

I Impact (-180 nsec)
O Shock reaches CS_2 (0)
A First shock reflects from back sapphire (44 nsec)
B Second shock reflects from front sapphire (68 nsec)
C Reverberating shocks exceed 118 kbars (136 nsec)
D Cell begins breaking up (≅ 1 μsec)

Fig. 16 Spectrogram and photomultiplier record for reflection experiment. Shot number 80-009, P_1 = 123 kbars.

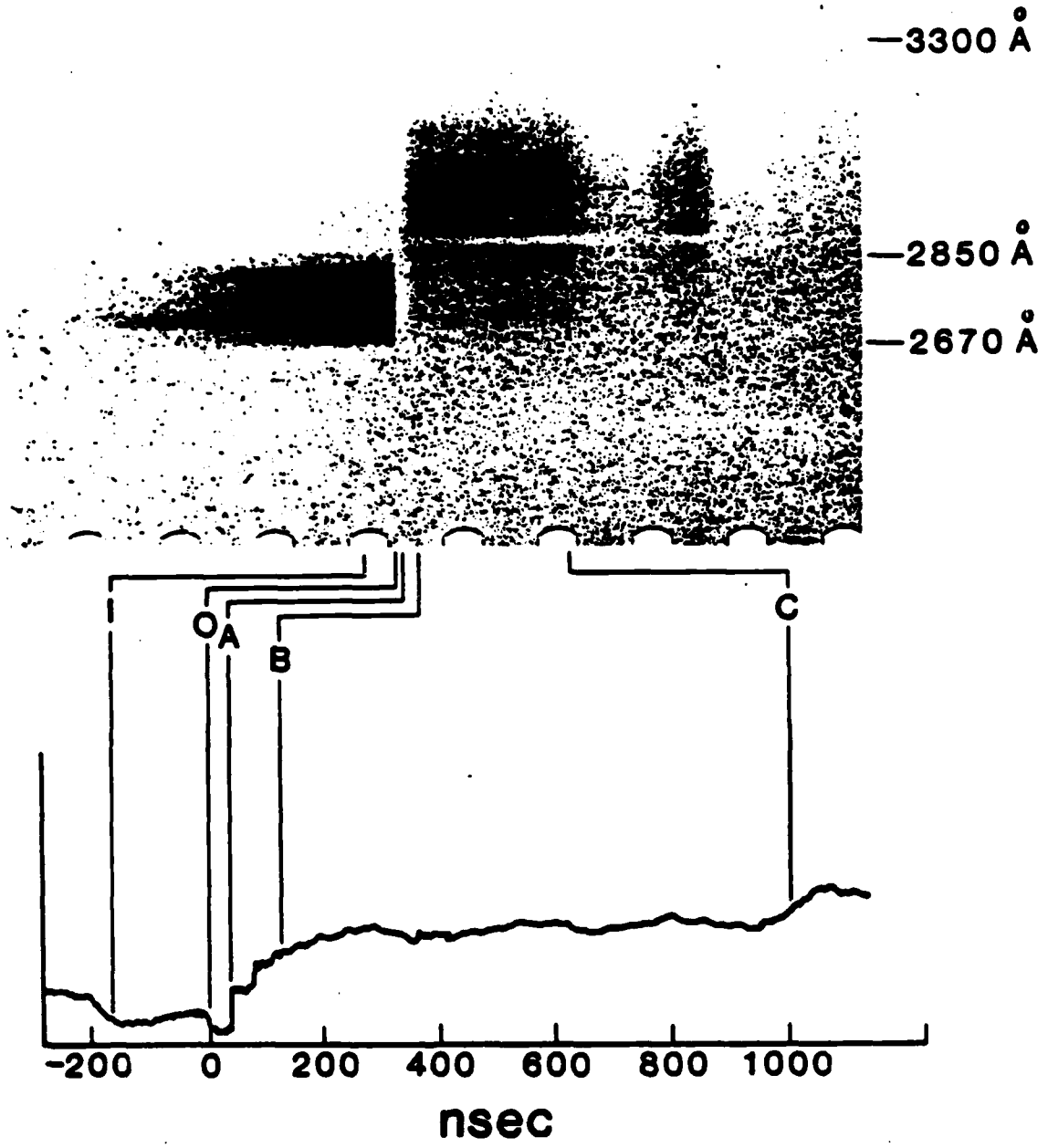

I Impact (-182 nsec)
O Shock reaches CS_2 (0)
A First shock reflects from back sapphire (36 nsec)
B Reverberating shocks exceed 79 kbars (128 nsec)
C Rarefactions enter optical path (≅ 1 μsec)

Fig. 17 Spectrogram and photomultiplier record for reflection experiment. Shot number 80-010, P_1 = 83 kbars.

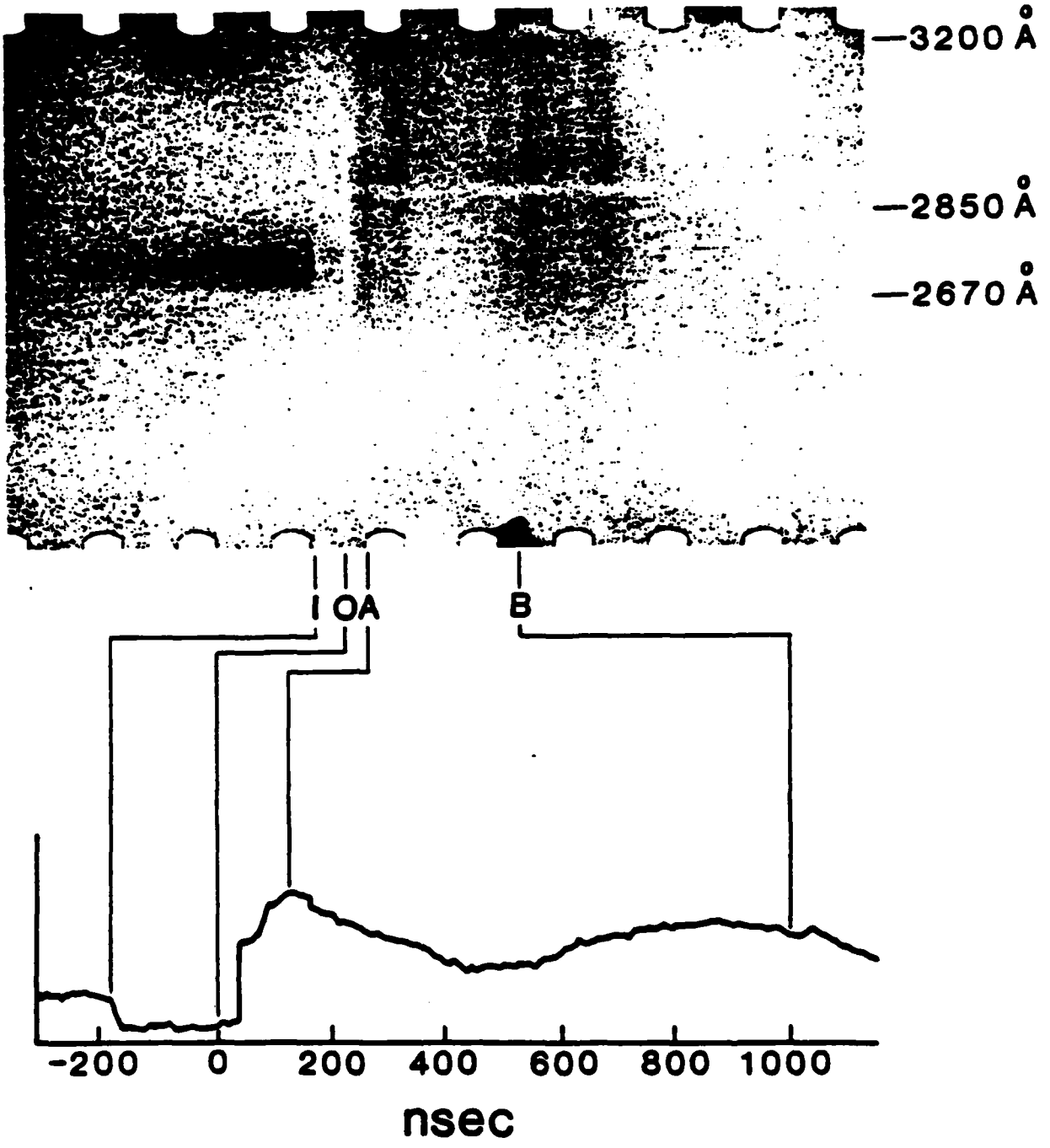

I Impact (-180 nsec)
O Shock reaches CS_2 (0)
A Pressure exceeds 119 kbars (123 nsec)
B Rarefactions enter optical path (≅ 1 μsec)

Fig 18 Reflection experiment with no mirror in the projectile. Shot number 80-013, P_1 = 127 kbars.

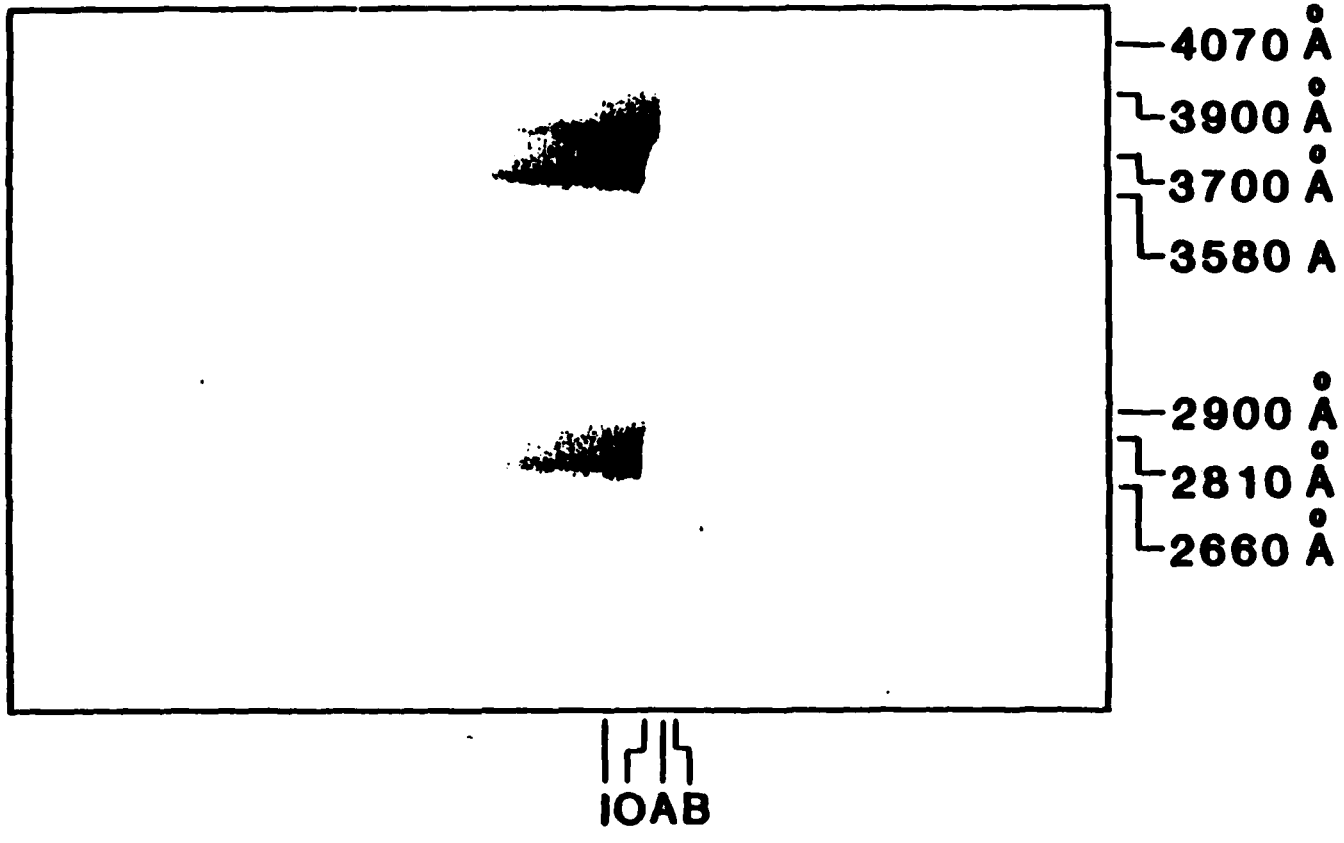

I Impact (-182 nsec)
O Shock reaches CS_2 (0)
A First shock reaches back sapphire (85 nsec)
B Second shock reaches front sapphire (141 nsec)

Fig. 19 Transmission experiment with 145 μm thick CS_2 sample. Shot number 81-010, P_1 = 55 kbars

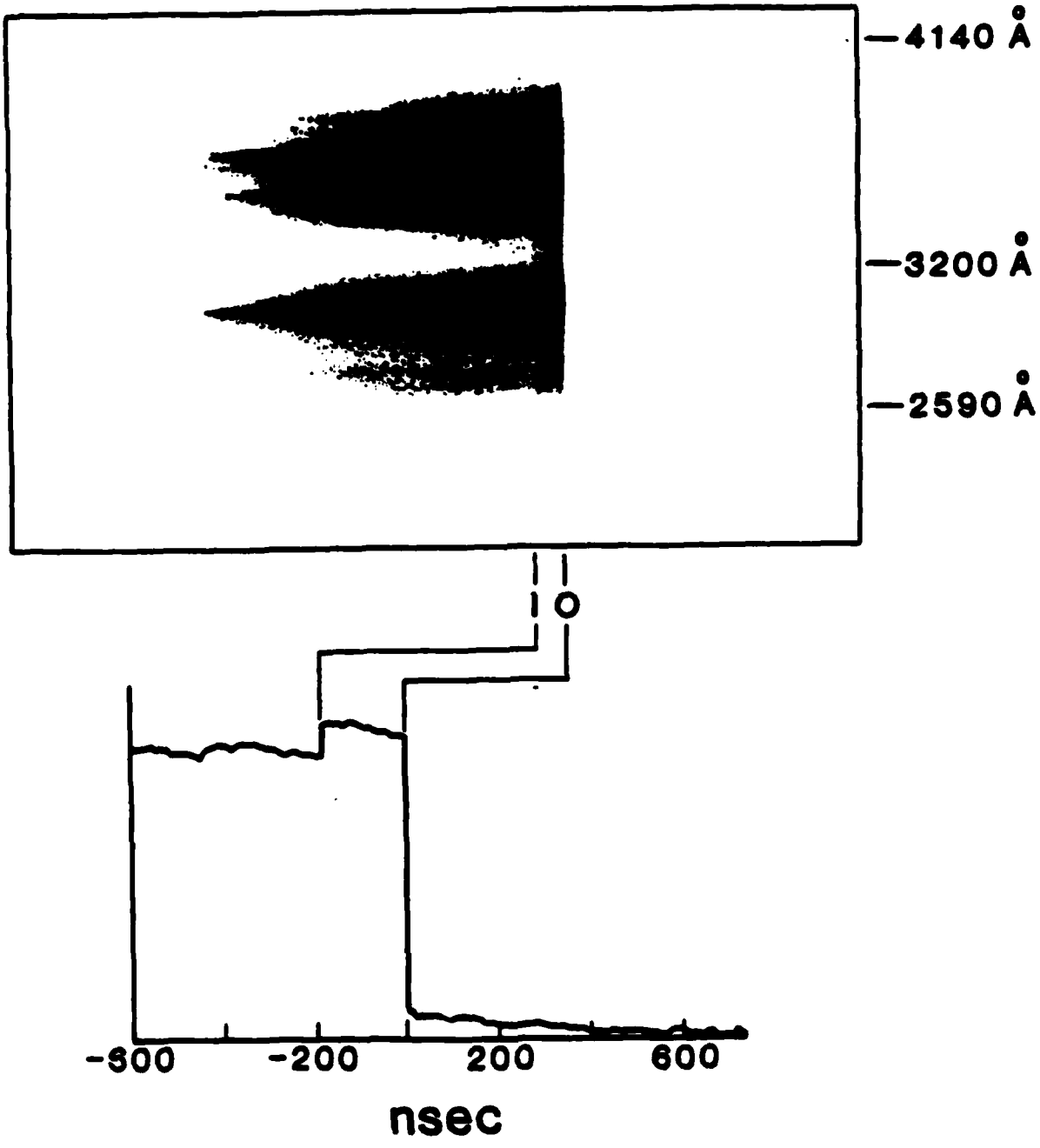

I Impact (-183 nsec)
O Shock reaches CS_2 (0)

Fig. 20 Transmission experiment with CS_2 thickness of 0.8 μm. Shot number 81-014, P_1 = 57 kbars.

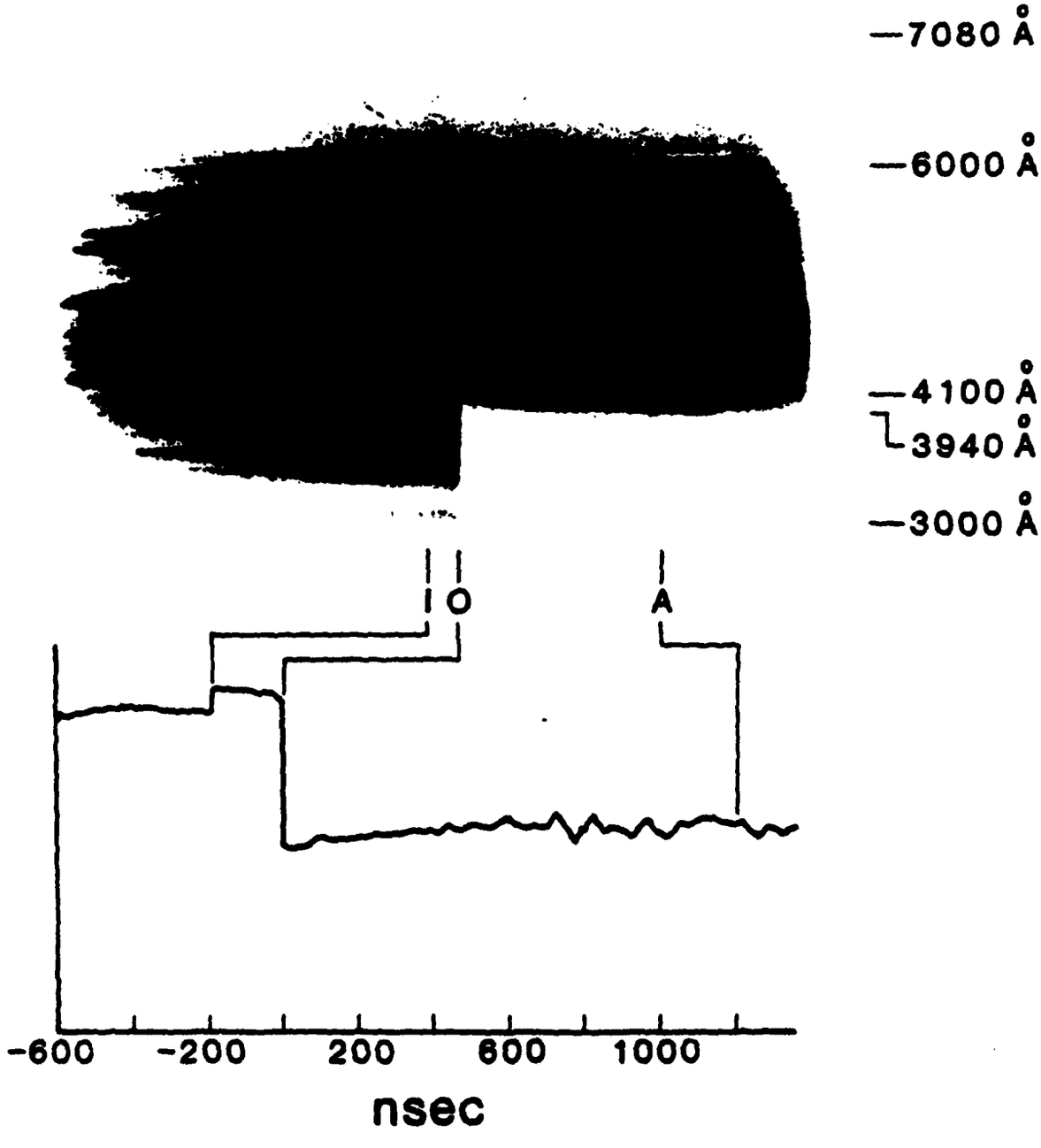

I Impact (-182 nsec)
O Shock reaches CS_2 (0)
A Rarefactions enter optical path (≅ 1.2 μsec)

Fig. 21 Transmission in near UV and visible. 0.6 μm cell. Shot number 81-017, P_1 = 58 kbars.

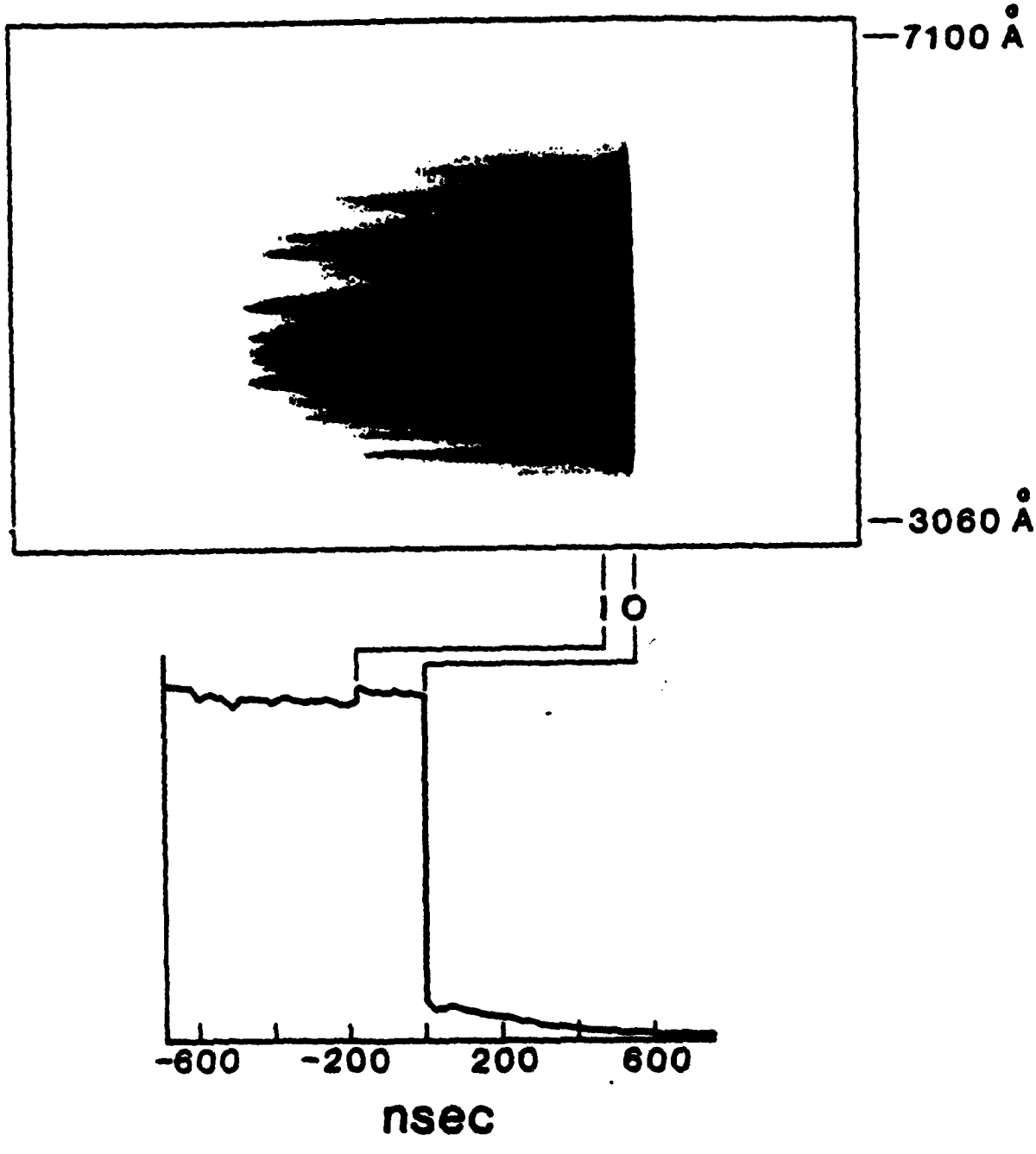

I Impact (-180 nsec)
O Shock arrival at CS_2 (0)

Fig. 22 Transmission experiment with 0.8 μm cell.
Shot number 81-021, P_1 = 121 kbars.

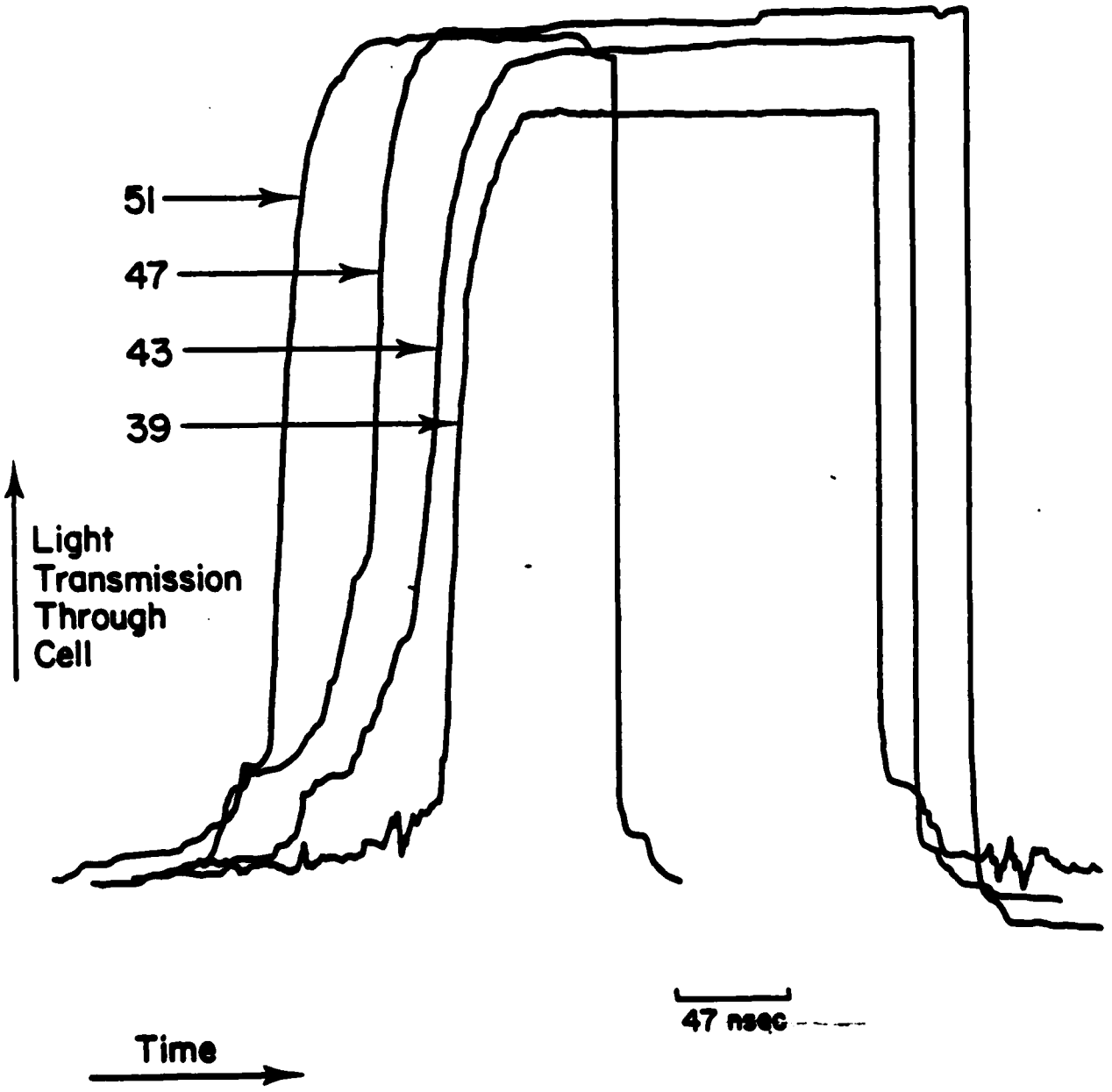

Fig. 23 Densitometer scans in the time direction for shot number 81-021. Curve number 51, 3700 Å; 47, 4350 Å; 43, 5000 Å; 39, 5640 Å.

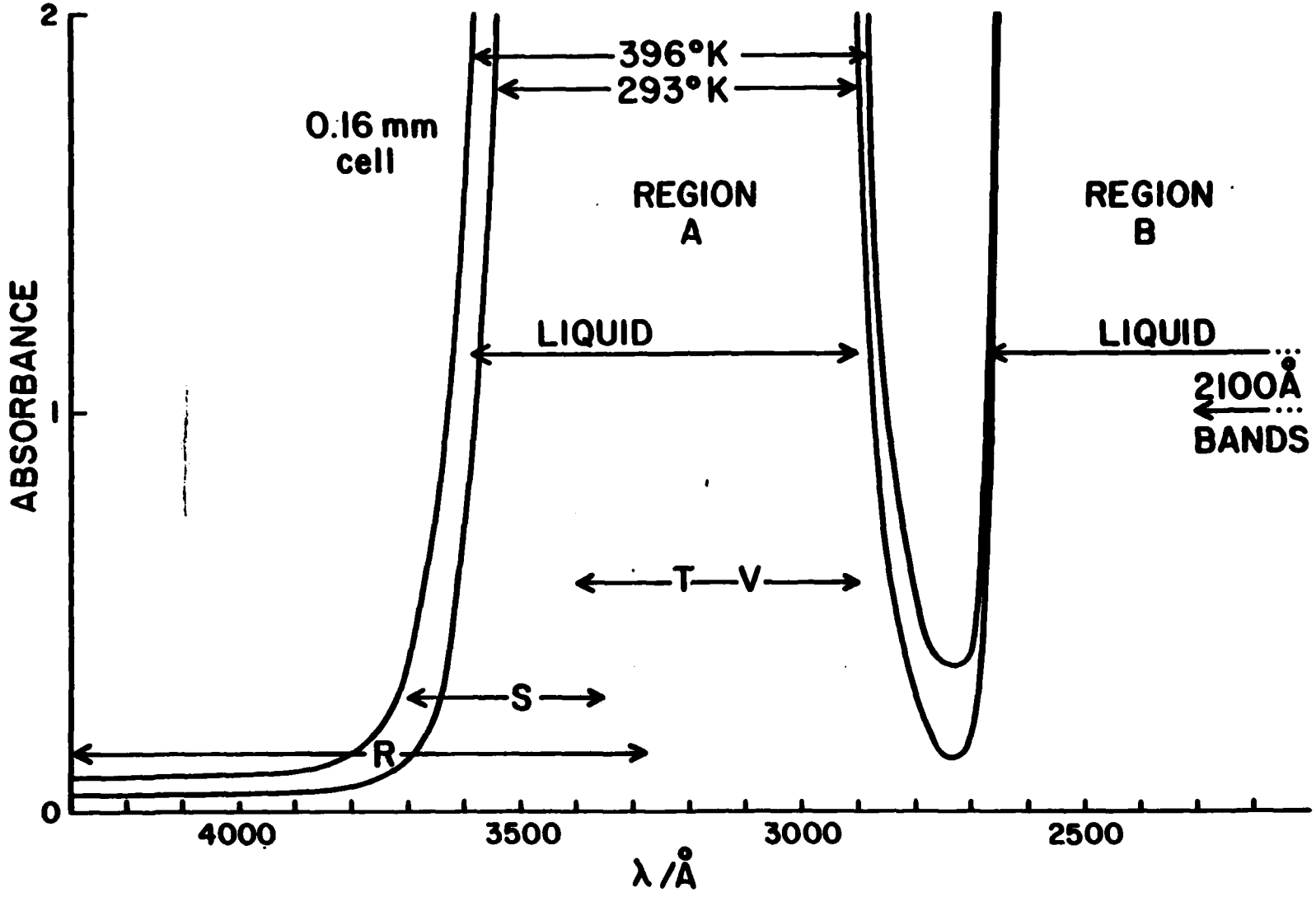

Fig. 24 Spectral regions of absorption in Carbon Disulfide. The R, S, T, V and 2100 Å bands are different electronic transitions in the gas phase. The curves labeled "liquid" show the extent of the unshocked absorption regions at two different temperatures.

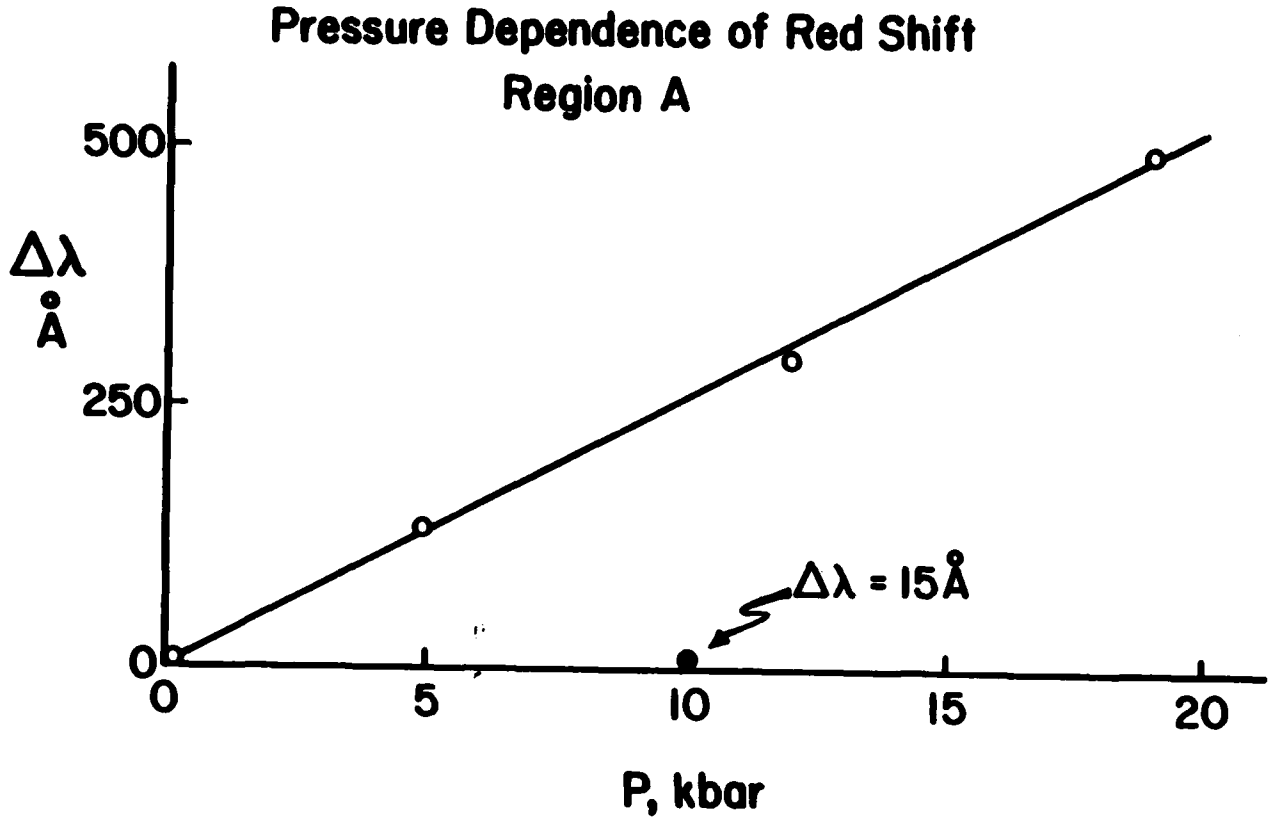

Fig. 25 Red shift of the red edge of absorption Region A (Fig. 24).

a) Pressure dependence b) temperature dependence

x = successive shock reverberations (Fig. 19).
● = static measurement in solution at room temperature (Ref. 1).
Δ = static temperature measurement (Fig. 24).
Slope is 26 Å/kb.

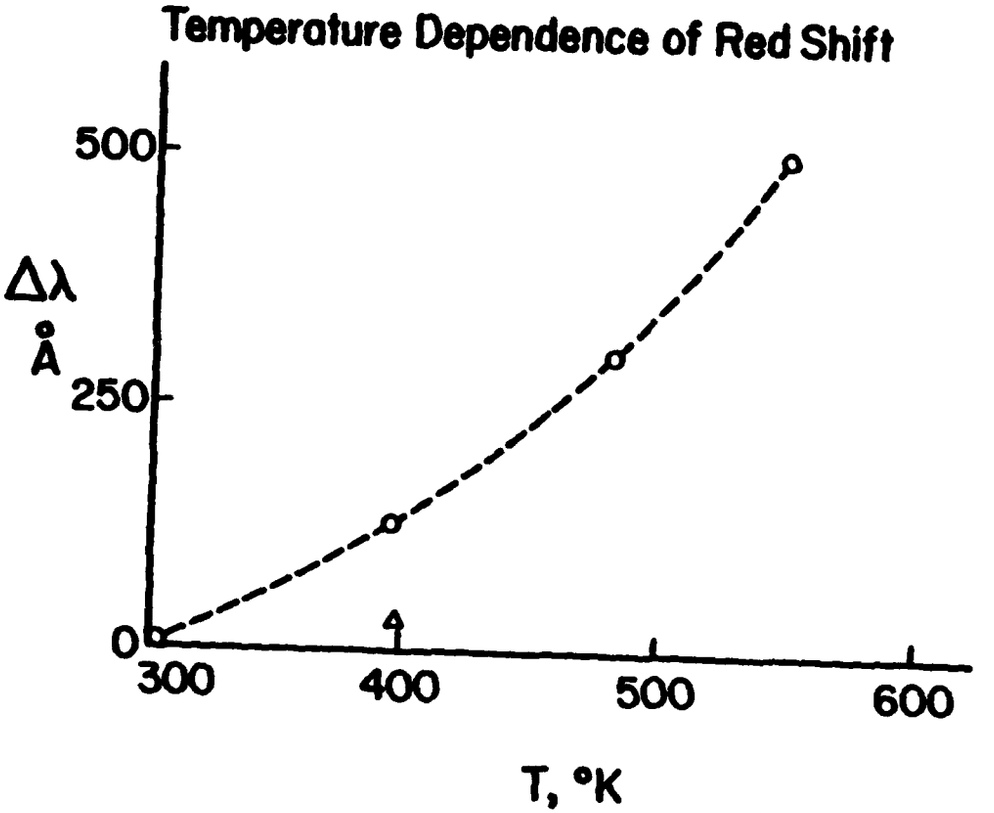

Fig. 25 continued

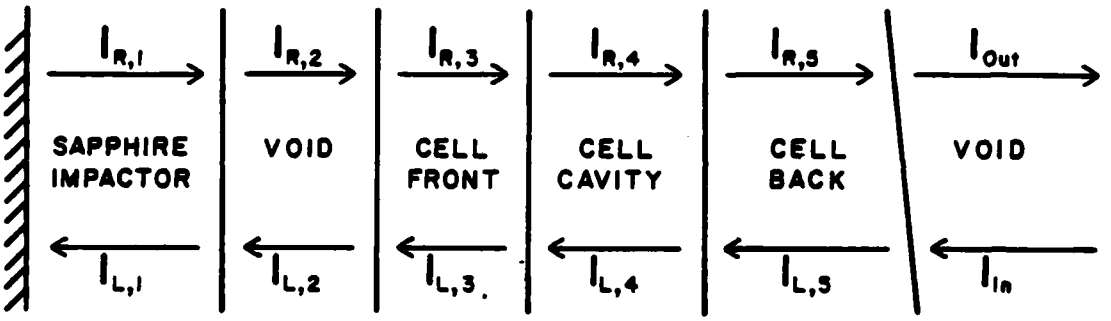

Fig. 26 Schematic for calculation of light intensities in the cell and impactor.

VI. DISCUSSION

There are basically two questions one wishes to address in the kinds of shock wave studies described here:

1. Do shock wave techniques provide a useful tool for studying the kinetics of chemical reactions?
2. Are shock-induced chemical reactions explicable in terms of conventional chemical kinetics, or are there hitherto unexplored areas of chemistry involved?

The answer to the first is certainly yes, as demonstrated by Sheffield's work in Section IV and to a lesser extent by Ogilvie's work in Section V. These, however, are but demonstrations of feasibility. The breadth of application and the utility of the information obtained remains for further investigation.

Answers to the second are not yet forth coming. It has several subdivisions: are the high pressures and temperatures produced by the shock sufficient to produce the observed effects? Are P and T along with the anticipated creation of defects by the shear accompanying the shock front enough? Are there non-equilibrium energy transfers from shock to molecule which increase its reactivity? Is there shear deformation of molecules which contribute to the observed effects? Answers to these questions will not be easily obtained. Spectroscopy is clearly a useful tool. As long as it produces unexpected results, its potential cannot be fully evaluated. The spectra are unusual; they are not the kind described in textbooks, but they clearly contain information.

Cumulative evidence suggests that the shock front is locally very thin--probably a few atomic spacings or less. This certainly makes it possible to think of impulsive energy transfer to vibrational states as a method of non-equilibrium excitation. The most clear-cut piece of data that relates to this is obtained from shot number 81-010, where a 120-150 Å shift of the red absorption edge is obtained from the initial 5 kbar shock. This appears to be out of agreement with static pressure and temperature measurments by a wide margine. But the static data are equivocal and additional experimental support is required. A new result obtained since Ogilvie's work was completed is surprising. Rapid adiabatic compression of the CS_2 sample by a high amplitude compressive ramp shows, within experimental error, the same rate of shift, approximately 25 Å/kbar, as the shock. In entirely different experiments, ultronsonic absorption, it has been found that liquid CS_2 has relaxation times of 5-50 nsec associated with vibrational states. Rise time in the ramp experiment was about ½ kilobar per nsec, which suggests a relation among the experiments.

Our research is continuing along the lines described in Section V, with support and cooperation of other laboratories, particularly J. Schnur and colleagues at NRL, and Kaufman and Koski at John Hopkins. Efforts are underway to do Raman spectroscopy in Shaner's group at Los Alamos, and Graham and colleagues at Sandia, Albuquerque, are preparing to do optical spectroscopy. With this concentration of effort, we may reasonably expect some definitive answers to Question 2 in the fairly near future. With these will come further clarification of the role of spectroscopy in shock wave chemistry.

APPENDIX A

Some Notes on the Transition from Deflagration to Detonation

APPENDIX A

Some Notes on the Transition from Deflagration to Detonation

Insufficient attention has been paid to the logical framework provided by the Chapman-Jouguet theory of detonation and deflagration for understanding of the deflagration to detonation transition. A brief outline of its application to the problem is presented here.

The C-J is a steady state theory, applying strictly only to those hydrodynamic and reaction processes which are plane, one-dimensional, and unchanging in time when viewed from the correct moving coordinate system. But we may expect that the theories will apply approximately to unsteady processes, provided significant changes do not occur during times the order of [reaction zone thickness/propagation velocity]. Moreover, the C-J theories are independent of reaction time and reaction zone thickness provided only that the flow into and out from the reaction zone is one-dimensional and steady. This means for example, that combustion involving propellant fracture falls within the framework of the theory as long as flow into and out from the fracture-combustion region is one-dimensional and steady. Deviations from steady flow can be treated as perturbations, if they are not too large. With this in mind one can proceed as follows.

AB in Fig. 1 is the unreacted R-H curve of the propellant, centered at (p_o, V_o). CDEF is the locus of states of the fully-reacted products reached from the initial state p_o, V_o by detonation or combustion in a plane reaction front. The line OD is parallel to the V-axis;

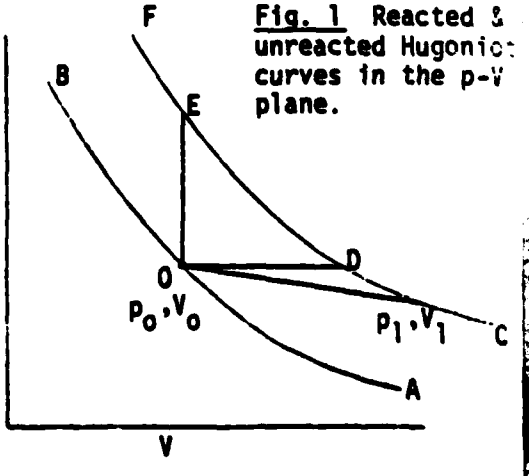

Fig. 1 Reacted & unreacted Hugoniot curves in the p-V plane.

OE is parallel to the p-axis. States on CD are reached from O by combustion; those on EF are reached by detonation. The speed of propagation of the plane reaction front with respect to the material ahead of it is

$$U^2 = V_o^2 \frac{p_1-p_o}{V_o-V_1}$$

On CD, $p_1 < p_o$, $V_o < V_1$. On EF, $p_1 > p_o$, $V_o > V_1$. In order for deflagration to progress, p_o must be greater than p_1. If $p_o = p_1$, $U = 0$ and the reaction zone does not move. Since unburned material must be consumed continually in order for the reaction to exist, such a constant pressure deflagration cannot exist, but it provides a bound to possible deflagrations. In order for the deflagration to accelerate p_1-p_o must get larger, V_o-V_1 smaller, or both. The reacted products are normally gaseous; if the unburned material is solid, the two curves AOB and CDF can be expected to converge at high pressures and diverge at low pressures. It is not possible, then, for U to become very large if (p_o,V_o) remains fixed and p_1 decreases. U may, in fact, decrease as p_1 decreases because of the rapid increase of V_1 at low pressures.

It follows, then, that if a deflagration is to accelerate, the point (p_o,V_o) must migrate upward, and it must do so more rapidly than (p_1,V_1). That is, the mean pressure in the deflagrating system must increase and p_o must remain greater than p_1. If p_o-p_1 remains constant as p_o increases, the wave will continue to accelerate because V_1-V_o will grow smaller. This requirement that $\bar{p} = (p_o+p_1)/2$ increase implies that the region of deflagration must somehow be protected from the influence of pressure-free boundaries. Otherwise the pressure-relief waves being continually produced by these boundaries will overtake the region of deflagration and will reduce $\bar{p}$, thus preventing the acceleration.

This isolation from the effects of pressure-free boundaries can be accomplished in two ways: by confining the explosive in a fixed volume so that the released energy

of combustion can drive the pressure up, or by causing the boundaries to be far-removed from the region of deflagration; i.e., by using a very large piece of explosive. "Large" in this context will depend on propagation velocities and reaction rates.

The conditions which must be created in order for the deflagration to transform to a detonation can now be described more precisely. If, by judicious adjustment of the mean pressure and the pressure difference, we can arrive at the situation indicated in Fig. 2, where the straight line connecting the "initial state", (p_o,V_o), and the undisturbed or reference state, (p_o',V_o') intersects or is tanget to the reacted Hugoniot, we will have arrived at a condition in which a non-reactive shock wave can produce the transition from p_o',V_o' to p_o,V_o. This, combined with subsequent deflagration to p_1,V_1, constitutes a detonation wave.

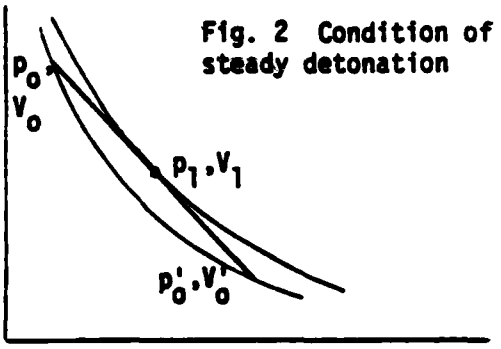

Fig. 2 Condition of steady detonation

These ideas are elementary, and for that reason may be useful. It is probably reasonable to assume that, in one-dimensional flow, we can always find a plane ahead of the reaction zone where no reaction has occurred and a plane behind where all reaction is complete, or nearly complete. If we make the separations between these planes, i.e., the reaction zone, as small as possible, we should be able to direct our attention to what is happening outside the reaction zone without too much concern about the details of what is happening inside. To be sure, one of the things that will occur is that the reaction zone thickness will change as the deflagration accelerates, but that effect may not be of primary significance.

I have made some preliminary attempts to map the course of an accelerating reaction in the p-u plane without notable success. It will require careful thought and probably the working out of examples with various boundary conditions. But I think it will be worth the effort.